Proceedings of the 5th International Young Earth Scientists (YES) Congress

9–13 September 2019
Berlin, Germany

edited by
Thomas Rose
Gino de Gelder
David Fernández-Blanco
Melanie J. Sieber

Recommended citation:
Rose, T., de Gelder, G., Fernández-Blanco, D., Sieber, M. (Eds.) 2020: Proceedings of the 5th International Young Earth Scientists (YES) Congress “Rocking Earth’s Future”, 9–13 September 2019, Berlin, Germany. German YES Chapter & GFZ German Research Centre for Geosciences, 148 p.
https://doi.org/10.2312/yes19.

Imprint

German YES Chapter
Helmholtz-Zentrum Potsdam Deutsches GeoForschungsZentrum GFZ –
DEUTSCHES YES CHAPTER
Telegrafenberg
D-14473 Potsdam

Published in Potsdam, Germany
August 2021

https://doi.org/10.2312/yes19

All contributions in this volume were reviewed by international peers.

Organising committee

Thomas Rose
Gamze Koç
Milena Latinovic
Gerlis Fugmann
Michael Haas
Lena Stark
Konstantin Kühnel
Christine Bismuth

Editorial Board

Thomas Rose
Gino de Gelder
David Fernández-Blanco
Melanie J. Sieber

Cover photo: The NASA/German Research Centre for Geosciences GRACE Follow-On spacecraft launches onboard a SpaceX Falcon 9 rocket, Tuesday, May 22, 2018, from Space Launch Complex 4E at Vandenberg Air Force Base in California. © NASA/Bill Ingalls

Contents

Society at Risk – Impacting Earth Phenomena

Brave New World – Advanced Technologies in Earth Sciences

Beyond Printing – Communicating Science

Foreword

The 5th International Young Earth Scientists (YES) Congress took place in 2019, a time of daily news about a changing climate, environmental contamination and reduction in the availability of primary natural resources. Humankind threatens its own habitability on our fragile planet Earth and approaches the “point of no return”. As part of humankind, we young earth scientists are inevitably affected by these problems, but uniquely positioned, thanks to our understanding of the complex Earth System, to prevent humankind from reaching the “point of no return”. Our knowledge is key to preserving a planet worth living in, and with it, we can help develop strategies to sustain resource management, as well as to prevent, minimise, and promote resilience against the negative impacts of human-made climate change.

Although geoscientists always had a globalised understanding of how Earth systems work, now it is time to communicate our knowledge about the wonders and mysteries of this exceptional planet to the wider public. In doing so, we have a unique opportunity to foster viable global solutions for global problems.

The congress brought together young earth scientists from more than 40 countries, specialists in all fields of Geoscience. It successfully provided an environment to facilitate state-of-the-art research exchange, strategies for tomorrow’s challenges and knowledge dissemination, to the wider public and to governmental institutions alike. It also helped to promote contacts and collaborations among young researchers and with other participants, and provided a unique possibility to gain insights from the research done by young geoscientists from all over the world.

In addition to the participants, many more young earth scientists successfully submitted abstracts but were not able to join the congress for numerous reasons. They all were invited to submit extended abstracts for this peer-reviewed proceedings volume.

The organisation of the YES 5th International Young Earth Scientist (YES) Congress required manpower and time. First and foremost, the rest of the organizational and editorial teams are indebted to the exceptional efforts of Thomas Rose, who made both the congress and the abstract proceedings a reality. Further, the congress would not have been possible without the support from our partners, the Geo.X network and the GFZ (Helmholtz Centre Potsdam German Research Centre for Geosciences). We are deeply acknowledged to Gamze Koç, Milena Latinovic, Gerlis Fugmann, Michael Haas, Lena Stark, Konstantin Kühnel, and Christine Bismuth for taking up the challenge to organise this conference. We also cherish the great efforts made by F&U confirm to ensure the success of YES Congress 2019. Only the support of our sponsors allowed us to organise the congress in its final form. Among them, the BGR (Federal Institute for Geosciences and Natural Resources) and the initiative “Research in Germany” not only offered financial support but also directly contributed to the programme by offering field trips, summer schools, and networking activities.

Significant efforts were also necessary to prepare the extended abstract proceedings, in part aggravated by the COVID-19 pandemic. We are thus especially grateful to our reviewers for their commitment in preparing their detailed constructive reviews, and to Dorothea Hansche and Ilka Wellm for their support in the online publication.

The editors
Thomas Rose, Gino de Gelder,
David Fernández-Blanco & Melanie J. Sieber

Partners and Sponsors

GFZ Helmholtz Centre Potsdam

GeoX

BGR Bundesanstalt für Geowissenschaften und Rohstoffe

Research in Germany Land of Ideas

Supported by

DFG Deutsche Forschungsgemeinschaft German Research Foundation

AWI

IUGS Commission on "Global Geochemical Baselines" Mapping the Geochemistry of the Earth's Land Surface

APECS Association of Polar Early Career Scientists

DAAD Deutscher Akademischer Austauschdienst German Academic Exchange Service

Reviewers

- Aribowo, Sonny; ISTerre, Université Grenoble-Alpes
- Bioresita, Filsa; Department of Geomatics Engineering, Institut Teknologi Sepuluh Nopember
- Blommaert, Hester; ISTerre, Université Grenoble-Alpes
- Brill, Fabio; GFZ Potsdam
- Cattaneo, Cristina; RFF-CMCC European Institute on Economics and the Environment and Centro euro-Mediterraneo sui Cambiamenti Climatici
- Chowdhury, Proteek; Keith-Weiss Geological Laboratories, Rise University
- De Gelder, Gino; ISTerre, Université Grenoble-Alpes
- Demetriades, Alecos; IUGS Commission on Global Geochemical Baselines
- Dewitte, Olivier; Royal Museum for Central Africa
- Erkan, Dilruba; Université de Paris 1 Panthéon-Sorbonne
- Fernández-Blanco, David; Barcelona Center of Subsurface Imaging, Institut de Ciències del Mar (CSIC)
- Franken, Gudrun; BGR
- Gallen, Sean F.; Colorado State University
- Gholamrezaie, Ershad; GFZ Potsdam
- Groth, Juliane; Helmholtz-Zentrum für Umweltforschung
- Gupta, Ratnamani; National Natural Resources and Fiscal Commission
- Jayangondaperumal, R.; Wadia Institute of Himalayan Geology
- Mahmoudian, Hossein; University of Tehran
- Marscheider-Weidemann, Frank; Fraunhofer Institute for Systems and Innovation Research ISI
- Massuyeau, Malcolm; University of Münster, Institut für Mineralogie
- Mathew, Manoj; Universiti Teknologi PETRONAS
- Meijers, Maud; Senckenberg Biodiversity and Climate Research Centre (SBiK-F)
- Oha, Ifeanyi; University of Nigeria
- Oji, Ruhollah; University of Guilan
- Öztürk, Ugur; GFZ Potsdam
- Papeschi, Samuele; University of Pisa
- Pedoja, Kevin; Université Caen
- Pownall, Jon; University of Helsinki
- Prasad, Ritika; University of Lucknow
- Provenzano, Giuseppe; ISTerre, Université Grenoble-Alpes
- Rault, Claire; BRGM
- Rose, Thomas; Ben Gurion-University of the Negev, Sapienza - University of Rome
- Sharma, Vishwa Raj; University of Delhi
- Sieber, Melanie Jutta; GFZ German Research Centre for Geoscience; University of Potsdam
- Singh, Bhanwar Vishvendra Raj; Department of Geography, Mohanlal Sukhadia University, Udaipur, India
- Taddeo, Sophie; Chicago Botanic Garden
- Wessels, Richard; Utrecht University
- Wittmer, Dominic; Joint Research Centre, European Commission
- Wolf, Isabelle; University of Wollongong
- Zareeipolgardani, Bahareh; ISTerre, Université Grenoble-Alpes
- Zeckra, Martin; University of Potsdam
- and 10 anonymous reviewers

Plenary lecture

High-Tech Metals Are Key Elements for Future Technologies – How Are Their Global Market Situations and What Are the Challenges?

Volker Steinbach[1,✉], Johannes Perger[1], Siyamend Al Barazi[1], Maren Liedtke[1]

[1] Federal Institute for Geoscience and Natural Resources, Germany
✉ volker.steinbach@bgr.de

Keywords: Emerging Technologies, E-Mobility, Renewables, Raw Material Requirements, Mineral Resource Markets

1. Future Technologies

New and emerging technologies have the potential to change global raw materials requirements substantially. This in turn can have significant impacts on the commodity markets such as sharp increases in prices and supply bottlenecks in the short-term as well as an increase in production in the mid-term.

An abrupt increase in demand driven by technological change rather than other economic developments can have implications on the availability of raw materials and their secure and sustainable supply. Hence, reliable estimates of potential future raw materials for emerging technologies are imperative to avoid negative economic impacts and supply shortages. This is particularly true for minor metals markets where future demand can potentially significantly outstrip current supply.

The study “Raw materials for emerging technologies 2016” (Marscheider-Weidemann, et al., 2016), looks at future raw material demand for 42 emerging technologies until 2035. Future mineral raw material demand is central to this publication and will be discussed for three of those technologies, namely wind energy and photovoltaics in the chapter renewables, and e-mobility. It is predicted that those technologies have the largest growth rates among renewable energy systems. Table 1 gives an updated overview of selected mineral raw materials, their demand in 2013 in key emerging technologies and their potential future demand in 2035 for these applications. A factor of 3.8 in the column D35/P17 means that we expect a sectoral demand of heavy rare earths (Dy/Tb) for magnets, e-cars, and wind power in 2035 accordingly 3.8 times the global production in 2017.

2. Renewables

To address the challenges of climate change, the global greenhouse gas emissions have to decrease drastically. The international community of states signed an agreement at the Climate Change Conference in Paris 2015. The Paris Agreement has the objective of holding the increase in global average temperature to well below 2 °C above pre-industrial levels. For that, the consumption of carbon dioxide intensive fossil-based energy carriers like oil or coal has to be diminished and substituted by low-carbon types of energy – mostly renewable energies. In 2017, renewables had a share of around 18 % of global primary energy consumption (BGR, 2019). Regarding global electricity generation, 25 % already came from renewable sources in 2018 (fig. 1, BP, 2019).

Global shares in electricity generation in 2018 from wind and photovoltaics were 4.8 % and 2.2 %, respectively (BP, 2019). This status quo is still significantly below the targets stipulated in the Paris Agreement, and thus requiring increased efforts to develop the sector. With renewable sources accounting for approximately 70 % of newly installed electricity worldwide in 2017 (BGR, 2019), the development of these technologies has implications on current and

Table 1: Estimated future sectoral demand for selected mineral raw materials for key emerging technologies – for a comparison the sectoral demand of these technologies in 2013, global primary production in 2017 and quotient of the sectoral demand in 2035 and the global production in 2017 are displayed as a factor (after Marscheider-Weidemann, et al., 2016).

Metal	Emerging technologies	Sectoral Demand 2013 [Tonnes]	Sectoral Demand 2035 [Tonnes]	Global primary Production 2017 [Tonnes]	Factor D35/P17[1] [rel. unit]
Heavy rare earths (Dy/Tb)	Magnets, e-cars, wind power	2.000	7.400	1,950[2]	3,8
Light rare earths (Nd/Pr)	Magnets, e-cars, wind power	29.000	64.000	24,000[2]	2,7
Lithium	Lithium-ion batteries, lightweight airframes	610	110.000	49,000[2]	2,3
Cobalt	Lithium-ion batteries, X[3] to Liquid	5.000	120.000	118,500[4]	1,0
Indium	Displays, thin layer photovoltaics	230	360	714[5]	0,5
Gallium	Thin layer photovoltaics, Integr. circuit, white LED	90	130	320[6]	0,4

[1] Demand for emerging technologies 2035 divided by primary production 2017; [2] BGR Database; [3] X = biomass, gas or coal; [4] Al Barazi, 2018; [5] Anderson, 2019; [6] Jaskula, 2019.

Proceedings of the 5th International YES Congress
DOI: 10.2312/yes19.13

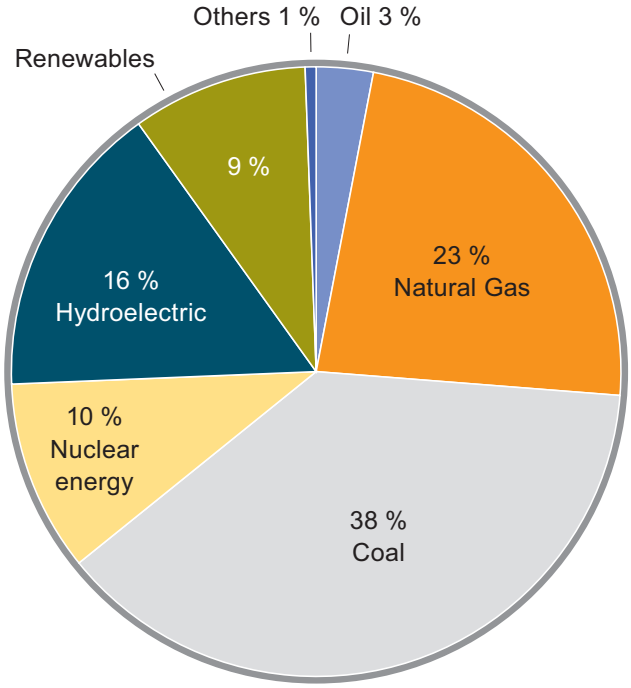

Figure 1: Global Electricity Generation by Fuel Type in 2018 (BP 2019). Hydroelectric is counted towards renewables in our definition.

future mineral raw materials demand.

2.1. Wind Energy

Wind turbines require a variety of different mineral raw materials for their construction including steel for tower and nacelle, cement for the base, compound materials for the rotor, different materials for the electronics and (especially in offshore facilities) rare earth elements, boron and iron for the permanent magnet for the generator. Low-maintenance offshore wind turbines contain neodymium, praseodymium, terbium and dysprosium in permanent magnets (Buchholz and Brandenburg, 2018). Until 2030, the wind offshore sector is expected to grow at a much higher rate (around 20 % per annum) than the onshore sector (around 10 % per annum) (IEA, 2019) and demand of rare earth elements for use in wind turbines will remain high (Xia-Bauer et al., 2013).

Metal	Demand for wind energy until 2030 [Million tonnes]	Production in 2017 [Million tonnes]
Iron	212	1264[R]
Copper	4,69	23.58[R]
Aluminium	4,69	61.24[R]
Chromium	2,23	7.38[R]
Nickel	1,64	2.04[R]
Tin	0,37	0.36[R]
Molybdenum	0,32	0.31[M]
Rare Earth Oxides	0,17	0.13[M]

[R] Refinery Production; [M] Mined Production

Table 2: Total sectoral demand of mineral raw materials for 1,625 GW wind energy capacities from 2018 to 2030 and their global production in 2017.

In 2017, a total of 1085 TWh was derived from wind energy worldwide (BP, 2019). Global installed capacities were 539 GW in 2017, of which 52 GW was newly added that year (WWEA, 2018). Our estimates show that 1 MW requires a mineral raw material demand of 130 t of iron, 2.8 t of copper, 2.8 t of aluminium, 1.4 t of chromium, 1 t of nickel, 0.22 t of tin, 0.2 t of molybdenum, and 0.11 t of rare earth elements (rough estimates from different sources; see legend fig. 2). Figure 2 shows the development of global installed wind power capacity as well as the raw material demand for the newly installed capacity in 2017.

According to the Sustainable Development Scenario of the International Energy Agency (IEA, 2019), energy derived from wind energy should reach a total of 4,355 TWh in 2030, requiring capacities of 2,164 GW to reach that goal (assuming a constant ratio between

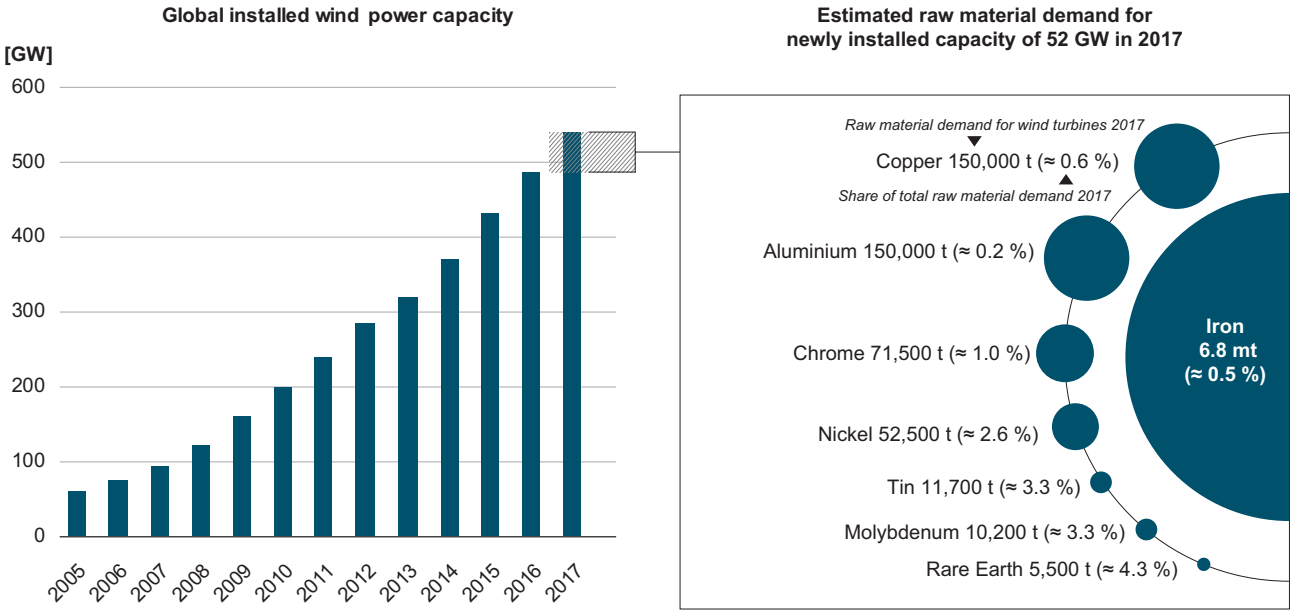

Figure 2: Global installed wind energy capacity (WWEA, 2018) and mineral raw material demand of the newly installed capacity in 2017 (Marscheider-Weidemann, et al., 2016, BGR Database; own calculations).

Metal	Demand for photovoltaics until 2030 [Million tonnes]	Production in 2017 [Million tonnes]
Iron	446	1264[R]
Copper	5,75	23.58[R]
Tin	1,21	0.36[R]
Lead	0,71	11.61[R]
Aluminium	0,27	61.24[R]
Zinc	0,01	13.22[R]

[R] Refined Production

Table 3: Total sectoral demand of mineral raw materials for 2,621 GW photovoltaic capacities from 2018 to 2030 and their global refinery production in 2017.

installed capacity and power generation). Taking the 539 GW installed capacity in 2017, an additional 1,625 GW would have to be added until 2030 (assuming current installed capacities stay in operation without power loss – hence the estimate is just an inferior limit). Table 2 lists the volumes needed until 2030, at current mineral raw material requirements, to achieve this goal.

The demand of powerful magnets for wind turbines has a particularly significant impact on the relatively small rare earth elements market. Rare Earth Elements (REE) are used in many high-tech sectors. Globally, they are used in catalysts (18 %), powerful magnets (30 %) and metallurgical applications (18 %), as well as in polishing, special glasses and ceramics (Kingsnorth, 2018). Producing wind energy is one of the key drivers for future REE demand.

REE are summarized as a group of 15 different elements which can be grouped into light and heavy REE (in most deposits, heavy REE have proportions below 10 %). Since the rare earth elements show similar chemical properties, they are jointly enriched in the ore forming processes. In consequence, they are mined and processed together.

In 2018, global mine production was approximately 175,000 t rare earth oxides (REO, official production excluding illegal mine production in China). Extraction is heavily concentrated in China (68 %). Additional rare earth elements production came from Australia (10.5 %, processing in Malaysia), Myanmar (9 %, processing in Myanmar and China), the USA (6 %, processing in China), Vietnam (2.7 %, processing in China and possibly Vietnam), Russia (1.5 %, processing in Estonia, Russia and Kazakhstan), India (1.1 %, processing in India and China), Thailand (0.6 %, processing in China), Burundi (0.4 %, processing in China), Brazil (0.3 %, processing in China) and Malaysia (processing in China).

There are only few processing facilities for rare earth oxides and elements with high-purity processing and refining facilities of rare earth ores worldwide. Today refining is taking place in China, Malaysia, Russia, Estonia and Kazakhstan. The processing of heavy rare earth elements is concentrated in China.

2.2. Photovoltaics

With approximately 90 % of shipped units and owing to their efficiency, thick-layer cells of the crystalline silicon wafer technology dominate the photovoltaics market. Thin-film technology could have the largest future potential because of their reduced raw material requirement (Buchholz and Brandenburg, 2018) as well as a continuously improving efficiency factor.

Photovoltaics had a global installed capacity of 402 GW in 2017, with 99 GW newly installed that year. Photovoltaics grew much faster than wind energy over the past few years. We estimate that 1 MW of installed photovoltaics capacity requires 170 t of iron, 2.2 t of copper, 0.46 t of tin, 0.27 t of lead, 0.10 t

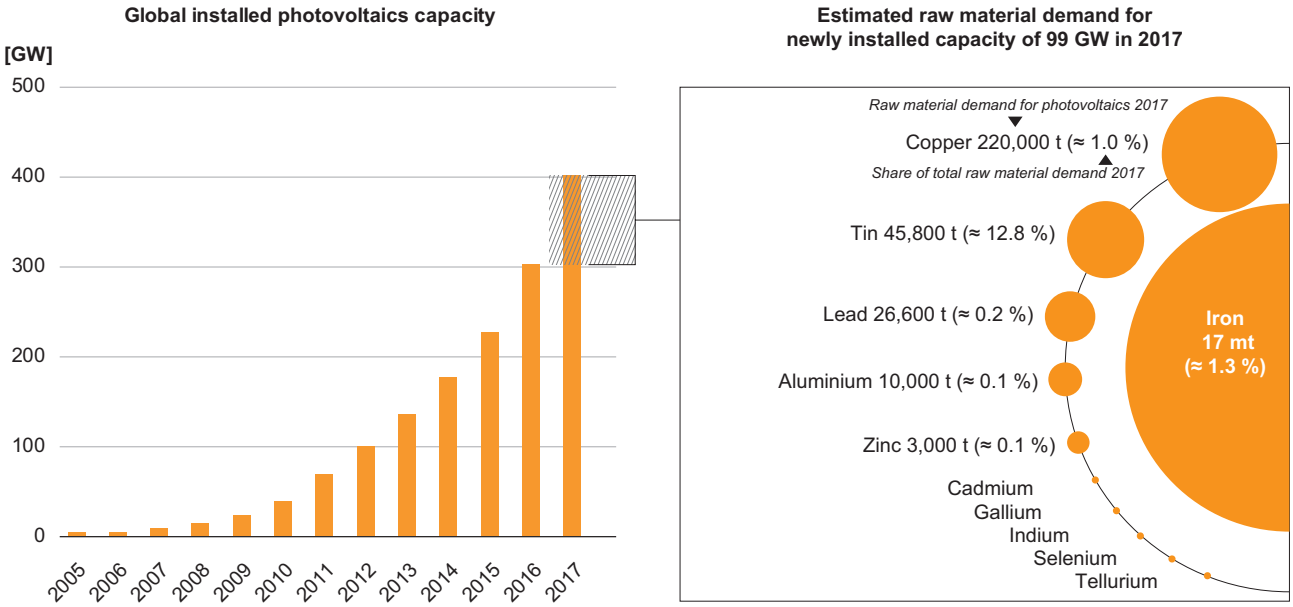

Figure 3: Global installed solar power capacity (SolarPower Europe, 2018) and mineral raw material demand of the newly installed capacity in 2017 (Müller, 2018, World Bank Group, 2017, BGR Database, own calculations).

of aluminium and 0.03 t of zinc (rough estimates from different sources; see legend fig. 3). Figure 3 shows the development of the global installed photovoltaic capacity as well as the raw material demand for the newly installed capacity in 2017.

According to the Sustainable Development Scenario of the International Energy Agency (IEA, 2019), energy derived from photovoltaics worldwide should reach 3,268 TWh in 2030, requiring additional capacities of 3,023 GW to achieve this target (assuming a constant ratio between installed capacity and power generation). In addition to global operating capacities in 2017, 2,621 GW would have to be added until 2030 (assuming current installed capacities stay in operation without power loss – hence the estimate is just an inferior limit). Table 3 lists the volumes needed until 2030, at current mineral raw material requirements, to achieve this goal.

Especially thin-film solar cells could have a huge impact on the small markets of indium, gallium, selenium, cadmium and tellurium. In thin-film solar cells, the coating materials consist, for example, of amorphous silicon (a-Si), copper indium (gallium) diselenide (CIGS) or cadmium telluride (CdTe). The technology-specific raw material demand of the semiconductor compounds of the thin-film elements of CdTe and CIGS thin-film modules is shown in table 4. The product-specific raw material content per electrical output (watt peak, Wp) depends on the layer thickness, the composition and efficiency of the solar cell, material losses during coating or rejects and the proportion of recycled material.

Gallium, germanium, indium, selenium, and tellurium are typical minor metals or high-tech metals. Minor metals share the following common characteristics (Gunn, 2014):

- low content in ores and minerals: few milligram to gram per tonne
- small markets with comparably low production rates: 10 to 100,000 tonnes/year
- mainly mined as by-products of principal metals
- complicated or undeveloped end-of-life recycling
- low substitution possibilities: very specific material characteristics

By-products can be produced from concentrates, mattes, slags or ash from primary or secondary sources due to market circumstances. Common sources for gallium are bauxite deposits and zinc ores. Coal and zinc ores can be the source for germanium, zinc ores further for indium, and copper ores for tellurium and selenium. The annual production as well as the country concentration is shown in figure 4.

3. E-mobility

In addition to autonomous driving, increasing digitalization and the principle of sharing, electric mobility stands for the mobility of the future. Electric mobility is growing at a rapid pace around the world. Approximately 2.1 million electric cars were sold globally in 2018, after 1.3 million in the previous year (fig. 5, EV Volumes, 2019). This number accounts for about 2.2 % of all vehicles newly registered in 2018 (ACEA, 2018). However, high annual growth rates for battery electric vehicles are expected in the coming years. This is associated with an increasing demand of battery raw materials, such as lithium, cobalt, nickel, graphite and manganese for lithium-ion (Li-ion) battery technology.

We modelled two demand scenarios until 2025 based on the following underlying fundamental: a base case scenario with roughly 7.4 million full electric vehicles (370 GWh – scenario 1) as well as a more optimistic scenario with 12 million full electric vehicles (600 GWh – scenario 2) in 2025. Commercial vehicles such as buses and trucks were not included. Automotive battery technology roadmaps identify Li-ion batteries as being the dominant battery type used from now to about 2050 (Concawe, 2019). Li-ion is a term applied to a group of battery chemistries that contain various materials. They all contain lithium in the cell cathode. Currently, there are six Li-ion battery technologies (Schmidt, 2017), the main difference between them being the composition of the cathode. For now, nickel manganese cobalt (NMC) chemistries are the preferred technology for the automotive industry. For our two demand scenarios we modelled the market share of different cathode chemistries. High-Ni NMC (8:1:1) cathode chemistries gain a market share of 54% in 2025.

Table 4: Worldwide production of selected raw materials and production-specific raw material demand in 2013 for CIGS or CdTe thin film photovoltaics (DS-PV) (Dorner and Liedtke, 2016; Marscheider-Weidemann, et al., 2016).

Metal	Production in 2013 [Tonnes]	Demand for thin-film photovoltaics in 2013 [Tonnes]	Specific raw material demand for CIGS* [g/kWp]	Specific raw material demand for CdTe [g/kWp]
Indium	790	35 – 103	23 – 67	-
Gallium	350	11 – 45	7 – 30	-
Selenium	3.000	92 – 230	60 – 150	-
Cadmium	22.750	178 – 315	-	60 – 105
Tellurium	500 – 550	201 – 355	-	67 – 119

* Stoichiometry: $Cu(In_{0.7}Ga_{0.3})Se_2$

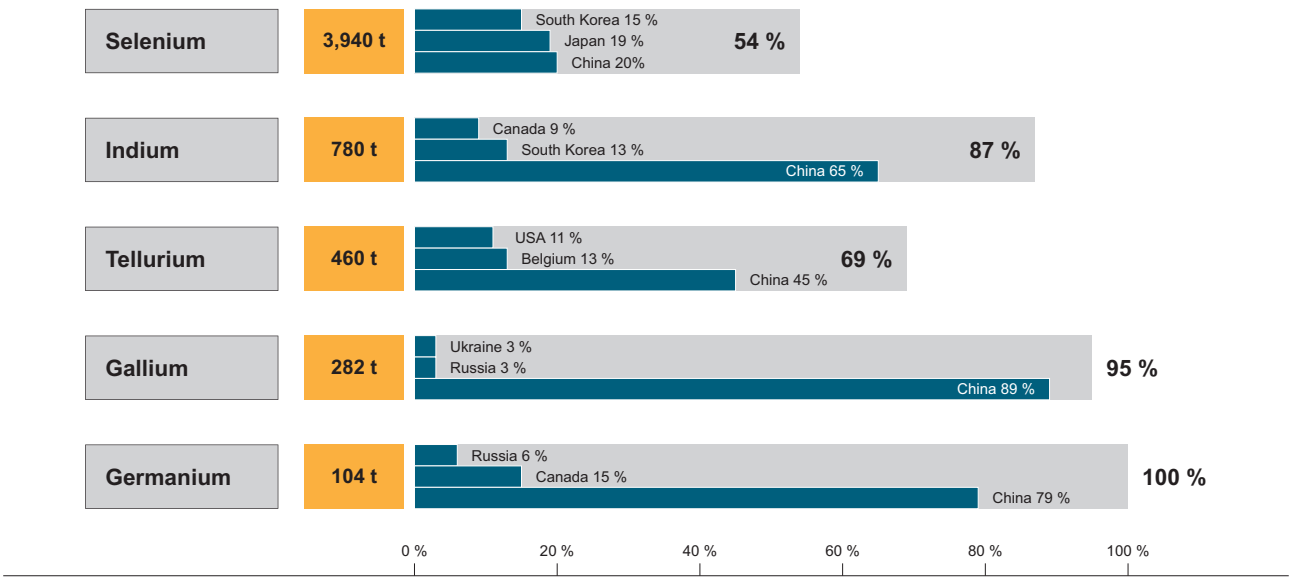

Figure 4: Global minor metals production and their country concentration in 2016 (DERA, 2019).

With the current NMC chemistry we estimate that 1 MWh of battery capacity requires on average 0.51 t of nickel, 0.22 t of cobalt, 0.2 t of manganese, 0.18 t of lithium and 0.57 t of graphite. The estimated raw material demand for the batteries of 1.3 million electric vehicles registered in 2017 is shown in figure 5.

Especially the cobalt and lithium markets have been very volatile in the last two years due to the industry's high expectations for the application of Li-ion batteries, particularly for e-mobility but also for renewable energy storage.

Lithium is mainly used for rechargeable batteries (about 37 % in 2015 and 50 % in 2018 of total demand), followed by the glass and ceramic industries. A number of further applications include polymers, metal powders, processing of air, non-rechargeable batteries, and aluminium alloys (Schmidt, 2017; Roskill, 2016).

Because of the booming e-mobility market, the demand for lithium in rechargeable batteries could increase dramatically from about 12,000 t in 2015 to about 84,000 t (scenario 1, 76 % of total demand) to 125,000 t (scenario 2, 82 % of total demand) in 2025 (Schmidt, 2017).

Global mine production was around 57,000 t lithium in 2018. About 86 % of global lithium mine production came from only three countries, namely Australia (27,000 t), Chile (15,900 t) and Argentina (6,240 t). Lithium is produced from salt brines located in large salars such as the Salar de Atacama in Chile or the Salar de Olaroz in Argentina. Furthermore, lithium is mined from pegmatite deposits, with the Greenbushes deposit in Australia currently being the largest.

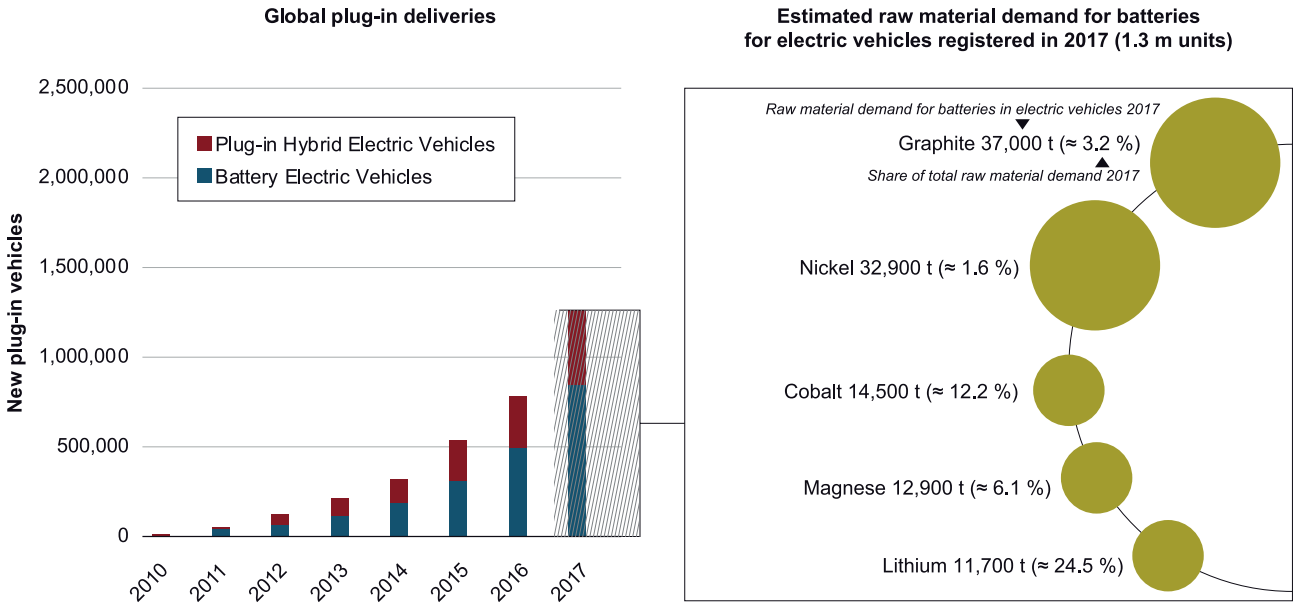

Figure 5: Global Electric vehicle registration from 2010 to 2017 (EV Volumes, 2019) and estimated raw material demand for EV-batteries in 2017 (BGR Database, own calculations).

Current supply and demand scenarios for 2025 indicate that future mine production could meet demand at annual growth rates of around 12.8 %. Higher growth rates for rechargeable batteries could, however, result in supply shortages for lithium (Schmidt, 2017).

Due to its specific properties, cobalt is used in many different applications such as the fabrication of rechargeable batteries, NiMH batteries, NiCd batteries, superalloys, carbides, dyes, and magnets amongst other applications (Al Barazi, 2018).

Cobalt is mainly mined as a by-product from copper and nickel mining. Global mine production was nearly 140,000 t in 2018. With 64 % of global supply, the Democratic Republic of the Congo (DRC) is currently the world's largest cobalt producer with production expected to increase to over 70 % in 2026. Additional supply from the DRC will mainly come from conventional industrial mining operations. However, artisanal and small-scale mining (ASM) of cobalt has long been established in the DRC and represents an essential livelihood for large parts of the population in the Haut-Katanga and Lualaba provinces. About 15 to 35 % of the DRC's total cobalt production is estimated to originate from ASM mine sites depending on the cobalt price. Amnesty International (2016) assumes that 110,000 to 150,000 people are involved in artisanal cobalt mining. Both industrial and artisanal and small-scale mining will remain relevant to meet future global demand for cobalt. Therefore, the establishment of internationally recognized and accepted standards for a responsible sourcing of cobalt from ASM is essential to improve working conditions in this sector (Al Barazi, 2018).

We assume that global cobalt demand for rechargeable batteries in the e-mobility sector will increase to 47.870 t (scenario 1, 26 % of total demand) or 77.680t (scenario 2, 36 % of total demand) by 2025, respectively. Our supply and demand scenarios for 2025 indicate that future mine production could meet demand at annual growth rates of around 8 %, assuming that all projects will commence production at full capacity.

4. Conclusions

Low-carbon technologies such as wind energy, photovoltaics and energy storage batteries for e-mobility are key for a shift to a low-carbon future. The expected dynamic change towards renewable energy systems will have a major impact on the mineral raw material markets in the next decades. The demand for base and minor metals for clean energy technologies is expected to rise substantially. Primary raw material production needs to provide most of the metals for low-carbon technologies, at least for the upcoming decade, because secondary raw material supply alone cannot accommodate the future demand. Therefore, upstream and end-of-life activities of low-carbon technologies must be taken into account to ensure firstly that the mining industry can meet the increasing demand using sustainable and responsible practices and secondly that the products can be recycled in the best possible way.

5. References

ACEA – European Automobile Manufacturers Association, 2018. Key Figures, [online] Available at: <https://www.acea.be/statistics/tag/category/key-figures> [Accessed 26 November 2019].

Amnesty International, 2016. This is what we die for - Human Rights Abuses in the Democratic Republic of the Congo Power the Global Trade in Cobalt. January 2016, [online] Available at: <https://www.amnesty.org/download/Documents/AFR6231832016ENGLISH.PDF> [Accessed 19 October 2020].

Al Barazi, S., 2018. Rohstoffrisikobewertung – Kobalt. DERA Rohstoffinformationen 36, [e-journal], 120 p., Available at: <https://www.deutsche-rohstoffagentur.de/DE/Gemeinsames/Produkte/Downloads/DERA_Rohstoffinformationen/rohstoffinformationen-36.pdf?__blob=publicationFile&v=2> [Accessed 19 October 2020].

Anderson, C. S., 2019. Indium. USGS Mineral Commodity Summaries 2019, [e-journal], pp. 78–79. https://doi.org/10.3133/70202434.

BGR, 2019. BGR Energiestudie 2018 - Daten und Entwicklungen der deutschen und globalen Energieversorgung (22), [online], 178 p., Available at: <https://www.bgr.bund.de/DE/Themen/Energie/Downloads/energiestudie_2018.pdf;jsessionid=3D137928004B67746BCD13898C751C2B.1_cid292?__blob=publicationFile&v=10> [Accessed 19 October 2020].

BP, 2019. BP Statistical Review of World Energy – all data, 1965-2018: Elec Gen by Fuel, [xlsx] Available at: <https://www.bp.com/en/global/corporate/energy-economics/statistical-review-of-world-energy.html> [Accessed 3 November 2019].

Buchholz, P. and Brandenburg T., 2018. Demand, Supply, and Price Trends for Mineral Raw Materials Relevant to the Renewable Energy Transition. Chemie Ingenieur Technik, [e-journal] 90(1-2), pp. 141–153. http://doi.org/10.1002/cite.201700098.

Concawe, 2019. Review. Volume 28, Number 1, October 2019, [online] Available at: <https://www.concawe.eu/wp-content/uploads/Concawe-Review-28-1-web-resolution-PDF.pdf> [Accessed 19 October 2020].

DERA, 2019. DERA Rohstoffliste 2019. DERA Rohstoffinformationen 40, [e-journal], 116 p., Available at: <https://www.deutsche-rohstoffagentur.de/DE/Gemeinsames/Produkte/Downloads/DERA_Rohstoffinformationen/rohstoffinformationen-40.pdf?__blob=publicationFile&v=5> [Accessed 19 October 2020].

Dorner, U. and Liedtke, M., 2016. Mineralische Rohstoffe für die Energiewende, Commodity TopNews 50, [online] Available at: <https://www.deutsche-rohstoffagentur.de/DE/Gemeinsames/Produkte/Downloads/Commodity_Top_News/Rohstoffwirtschaft/50_rohstoffe-energiewende.pdf?__blob=publicationFile&v=2> [Accessed 19 October 2020].

EV Volumes, 2019. Global Plug-In Deliveries BEV &PHEV – Light Vehicles, [online] Available at: <http://www.ev-volumes.com/country/total-world-plug-in-vehicle-volumes/> [Accessed 22 May 2019].

Gunn, G. ed., 2014. Critical metals handbook. British Geologival Survey, Chichester: John Wiley & Sons, Ltd., 454 p.

IEA, 2019. Tracking Power, [online] Available at: <https://www.iea.org/reports/tracking-power-2019> [Accessed 6 November 2019].

Jaskula, B. W., 2019. Gallium. USGS Mineral Commodity Summaries 2019, [e-journal], pp. 62–63. https://doi.org/10.3133/70202434.

Kingsnorth, D. J., 2018. Rare Earth Supply Today: Lacking Diversity for Long Term Sustainabilty October 2018. 16 p. Curtin Uni-

versity Industrial Minerals Company of Australia Pty Ltd (IMCOA).
Marscheider-Weidemann, F., Langkau, S., Hummen, T., Erdmann, L., Tercero Espinoza, L., Angerer, G., Marwede, M. and Benecke, S., 2016. Rohstoffe für Zukunftstechnologien 2016. DERA Rohstoffinformationen 28, [e-journal], 351 p., Available at: <https://www.deutsche-rohstoffagentur.de/DERA/DE/Downloads/Studie_Zukunftstechnologien-2016.pdf?__blob=publicationFile&v=5> [Accessed 19 October 2020].
Müller, A., 2018. Rohstoffe für die Energiewende, [online] Available at: <https://www.misereor.de/fileadmin/publikationen/studie-rohstoffe-fuer-die-energiewende.pdf> [Accessed 19 October 2020].
Schmidt, M., 2017. Rohstoffrisikobewertung – Lithium. DERA Rohstoffinformationen 33, [e-journal], 116 p., Available at: <https://www.deutsche-rohstoffagentur.de/DERA/DE/Downloads/Studie_lithium_2017.pdf?__blob=publicationFile&v=3> [Accessed 19 October 2020].
SolarPower Europe, 2018. Global Market Outlook – for Solar Power 2018 - 2022, [pdf] Available at: <https://www.solarpowereurope.org/wp-content/uploads/2018/09/Global-Market-Outlook-2018-2022.pdf> [Accessed 19 October 2020].
Roskill, 2016. Lithium-Ion Batteries: Market Developments, Raw Materials, 297 p., London: Roskill Information Services Ltd.
World Bank Group, 2017. The Growing Role of Minerals and Metals for a Low Carbon Future, June 2017, [online] Available at: <http://documents.worldbank.org/curated/en/207371500386458722/The-Growing-Role-of-Minerals-and-Metals-for-a-Low-Carbon-Future> [Accessed 19 October 2020].
WWEA - World Wind Energy Association, 2018. Global Total Installed Capacity, [online] Available at: <https://library.wwindea.org/global-statitistics-1980/> [Accessed 5 July 2019].
Xia-Bauer, C., Saurat, M. and Wittmer, D., 2013. Onshore Wind Energy Development in China and its Implications on Natural Resources. Hanse Studies, Institute for Advanced Study, 9, pp. 35–47. [online] Available at: <oops.uni-oldenburg.de/2545/1/pehsus13.pdf> [Accessed 19 October 2020].

Ashes to Ashes – Understanding Earth processes

Tectonic Geomorphology of NW Borneo, Malaysia

B. Bazliah[1, ✉], S. Sahari[1], A. A. Shah[1], B. Navakanesh[2], N. Syafiqah[1]

[1] [1]Universiti Brunei Darussalam, Brunei Darussalam
[2] *Universiti Kebangsaan Malaysia;*
✉ arifahbazliahbadar@gmail.com

Keywords: *strike-slip, fault, Borneo, Sabah, tectonic forces*

1. Introduction

The regional tectonic map of northwest Borneo indicates its position within an active network of plate boundaries of the Sunda, Indo-Australian, and Philippine Sea plates (Fig. 1A). The earthquake distribution shows seismicity clusters surrounding NW Borneo, which are largely along the active subduction zones. However, the small number of earthquakes recorded in NW Borneo could suggest that it is currently located far from the active plate margins and largely shielded from active plate tectonic movements (e.g. Hall, 2013). The earthquake moment tensor data shows dominance of shallow focused (5 to 13 km) normal and strike-slip faults, which indicates that crustal deformation is ongoing but apparently slower than on the neighbouring plate margins. The prominent structural and topographical expression of mountains, as well as the orientation of Holocene sediment-filled valleys in the region also suggests active faulting (Fig. 1B). The topographic expression of these intermontane valleys is near parallel to the strike of the active Crocker fault system, which could suggest that these small basins are a product of active faulting in the region, which needs explanation. Although the occurrence of earthquakes in NW Borneo is scarce, the shallow rupture depths suggest a shallow nature of crustal faulting, which could be related to either tectonic or gravitational forcing, or a combination of the two. This problem could be partially solved if careful and detailed mapping of geomorphic landforms is done by using digital elevation data, which is largely missing in previous works (e.g. Wang et al., 2016; Wang et al., 2017, Mustafar et al., 2017; Tongkul, 2017). Therefore, this work uses 30 m shutter radar topography extensively to map the geomorphic features of active faulting, including triangular facets, fault scarps, topographic breaks, bedding, etc.

2. Summary of the Active tectonic framework of NW Borneo

The study area (Fig. 1) is surrounded by the active tectonic boundaries of the Eurasian, Indo-Australian, and Pacific-Philippines Sea plates (Fig. 1). The continuous interaction of the plates occurs at variable rates, which over the geological past has produced a network of active structures that largely dictate the topographic framework of the region. Thus, the onshore and offshore geomorphology and topography preserve evidence and chronology of the geological past (Simons et al., 2007, Shah, 2013). The region is relatively far-off (e.g. ~800 km in the east) from the active plate margins (Fig. 1) and the evidence for active plate convergence at the Borneo-Palawan Trough is not satisfactory, which is why it is not considered a plate boundary in the plate tectonic map of the world (Bird, 2003). Therefore, the cause of active faulting in NW Borneo has largely remained divided into two major suggestions, which are related to gravity, and gravity plus tectonics (e.g. Ingram et al., 2004; Hesse et al., 2009; Sapin et al., 2013; Wang et al., 2017,

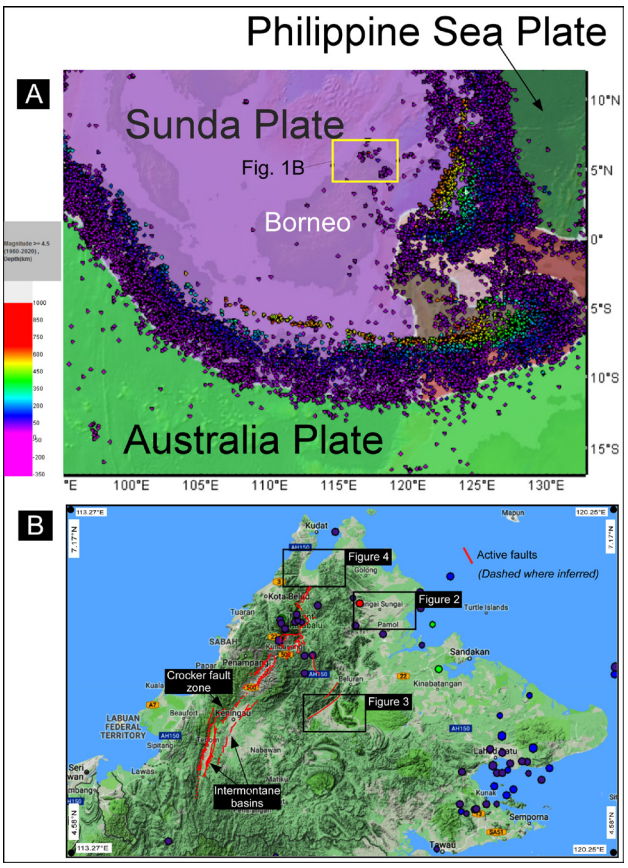

Figure 1: (A) The regional tectonic map shows the location of Borneo in the middle of active tectonic plates (plate boundaries after Bird, 2003) and the coloured dots are earthquakes; (B) shows the Google satellite image with three specific study locations in NW Borneo that are mapped in detail (see Figs. 2-4). It also shows the earthquake distribution across the region. Image extracted from IRIS Earthquake Browser on 25th March 2020.

DOI: 10.2312/yes19.08

Tongkul, 2017; Shah et al., 2018, Wu et al., 2020; Navakanesh et al., in press). The previously mapped active faults in the region are mainly related to normal, thrust, and strike-slip faults (e.g. Shah, 2016; Wang et al., 2016; Wang et al., 2017, Mustafar et al., 2017; Navakanesh et al., 2019). The active normal fault system (known as Crocker fault system) has hosted a moderate-sized (M_w 6.0) earthquake on 5th June 2015, in Ranau, Sabah, which caused significant loss of life. Furthermore, on 8th March 2018, another moderate-sized (M_w 5.2) earthquake occurred on the same fault system. These events were shallow focus and ruptured the crust at 10 to 13 km depth. The pattern of faulting in NW Borneo is consistent with the fanning of the major strike-slip fault system that runs through the middle of Borneo Island that was envisaged by Shah et al. (2018) but the sense could be dextral.

3. Methodology

Geoscientists have extensively used remote sensing data to map geologic and geomorphic landforms (e.g. Molnar and Tapponnier, 1978; Nakata, 1989; Taylor and Yin, 2009; Shah, 2013; Shah & Malik, 2017). These studies have increased our understanding of the geologic, geomorphic, and tectonic architecture of different regions (e.g. Taponnier and Molnar, 1997; Molnar and Tapponnier, 1978). Field investigations are one of the major components of active fault mapping and for the collection of primary data on the geological, structural, and topographic settings of the region. Complementarily, satellite data are particularly important for regional studies and are useful in areas where fieldwork is impossible or difficult (e.g. Shah et al., 2018). The geomorphic analysis presented here uses a 30 m shuttle radar topography. The mapping is done by looking for evidence for faulting, which includes tracing of ridge crests to observe sudden changes, which could be related to faulting (e.g. Fig. 2). Triangular facets are a useful tool to investigate the active landforms and are used to map the bedding planes, aided by the rule of “V’s”, in which river valleys “V” towards the dip direction of the beds (Figs. 2-4). This rule is a very useful indicator where bedding dip direction is not known (Shah et al., 2018), and it works best for structural mapping on high-resolution images or maps. The technique is simple: rock beds interact with river erosion at various angles, which are usually a reflection of the dip angle, and the beds form triangular facets and valleys (e.g. Fig. 2-4) as erosion progresses, which makes the rule of “V’s” a robust tool to know the dip direction of beds or fault.

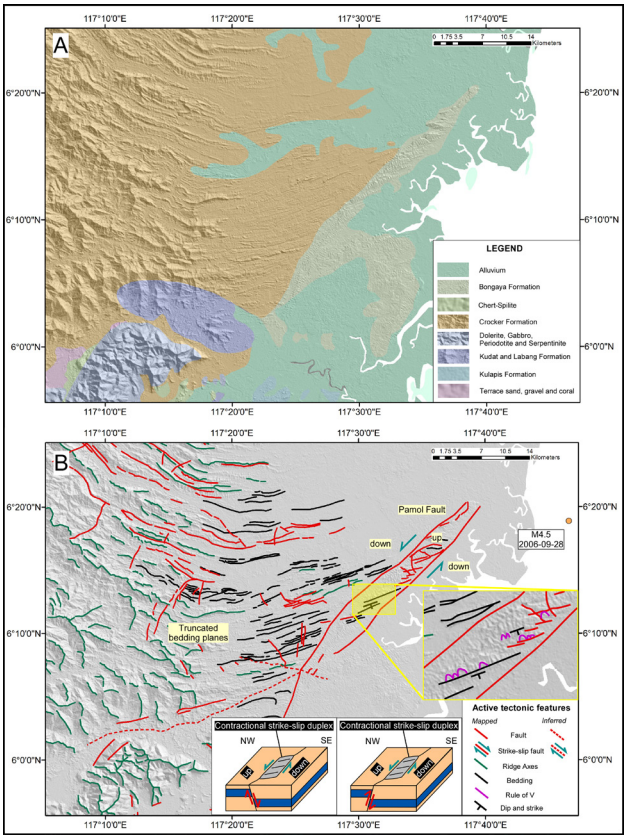

Figure 2: (A) Uninterpreted 30 m SRTM image with geology overlaid on it; (B) Interpreted image shows the various geologic and geomorphic features that are used as evidence for faulting. The contractional duplex feature is interpreted, and 3-dimensional illustrations are shown to explain the formation of the duplex with both normal (left illustration) and reverse (right illustration) fault geometries. We think the left illustration is representative of the fault zone.

4. Results and Interpretation

Three key areas (Fig. 1B) are studied in detail (Figs. 2–4). The rectangular windows in Fig. 1B show the extent of these areas of investigation. The lithological boundaries are mapped in Fig. 2B, and it shows the changes in bedding strike from ~E-W to ~NE-SW. This transition is sharp at the abrupt appearance of a chain of discontinuous ridges (Fig. 2B). The beds are truncated by ridges that exposed the Bongaya Formation, which are relatively younger rocks than the Crocker Formation that is exposed in much of the region under study. We have mapped this sharp truncation as a fault, which is oriented in ~NE-SW direction, and a series of ridges that are enclosed within the fault zone (Fig. 2B) are also faulted. A closer look reveals that these faulted ridges preserve ~SE dipping beds (see the yellow window in Fig. 2B).

The abrupt rise of topography in an area that is otherwise flat further suggests faulting. The fluctuations in the sea-level could be argued to have played a role in the formation of subdued topography but such variations over the geological past cannot produce the topography as observed in the region. This

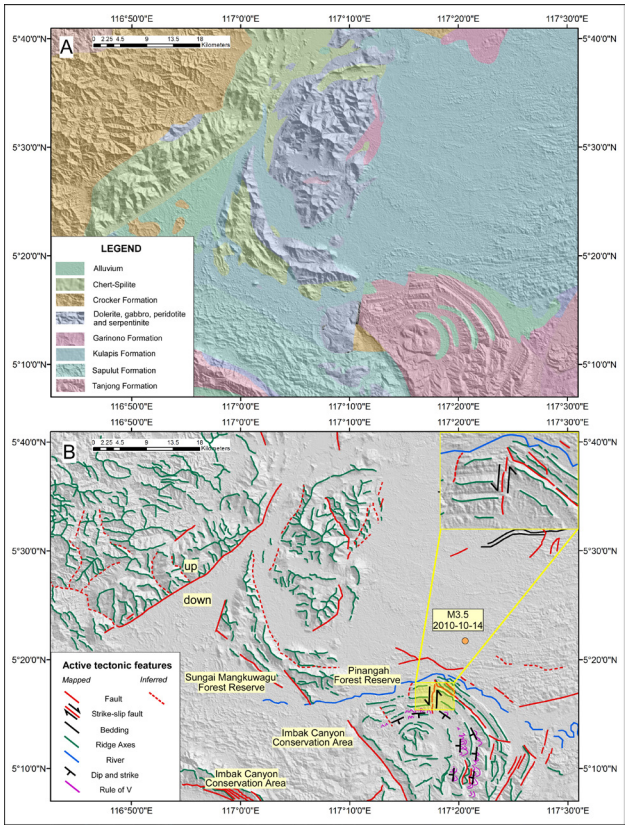

Figure 3: (A) Uninterpreted 30 m SRTM image with geology overlaid on it; (B) Interpreted image shows the mapped geologic and geomorphic features that support the existence of active faults. The truncation of syncline at the western portions is interpreted as a fault. The syncline is exposed as a circular basin with clear evidence for faulting. Small left-lateral strike-slip faults are also mapped (see the yellow rectangular area).

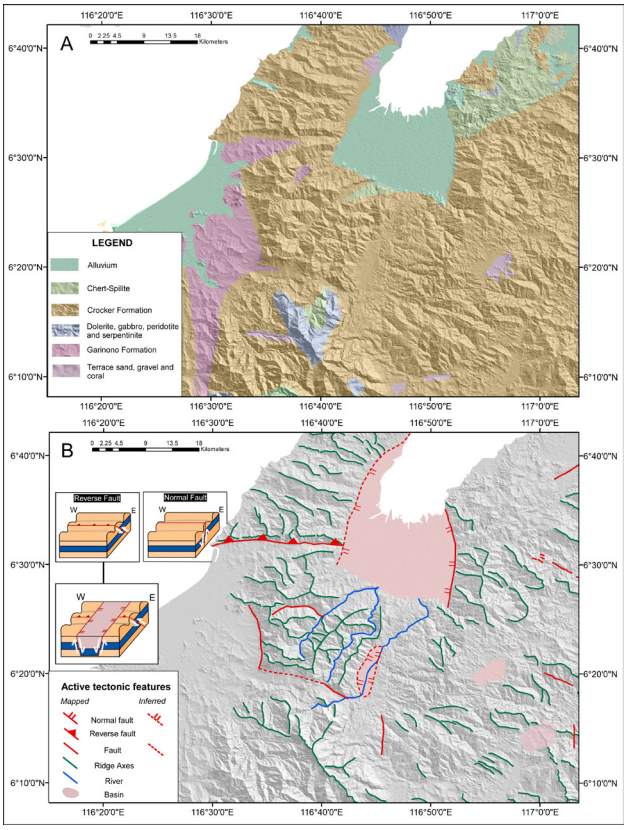

Figure 4: (A) Uninterpreted 30 m SRTM image with geology overlaid on it; (B) Interpreted image shows the mapped geologic and geomorphic features that support the evidence for active faults. The ~E-W reverse faults are truncated by the younger ~N-S trending normal faults, which suggests ~N-S convergence and ~E-W extension.

is because the geomorphic expression of landforms is consistent throughout the region and coincides with the mapped faults and folds (Figs. 2 and 3). We think the entire region is shaped by faulting, and topography is structurally controlled at depth. The mountains are slowly fading from the longitude 117°5′E towards the east, and then the abrupt rise of the ~NE-SW trending ridge is observed (Fig. 2A).

The pattern of discontinuous ridges caught within the fault zone for a total length of ~45 km is consistent with a characteristic fault bend geometry that fits a contractional duplex geometry (Fig. 2B). We are unable to find a clear strike-slip displacement that could be measured and qualified, but we interpret the topographic expression of faulting to be consistent with a fault that has a strike-slip component to it. Therefore, the major fault plane is either dipping ~NW or ~SE, and we have interpreted it as ~SE dipping normal fault with a strike-slip component. This interpretation is based on the topographic expression where upthrown and down-thrown movements are consistent with a normal fault geometry. We named this fault the Pamol Fault, homonym to the nearby city, as we are unaware of any previous references to this fault in the published literature. We have observed and mapped asymmetrical anticlinal structures at the base of the fault zone (Fig. 2B), and these are related to faults, and in good agreement with a fault-bend fold geometry, which suggests oblique extension with strike-slip movement as the ideal condition for the formation of such structures (Fig. 2b).

On the NE side, the fault runs into the Sulu Sea, where its continuation cannot be traced based on satellite data. However, the south-western termination of the fault seems to root at the Crocker fault zone (Fig. 4; Shah 2016; Wang et. al., 2017), which could mean that the fault is a major fault with more than 250 km in length. The fault zone is discontinuous and often segmented (Figs. 2–4), which is suggested by the mapping of the fault zone in the southwest (Fig. 3B). A clear truncation of the ridge crests is observed where mountains suddenly disappear in a valley that is part of the down-thrown block across the fault zone. The fault is consistent with ~SE dipping normal fault geometry, and this portion of the fault zone seems purely normal with no indication of strike-slip. However, we have mapped clear evidence of left-lateral strike-slip where a portion of the syncline is offset by a small ~N-S trending fault (Fig. 3B, see the yellow rectangular area). The ~NW-SE trending fault zone is the major fault (Fig. 3B) where some of the peculiarly

shaped basins known as "circular basins' exist and these are cut across by the fault. The circular basin preserves triangular facets that show the dip direction of the beds and it suggests a synclinal geometry for the basin. We have interpreted the structure as a normal fault that dips ~SW. This fault stops at the Pamol Fault, which indicates that the two faults interact and could be related to each other.

The northern portion of NW Borneo has a near rectangular bay area, which is bounded by mountains on three sides (Fig. 4A and 4B). We have mapped an ~E-W trending fault that could either be dipping north or south, and we interpret this fault as a north dipping reverse fault. It suddenly truncates the onshore extension of the basin area, which we have interpreted as a normal fault (Fig. 4B). We think the basin is bounded on two sides by normal faults, and we have mapped one that is shown in solid, and the other as inferred because the evidence of faulting is not clear.

The abrupt termination of the mountain range and opening of the basin within the mountains is a reflection of faulting, which was confirmed by our geomorphological mapping where ~N-S trending active faults bound the basin in east and west (Fig. 4B). The structural configuration and geometry of the basin could be possible with two normal faults that terminate in the south. The existence of ~E-W to ~NW-SE trending fold and thrust faults on the eastern and western portions of the basin (Fig. 4B) suggests that these faults are older and the bay region has formed recently. We interpret that the older faults are dominantly reverse faults, and are later cut by younger ~N-S trending normal faults (Fig. 4B). This indicates that older faults used to continue throughout the region before the bay was formed, and now those faults are cut by the normal faults of the bay region.

5. Discussion

We have mapped a variety of previously unreported active geomorphic features and fault scraps in northern Borneo, and also refined the previously known structures (Figs. 2–4). The presence of the Pamol Fault that possibly extends for >250 km and merges with the Crocker fault zone suggests that deformation in the region is tectonically controlled because gravity alone cannot explain the scale, extent, and morphology of the fault system that we have shown here (Figs. 2–4). Our mapping suggests that the fault is possibly sinistral in the northeastern portions (Fig. 2B), which is shown by the sudden occurrence of ridges in the otherwise low lying regions. We relate this to the restraining bend geometry of the major normal fault with a sinistral component (Fig. 2B). The overall morphology of the entire fault zone resembles the geometry of a major normal fault that dips ~SE and has possibly a strong strike-slip component in the northeast, which is not observable in the southwest and along the track where it eventually merges with the Crocker fault zone.

Alternatively, if we consider the Pamol Fault as a SE dipping reverse fault, as has been mapped in some of the earlier works (JMG, 2012; Wang et al., 2016; Mustafar et al., 2017), then the hanging wall portions should be up, and not down (Fig. 2B). The geomorphic expression of faulting is consistent with up-thrown blocks on the NW and down-thrown portions on the SE of the fault.

Another possibility, which seems consistent with the geomorphic expression, is that the fault is a NW dipping reverse fault with a sinistral strike-slip component. Yet, the NW Borneo region is experiencing crustal extension, which has been suggested by a number of normal fault-related earthquakes in the past and further supported by the field and earthquake moment tensor data (Shah, 2016).

We therefore interpret the Pamol Fault as the SE dipping normal fault. This fault could be related to the major strike-slip fault system that was anticipated earlier and runs through the spine of Borneo Island (Shah et al., 2018; Navakanesh et al., 2020). We have also mapped the ~NW-SE trending normal fault that has ruptured a synclinal circular basin (Balaguru et al., 2003; Chang et al., 2019) and it merges with the Pamol fault at the north (Fig. 3B). We think there is a broad fault zone between the synclinal circular basin and regions north of Pinangah Forest Reserve (Fig. 3B) but the evidence is subtle, and work on the ground is needed.

The earthquake centroid moment tensor data (Navakanesh et al., 2019; Navakanesh et al., 2020) show one earthquake event closer to the Pamol fault, and that has occurred on a strike-slip with either ~N-S strike or ~E-W. The ~N-S trend is closer to the fault, and therefore it appears to have ruptured a sinistral strike-slip fault at 12 km depth, which is consistent with the local origin of the earthquake. This further suggests that the mapped fault could be an oblique fault with a strike-slip component in the northeast and dominantly dip-slip in the southwest. The Pamol Fault is a major fault that could be >250 km long, and the examination of available earthquake centroid moment tensor data suggests that Borneo is dominantly undergoing normal and strike-slip faulting, and our work shows that the entire region is undergoing transtension.

6. Conclusions

Our geomorphological mapping has demonstrated that active faults exist in NW Borneo, which are mainly related to oblique crustal extension that is accommodated by the formation of normal and strike-slip faults. The evidence for active faulting (Figs. 2–4) is widespread, and broadly the Pamol fault zone belongs to a family of faults that exist in northern Borneo, which is related to the ongoing oblique crustal extension on the island. The scale, extent, and youthfulness of landforms suggest that tectonics is driving the ongoing deformation of Borneo, which could also be facilitated by gravity-induced deformation but gravity alone cannot be the major source of active deformation in the region.

7. References

Balaguru, A., Nichols, G., Hall, R., 2003. The origin of the ‚circular basins' of Sabah, Malaysia. Bulletin of the Geological Society of Malaysia 46, pp. 335–351.

Bird, P., 2003. An updated digital model of plate boundaries, Geochemistry Geophysics Geosystems 4(3), 1027. https://doi.org/10.1029/2001GC000252.

Chang, S.-P., Jamaludin, S. N. F., Pubellier, M., Zainuddin, N. M., Choong, C.-M., 2019. Collision, mélange and circular basins in north Borneo: A genetic link? Journal of Asian Earth Sciences 181, 103895. https://doi.org/10.1016/j.jseaes.2019.103895.

Hall, R., 2013. Contraction and extension in northern Borneo driven by subduction rollback. Journal of Asian Earth Sciences 76, pp. 399–411. https://doi.org/10.1016/j.jseaes.2013.04.010.

Hesse, S., Back, S., Franke, D., 2009. The deep-water fold-and-thrust belt offshore NW Borneo: Gravity-driven versus basement-driven shortening. GSA Bulletin 121, pp. 939–953. https://doi.org/10.1130/B26411.1.

Ingram, G. M., Chisholm, T. J., Grant, C. J., Hedlund, C. A., Stuart-Smith, P., Teasdale, J., 2004. Deepwater North West Borneo: hydrocarbon accumulation in an active fold and thrust belt. Marine and Petroleum Geology 21, pp. 879–887. https://doi.org/10.1016/j.marpetgeo.2003.12.007.

JMG, 2012. Mineral and Geoscience Department Malaysia 2012: Annual Report. Ministry of Natural Resources and Environment, Kuala Lumpur, 198 pp.

Molnar, P., Tapponnier, P., 1978. Active tectonics of Tibet. Journal of Geophysical Research 83(11), pp. 5361–5375. https://doi.org/10.1029/JB083iB11p05361.

Mustafar, M. A., Simons, W. J. F., Tongkul, F., Satirapod, C., Omar, K. M., Visser, P. N. A. M., 2017. Quantifying deformation in Northern Borneo with GPS. Journal of Geodesy 91, pp. 1241–1259. https://doi.org/10.1007/s00190-017-1024-z.

Nakata, T., 1989. Active faults of the Himalaya of India and Nepal. Geological Society of America Special Publication 232, pp. 243–264. https://doi.org/10.1130/SPE232-p243.

Navakanesh, B., Shah, A. A., Prasanna, M. V., 2019. Earthquake Education Through the Use of Documentary Movies. Frontiers in Earth Science 7, 42. https://doi.org/10.3389/feart.2019.00042.

Navakanesh, B. and Shah, A. A., in press. Is the active deformation in NW Borneo tectonically driven or gravity-induced?. In: Rose, T., de Gelder, G., Fernández-Blanco, D., Nshokano Mweze, J.-R., Sieber, M., Singh, B. V. R. (Eds.). Proceedings of the 5th International Young Earth Scientists (YES) Congress "Rocking Earth's Future", 9–13 September 2019, Berlin, Germany. German YES Chapter & GFZ Potsdam, in press.

Navakanesh, B., Shah, A. A., Phmy, A., 2020. Miri Hill Structure has Formed by Normal Faulting at the Releasing Bend Geometry of Strike-Slip Faulting. 82nd EAGE Annual Conference & Exhibition, pp. 1–5. https://doi.org/10.3997/2214-4609.202011395.

Sapin, F., Hermawan, I., Pubellier, M., Vigny, C., Ringenbach, J. C., 2013. The recent convergence on the NW Borneo Wedge – a crustal-scale gravity gliding evidenced from GPS. Geophysical Journal International 2, pp. 549–556. https://doi.org/10.1093/gji/ggt054.

Shah, A. A., 2013. Earthquake geology of Kashmir Basin and its implications for future large earthquakes. International Journal of Earth Sciences 102(7), pp. 1957–1966.

Shah, A. A., 2016. Understanding the recent Sabah Earthquake, and other seismogenic sources in North West Borneo. Scientific Malaysia 12, pp. 7–10. https://doi.org/ 10.1007/s00531-013-0874-8.

Shah, A., Zhafri, M., Delson, J., Navakanesh, B., 2018. Major Strike-Slip Faults Identified Using Satellite Data in Central Borneo, SE Asia. Geosciences 8(5), 156. https://doi.org/10.3390/geosciences8050156.

Shah, A. A., Malik, J. N., 2017. Four major unknown active faults identified, using satellite data, in India and Pakistan portions of NW Himalaya. Natural Hazards 88(3), pp. 1845–1865. https://doi.org/10.1007/s11069-017-2949-5.

Simons, W. J. F., Socquet, A., Vigny, C., Ambrosius, B. A. C., Haji Abu, S., Promthong, C., Subarya, C., Sarsito, D. A., Matheussen, S., Morgan, P., Spakman, W., 2007. A decade of GPS in Southeast Asia: Resolving Sundaland motion and boundaries. Journal of Geophysical Research 112, B06420. https://doi.org/10.1029/2005JB003868.

Taylor, M., Yin, A., 2009. Active structures of the Himalayan-Tibetan orogen and their relationships to earthquake distribution, contemporary strain field, and Cenozoic volcanism. Geosphere 5(3), pp. 199–214. https://doi.org/10.1130/GES00217.1.

Tapponnier, P., Molnar, P., 1977. Active faulting and tectonics in China. Journal of Geophysics Research 82(20), pp. 2905–2930. https://doi.org/10.1029/JB082i020p02905.

Tongkul, F., 2017. Active tectonics in Sabah – seismicity and active faults. Bulletin of the Geological Society of Malaysia 64, pp. 27 – 36. https://doi.org/10.7186/bgsm64201703.

Wang, P. C., Li, S. Z., Guo, L. L., Jiang, S. H., Somerville, I. D., Zhao, S. J., Han, N., 2016. Mesozoic and Cenozoic accretionary orogenic Processes in Borneo and their mechanisms. Geological Journal 51, pp. 464–489. https://doi.org/10.1002/gj.2835.

Wang, Y., Wei, S., Wang, X., Lindsey, E.O., Tongkul, F., Tapponnier, P., Bradley, K., Chan, C.-H., Hill, E. M., Sieh, K., 2017. The 2015 M_w 6.0 Mt. Kinabalu earthquake: an infrequent fault rupture within the Crocker fault system of East Malaysia. Geoscience Letters 4, 6. https://doi.org/10.1186/s40562-017-0072-9.

Wu, J., McClay, K., de Vera, J., 2020. Growth of triangle zone fold-thrusts within the NW Borneo deep-water fold belt, offshore Sabah, southern South China Sea. Geosphere 16(1), pp. 329–356. https://doi.org/10.1130/GES02106.1.

Evidence of Land-Sea Interaction during Mid-Late Holocene from Sedimentary Records, Western India

Upasana S. Banerji[1,✉], Ravi Bhushan[2], Shilpa Pandey[3]

[1] National Centre for Earth Science Studies, Thiruvananthapuram-695583, Kerala, India
[2] Physical Research Laboratory, Ahmedabad-380009, Gujarat, India
[3] Birbal Sahni Institute of Palaeosciences, Lucknow-226007, Uttar Pradesh, India
✉ upasana.s.banerji@gmail.com

Keywords: mid-late Holocene, Sea-level, tectonics, Saurashtra, Geochemical Proxies

1. Introduction

The investigation of Holocene sea level histories and coastal landscape responses can yield vital information on the coastal environment and future sea-level rise (Sloss et al., 2018). However, Holocene sea-level records are fraught due to lack of regional geological investigations and constraints in tectonic setting (tectonic upheaval or hydro-isostatic warping) of the coastal track (Williams et al., 1998). Such lacuna leads to discordance in the Holocene sea-level at the regional scale (Li et al., 2012). Further, on the contrary to the glacial-interglacial period, the mid-late Holocene Period remained deprived of drastic sea level variations. Thus, local or regional coastal tracts responded distinctly during the mid-late Holocene Period, which in turn demands localised sea-level curves instead of generalised sea level changes generated for other regions (Hashimi et al., 1995). However, based on the available local or regional sea level curve this can be collated to produce a generalised sea level variability. On the basis of coastal geomorphic features (Pant and Juyal, 1993; Rust and Kershaw, 2000), stable isotopic variation (Waelbroeck et al., 2002; Lamb, Wilson and Leng, 2006) and instrumental records (Douglas, 1991; Holgate, 2007) several studies have addressed sea level changes.

Sheltered coastal environments such as mudflats, estuaries, lagoons, bays, inlets, rias, and isolation basins are potential regions for preserving thick sequences of Holocene sediments and respond in accordance with the pace of sea level and coastal changes during the Holocene (Allen and Haslett, 2002). Several studies constraining Holocene sea level variability have conducted investigations on the intertidal region (Wilson et al. 2005; Zhan et al. 2011 and references therein). In the present study we conducted a geochemical investigation on the mudflats of Gujarat, Western India to address sea level variability and possible tectonic influences during the mid-late Holocene period.

2. Study Area

The coastal landscape of Saurashtra, western Gujarat, India is a result of both, eustatic sea level changes and tectonics (Ganpathi, Patel and Merh, 1982). The southern Saurashtra coast is marked by 40 to 50 m vertical cliffs of limestone. The coast is irregular and dissected further east up to Diu. The northeast of Diu Island consists of extensive tidal flats and the southern coast is cliffy. Beyond Diu, the coast is characterised by the presence of a rocky foreshore with occasional beaches and limestone cliffs. An extensive mudflat is located along the Saurashtra coast near Diu Island and Jaffrabad. The limestone (miliolitic) cliffs are located along the southern coast of Diu Island. The age of the miliolites was estimated to be of three generations: 200–140, 115–75, and 70–50 ka BP (Baskaran et al., 1986).

3. Material and methods

Both, relict Vasoj (VV) and active Diu (DV) mudflats (Fig. 1) located in the NE of Diu Island, near the southern Saurashtra coast, were investigated to study the Holocene sea-level changes along Saurashtra coast. Sampling details and chronology for VV and DV have been discussed in Banerji et al. (2015) and Banerji et al. (2017), respectively. The relict mudflat VV recorded a depositional history from 4700 to 1500 cal BP and the sedimentation ceased after 1500 cal BP (Banerji et al., 2015). The core location DV inundates and receives sediment only during exceptionally high tide and has recorded a depositional history between 4100 and 71 cal BP (Banerji et al., 2017).

The sediment samples from different depths of the VV relict section (~ 100 cm, ~ 10 samples) and DV sediment core (~ 70 cm, ~ 35 samples) were dried (at ~ 80 °C), crushed and homogenised with the help of an agate mortar to avoid any metallic contamination. The chronology of VV was estimated from three carbon-14 ages (Banerji et al., 2015), while in the case of DV, the chronology was supported by carbon-14, caesium-137, and lead-210 dating techniques (Banerji et al., 2017). Nearly 300 mg of bulk, dried

DOI: 10.2312/yes19.07

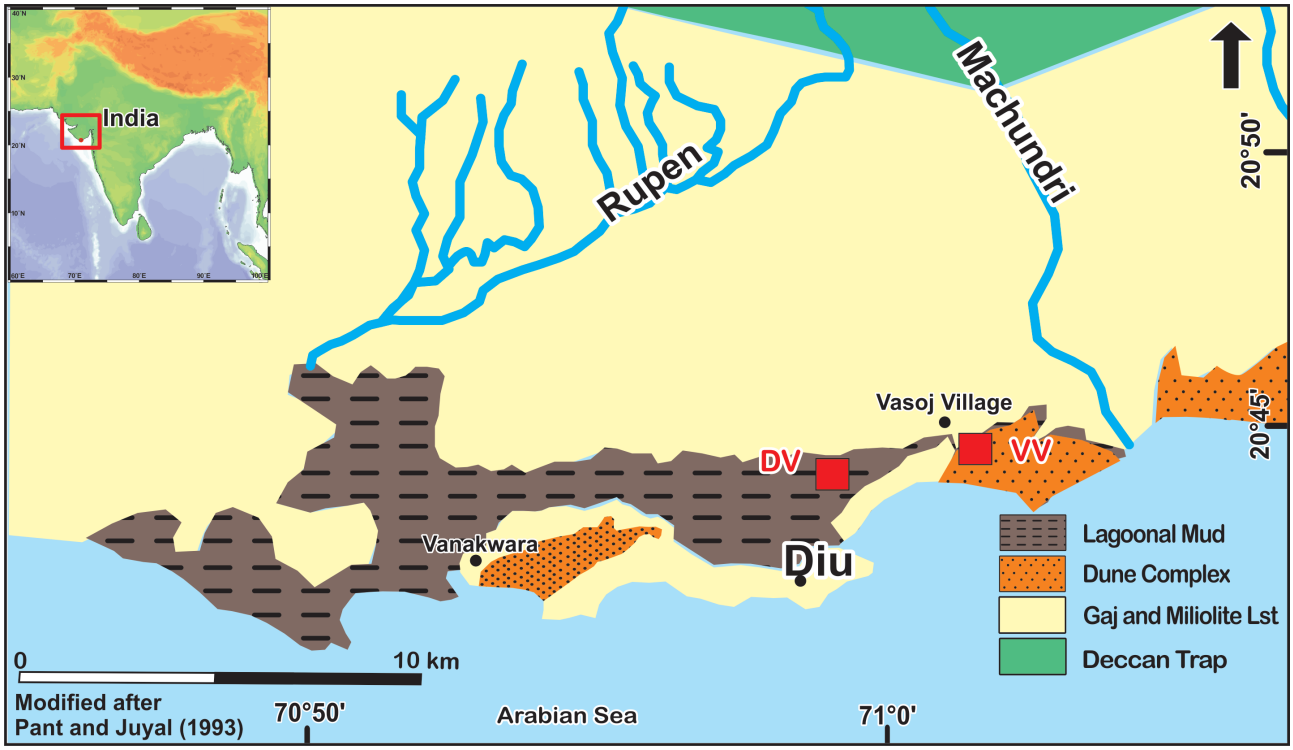

Figure 1: Map showing the geology of the relict (VV) and active (DV) mudflat region along the southern Saurashtra, Gujarat, western India.

crushed sediment samples were subjected to closed digestion (Thermo Microwave digestion system) by treating them with concentrated acids (HCl, HF, and HNO_3). The digested sample solution was aspirated in the ICP-AES (Jobin Yvon 38S) for the measurement of Al, and in the ICP-MS (Thermo-X series2) for the measurement of Mn, Ni, Mo, V, Cr, and Co. The analytical precision and accuracy were better than ±5 % for major and trace elements (Agnihotri, 2001; Banerji et al., 2017). The sediment samples for estimation of Total Organic Carbon (TOC) were decarbonated with 10% HCl and thoroughly washed with distilled water and dried. The TOC was estimated in FISONS NA1500 NC Elemental Analyzer (Fisons Inc.) by introducing ~ 10 to 20 mg decarbonated sediment samples packed in a tin capsule into a combustion tube through an auto-sampler. The analytical precision and accuracy for TOC were better than 4 % (Bhushan et al., 2001).

4. Results and Discussion

4.1. Geochemical Variations

Sediments record only a fraction of total biological productivity, as the organic matter that is delivered to the water-sediment interface passes through bacterial degradation within the water column (Tribovillard et al., 2006). Generally, mangrove forests in the intertidal region are extensively productive areas with high rates of organic carbon accumulation (Kristensen et al., 2008; Marchand, Lallier-Vergès and Allenbach, 2011). High TOC during 4710 to 3200 cal BP in VV (Fig. 2a) suggests improved productivity associated with extensive mangrove forests that flourished in the region due to high sea level and enhanced monsoon intensities (Banerji et al., 2015). A similar observation of high productivity supported by TOC, Cu/Al_2O_3, and Ni/Al_2O_3 during 4105 to 2640 cal BP with high sea level has been delineated from DV (Banerji et al., 2017).

The simultaneous enrichment of V/Al_2O_3 and Mo/Al_2O_3 (Fig. 2a) in the VV section during 4710 to 4000 cal BP implies anoxic conditions, but depleted values for Ni/Al_2O_3 suggests that Ni is not scavenged by settling organic particles (Tribovillard et al., 2006). The marginal increase of Ni/Al_2O_3 observed between 4000 and 3200 cal BP indicates the possible formation of insoluble sulphides that can be taken up by authigenic pyrite (Algeo and Maynard, 2004) and thereby suggests euxinic conditions (Banerji, Bhushan and Maurya, 2016). The prevalence of euxinic conditions in VV is further supported by the increasing trend in Mo/Al_2O_3 and V/Al_2O_3, as V resides predominantly in the sulfidic fraction under euxinic conditions (Algeo and Maynard, 2004). However, the simultaneous enrichment of V/Al_2O_3 and TOC with low values in Mo/Al_2O_3 in DV (Fig. 2b) during 4100 to 3000 cal BP suggests anoxic conditions (non-sulfidic), as the V mainly resides in TOC (Algeo and Maynard, 2004).

Under anoxic conditions, Cr^{4+} reduces to Cr^{3+} forming aquahydroxyl and hydroxyl cations that readily form a complex with humic/fluvic acids or gets adsorbed to Fe- and Mn-oxyhydroxides (Breit and Wan-

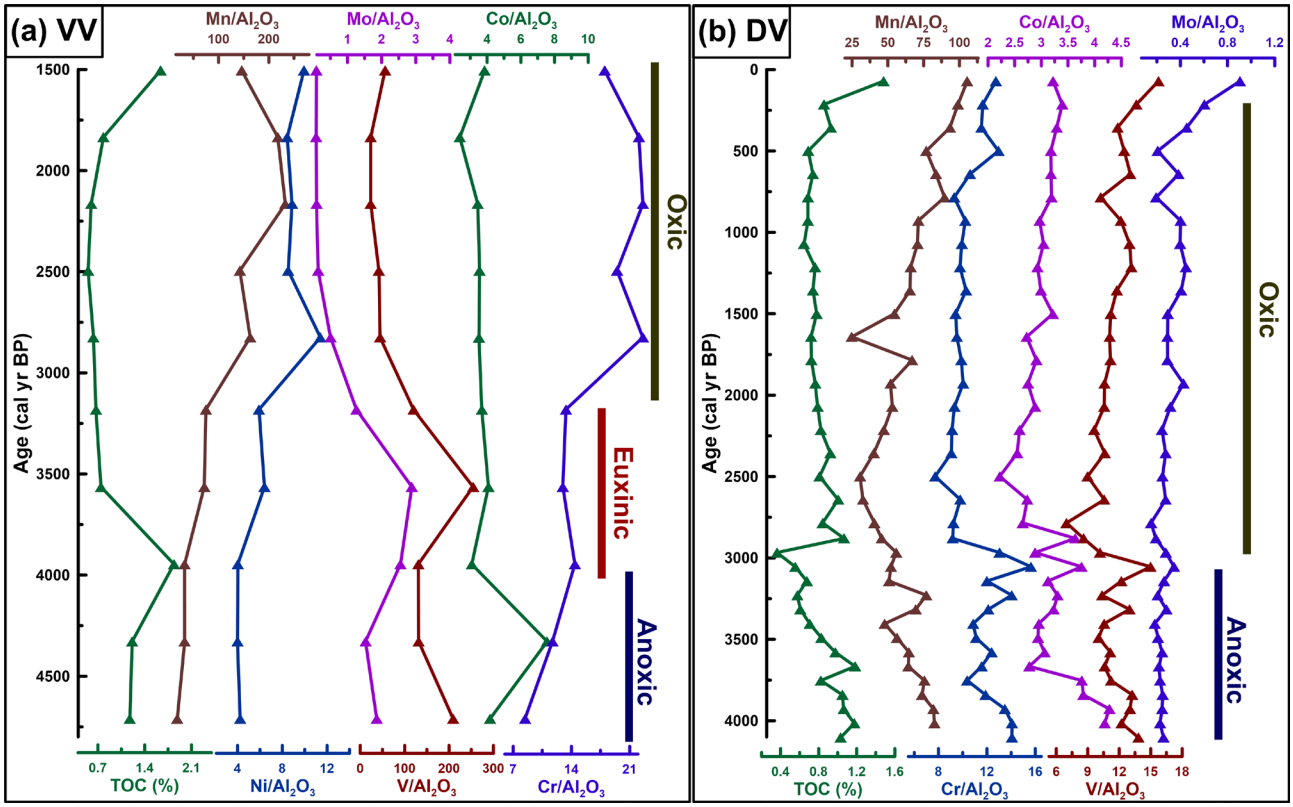

Figure 2: Enriched redox sensitive elements in VV (a) and DV (b) mudflat sections during 4710 to 4000 cal BP and 4100 to 3200 cal BP suggests anoxic conditions, while an intermittent euxinic environment during 4000 to 3200 cal BP prevailed in VV. Since 3000 cal BP, both regions (VV and DV) witnessed oxic conditions.

ty, 1991; Algeo and Maynard, 2004). In DV, the high Cr/Al_2O_3 during 4100 to 3000 cal BP suggests anoxic conditions. But the low Cr/Al_2O_3 in VV during 4000 to 3200 cal BP (Fig. 2b), in spite of the euxinic conditions, has been attributed to the limited uptake of Cr^{3+} by Fe-sulphides due to the incompatibility of Cr with pyrite (Huerta-Diaz and Morse, 1992; Morse and Luther, 1999). Under anoxic conditions, Co forms insoluble sulphides (CoS), which are taken up as solid solution by authigenic Fe-sulphides (Huerta-Diaz and Morse, 1992). Thus, the increased Co/Al_2O_3 in VV and DV confirms the prevalence of oxygen-deficient/anoxic conditions in the region.

Surprisingly, Mn/Al_2O_3 is low in VV but high in DV, even though both witnessed anoxic conditions. Generally under anoxic conditions, Mn reduces to Mn^{2+}, which is a soluble cation (Mn^{2+} or $MnCl^{+}$). As the dissolved Mn is not readily taken up by the organic matter or sulphide phase, it diffuses upwards till oxic conditions are encountered. The reduced Mn/Al_2O_3 in the DV suggested the prevalence of anoxic conditions. However, the increased Mn/Al_2O_3 in VV under anoxic conditions must be a result of the formation of $MnCO_3$ or Mn-Ca carbonate (Calvert and Pedersen, 1993). The possible formation of $MnCO_3$ or Mn-Ca carbonate can be confirmed from the high values of CaO, $CaCO_3$, and CaO/Al_2O_3 (Banerji et al., 2017, 2019).

4.2. Evidence of tectonic uplift

The southern Saurashtra coast has provided evidence of past sea level highstands and tectonic imprints (Pant and Juyal, 1993; Juyal et al., 1995). The palynological investigation of the VV section suggests high sea level with dense mangrove forest during 4710 cal BP. The mangrove forest led to anoxic conditions in VV, which is in agreement with the enriched redox-sensitive elements in the DV core, as they were part of the same lagoon. The present day elevation of VV and DV are ~ 5 m and ~ 3 m respectively and both witnessed a high sea level during 4710 to 1500 cal BP. The marine influence in VV ceased after 1500 cal BP, whereas the DV continued to receive sediment under exceptionally high tide conditions. Thus, there was a sea regression of ~2 m during 4710 cal BP. The estimated high sea level is in line with the radiocarbon age of an oyster bed (3.4 ± 0.05 ka) located at an elevation of 2 m above the present-day sea-level in Rupen River near Diu (Juyal et al., 1995). However, the sea level during the mid-Holocene could be an interplay of sea level and land level changes, as the southern Saurashtra coast near Diu and adjoining areas witnessed pulsating uplift during the late Quaternary period (Pant and Juyal, 1993). The prevalence of a tectonic component during the last 3 ka was inferred by the study conducted on the tidal notches around Diu Island (Bhatt and Bhonde, 2006). Further,

two tidal notches of Diu Island were examined near Vankwara (Diu), which suggested ~1 m of tectonic uplift (Banerji et al., 2015). This implies that the effective sea-level was ~2 m high during the ~4710 cal BP, which included ~1 m of tectonic uplift (Banerji et al., 2015).

4.3. Phases of sea level and tectonics along southern Saurashtra coast

The present study interprets four phases of transformation of the coastal lagoon into mudflat during the mid-Holocene period along the southern Saurashtra coast. The palynological investigation on the relict mudflat section VV demonstrated several mangrove species (Banerji et al., 2015), while the presence of shells in DV (Banerji et al., 2017) suggested high sea level during 4710 to 4000 cal BP.

The presence of mangroves led to high *in-situ* productivity resulting in anoxic conditions as seen from the enriched redox-sensitive elements (Fig. 3a). Thus, a lagoonal condition prevailed at both study locations and they formed part of a single lagoon system. Marginal sea regression during 4000 to 3200 cal BP led to poor water ventilation at VV site resulting in euxinic conditions, but the anoxic condition continued till 3200 cal BP at DV (Fig. 3b). Further sea regression after ~3200 cal BP transformed the lagoon into a mudflat region as the VV showed the presence of Turritella sp. between 3200 and 2825 cal BP (Fig. 3c) (Banerji, Bhushan and Maurya, 2016; Banerji et al., 2015) and the oxic conditions started prevailing in both locations (VV and DV). The sea regression after 3200 cal BP was also accompanied by a tectonic uplift which can be elucidated from the elevation of the older tidal notch of Vanakwara (Diu Island). The VV mudflat remained active till 1500 cal BP after which sediment deposition ceased due to sea regression and/or tectonic uplift, while DV continued to receive sediment under exceptionally high tide conditions (Fig. 3d). The sea regression and transformation of the lagoon to mudflat was accompanied by tectonic uplift in the region.

5. Conclusions

The present study attempts to identify mid-late Holocene sea-level change accompanied by a tectonic component. The study demonstrated that the high sea level led to the prevalence of lagoonal conditions behind the barrier bars of the southern Saurashtra coast during 4710 cal BP. The high sea level supported the extensive mangrove forests thereby leading to an anoxic environment during 4710 to 4000 cal BP. Later, the sea regression leading to poor water ventilation

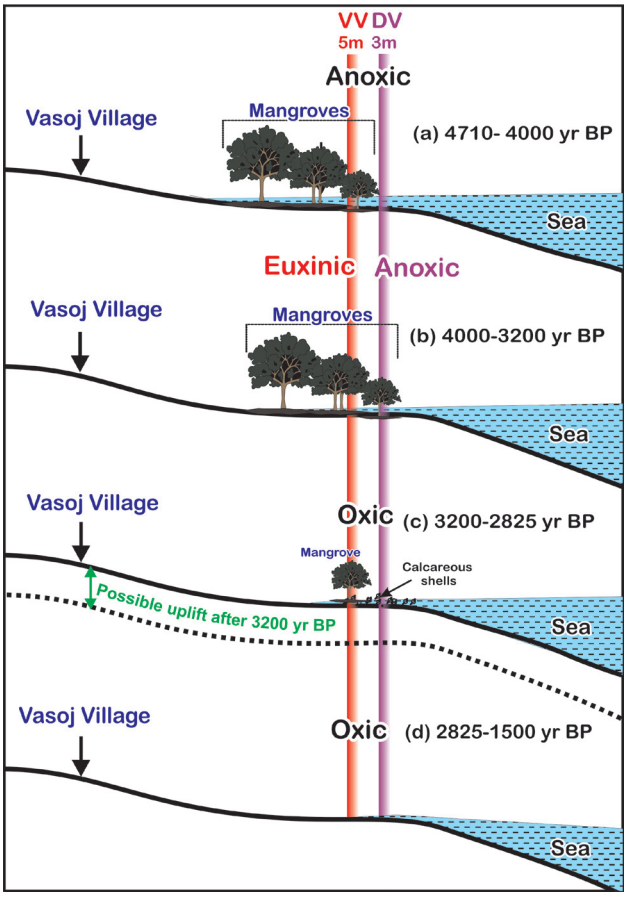

Figure 3: A schematic drawing of changing redox conditions at VV and DV locations wherein (a) the coastal lagoon with anoxic conditions prevailed due to high sea level and mangrove forest during 4710 to 4000 cal BP. (b) Gradual sea regression resulted in euxinic and anoxic conditions at VV and DV till 3200 cal BP, respectively. (c) An upliftment accompanied by sea regression transformed the coastal lagoon into a mudflat causing an oxic environment after 3200 cal BP. (d) A possible tectonic/sea regression after ~ 1500 cal BP terminated the sedimentation at VV.

at VV caused the prevalence of euxinic conditions, but the DV continued to witness an anoxic environment. After 3200 cal BP, both sites were transformed from lagoon to mudflats as a result of sea regression and tectonic influence. Further, sea regression and/or tectonic uplift after 1500 cal BP transformed VV region into a relict mudflat while DV continued receiving sediment under exceptionally high tides. Thus, the present coastal configuration was attained possibly after ~1500 cal BP and since then the coast seems to be stable. Nevertheless, other mudflats of coastal Saurashtra need to be investigated to ascertain the mid-late Holocene sea level fluctuations along with the tectonic components and should be compared with other regional and global coastal environments to generate a sea level curve exclusively for the mid-late Holocene Period.

6. References

Agnihotri, R., 2001. Chemical and Isotopic studies of sediments from Arabian sea and Bay of Bengal. PhD thesis. Faculty of Science. Mohanlal Sukhadia University. 131 pp.

Algeo, T.J. and Maynard, J.B., 2004. Trace-element behavior and

redox facies in core shales of Upper Pennsylvanian Kansas-type cyclothems. Chemical Geology 206(3), pp. 289–318. https://doi.org/10.1016/j.chemgeo.2003.12.009.

Allen, J.R.L. and Haslett, S.K., 2002. Buried salt-marsh edges and tide-level cycles in the mid-Holocene of the Caldicot Level (Gwent), South Wales, UK. The Holocene 12(3), pp. 303–324. https://doi.org/10.1191/0959683602hl537rp.

Banerji, U.S., Bhushan, R. and Jull, A.J.T., 2017. Mid-Late Holocene monsoonal records from the partially active mudflat of Diu Island, Southern Saurashtra, Gujarat, Western India. Quaternary International 443, pp. 200–210. https://doi.org/10.1016/j.quaint.2016.09.060.

Banerji, U.S., Bhushan, R. and Jull, A.J.T., 2019. Signatures of global climatic events and forcing factors for the last two millennia on the active mudflats of Rohisa, southern Saurashtra, Gujarat, western India. Quaternary International 507, pp. 172–187. https://doi.org/10.1016/j.quaint.2019.02.015.

Banerji, U.S., Bhushan, R. and Maurya, D.M., 2016. Sedimentary records of paleoredox conditions at relict mudflat of Vasoj, Southern Saurashtra coast, Gujarat. Earth Science India 9(II), pp. 114–125. https://doi.org/10.31870/ESI.09.2.2016.5.

Banerji, U.S., Pandey, S., Bhushan, R. and Juyal, N., 2015. Mid-Holocene climate and land-sea interaction along the southern coast of Saurashtra, western India. Journal of Asian Earth Sciences 111, pp. 428–439. https://doi.org/10.1016/j.jseaes.2015.06.021.

Baskaran, M., Marathe, A.R., Rajaguru, S.N. and Somayajulu, B.L.K., 1986. Geochronology of palaeolithic cultures in the Hiran Valley, Saurashtra, India. Journal of Archaeological Science 13(6), pp. 505–514. https://doi.org/10.1016/0305-4403(86)90037-3.

Bhatt, N. and Bhonde, U., 2006. Geomorphic expression of late Quaternary sea level changes along the southern Saurashtra coast, western India. Journal of Earth System Science 115(4), pp. 395–402. https://doi.org/10.1007/BF02702868.

Bhushan, R., Dutta, K. and Somayajulu, B.L.. L.K.K., 2001. Concentrations and burial fluxes of organic and inorganic carbon on the eastern margins of the Arabian Sea. Marine Geology 178(1–4), pp. 95–113. https://doi.org/10.1016/S0025-3227(01)00179-7.

Breit, G.N. and Wanty, R.B., 1991. Vanadium accumulation in carbonaceous rocks: a review of geochemical controls during deposition and diagenesis. Chemical Geology 91(2), pp. 83–97. https://doi.org/10.1016/0009-2541(91)90083-4.

Calvert, S.E. and Pedersen, T.F., 1993. Geochemistry of recent oxic and anoxic marine sediments: Implications for the geological record. Marine Geology 113(1–2), pp. 67–88. https://doi.org/10.1016/0025-3227(93)90150-T.

Douglas, B., 1991. Global sea level rise. Journal of Geophysical Research 96(C4), pp. 6981–6992. https://doi.org/10.1029/91JC00064.

Ganapathi, S., Patel, M.P., Merh, S.S., 1982. Evolution of the coastline between okha-madhi and Kodinar, western Saurashtra with special reference to Quaternary morphology and sedimentation, in: Merh, S.S. (Ed.), Geology and Geomorphology of Quaternary Terrains of Gujarat with Special Reference to Coastline Evolution. M.S. University of Baroda, Vadodara, pp. 95–122.

Hashimi, N.H., Nigam, R., Nair, R.R., Rajagopalan, G., 1995. Holocene sea level fluctuations on western Indian continental margin: an update. Geological Society of India 46, pp. 157–162.

Holgate, S.J., 2007. On the decadal rates of sea level change during the twentieth century. Geophysical Research Letters 34(1), L01602. https://doi.org/10.1029/2006GL028492.

Huerta-Diaz, M.A. and Morse, J.W., 1992. Pyritization of trace metals in anoxic marine sediments. Geochimica et Cosmochimica Acta 56(7), pp. 2681–2702. https://doi.org/10.1016/0016-7037(92)90353-K.

Juyal, N., Pant, R.K., Bhushan, R. and Somayajulu, B.L.K., 1995. Radiometric dating of late Quaternary sea levels of the Saurashtra coast, Western India: An experiment with oyster and clam shells. Geological Society of India Memoir 32, pp. 372–379.

Kristensen, E., Bouillon, S., Dittmar, T. and Marchand, C., 2008. Organic carbon dynamics in mangrove ecosystems: A review. Aquatic Botany 89(2), pp. 201–219. https://doi.org/10.1016/j.aquabot.2007.12.005.

Lamb, A.L., Wilson, G.P. and Leng, M.J., 2006. A review of coastal palaeoclimate and relative sea-level reconstructions using $\delta^{13}C$ and C/N ratios in organic material. Earth-Science Reviews 75(1), pp. 29–57. https://doi.org/10.1016/j.earscirev.2005.10.003.

Li, Z., Saito, Y., Mao, L., Tamura, T., Song, B., Zhang, Y., Lu, A., Sieng, S. and Li, J., 2012. Mid-Holocene mangrove succession and its response to sea-level change in the upper Mekong River delta, Cambodia. Quaternary Research 78(2), pp. 386–399. https://doi.org/10.1016/j.yqres.2012.07.001.

Marchand, C., Lallier-Vergès, E. and Allenbach, M., 2011. Redox conditions and heavy metals distribution in mangrove forests receiving effluents from shrimp farms (Teremba Bay, New Caledonia). Journal of Soils and Sediments 11(3), pp. 529–541. https://doi.org/10.1007/s11368-010-0330-3.

Morse, J.W. and Luther, G.W., 1999. Chemical influences on trace metal-sulfide interactions in anoxic sediments. Geochimica et Cosmochimica Acta 63(19), pp. 3373–3378. https://doi.org/10.1016/S0016-7037(99)00258-6.

Pant, R.K. and Juyal, N., 1993. Late Quaternary coastal instability and sea level changes: New evidence from Saurashtra coast, Western India. Zeitschrift für Geo-morphologie N.F. 37, pp. 29–40.

Rust, D. and Kershaw, S., 2000. Holocene tectonic uplift patterns in northeastern Sicily: evidence from marine notches in coastal outcrops. Marine Geology 167(1), pp. 105–126. https://doi.org/10.1016/S0025-3227(00)00019-0.

Sloss, C.R., Nothdurft, L., Hua, Q., O'Connor, S.G., Moss, P.T., Rosendahl, D., Petherick, L.M., Nanson, R.A., Mackenzie, L.L., Sternes, A., Jacobsen, G.E. and Ulm, S., 2018. Holocene sea-level change and coastal landscape evolution in the southern Gulf of Carpentaria, Australia. Holocene 28(9), pp. 1411–1430. https://doi.org/10.1177/0959683618777070.

Tribovillard, N., Algeo, T.J., Lyons, T. and Riboulleau, A., 2006. Trace metals as paleoredox and paleoproductivity proxies: An update. Chemical Geology 232(1–2), pp. 12–32. https://doi.org/10.1016/j.chemgeo.2006.02.012.

Waelbroeck, C., Labeyrie, L., Michel, E., Duplessy, J.C., McManus, J.F., Lambeck, K., Balbon, E. and Labracherie, M., 2002. Sea-level and deep water temperature changes derived from benthic foraminifera isotopic records. Quaternary Science Reviews 21(1–3), pp. 295–305. https://doi.org/10.1016/S0277-3791(01)00101-9.

Williams, M., Dunkerley, D., Deckker, P.D., Kershaw, P., Chappell, J., 1998. Quaternary Environments. Arnold, London, 329 pp. https://doi.org/10.1002/1099-1417(200009)15:6<662::AID-JQS576>3.0.CO;2-3.

Wilson, G.P., Lamb, A.L., Leng, M.J., Gonzalez, S. and Huddart, D., 2005. $\delta^{13}C$ and C/N as potential coastal palaeoenvironmental indicators in the Mersey Estuary, UK. Quaternary Science Reviews 24(18–19), pp. 2015–2029. https://doi.org/10.1016/j.quascirev.2004.11.014.

Zhan, Q., Wang, Z., Xie, Y., Xie, J. and He, Z., 2011. Assessing C/N and $\delta^{13}C$ as indicators of Holocene sea level and freshwater discharge changes in the subaqueous Yangtze delta, China. The Holocene, 22(6), p. 697–704. https://doi.org/10.1177/0959683611423685.

Is the Active Deformation in NW Borneo Tectonically-Driven or Gravity-Induced?

Navakanesh M. Batmanathan[1,✉], Afroz Ahmad Shah[2]

[1] Curtin University Malaysia
[2] University of Brunei Darussalam
✉ batmanathannavakanesh@gmail.com

Keywords: Sabah, Gravity, Tectonics, Earthquake, Strain

1. Introduction

The cause of active deformation of NW Borneo is a controversial topic. While some studies have shown evidence for active plate convergence along at the NW Borneo-Palawan Trough (Hutchison, 2010), others consider that evidence for plate convergence is lacking, and argue for episodes of crustal extension as the cause of Neogene deformation. For example, Hall (2013) suggests that the Borneo-Palawan Trough lacks features associated with a typical subduction zone, and therefore it is not a subduction-related trench, and instead interprets the structure as gravity-driven with a contribution from deep crustal movement. This raises questions on what is causing active deformation in the region, gravity or tectonics, and that is the focus of our study.

The interaction of the Indo-Australian, Sunda, and Philippine Sea plates creates a buzz of seismicity that encloses the Island of Borneo and confirms the active plate tectonic processes in the neighborhood. A closer look at the centroid moment tensor data of the earthquake events in NE Borneo shows that the regional tectonic deformation is accommodated by normal, thrust, and strike-slip faults, which could very well be related to crustal deformation related to plate tectonic processes, or alternatively, a product of local topographic effects and gravity-induced faulting. The answer to this problem is not a straightforward yes or no, and instead requires a comprehensive examination of various data such as seismological, geomorphological, geological, and geodetic.

On the regional scale, the tectonic strain is usually released by the occurrence of medium to large magnitude earthquakes (Fig. 1A). However, the occasional occurrence and sparse distribution of earthquakes on the Island of Borneo means that the region is not as active as the neighboring regions (e.g. Sapin et al., 2009). The present tectonic map of the region places Borneo as part of the Eurasian plate, and more specifically the Sunda plate (Fig. 1A), which seems to be tectonically stable when only earthquakes are used as the criteria of active tectonism. Therefore, the cause of active deformation in this region remains debated with two broader outlooks: either driven by gravity (Hazebroek and Tan, 1993; Hall, 2013), or by gravity and far-field compression (Ingram et al, 2004; Sapin et al., 2013). Here we review all of the major published works on the active deformation of NW Borneo and re-evaluate the structural data with the main focus on the causes of active deformation in the region. The field observations are supplemented with the centroid moment tensor data to support the new synthesis, which is presented below.

2. Active tectonics in NW Borneo

The active deformation in NW Borneo has been discussed extensively (e.g. Ingram et al., 2004; Mathew et al., 2016; Shah, 2016; Tongkul, 2016; Tongkul, 2017; Wang et al., 2017; Shah et al., 2018, Wu et al, 2020), and the largest earthquake in the recorded history occurred in June 2015 when a normal fault system ruptured in Sabah (Fig. 1D). The cause of active faulting in the region is broadly related to either non-tectonic (gravity-driven) or gravity plus tectonic causes (e.g. Ingram et al., 2004; Hesse et al., 2009; Sapin et al., 2013; Wang et al., 2017, Shah et al., 2018, Wu et al., 2020). These interpretations emerge from the fact that earthquake distribution on the Island of Borneo is very sparse and mostly concentrated in the far north (Fig. 1A), and the active structures that are mapped in the region are usually related to typical gravity-driven local deformation and not tectonics (e.g. Hazebroek and Tan, 1993). But there are many problems in a solely gravity-driven active deformation model, which are discussed below, and are supported by the mapping of new geomorphic evidence for active tectonic structures.

3. Methodology

The data on previously published structural maps are compiled (Fig. 1) from various sources that include Wang et al. (2016), Shah (2016), Wang et al., (2017), Mustafar et al. (2017), and JMG (Malaysian Government Agency), and references therein. These are plotted on the digital elevation model (DEM) derived image to show the extent and type of faulting

Proceedings of the 5th International YES Congress
DOI: 10.2312/yes19.19

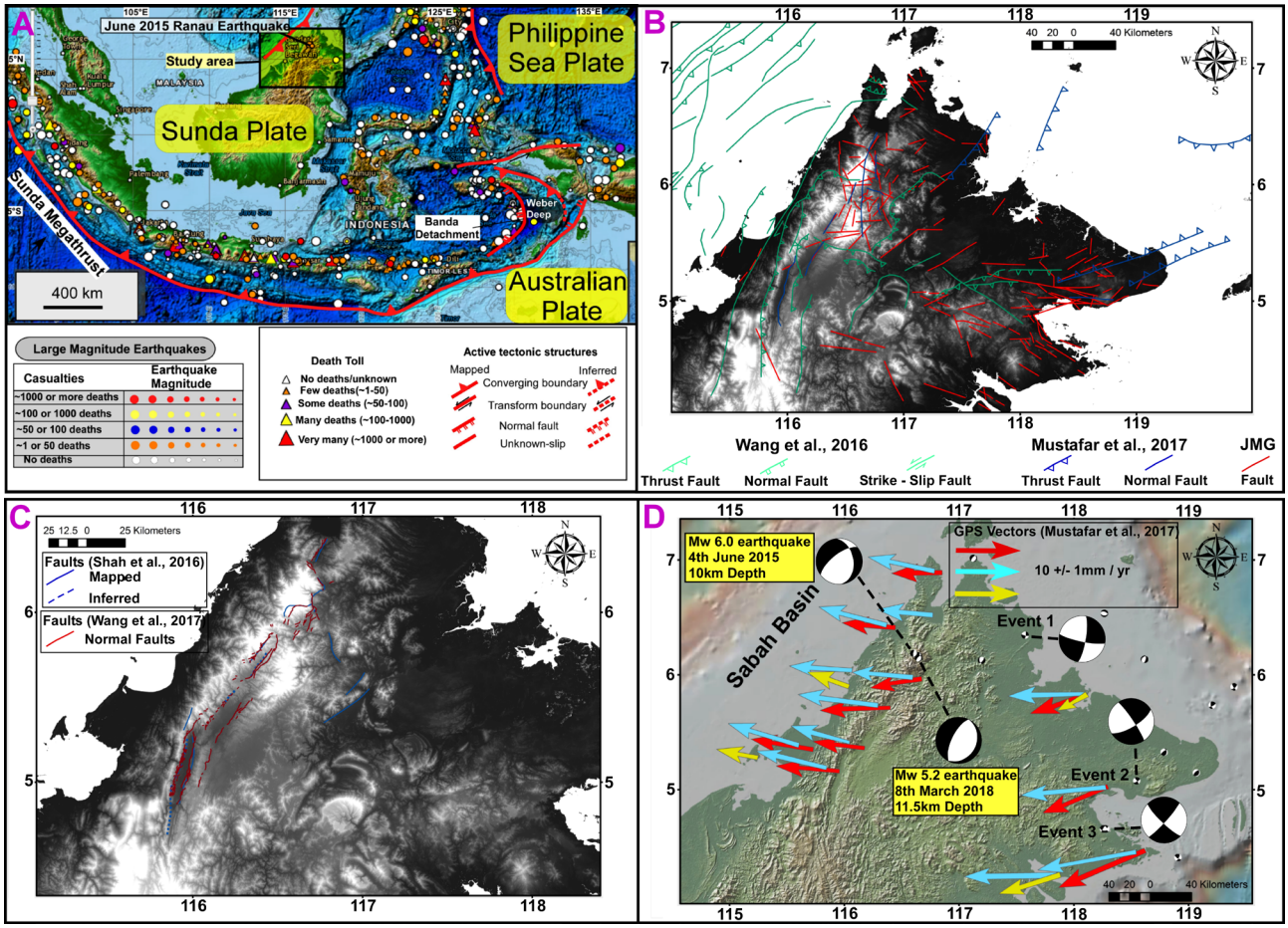

Figure 1: (A) Regional tectonic map of SE Asia that mainly shows the active tectonic plate boundary faults systems. The color filled circles show significant earthquakes that have caused damage to life and property (modified after Shah et al., 2018). (B) Digital elevation model (DEM) derived image with previously mapped fault data that are sourced from Wang et al. (2016), Mustafar et al. (2017) and JMG (Malaysian Government Agency). (C) The presence of active faults in Sabah (after Shah, 2016 and Wang et al., 2017). (D) The GPS vectors show a NW to W directed present day crustal movement, which suggests oblique extension on Crocker fault system (GPS data after Mustafar et al., 2017).

(Fig. 1B,C) (Shah and Malik, 2017). We have also collected data (Fig. 2) on the exact position of the West Baram Line, known as Tinjar Line onshore (Cullen, 2014), which has been mapped and interpreted either as a transform boundary, a fault, or a structural discontinuity with unknown slip. The exact location is also a controversial topic (Fig. 2). The GPS vectors (Mustafar et al., 2017) are plotted on the satellite data using the open-source GeoMap App application. The centroid moment tensor solutions of the available earthquakes are extracted from the GeoMap App and examined to find a possible correlation with the faults that are mapped on the images (Fig. 1D). This involved recording the strike, dip, depth, and rake of each event. We only included earthquakes that originated at < 50 km depth because we focus on crustal deformation only. Fieldwork was conducted in parts of Sabah, Malaysia, to map evidence of active faulting (details in Navakanesh et al., 2019).

4. Results and Interpretations

The investigation of previously published structural maps of NW Borneo (Fig. 1A–C) shows that a number of faults have been mapped but the data in Wang et al. (2017) and Shah et al. (2016, 2018) fit well with the field (Fig. 3) and seismological data. The earthquake centroid moment tensor data show the dominance of normal and strike-slip faulting in the region (Fig. 2), with a normal faulting mechanism in Sabah and adjacent regions (Fig. 1D). Note the occurrence of normal faults in the northern tip of Borneo, which suggests either ~SE or ~NW dipping faults. Both these possibilities exist, which is supported by our geomorphic and field evidence, and the ~NW dipping normal fault system that ruptured at ~12 km depth on 4th June 2015 and on 8th March 2018 (Shah et al., 2018; Navakanesh et al., 2019), resembles that fault that we have mapped in the field (Fig. 3).

A number of strike-slip earthquake events are also very distinct in the region, and particularly those that have occurred in eastern Borneo (Fig. 1D). The strike-slip earthquake (Fig. 1D, event 1) could have

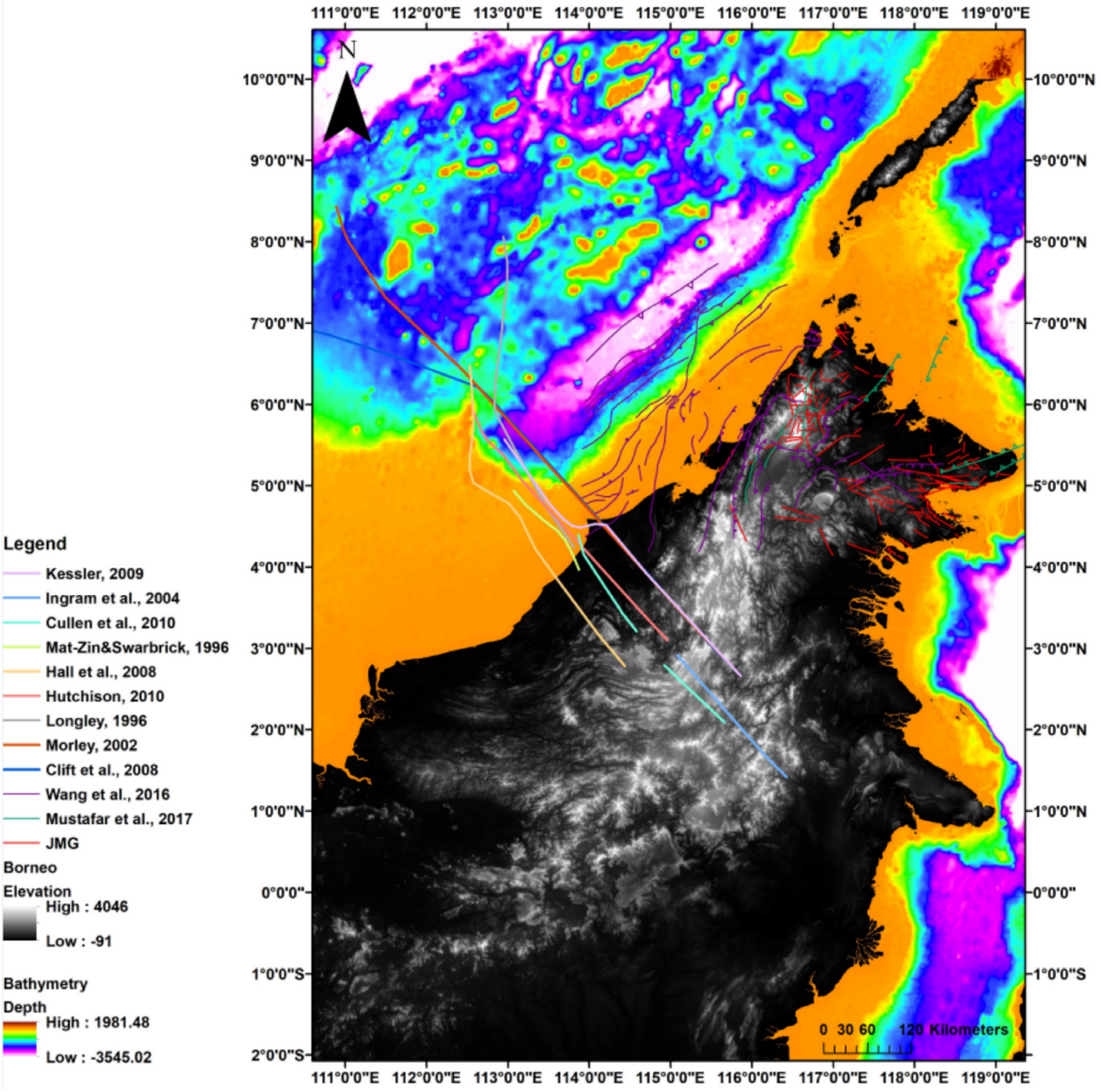

Figure 2: The ongoing active deformation of NW Borneo region is controversial, and this is also reflected in the mapping of major structures. For example the West Baram Line (known as Tinjar Line onshore) is either considered a transform boundary, a fault, or a structural discontinuity with unknown slip. And the exact location also remains a controversial topic.

occurred following left-lateral strike-slip movement along a ~NE-SW trending fault or by dextral strike-slip movement on a ~E-W trending fault. The existence of a similar fault was shown by Navakanesh et al. (2019) and that fits the left-lateral strike-slip faulting (Fig. 1D, event 1). The oblique strike-slip earthquakes that are recorded in eastern Borneo (Fig. 1D, events 2 and 3) show either dextral or sinistral faulting. The topographic expression of active strike-slip faulting in Borneo was shown by Shah et al. (2018) and the centroid moment tensor data clearly back such type of faulting in the region. This suggests that the occurrence of active strike-slip faulting in Borneo is perhaps common. Details on this faulting could be obtained through paleoseismological work on some of the major faults.

The pattern of earthquakes and the previously published structural data show active deformation in NW Borneo, and field data shows the dominance of normal faulting (Wang et al., 2017; Navakanesh et al., 2019). The field data are collected after the June 2015 event but the evidence for co-seismic surface rupturing was not observed, which suggests blind normal faulting. During our fieldwork, we have mapped old fault systems that show similar structural parameters (Fig. 2), which include the fault dip angle and direction. For example, a number of normal faults are mapped with both NE and SW dip directions (Fig. 2), and the faults are not observed to have ruptured any of the Holocene deposits. Therefore, the normal

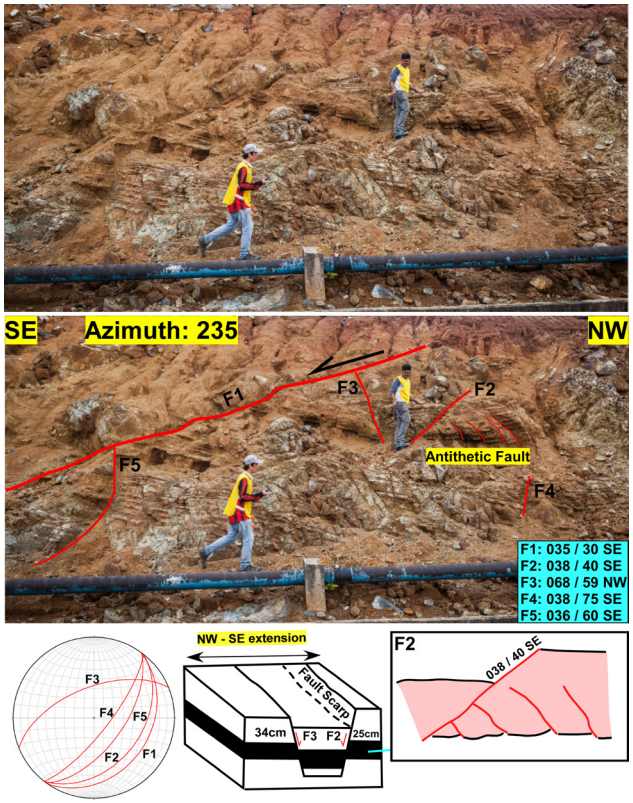

Figure 3: The un-interpreted field photograph is shown at the top, and the Interpreted (bottom) shows the occurrence of NW and SE dipping normal faults in the region. The stereonet plots show the same, and suggest an older normal fault system with NW-SE directed regional extension.

faulting event that struck Sabah in June 2015 was a common occurrence and similar earthquakes should have occurred in the past, as is clearly visible from the bedrock faulting. However, the age of recent activity on these faults is not known, which requires further work on the ground.

5. Discussion and Conclusions

Understanding the cause and occurrence of intra-plate earthquakes remains a challenge, particularly in regions that are considered tectonically stable. The notion of this is vigorously debated after the 4th June 2015 earthquake that caused significant damage and loss of life (Wang et al., 2017; Shah et al., 2018; Navakanesh et al., 2019). The geomorphic, geologic, and structural mapping details available from the region have clearly demonstrated that NW Borneo is active. Although the geomorphic analysis indicates the presence of active tectonic fault scarps (Hutchison, 2005; Cullen, 2010), such evidence is not observed in the field because it is usually buried under sediments. The evidence of mapped normal faults that have displaced the basement rocks and show similar structural parameters that were recorded during the June 2015 and March 2018 events (Fig. 1) seems to suggest that older faults have been reactivated. The lack of Holocene earthquake ruptures suggests that faulting is either blind, or the earlier evidence for fault ruptures has been erased in the tropical conditions of the Island. Regionally, the currently occurring direction of extension is ~NW-SE, and it seems that the deformation is controlled at depth by the major strike-slip fault (Shah et al., 2018) that runs through the backbone of the Island. This means that the deformation is a product of oblique convergence, and if that is true, then this part of the Sunda plate is undergoing active extension (Fig. 4). Since the region is apparently not influenced by the nearby subduction systems, this kind of deformation could be related to intra-plate deformation processes or far-off stresses. Alternatively, the active tectonic convergence along the Borneo-Palawan Trench could explain active deformation onshore NW Borneo. However, evidence for subduction is subtle or even not convincing, and Hall (2013) argues against the active tectonic convergence at the trough. We also suggest that Borneo-Palawan trench does not resemble a typical subduction zone and its abrupt termination at the southwest questions the association with a tectonic trench. It is more like a crustal extensional feature that was later filled with sediments that are undergoing active deformation induced by gravity, and far-field tectonics.

The cause of active deformation in this region could be attributed to gravitational causes that require a subsurface stratum onto which the sliding is possible, and previous work has suggested that a pressured shale lithology at depth could provide suitable conditions to make sliding possible (Sandal, 1996; Sapin et al., 2013). And in NW Borneo, the Setap shale, which sits at the base, is a good candidate to act as a décollement onto which rocks can glide like a large-scale landslide. However, if this is true, structural and geometrical constraints apply and one would expect a more or less systematic orientation of structures that would be expected from this type of deformation model. Figure 4A illustrates the gravity-driven deformation model, and such a model would predict a ~NE-SW strike of normal faults in onshore regions, and similar but reverse faults at the toe. It also requires strike-slip faults at both sides as bounding structures that limit the deformation of the Baram delta (Tjia, 2003). However, large-scale strike-slip faults have not been mapped in the region. The only structures that are mapped are the largely undifferentiated West Baram Line (Tinjar line), which could be a good fit (Fig. 2) but presently would be expected to follow a sinistral sense of movement, which needs to be tested. However, the gravity-driven deformation model cannot explain the deformation within central and eastern

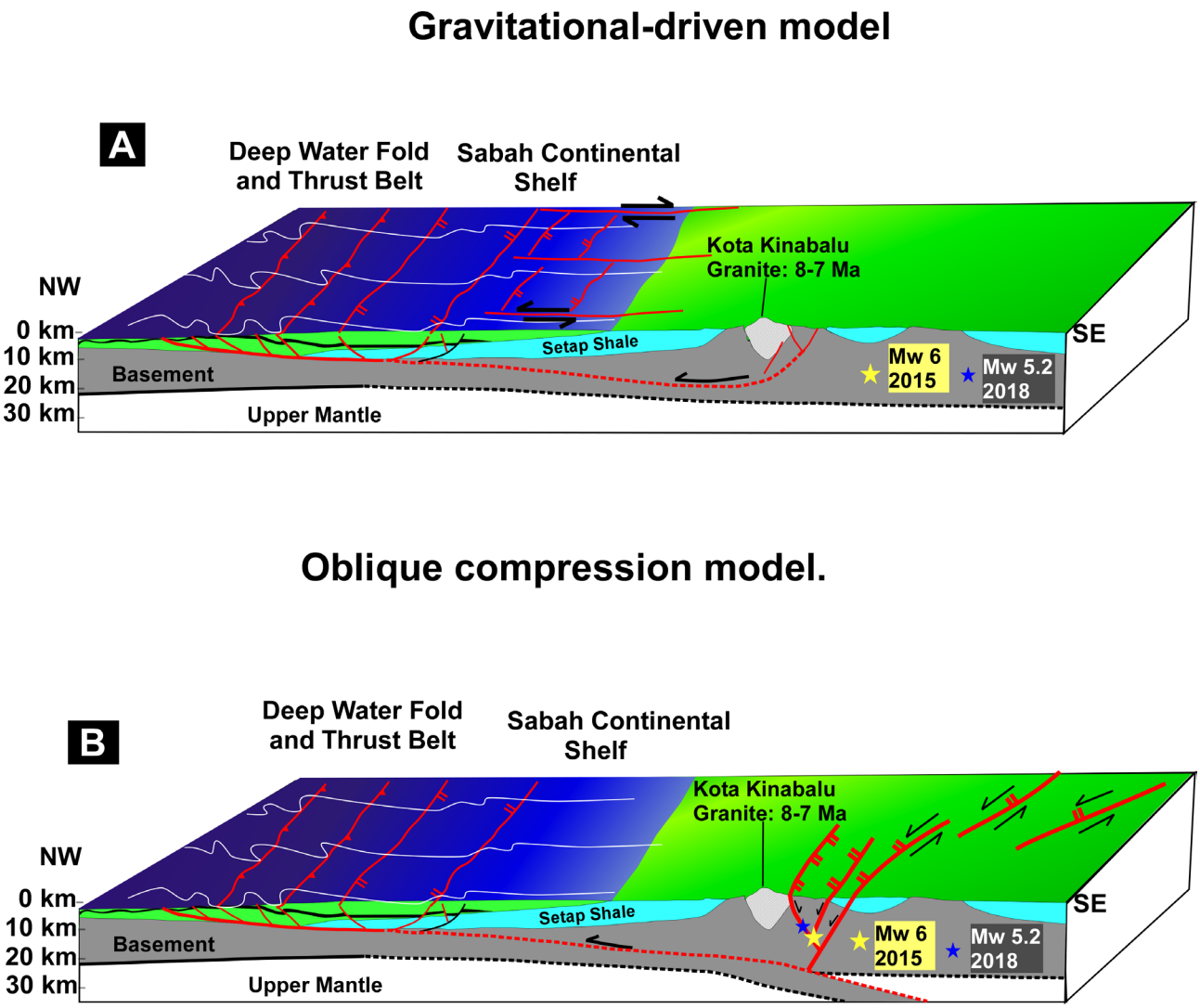

Figure 4: (A) Gravitational-driven model. The model illustrates gravity alone could not explain the deformation in NW Borneo. The conceptual idea here is the strike slip systems must have initiated transtensional settings along the Sabah continental shelf. At depths of 10 km, the gravitational deformational seems ineffective without an active influence of additional forces that are usually tectonic in origin. (B) The oblique compression model of Shah et al (2018) shows the occurrence of a major strike slip system along the backbone of Borneo Island, which could be controlling the additional deformation that gravity alone cannot explain.

Borneo, where active deformation is ongoing (Shah et al., 2018). Therefore, we argue that strike-slip fault-related events recorded in Borneo are related to active deformation onshore, and suggest that the Island is slowly accumulating strain that could be related to far-field tectonic stresses and not just sliding under the influence of gravity (Shah et al., 2018). Finally, the depth, scale, extent, and type of faulting in Borneo are challenging and cannot be simply explained by just gravity-driven deformation models. Therefore, we propose that gravity-driven deformation and tectonic stresses work together to explain the deformation in Borneo. Similar conclusions are drawn by some of the past studies where the amount of shortening and extension within NW Borneo has been interpreted to understand and quantify the deformation related to gravity-driven and far-field tectonic processes in northern Borneo since the late Pliocene (Hesse et al., 2009; King et al., 2010). The recent data have demonstrated that the amount of shortening within the NW Borneo deep-water fold belt cannot be fully explained by just gravity-driven shortening, and it most likely involves tectonic shortening (Wu et al., 2020).

6. Acknowledgement

We would like to thank the National Geographic Society, USA, for providing us the Young Explorer Grant to complete the fieldwork in Sabah, Malaysia.

7. References

Clift, P., Lee, G.H., Nguyan, A.D., Barckhausen, U., Long, H., Zhen, S., 2008. Seismic reflection evidence for a Dangerous Grounds miniplate: no extrusion origin for the South China Sea. Tectonics 27, pp. 1–16. https://doi.org/10.1029/2007TC002216.

Cullen, A., 2010. Transverse segmentation of the Baram – Balabac Basin, NW Borneo: refining the model of Borneo's tectonic evolution. Petroleum Geoscience 16, pp. 3–29. https://doi.org/10.1144/1354-079309-828.

Cullen, A., 2014. Nature and significance of the West Baram and Tinjar Lines, NW Borneo. Marine and Petroleum Geology 51, pp. 197–209. https://doi.org/10.1016/j.marpetgeo.2013.11.010.

Hall, R., 2013. Contraction and extension in northern Borneo driven by subduction rollback. Journal of Asian Earth Science 76, pp.

399–411. https://doi.org/10.1016/j.jseaes.2013.04.010.
Hall, R., van Hattum, M., Spakman, W., 2008. Impact of India-Asia collision on SE Asia: the record in Borneo. Tectonophysics 451, pp. 366–369. https://doi.org/10.1016/j.tecto.2007.11.058.
Hazebroek, H.P., Tan, D.N.K., 1993. Tertiary tectonic evolution of the NW Sabah Continental Margin. Bulletin of the Geological Society of Malaysia 33, pp. 195–210.
Hesse, S., Back, S., Franke, D., 2009. The deep-water fold-and-thrust belt offshore NW Borneo: Gravity-driven versus basement-driven shortening. Bulletin of Geological Society of Amsterdam 121, pp. 939–953. https://doi.org/10.1130/B26411.1.
Hutchison, C.S., 2005. Geology of North-West Borneo: Sarawak, Brunei and Sabah. Elsevier, Amsterdam. 444 p.
Hutchison, C.S., 2010. Oroclines and paleomagnetism in Borneo and south-east Asia. Tectonophysics 496, pp. 53–67. https://doi.org/10.1016/j.tecto.2010.10.008.
Ingram, G.M., Chisholm, T.J., Grant, C.J., Hedlund, C.A., Stuart-Smith, P., Teasdale, J., 2004. Deepwater North West Borneo: hydrocarbon accumulation in an active fold and thrust belt. Marine and Petroleum Geology 21, pp. 879–887. https://doi.org/10.1016/j.marpetgeo.2003.12.007.
JMG, 2012. Geological Study of the Seismic Activities in the Bukit Tinggi Area. Jabatan Mineral dan Geosains Malaysia, Kuala Lumpur, 72 p.
King, R.C., Backé, G., Morley, C.K., Hillis, R.R., and Tingay, M.R.P., 2010. Balancing deformation in NW Borneo: Quantifying plate-scale vs. gravitational tectonics in a delta and deepwater fold-thrust belt system: Marine and Petroleum Geology 27, pp. 238–246, https://doi.org/10.1016/j.marpetgeo.2009.07.008.
Longley, I.M., 1996. The tectonostratigraphic evolution of SE Asia. In: Murphy, R.W. (Ed.), Petroleum Geology of Southeast Asia, Geological Society of London Special Publication, 126, pp. 311–339.
Mathew, M.J., Menier, D., Siddiqui, N., Kumar, S.G., Authemayou, C., 2016. Active tectonic deformation along rejuvenated faults in tropical Borneo: Inferences obtained from tectono-geomorphic evaluation. Geomorphology 267, pp. 1–15. https://doi.org/10.1016/j.geomorph.2016.05.016.
Mat-Zin, I.C., Swarbrick, R.E., 1997. The tectonic evolution and associated sedimentation history of Sarawak Basin, eastern Malaysia: a guide for future hydrocarbon exploration. In: Fraser, A.J., Matthews, S.J., Murphy, R.W. (Eds.), Petroleum Geology of Southeast Asia, Geological Society Special Publication 126, pp. 237–245.
Morley, C.K., 2002. A tectonic model for the Tertiary evolution of strike-slip faults and rift basins in SE Asia. Tectonophysics 347, pp. 189–215. https://doi.org/10.1016/S0040-1951(02)00061-6.
Mustafar, M.A., Simons, W.J.F., Tongkul, F., Satirapod, C., Omar, K.M., and Visser, P.N.A.M., 2017. Quantifying deformation in North Borneo with GPS. Journal of Geodesy 91, pp. 1241–1259, https://doi.org/10.1007/s00190-017-1024-z.
Navakanesh, B., Shah, A.A., Prasanna, M.V., 2019. Earthquake Education Through the Use of Documentary Movies. Frontiers in Earth Science, 7, 42. https://doi.org/10.3389/feart.2019.00042.
Sandal, S.T., 1996. The Geology and Hydrocarbon Resources of Negara Brunei Darussalam, Brunei Shell Petroleum, Bandar Seri Begawan, 243 p.
Sapin, F., Pubellier, M., Ringenbach, J.C., Rives, T., 2009. The Brunei fold-and-thrust belt: Tectonically-or Gravity-driven? AAPG Hedberg Conference, 6 p.
Sapin, F., Hermawan, I., Pubellier, M., Vigny, C., Ringenbach, J.C., 2013. The recent convergence on the NW Borneo Wedge: a crustal-scale gravity gliding evidenced from GPS. Geophysical Journal International 2, pp. 549–556. https://doi.org/10.1093/gji/ggt054.
Shah, A. A., 2016. Understanding the recent Sabah earthquake and other seismogenic sources in North West Borneo. Scientific Malaysian 11/2015, pp. 7–10.
Shah, A.A., Malik, J.N., 2017. Four major unknown active faults identified, using satellite data, in India and Pakistan portions of NW Himalaya. Natural Hazards 88(3), pp. 1845–1865. https://doi.org/10.1007/s11069-017-2949-5.
Shah, A.A., Zhafri, M.N., Delson, J., Navakanesh, B., 2018. Major Strike – Slip Faults Identified Using Satellite Data in Central Borneo, SE Asia. Geosciences 8, 156. https://doi.org/10.3390/geosciences8050156.
Tjia, H. D., 2003. Northwest Sabah Overthrust System. Geological Society of Malaysia 46, pp. 5–10. https://doi.org/10.7186/bgsm46200302.
Tongkul, F., 2016. The 2015 Ranau earthquake: Cause and Impact. Sabah Society Journal 32, pp. 1–28.
Tongkul, F., 2017. Active tectonics in Sabah – seismicity and active faults. Bulletin of the Geological Society of Malaysia 64, pp. 27–36. https://doi.org/10.7186/bgsm64201703.
Wang, Y., Wei, S., Wang, X., Lindsey, E.O., Tongkul, F., Tapponnier, P., Bradley, K., Chan, C.H., Hill, E.M., Sieh, K., 2017. The 2015 Mw 6.0 Mt. Kinabalu earthquake: an infrequent fault rupture within the Crocker fault system of East Malaysia. Geoscience Letters 4, 6. https://doi.org/10.1186/s40562-017-0072-9.
Wu, J., McClay, K., de Vera, J., 2020. Growth of triangle zone fold-thrusts within the NW Borneo deep-water fold belt, offshore Sabah, southern South China Sea. Geosphere 16(1), pp. 329-356. https://doi.org/10.1130/GES02106.1.

Metasomatism in the Uppermost Subcontinental Mantle in the Presence of Ti-Rich Hydrous Carbonated Silicate Melt

Naina Goswami[1,✉]

[1] Research School of Earth Sciences, Australian National University, Canberra, Australia

✉ u5960582@anu.edu.au

Keywords: Metasomatism, ultramafic xenoliths, trace elements, carbonatite

1. Introduction

Carbonate-rich melts are characterized by low viscosity and low density (Bodinier et al., 1989; Song and Frey, 1989; Rudnick et al., 1993; Grégoire et al., 2003). These highly mobile primary magmatic liquids have long been recognized as important metasomatic agents altering the mantle geochemistry (Yaxley et al., 1991; Grégoire et al., 2003; Pilet et al., 2016). The origin of carbonatite melts is hypothesized. Hypotheses propose that carbonatite melts are formed either by immiscible separation of parental carbonated silicate magmas at crustal or mantle pressures, crystal fractionation of parental carbonate-silicate magmas and/or low-degree of partial melting of carbonated mantle peridotite below 70 km depth (Yaxley et al., 1991; Yaxley et al., 1998; Pilet et al., 2016; Simandl and Paradis, 2018). Carbonatites can possibly be derived from Earth's crust or mantle with some crustal contribution (e.g. subducted crustal component) (Pilet et al., 2016). Carbonatites and alkaline-carbonatite complex can be emplaced in continental settings (extensional settings related to large-scale intraplate fracture zones), slab windows in subducted plates and in post-collisional orogenic settings, as in British Columbia Alkaline province, Canada (Pell, 1994, Millonig et al., 2012), and the Himalayan collisional zone, western Sichuan, China (Hou et al., 2006). They have also been identified in oceanic island regions, e.g. the Canary Islands, the Cape Verde Islands and the Kerguelen Islands. The commonly observed enrichment in LILE (large-ion lithophile elements) and REEs (rare earth elements) in many peridotite xenoliths hosted by alkali basalts is attributed to cryptic metasomatism by LILE-rich silicate-carbonate fluids (Yaxley et al., 1991; O'Reilly et al., 1991; Dautria et al., 1992) The presence of hydrous phases such as phlogopite and/or pargasite has been attributed to modal metasomatism introduced by Si-undersaturated fluids (Dawson, 1984; Bodinier et al., 1988; Green and Wallace, 1988; Song and Frey, 1989; O'Reilly et al., 1991; Rudnick et al., 1993). Occurrences of such metasomatic episodes have been reported globally (Bodinier et al., 1989; Yaxley et al., 1991; Pilet et al., 2016; Groves et al., 2020; Aulbach et al., 2020). Wallace and Green (1988) first determined experimentally the genesis of the metasomatic melt as a carbonated silica-undersaturated melt generated from the partial melting of periodite + carbonatite + H_2O at varied pressure and temperature conditions. They predicted that a melt with > 40 wt% CO_2 and 1-2 wt% H_2O would be an effective metasomatic agent in transferring LILEs to the upper mantle. Once this melt interacts with the mantle assemblage, it then evolves to a sodic-dolomitic composition (documented as CM1 in Wallace and Green, 1988). Metasomatism of xenoliths by ephemeral carbonate melts leads to the formation of accessory mineral phases like apatites or amphiboles, with simultaneous enrichment in LILEs and REEs in primary clinopyroxenes (Green and Wallace, 1988; Yaxley et al., 1991; Sweeney, 1994; Hammouda and Keshav, 2015). The formation of secondary clinopyroxene and olivine may follow the consumption of orthopyroxene as described by the univariant reaction (Eq. 1)

$$4MgSiO_3 + CaMg(CO_3)_2 = 2Mg_2SiO_4 + CaMgSi_2O_6 + 2CO_2 \quad \textit{(Eq. 1)}$$

$$Orthopyroxene + Dolomite = Olivine + Clinopyroxene + fluid$$

This reaction is controlled by the prevailing mantle conditions i.e. pressure, temperature and redox state. The influx of multiple flows of carbonatitic melts could ultimately lead to the conversion of harzburgite or lherzolitic mantle to orthopyroxene-free wehrlite. These occurrences have been previously documented in peridotite xenoliths (Yaxley et al., 1991; Dautria et al., 1992).

Here we report and investigate first occurrences of carbonate-bearing spinel peridotite xenoliths from a sub-surface Mesozoic basaltic dyke intruding into Palaeozoic granites of Tumut-Eucumbene Tunnel, in Snowy Mountains Region, New South Wales, Australia. To our knowledge, no prior research has been done on the samples recovered from basanite dyke(s) in this region, but numerous studies have investigated the granitic rocks of the area (e.g. Black, 1965; McDougall and Wellman, 1976). This study aims at determining the nature and origin of carbonates by analysing the spinel-peridotite xenoliths from this sample suite and other features they host.

Proceedings of the 5th International YES Congress
DOI: 10.2312/yes19.20

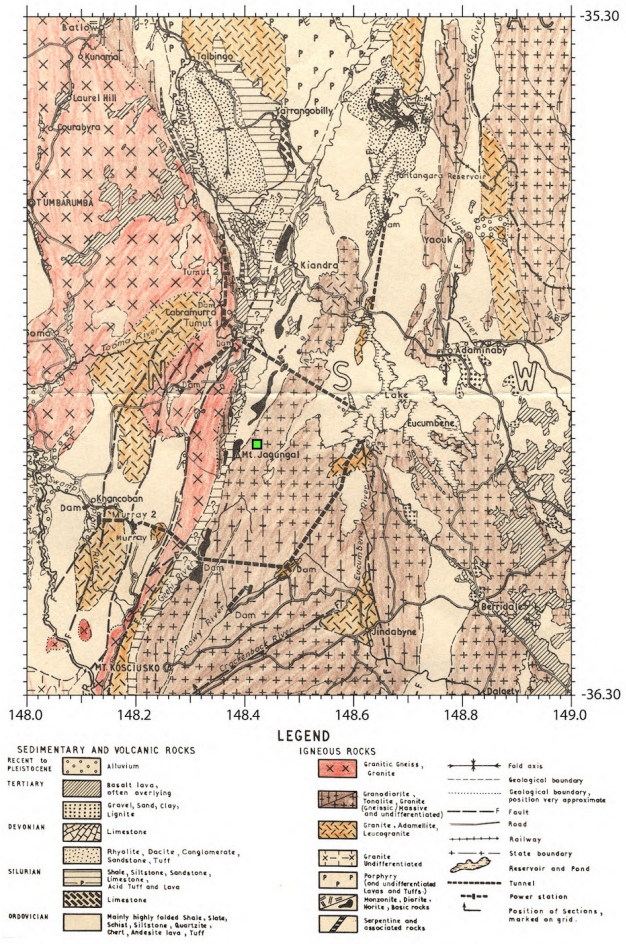

Figure 1: Geological map of Snowy Mountains area highlighting the location of the sampled basanite dyke (modified after Molnar 1963).

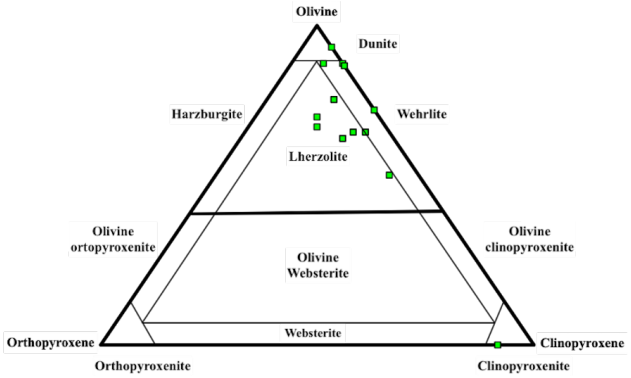

Figure 2: Ternary Diagram describing the modal classification of our suite of xenoliths based on the modal proportions of Olivine (Ol), Orthopyroxene (opx) and Clinopyroxene (cpx).

2. Sample location and Petrography

2.1. Sample location

The samples are spinel lherzolites to wehrlites collected from a sub-surface basanite dyke cutting through the Tumut-Eucumbene Tunnel in Snowy Mountains region, New South Wales, Australia (35.878568° S, 148.420076° E; Fig. 1).

Due to the subsequent flooding of Lake Eucumbene in 1958, any opportunity of further sampling was lost, thus making these samples novel. This intrusion was mapped to be about 2.5 m across and composed of massive, fine-grained alkaline basalt enveloping rounded inclusions of peridotite. The matrix basalt was texturally very similar to the Tertiary flows of the area and was assumed to be associated with the Monaro Volcanics. K-Ar ages on whole-rock from this dyke gave an age of 168 ± 7 Ma (McDougall and Wellman, 1976), similar to the ages of the igneous units in Cooma region.

2.2. Petrography

Petrographically, the samples are a suite of ultramafic spinel peridotites ranging from lherzolitic to wehrlitic mineralogy (Fig. 2).

The samples consist of neoblasts and porphyroblasts of olivine + clinopyroxene + spinel ± orthopyroxene. The majority of these samples are devoid of orthopyroxene along with concomitant presence of apatite, amphibole and patches of carbonate. Minor proportions of apatite, sulphide and ilmenite precipitates are also found. Chemical equilibrium between the minerals and matrix in the samples is reasonably assumed from absence of compositional zoning in the minerals. The mineral grains in the entire suite are heavily fractured by basanite melt veins, carbonate patches and serpentine mesh, producing a range of textures.

3. Analytical Methods

Major element compositions of our samples were analysed using the electron probe micro analyser CAMECA SX-100 and JEOL 8310 at the Research School of Earth Sciences (RSES) and the Centre for Advanced Microscopy (CAM), respectively, at Australian National University (ANU). All analyses were operated with an accelerating voltage of 15 kV, a beam current of 20 nA, and beam diameters varying between 1 µm and 5 µm with a counting time of 10 to 30 s. A minimum of 3 analyses per grain was performed on each sample.

Along with major elements, trace element compositions were also analysed in these samples with laser ablation mass spectrometry using the single collector ICP-MS Agilent 7700 coupled with the ArF EXCIMER laser (193 nm wavelength, 20 ns pulse width, 103 µm diameter) at RSES, ANU. Polished thin sections (50 to 100 µm thick) were ablated to carry out spot analyses using NIST SRM-610 as calibration standard and NIST SRM-612 and BCR-2g as secondary standards. A 81 µm spot size was used for clinopyroxene and amphibole analyses. The analyses followed the “sandwich method” i.e. the sample analyses (7 to 8

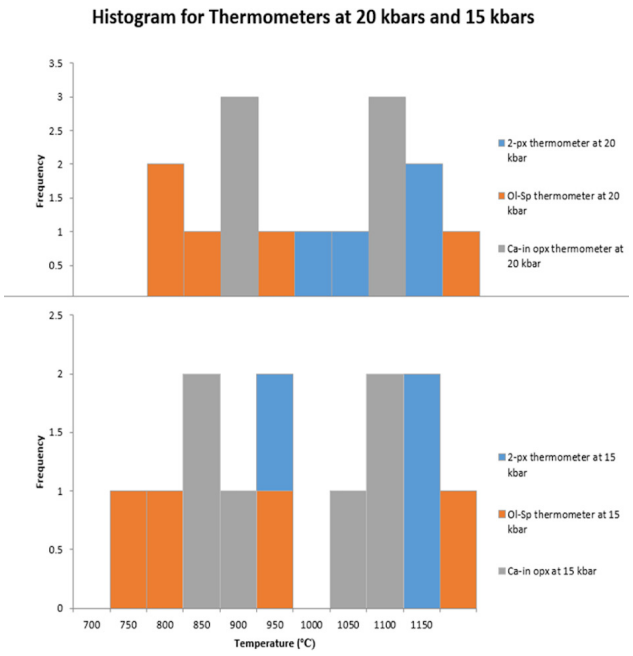

Figure 3: Histogram of equilibration temperatures estimated for the sample suite at 20 kbars (top) and 15 kbars (bottom), as calculated from various experimentally-derived thermometers (2-pyroxene and Ca-in-orthopyroxene methods from Brey and Köhler (1990); olivine-spinel method from Balhaus et al. (1990)).

analyses per sample) were bracketed between the secondary standards. Clinopyroxene and amphiboles trace element data was reduced using ^{43}Ca concentrations.

4. Thermometry

Equilibration temperatures (°C) for our xenoliths were calculated using 3 different thermometers based on cation exchange in/between minerals at 15 and 20 kbars (assumed representative pressures for spinel peridotite facies).

4.1. Ca-in orthopyroxene thermometer

Temperatures were calculated using Ca content in orthopyroxene (Ca-in-opx) as a thermometer using the formula given by Brey and Köhler (1990).

4.2. Two-pyroxene thermometer

Temperatures were also calculated employing the two-pyroxene thermometer based on the partitioning of Ca between orthopyroxene and clinopyroxene given by Brey and Köhler (1990).

4.3. Olivine-Spinel Fe-Mg exchange thermometry

Temperatures were also calculated using exchange of Fe and Mg between olivine and spinels given by Balhaus et al. (1991).

4.4. Calculation of ferric ion (Fe^{3+}) in spinels

Fe^{3+} content of spinel was calculated using a simple equation by Droop (1987) in ferromagnesian oxides and silicates using microprobe analyses assuming perfect stoichiometry. This equation has been derived assuming stoichiometric criteria where iron is the only element with a variable valency and oxygen is the only present anion. The equation (Eq. 2) is given as

$$F = 2X\left(1 - \frac{T}{S}\right) \qquad \textit{(Eq. 2)}$$

Here, F is the number of Fe^{3+} per X number of oxygen ions in a mineral formula. T is the ideal number of cations per formula unit, and S corresponds to the observed cation total for X oxygen ions assuming all iron to be Fe^{2+}.

4.5. Oxygen Fugacity

Oxygen fugacity f_{O2} was calculated using data obtained from the Olivine-spinel thermometer of Balhaus et al. (1991), and is calculated relative to FMQ (Fayalite-Magnetite-Quartz) buffer. The estimates were found to be ± 1.5 log units relative to FMQ. The element concentrations were obtained from microprobe analyses using Eq. 3:

$$\Delta log(fO)_2^{FMQ} = 0.27 + \frac{2505}{T} - \frac{400P}{T} - 6\log(X_{Fe}^{olv}) - \frac{3200(1 - X_{Fe}^{Olv})^2}{T} + 2\log\left(X_{Fe^{2+}}^{Sp}\right) + 4\log\left(X_{Fe^{3+}}^{Sp}\right) + \frac{2630\left(X_{Al}^{Sp}\right)^2}{T} \qquad \textit{(Eq. 3)}$$

where Fe^{3+}, Fe, Fe^{2+} and Al are the respective concentrations in spinels and olivines to calculate the molar ratio *X*, *P* is the assumed pressure in GPa and *T* the temperature calculated from the Fe-Mg olivine-spinel exchange thermometer in K.

5. Discussion

5.1. Equilibration Conditions

Temperatures calculated using various thermometers are consistent with those expected for spinel lherzolite facies in the upper mantle. The temperatures calculated using the above thermometers are within ± 50°C of each other at 15 and 20 kbars and range from 800°C to 1200°C, and are thus reasonable for samples to be spinel lherzolites facies (Fig. 3). The differences in temperature estimates from the Ca-in-opx and the 2-pyroxene thermometer are higher at 15 kbars than at 20 kbars. The reason for $T_{Ca\text{-}in\text{-}opx} > T_{2\text{-}px}$ could be attributed to calibration errors but could also be theoretically inferred from the shape of the miscibility gap in the orthopyroxene-clinopyroxene phase diagram (Balhaus et al., 1991). The Ca-in-opx thermometer becomes more sensitive and hence reliable at low temperatures, while 2-pyroxene thermom-

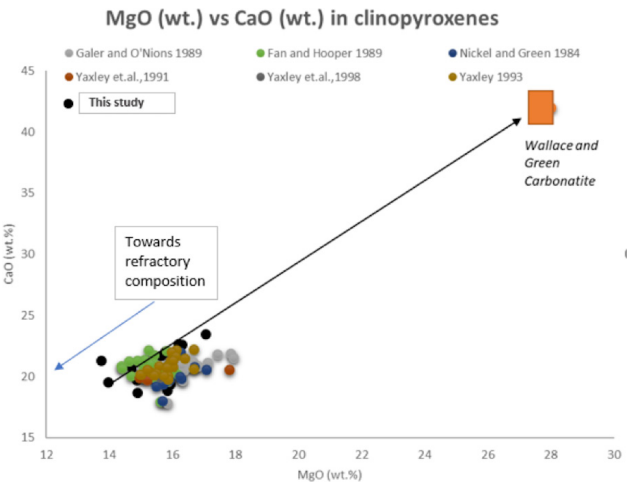

Figure 4: Plot of MgO vs CaO for clinopyroxene in spinel peridotite. Note the mixing relationship between a pure carbonatite melt (Wallace and Green, 1988) and pre-metasomatic lithosphere to generate the carbonatized xenoliths and enrichment in CaO concentrations.

eter is sensitive and reliable at higher temperatures (Balhaus et al., 1991). The temperatures calculated using Fe-Mg exchange olivine-spinel thermometry are reasonable estimates and are within ± 100°C of the other thermometers. Differences in temperature estimates from this thermometer could be ascribed to systematic errors in calculating $Fe^{3+}/\sum Fe$.

5.2. Evidence for Metasomatism

5.2.1. Major Elements

Olivines in the sample suite have Mg# (molar Mg/(Mg+Fe)) ranging from 85.04 to 90.06 and averaging to 87.75, typical for primitive peridotites.

Clinopyroxenes from this suite exhibit increasing CaO and P_2O_5 trends with increasing MgO, while Al_2O_3 and SiO_2 decrease. These diminutions could be indicative of adding a component to these xenoliths at depth, which is substantially rich in CaO and P_2O_5 and depleted in Al and Si. This interpretation is consistent with a metasomatic process involving the uptake of components by refractory lithosphere being dolomitic, Si-undersaturated, phosphate-rich and accompanied by a substantial loss of a CO_2-rich fluid during ascent (Fig. 4).

5.2.2. Trace Elements

In this study, clinopyroxenes have subchondritic Y/Ho, Ti/Eu, Nb/La and Nb/Ta ratios with superchondritic Zr/Hf ratios. Amphiboles are major hosts for Nb and Ti along with Ta. Nb/Ta in xenoliths is a metasomatic signature or a consequence of Ti-oxide fractionation. $(La/Yb)_N$ (N = mantle normalized) in the clinopyroxenes range from 2.10 to 5.35, averaging to 3.35. This dominant $(La/Yb)_N > 1$ in xenoliths is consistent with a commonly held view of widespread metasomatic effect on lithosphere (Kalfoun and Merlet, 2002).

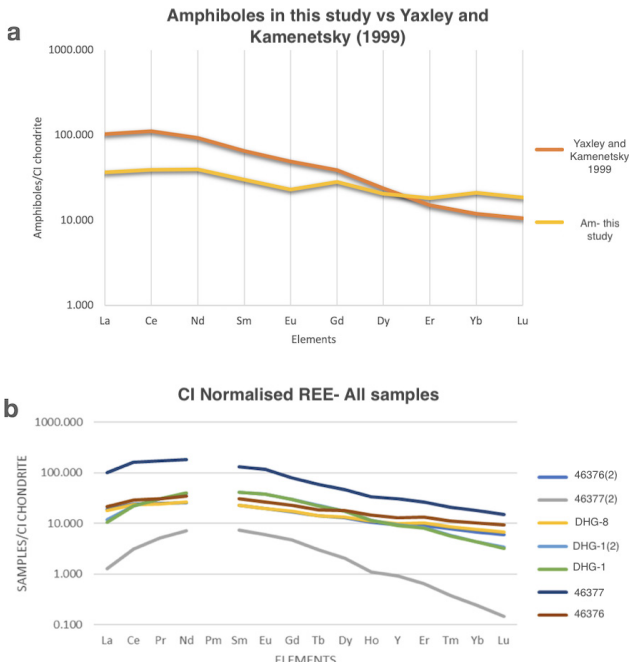

Figure 5: CI chondrite normalized plot for (a) amphiboles from this study and in Yaxley and Kamenetsky (1999) and (b) clinopyroxenes from this study.

The amphiboles from this study are richer in HREE compared to amphiboles from those in Yaxley and Kamenetsky (1999) (Fig. 5).

5.3. Nature of Metasomatic Process

The spinel peridotites equilibrated at assumed pressures of 15 and 20 kbars (for spinel peridotite facies) are metasomatised and are suggestive of a two-stage metasomatic process:

The first stage is the precipitation of hydrous phases (amphiboles ± phlogopite) which may be related to

$$orthopyroxene\ (P) + Al\text{-}spinel\ (P) + Cr\text{-}diopside\ (P) + fluid = amphibole\ (P) + phlogopite\ (P) + Al\text{-}Cr\text{-}spinel\ (S) + olivine\ (S) \quad \textit{(Eq. 4)}$$

Eq. 4, obtained from Dautria et al. (1992):

where *P* and *S* are primary and secondary mineral lithologies, respectively. This reaction would require the fluid to be H_2O- rich and high in Na, K, Ti and Fe. Such a fluid could be a silicate melt of alkali basaltic composition.

The second stage is characterized by the percolation of a sodic-dolomitic melt reacting with orthopyroxene producing secondary olivine, clinopyroxene and carbonates (calcite + magnesite), represented through Eq. 1.

This leads to the decarbonation of the carbonatite melt and transformation of the whole rock mineralogy from spinel lherzolite to orthopyroxene-free spinel wehrlite. During this process, other components of the carbonatite (Ti, P, K, Na, H_2O) contribute to the precipitation of Ti-rich amphiboles, phlogopites and apatites.

6. Summary

The study of spinel peridotites from a basanite dyke in Tumut-Eucumbene tunnel highlights their primitive origin and fertile nature. The presence of a variety of primary and secondary mineral assemblages in these samples is indicative of a fluid event. Elemental analyses of clinopyroxenes and amphiboles hints at a metasomatic process where interaction of LILE-rich carbonatite melt exhausted most of the orthopyroxene within the sample suite precipitating new secondary mineral phases. Such events have been commonly documented globally, especially in Western Victoria, Australia (Yaxley et al., 1991, Yaxley et al., 1998). Based on textural and element analyses, a metasomatic model is proposed in this study, where the consumption of orthopyroxene by carbonatite melts at ~15 to 20 kbars is accompanied by the precipitation of secondary amphibole, phlogopite, Al-Cr-spinel and olivine. This reaction follows the early precipitation of hydrous phases such as amphibole and/or phlogopite at the expense of primary orthopyroxene, Al-spinel and Cr-diopside on reacting with a hydrous, alkali and LILE-rich silicate carbonated melt. Such fluids have been envisaged as metasomatic agents in the past, hinting at the vast LILE- and carbonate-rich budget of the mantle. This has implications on the nature of fluids/melts involved and their genesis. The usage of approximated pressure values in this study opens up the possibility to evaluate them precisely. This study encourages to analyse in detail the mechanisms involved in metasomatism and understand them more precisely. It would be useful to look for water concentrations in mineral phases to identify the role of the hydrous mantle aiding in the precipitation of hydrous minerals, and its effects on the process of partial melting. Analyzing $\delta^{13}C$ and $\delta^{18}O$ of carbonates could assist in establishing the source of carbonates – whether they are subducted sedimentary carbonates or sourced at depth in earth's mantle.

7. Acknowledgement

I would like to thank Greg Yaxley (supervisor), Marnie Forster, and Thomas Rose for their endless support.

8. References

Aulbach, S., Viljoen, K.S., Gerdes, A., 2020. Diamondiferous and barren eclogites and pyroxenites from the western Kaapvaal craton record subduction processes and mantle metasomatism, respectively. Lithos 368-369, 105588. https://doi.org/10.1016/j.lithos.2020.105588.

Balhaus, C., Berry, R. F., Green, D. H., 1991. Oxygen fugacity controls in the Earth's upper mantle. Nature 348, pp. 437–440. https://doi.org/10.1038/348437a0.

Black, P., 1965. Geology of the Eucumbene Area. Canberra, Australian National University, unpublished BSc (Hons) thesis.

Bodinier, J.-L., Dupuy, C., Dostal, J., 1988. Geochemistry and petrogenesis of Eastern Pyrenean peridotites. Geochimica et Cosmochimica Acta 52, pp. 2893–2907. https://doi.org/10.1016/0016-7037(88)90156-1.

Bodinier, J.-L., Vasseur, G., Vernierres, J., Dupuy, C., Fabries, J., 1989. Mechanims of Mantle Metasomatism: Geochemical Evidence from the Lherz Orogenic Peridotite. Journal of Petrology 31(3), pp. 597–628. https://doi.org/10.1093/petrology/31.3.597.

Brey, G. P., Köhler, T., 1990. Geothermobarometry in Four-phase Lherzolites II. New Thermobarometers, and Practical Assessment of Existing Thermobarometers. Journal of Petrology 31(6), pp. 1353–1378. https://doi.org/10.1093/petrology/31.6.1353.

Dautria, J. M., Dupuy, C., Takherist, D., Dostal, J., 1992. Carbonate metasomatism in the lithospheric mantle: peridotitic xenoliths from a melilitic district of the Sahara Basin. Contributions to Mineralogy and Petrology 111(1), pp. 37–52. https://doi.org/10.1007/BF00296576.

Dawson, J. B., 1984. Contrasting Types of upper-Mantle Metasomatism? Developments in Petrology 11(2), pp. 289–294. https://doi.org/10.1016/B978-0-444-42274-3.50030-5.

Droop, G. T., 1987. A general equation for estimating Fe^{3+} concentrations in ferromagnesian silicates and oxides from microprobe analyses, using stoichiometric criteria. Mineralogical Magazine 51(361), pp. 431–435. https://doi.org/10.1180/minmag.1987.051.361.10.

Green, D. H., Wallace, M. E., 1988. Mantle metasomatism by ephemeral carbonatite melts. Nature 336, pp. 459–462. https://doi.org/10.1038/336459a0.

Grégoire, M., Bell, D. R., Le Roex, A. P., 2003. Garnet Lherzolite from the Kaapvaal Craton (South Africa): Trace Element Evidence for a Metasomatic History. Journal of Petrology 44(4), pp. 629–657. https://doi.org/10.1093/petrology/44.4.629.

Groves, D. I., Zhang, L., Santosh, M., 2020. Subduction, mantle metasomatism, and gold: A dynamic and genetic conjunction. Geological Society of America Bulletin 132(7-8), pp. 1419–1426. https://doi.org/10.1130/B35379.1.

Hammouda, T., Keshav, S., 2015. Melting in the mantle in the presence of carbon: Review of experiments and discussion on the origin of carbonatites. Chemical Geology 418, pp. 171–188. https://doi.org/10.1016/j.chemgeo.2015.05.018.

Hou, Z., Tian, S., Yuan, Z., Xie, Y., Yin, S., Yi, L., Fei, H., Yang, Z., 2006. The Himalayan collision zone carbonatites in western Sichuan, SW China: Petrogenesis, mantle source and tectonic implication. Earth and Planetary Science Letters 244(1-2), pp. 234–250. https://doi.org/10.1016/j.epsl.2006.01.052.

Kalfoun, I. D., Merlet, C., 2002. HFSE residence and Nb/Ta ratios in metasomatised, rutile-bearing mantle peridotites. Earth and Planetary Science Letters 199(1-2), pp. 49–65. https://doi.org/10.1016/S0012-821X(02)00555-1.

McDougall, I., Wellman, P., 1976. Potassium-Argon ages for some Australian Mesozoic Igenous Rocks. Journal of the Geological Society of Australia 23, pp. 1–9. https://doi.org/10.1080/00167617608728916.

Millonig, L. J., Gerdes, A., Groat, L. A., 2012. U–Th–Pb geochronology of meta-carbonatites and meta-alkaline rocks in the southern Canadian Cordillera: A geodynamic perspective. Lithos 152(1), pp. 202–217. https://doi.org/10.1016/j.lithos.2012.06.016.

Molnar, A., 1963. Geological Map of Snowy Mountains Area. Cooma, Snowy Mountains Hydro electric authority. http://hdl.handle.net/11343/23948.

O'Reilly, S. Y., Griffin, W. L., Ryan, C. G., 1991. Residence of trace elements in metasomatised spinel lherzolite xenoliths: a proton-microprobe study. Contributions to Mineralogy and Petrology 109, pp. 98–113. https://doi.org/10.1007/BF00687203.

Pell, J., 1994. Carbonatites, Nepheline syenites, Kimberlites and related rocks; in British Columbia, Bulletin (British Columbia. Ministry of Energy, Mines and Petroleum Resources) 88, 136 p. [online] Available at: http://cmscontent.nrs.gov.bc.ca/geoscience/PublicationCatalogue/Bulletin/BCGS_B088.pdf [Accessed 21 November 2020].

Pilet, S., Abe, N., Rochat, L., Kaczmarek, M.-A., Hirano, N., Machida, S., Buchs, D. M., Baumgartner, P. O., Müntener, O., 2016. Pre-subduction metasomatic enrichment of the oceanic lithosphere induced by plate flexure. Nature Geoscience 9, pp. 898–903. https://doi.org/10.1038/ngeo2825.

Rudnick, R. L., McDonough, W. F., Chappell, B. W., 1993. Carbonatite metasomatism in the northern Tanzanian mantle: petrographic and geochemical characteristics. Earth and Planetary Science Letters 114, pp. 463–475. https://doi.org/10.1016/0012-821X(93)90076-L.

Simandl, G. J., Paradis, S., 2018. Carbonatites: related ore deposits, resources, footprint, and exploration methods, Applied Earth Science 127(4), pp. 123–152. https://doi.org/10.1080/25726838.2018.1516935.

Song, Y., Frey, F. A., 1989. Geochemistry of peridotite xenoliths in basalt from Hannuoba, Eastern China: Implications for subcontinental mantle heterogeneity. Geochimica et Cosmochimica Acta 53(1), pp. 97–113. https://doi.org/10.1016/0016-7037(89)90276-7.

Sweeney, R. J., 1994. Carbonate melt compositions in the Earth's mantle. Earth and Planetary Science Letters 128, pp. 259–270. https://doi.org/10.1016/0012-821X(94)90149-X.

Wallace, M. E., Green, D. H., 1988. An experimental determination of primary cabonatite magma composition. Nature 335, pp. 343–346. https://doi.org/10.1038/335343a0.

Yaxley, G. M., Crawford, A. J., Green, D. H., 1991. Evidence for carbonatite metasomatism in spinel peridotite xenoliths from western Victoria, Australia. Earth and Planetary Science Letters 107(2), pp. 305–317. https://doi.org/10.1016/0012-821X(91)90078-V.

Yaxley, G. M., Green, D. H., Kamenetsky, V., 1998. Carbonatite Metasomatism in the Southeastern Australian Lithosphere. Journal of Petrology 39, pp. 1917–1930. https://doi.org/10.1093/petroj/39.11-12.1917.

Yaxley, G. M., Kamenetsky, V., 1999. In situ origin for glass in mantle xenoliths from southeastern Asutralia: insights from trace element compositions of glasses and metasomatic phases. Earth and Planetary Science Letters 172(1-2), pp. 97-109. https://doi.org/10.1016/S0012-821X(99)00196-X.

Deep Structures and Geodynamic Processes in the Present-Day Tien Shan

Kseniia Nepeina[1,✉], Elena Bataleva[1], Anatoly Rybin[1]

[1] Research Station of the Russian Academy of Sciences in Bishkek, Kyrgyzstan
✉ nepeina.k@mail.ru

Keywords: Tien Shan, geodynamic processes, geophysics, deep structures

1. Introduction

The Kyrgyz Tien Shan covers an area of intense intracontinental seismicity, for most earthquakes in southern Kyrgyz Tien Shan occur within the Indo-Eurasian convergence zone, and those in Eastern Kyrgyzstan mainly occur along major faults (Nikolaev line, Shamshi-Tunduk, Atbashi, Inylchek). The Tien Shan Orogeny occurred approximately 10 Ma (Jolivet, 2015). The upper-crust tectonic structures that formed during the intercontinental orogen of the Central Asian belt are of interest because existing modelling of these features is inaccurate and too general. Tracking of geological structures is key for robust geological reconstructions and geomechanical simulations, but distinction among individual crustal blocks is a complex task.

Many researchers, when isolating crustal blocks, rely on their definition by fault positions and offset. Geological and geophysical studies have been used to define the characteristics of the block structure of the Tien Shan (Brunet, McCann & Sobel, 2017; Umirova, Istekova & Modin, 2016; Rybin et al., 2015; Bielinski et al., 2003; Thompson et al., 2002). Previous works explain the state of the lithosphere beneath Tien Shan using the petrology and electrical conductivity of xenoliths (Batalev et al., 2011; Bagdassarov, Batalev & Egorova, 2011). Here, we use the geophysical technique called magnetotelluric soundings (MTS) to extend the study of geodynamic processes and geological block description with physical parameters. In this paper we show that the MTS approach is beneficial for the characterization of underground structures in the Earth's crust. Underground structures with different resistivity result in a distribution of electrical currents that can be measured with MTS soundings on the surface. This paper shows how the MTS technique can image geological structures up to 100 km depth as a geoelectric cross-section.

The record of annual geoelectric variation confirms a relationship with the underlying geodynamic processes in the Earth's crust (Bataleva, Rybin & Matiukov, 2019). The variations in geoelectric parameters are observed through geomagnetic measurements at geomagnetic stations or MTS profiles (Bataleva & Mukhamadeeva, 2018). It helps us to construct geophysical models of contemporary geodynamic processes. These contemporary geodynamic processes partly reflect the ongoing deformation of the orogenic system, specifically regional crust folding caused by the mountain-building mechanism.

2. Methods and techniques

The Research Station of the Russian Academy of Sciences (RS RAS) in Bishkek produces magnetotelluric sounding (MTS) profiles (Bataleva, Rybin & Matiukov, 2019; Bataleva & Mukhamadeeva, 2018). MTS is a technique for observations of the distribution of the geoelectric parameters of the Earth's crustal rocks. The physical signal source of the electromagnetic field is generated by variations due to heliospheric and terrestrial interactions in the magnetic field. For this reason, MTS observations are useful to link the electromagnetic parameter variations to the geodynamic processes. MTS data is useful to determine material properties and structure at depths greater than 5 km, as MTS inversion results delineate the nature of buried structures. The objective of this study is to use the MTS technique to identify the main crustal units (blocks, their boundaries, and basement horizons) in the Tien Shan region.

The presented cross-sections are the result of interpretation of MTS data. This procedure contains the starting and the resulting models. An inversion needs a 1D starting model, based on processed raw MTS data in MT-corrector software by North-West Ltd. (Zorin et al., 2020). Afterwards, we get apparent resistivity curves and impedance phases for the observation point. The starting model (Fig. 1b) of the geoelectric section contains in situ geological information, such as anomalies of the electromagnetic parameters (Przhiyalgovskii et al., 2018). The final model is a product of an iterative selection method after an automated inversion algorithm. We adjust the resulting model to ensure the best match between the observed and model curves of the apparent resistivity and impedance phases with the Tikhonov's regularizing function and its subsequent nonlinear minimization (Przhiyalgovskii et al., 2018; Berdichevsky et al., 2010). The numerical solution is a finite-element algorithm that allows the calculation of electromagnetic

DOI: 10.2312/yes19.04

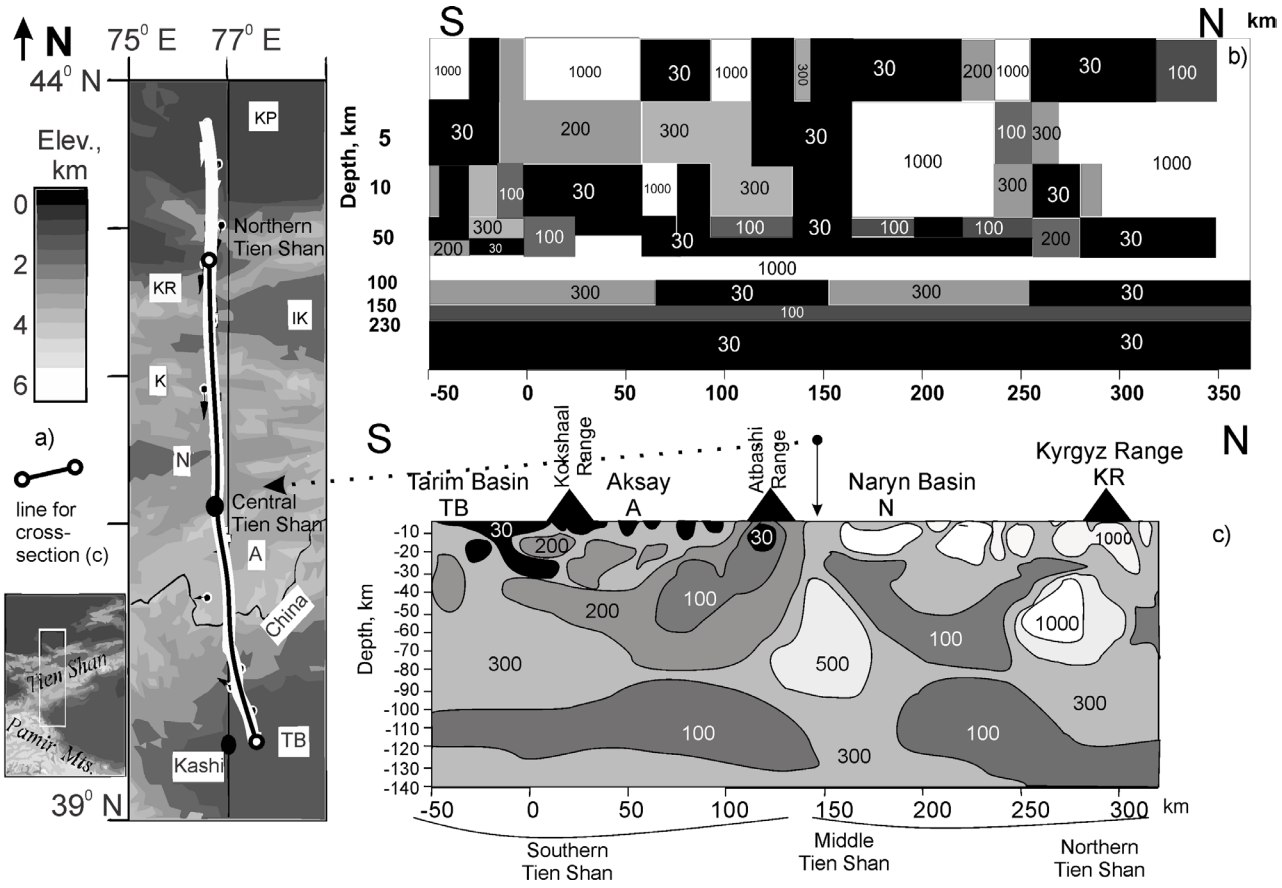

Figure 1: Map of the Tien Shan (MTS Naryn profile, 76° E) across the Kyrgyz Tien Shan and its' geoelectric cross-sections. (a) general map (after Bielinski et al., 2003); (b) geoelectric 1D starting model. Inside the model nodes the resistivity is indicated in Ohm·m (after Berdichevsky et al., 2010); (c) 2D inversion result model along the Naryn profile (adopted after Batalev et al., 2011). Inside the bodies, the resistivity is indicated in Ohm·m. Abbreviations: A - Aksay Basin; IK - Issyk-Kul; KR - Kyrgyz range; KP - Kazakh Platform; N - Naryn Basin; TB - Tarim Basin.

fields in 2D and 3D inhomogeneous media (Rodi and Mackie, 2001).

3. Results

The location of the interpretation of the Naryn profile (situated in the Tien Shan region along the 76° E meridian) is presented as Fig. 1a. Geoelectric models of the Naryn profile are shown in Fig. 1b and 1c. The starting 1D model is presented in Fig. 1b, a minimum block width of 25 km has been adopted (Fig. 1b).The final, interpretative model (Fig. 1c) presents the result of a 2D inversion with a simplified view. We restyled the cross-section view graphically using a rescaled boundary geometry of major bodies after Bielinski et al. (2003). Block structure is important during the profile construction to distinguish between areas of depressions and elevations.

We observe (Fig. 1c) in the southern part of the Naryn profile that the low-resistivity bodies extend in a horizontal plane at depths of at least 25 km. In the upper crust, there are relatively isometric isolated bodies that extend vertically. Objects with high resistivity values (> 500 Ohm·m) are mostly isometric and placed at 5 to 15 km depth in the Northern part of the profile.

Based on the distributions of geoelectric resistivity, we can conclude that the overall structure under the block of the Northern and the Middle Tien Shan (North of Atbashi Range, in Fig. 1c the right side from the central point with an arrow), adjacent to the Naryn depression, is significantly different from the Southern area (Fig. 1 c, left side). The difference suggests an essential 2D/3D heterogeneity. The Southern edge of the Naryn Basin, in connection with the Atbashi Range, has an area of increased resistivity (500 Ohm·m) below 35 to 40 km depth. On the west side, we observe more low-resistivity rock bodies – conductors (30 Ohm·m to 100 Ohm·m) – in the upper part of the cross-section (depths of 0 to 30 km). On the east side, we find high-resistivity rock bodies – dielectrics (600 to 1000 Ohm·m) – in the upper part of the cross-section (depths of 0 to 40 km). The anomalies in electric conductivity are revealed as sub-vertical conductors (30 to 200 Ohm·m) oriented along the flanks of the basins. The basement displays the resistivity values ≈ 200 to 300 Ohm·m.

Horizontal boundaries at depth correspond to the basement horizons, such as Moho (M), and vertical interfaces are clearly visible in the MTS cross-sections as resistivity contrast. We characterize the

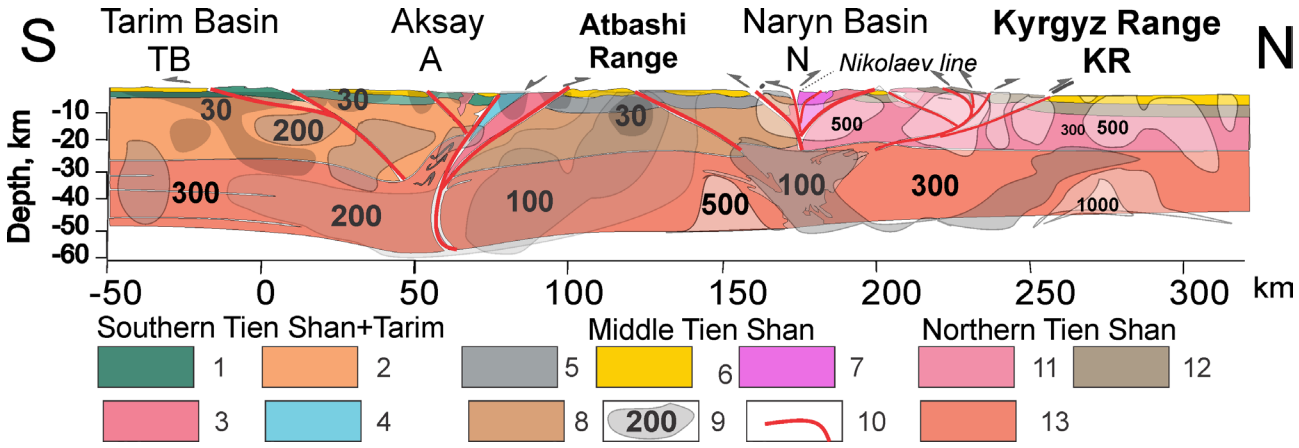

Figure 2: Interpretative crustal cross-section of the Tien Shan (Naryn profile) adopted after Jourdon et al. (2018), as the combination of the surface geological data (Przhiyalgovskii et al., 2018; Bataleva et al., 2017), thermo-mechanical model (presented in Jourdon et al., 2018) with the addition of geophysical data (restyled accordingly to results after Berdichevsky et al., 2010 and Bielinski et al. 2003). Legend: Southern Tien Shan: 1 - Paleozoic cover, 2 – Basement, 3- High pressure mica schists, 4 - Accretionary wedge; Middle Tien Shan: 5 - Paleozoic cover, 6 - Cenozoic cover, 7 - Permian granites, 8 – Basement; 9 – geoelectric bodies contours with apparent resistivity values, 10 – active faults (after Thompson et al., 2002); Northern Tien Shan: 11 – Ordovician plutons + basement, 12 – Paleozoic cover, 13 – Lower crust.

regional tectonics through the integration of our interpretation of the MTS profiles and in situ geologic studies (lithotypes, transversal faults, and crustal structures' geometry). We take into account geologic studies from Thompson et al. (2002) and Brunet, McCann, & Sobel (2017) for further interpretation.

The comparison (Fig. 2), adopted after Jourdon et al. (2018), shows the distinction between different parts of the Tien Shan. Overall in the Southern Tien Shan, the upper part of the sediment rock mass (Paleozoic cover) has resistivity values ≈ 30 to 50 Ohm·m. The lower crust below 30 km depth is about ≈ 300 to 500 Ohm·m with extensive dielectric areas (500 Ohm·m and above). The Naryn Basin is heavily compressed (Abdrakhmatov et al., 2001). In the upper part, we observe conductors (above 500 Ohm·m). The Atbashi Basin contains horizontal, slightly disturbed rocks at 0 to 10 km below the surface. The upper part at the Naryn Basin and Kyrgyz Ridge are distinguished with high resistivity values (500 to 1000 Ohm·m). The deep vertical areas at 30 to 50 km depth have the lowest-resistivity (100 Ohm·m). Moho (M) depths are taken from Vinnik et al. (2006). The Moho depth varies from 40 km in the North (Kyrgyz Range), up to 70 km in the South (near the Tarim Basin). The Moho geometry shows that the crust consists of isolated high resistivity bodies (> 1000 Ohm·m) separated by slightly more conductive zones.

4. Discussion

The Kyrgyz Tien Shan, in general, is defined as a 2-floor formation (the basement and the sediments). The basement is composed of volcanic-sedimentary and metamorphic rocks of Precambrian and Paleozoic age (Alexeiev et al., 2019). The Late Ordovician and Early Silurian granitoids penetrate the basement (Leonov et al., 2020). During the structural-geological mapping of various sections of the Northern and Middle Tien Shan, we acquired a material constitution and accurate description of disintegrated, clastic and weathered granites (Przhiyalgovskii et al., 2018; Rybin et al., 2018). Partially, unlike the host rocks, granites are intensely tectonized and have an extrusive nature (Przhiyalgovskii et al., 2018). Deformations of rocks are manifested in the form of various cataclasites (Bataleva et al., 2017), with most of them spread in brittle shear zones, especially in the upper parts of the crust. These zones are characterized by the products of dislocation metamorphism.

The difference in the left and right sides of Fig. 1b and 1c of the Naryn profile results from the different crustal architecture in the Southern and Northern Tien Shan. In the southern part of the Naryn profile, for example, we have interpreted low-resistivity bodies below 25 km depth to be the lower crust, and the presence of vertically isolated bodies in the upper crust suggests the fragmentation of the surface layer to a depth of 5 km. We date resistivity anomalies as the Permian granites in the upper Northern part of the profile. At the Naryn Basin and Kyrgyz Ridge, we have interpreted the near-surface bodies as granites with fragmentation. We consider they are cataclasites – a fine-grained, cohesive fault rock that forms dominantly by brittle deformation processes such as microcracking and abrasion. Sub-vertical conductive bodies may be controlled by the zones of the dynamic influence of faults and cataclasis of granite. At the Middle Tien Shan, the geologic bodies are folded as a "flower structure" and intersected by a series of faults

(Fig. 2), which were studied for the 76° E profile by Thompson et al. (2002). Moho depth variation is a result of the deformation of the crust in these regions.

Horizontal boundaries in the MTS cross-sections can be potentially associated either with faults, zones of deformation, zones of redistribution of matter, the presence of fluids, or with contrasts in rock formations and their chemical composition. We consider that the vertical areas with low resistivity (here termed 'conductor blocks') can potentially be saturated with fluids, and that these areas correlate only partially with surface faulting (as suggested by Thompson et al., 2002). This approach is partly confirmed in Bielinski et al. (2003), who suggested that these areas result from thrusting of a weaker crust of the Kyrgyz range southward over the strong crust of the Naryn block. According to these observations, it is possible to draw the vertical boundaries of blocks along gradient zones, where the dielectric blocks are separated from conductor blocks along of heterogeneity of conductivity.

5. Conclusions

We produce a geoelectric model for the Naryn profile. We interpret it on the basis of geologic features. We analyse our models and divide the Naryn profile into two parts, the southern and the northern, distinguished by geologic formation. The observed Moho depth is marked by high-resistivity anomalies and correlates with receiver function tomography results.

We investigate and explain the boundaries of blocks along gradient zones in geophysical results for geodynamic issues. We consider the low-resistivity layers below 25 km as the lower crust and prove the fragmentation of the surface layer in the southern part of the Naryn profile. Because the granites are disintegrated in the upper part of the profile, we assume deep saturation of the fluids.

The anomalies in electric conductivity help in rock state definition. Using MTS studies in the region, we clarify the variable degrees of the weathered, deformed, or water-saturated granite layers using low resistivity as an indicator for cataclasites. It means that they are broken with fractures. It proves a block structure at the meso-scale. The question of cataclastic fluid permeability is essential for earthquake modeling or looking for water- and fluid-bearing rocks.

6. Acknowledgements

This study is carried out with the support of the Russian Scientific Foundation under the project RSF No. 16-17-10059 "The relationship of tectonic and morphological characteristics of upper crust structures of intercontinental orogens between deep structure, minerageny and geological risks (on the example of the Tien Shan)". The authors are grateful to Nord-West Ltd. for MT-corrector software. We also acknowledge the editor, Dr. Fernández-Blanco, and anonymous reviewers for their comments, and Dr. Gunn and Dr. Fernández-Blanco for help improving the quality of the manuscript language.

7. References

Abdrakhmatov, K., R., Weldon, S., Thompson, D., Burbank, C., Rubin, M., Miller, M., Molnar, P. 2001. Origin, direction, and rate of modern compression of the central Tien Shan (Kyrgyzstan). Russian Geology and Geophysics. 10. pp. 1502–1526.

Alexeiev, D.V., Kröner, A., Kovach, V.P., Tretyakov, A.A., Rojas-Agramonte, Y., Degtyarev, K.E., Mikolaichuk, A. V., Wong, J., Kiselev, V. V. 2019. Evolution of Cambrian and Early Ordovician arcs in the Kyrgyz North Tianshan: Insights from U-Pb zircon ages and geochemical data. Gondwana Research 66. pp. 93–115. https://doi.org/10.1016/j.gr.2018.09.005.

Bagdassarov, N., Batalev, V., Egorova, V. 2011. State of lithosphere beneath Tien Shan from petrology and electrical conductivity of xenoliths. Journal of Geophysical Research. 116. B01202. https://doi.org/10.1029/2009JB007125.

Batalev, V.Y., Bataleva, E.A., Egorova, V.V., Matyukov, V.E. and Rybin, A.K. 2011. The lithospheric structure of the Central and Southern Tien Shan: MTS data correlated with petrology and laboratory studies of lower-crust and upper-mantle xenoliths. Russian Geology and Geophysics. 52(12). pp. 1592–1599. https://doi.org/10.1016/j.rgg.2011.11.005.

Bataleva, E., Rybin, A. and Matiukov, V. 2019. System for collecting, processing, visualization, and storage of the MT-monitoring data. Data. 4(3). https://doi.org/10.3390/data4030099.

Bataleva, E.A. and Mukhamadeeva, V.A. 2018. Complex electromagnetic monitoring of geodynamic processes in the Northern Tien Shan (Bishkek Geodynamic Test Area). Geodynamics & Tectonophysics. 9(2). pp. 461–487 (in Russian). https://doi.org/10.5800/GT-2018-9-2-0356.

Bataleva, E.A., Przhiyalgovskii, E.S., Batalev, V.Y., Lavrushina, E. V., Leonov, M.G., Matyukov, V.E. and Rybin, A.K. 2017. New data on the deep structure of the South Kochkor zone of concentrated deformation. Doklady Earth Sciences. 475(2). pp. 930–934. https://doi.org/10.1134/S1028334X1708013X.

Berdichevsky, M.N., Sokolova, E.Y., Varentsov, I.M., Rybin, A.K., Baglaenko, N. V., Batalev, V.Y., Golubtsova, N.S., Matyukov, V.E. and Pushkarev, P.Y. 2010. Geoelectric section of the Central Tien Shan: Analysis of magnetotelluric and magnetovariational responses along the Naryn geotraverse. Izvestiya, Physics of the Solid Earth. 46(8). pp. 679–697. https://doi.org/10.1134/S1069351310080057.

Bielinski, R.A., Park, S.K., Rybin, A., Batalev, V., Jun, S. and Sears, C. 2003. Lithospheric heterogeneity in the Kyrgyz Tien Shan imaged by magnetotelluric studies. Geophysical Research Letters. 30(15). 1806. https://doi.org/10.1029/2003GL017455.

Brunet, M.-F., McCann, T., Sobel, E.R. 2017. Geological Evolution of Central Asian Basins and the Western Tien Shan Range. Geological Society, London, Special Publications. 427. pp. 1–17. https://doi.org/10.1144/SP427.17.

Jourdon, A., Le Pourhiet L., Petit C., Rolland Y. 2018. The Deep Structure and Reactivation of the Kyrgyz Tien Shan: Modelling the Past to Better Constrain the Present. Tectonophysics. 746. pp. 530–548. https://doi.org/10.1016/j.tecto.2017.07.019.

Jolivet, M. 2015. Mesozoic tectonic and topographic evolution of Central Asia and Tibet: a preliminary synthesis. In: Brunet, M.-F., McCann, T., Sobel, E.R. Central Asian Basins And Tien Shan Range 13 Geological Evolution of Central Asian Basins and the Western Tien Shan Range. Geological Society, London, Special Publications. 427. pp. 19–55. https://doi.org/10.1144/SP427.2.

Leonov, M.G., Morozov, Y.A., Przhiyalgovskii, E.S., Rybin, A.K., Bakeev, R.A., Lavrushina, E.V., Stefanov, Y.P. 2020. Tectonic Evolution of the Basement–Sedimentary Cover System and Morh-

postructural Differentiation of Sedimentary Basins. Geotectonics. 54. pp. 147–172. https://doi.org/10.1134/S0016852120020089.
Przhiyalgovskii, E.S., Lavrushina, E. V., Batalev, V.Y., Bataleva, E.A., Leonov, M.G. and Rybin, A.K. 2018. Structure of the basement surface and sediments in the Kochkor basin (Tien Shan): geological and geophysical evidence. Russian Geology and Geophysics. 59(4). pp.335–350. https://doi.org/10.1016/j.rgg.2017.09.003.
Rodi, W. and Mackie, R.L. 2001. Nonlinear conjugate gradients algorithm for 2-D magnetotelluric inversion. Geophysics. 66(1). pp. 174–187. https://doi.org/10.1190/1.1444893.
Rybin, A.K., Bataleva, E.A., Morozov, Y.A., Leonov, M.G., Batalev, V.Y., Matyukov, V.E., Zabinyakova, O.B. and Nelin, V.O. 2018. Specific Features in the Deep Structure of the Naryn Basin–Baibichetoo Ridge–Atbashi Basin System: Evidence from the Complex of Geological and Geophysical Data. Doklady Earth Sciences. 479(2). pp. 499–502. https://doi.org/10.1134/S1028334X18040165.
Rybin, A.K., Pushkarev, P.Y., Palenov, A.Y., Ivanova, K.A., Mansurov, A.N. and Matyukov, V.E. 2015. New geophysical data on the depth structure of the Tien Shan intermontane depressions. Moscow University Geology Bulletin. 70(1). pp. 62–68. https://doi.org/10.3103/S0145875215110010.
Thompson, S.C., Weldon, R.J., Rubin, C.M., Abdrakhmatov, K., Molnar, P. and Berger, G.W. 2002. Late Quaternary slip rates across the central Tien Shan, Kyrgyzstan, Central Asia. Journal of Geophysical Research. 107(B9), 2203. https://doi.org/10.1029/2001JB000596.
Umirova, G.K., Istekova, S.A. and Modin, I.N. 2016. Using magnetotelluric sounding for estimation of oil-and-gas content of mesozoic era in Western Kazakhstan. Moscow University Bulletin. Series 4. Geology. 4, pp. 52–58 (in Russian). https://doi.org/10.33623/0579-9406-2016-4-52-58.
Vinnik, L.P., Aleshin, I.M., Kaban, M.K., Kiselev, S.G., Kosarev, G.L., Oreshin, S.I. and Reigber, C. 2006. Crust and mantle of the Tien Shan from data of the receiver function tomography. Izvestiya, Physics of the Solid Earth. 42(8). pp. 639–651. https://doi.org/10.1134/S1069351306080027.
Zorin, N., Aleksanova, E., Shimizu, H., Yakovlev, D. 2020. Validity of the dispersion relations in magnetotellurics: Part I—theory. Earth, Planets and Space. 72. 9. https://doi.org/10.1186/s40623-020-1133-4.

Active Transtensional Structures Mapped in the West of Karakoram Fault (KF), Kashmir Himalayas

Dk Nurul Azeerah Pengiran Omar[1,✉], Afroz Ahmad Shah[1], Nurhafizah Abd Manan[1]

[1] University Brunei Darussalam, Brunei Darussalam
✉ azeerahpgo@hotmail.com

Keywords: NW Himalaya, normal fault, transtension, Kashmir

1. Introduction

Over the geological past the continent-continent collision between the lithospheric plates of India and Eurasia has caused the formation, orientation, pattern, and chronology of geological structures throughout the Himalaya orogen (Yin, 2006; Stevens and Avouac, 2015; Shah, 2016; Shah and Malik 2017; Burg and Bouilhol, 2019; Shah et al., 2020). These structures have formed, and evolved differently along and across the orogen, and it is estimated that about 50 % of the ongoing convergence is mainly absorbed by the Main Himalayan Thrust (MHT), which on surface emerges as the Main Frontal Thrust (MFT) (Stevens and Avouac, 2015; Bilham, 2019). Interior faults are known to accommodate some amount of the plate convergence (Shah, 2013), but the quantitative measurements are usually missing, which is primarily because not all active faults have been studied in detail. The presence of unknown active faults (Shah et al., 2018) further complicates this story.

Broadly, the geological structures are distributed differently along and across the Himalaya and Tibet (Tapponnier and Molnar, 1977; Shah et al., 2018) which are the two major landmasses that preserve the evidence of tectonic processes like subduction, plutonism, and ongoing collision. Geologically, the Himalayan-Tibetan orogen is composed of a complex tectonic collection that preserves evidence of geological events in a chronological order from north to south (Zhao, and Xie, 1993). It includes accretion of microcontinents, flysch complexes, and island arcs, against the southern boundary of the Eurasian plate since the early Paleozoic (e.g. Yin and Harrison, 2000; Murphy et al., 2002). The tectonic topography preserves such evidence, and in particular the younger structures that have formed as a result of the ongoing collisional processes across, and along the orogen. Such structures are remarkably observable on the satellite images, and a quick glance on them reveals that a relatively narrow width of deformation zones is noticeable in NW portions of the orogen, while they are much wider in the eastern regions (Fig. 1A). This transition is marked on either side of the Karakoram fault (KF), which is the major dextral strike-slip fault and accommodates the regional oblique convergence between the two plates (Fig. 1). It defines the tectonic boundary where the western Tibetan plateau meets the Himalayan fold-and-thrust belt (Murphy et al., 2002).

Previous works have extensively produced data on the frontal portions of the Himalayas because most of the ongoing convergence is reported on the Himalayan frontal thrust system, which has also caused many larger magnitude earthquakes in the region (e.g. Bilham, 2019). The work presented here however aims to explore the regions in the west and northwest of the KF (Fig. 2). The motivation is to map the existence of what have been traditionally called out-of-sequence faulting in the NW Himalayas and to produce data on the active versus inactive nature of deformation in the interior Himalayas, and to reevaluate the earthquake geology and tectonics of the region.

2. Methodology

Satellite images have truly transformed the regional and local mapping of geological structures, and over the decades these data have been extensively useful in mapping of the structural details that were impossible to achieve on foot. This is particularly true for regional mapping exercises, which require a broader outlook (e.g. Tapponnier and Molnar, 1977, Nakata, 1989; Malik, and Nakata, 2003; Sahoo and Malik, 2017; Shah 2013; Shah et al., 2020). Additionally, regional mapping is hard to achieve during traditional geological fieldworks where limitations of time, resources, accessibility, and the fear of crossing international borders often complicates and exhausts the mapping motivations (Shah and Malik, 2017). Therefore, we take full advantage of 30 m Shuttle radar topography (SRTM) data here to map the regional geological structures. The mapping of geomorphic features was done by manually tracing topographic breaks, triangular facets, ridge crests, ruptured Holocene sedimentary deposits (e.g. alluvial fans, fluvial terraces etc.), and glacial landforms. Wherever applicable, the rule-of-V was used to mark the dip direction of bedding and faults. The moment tensor solutions are extracted from the GeoMap App

DOI: 10.2312/yes19.12

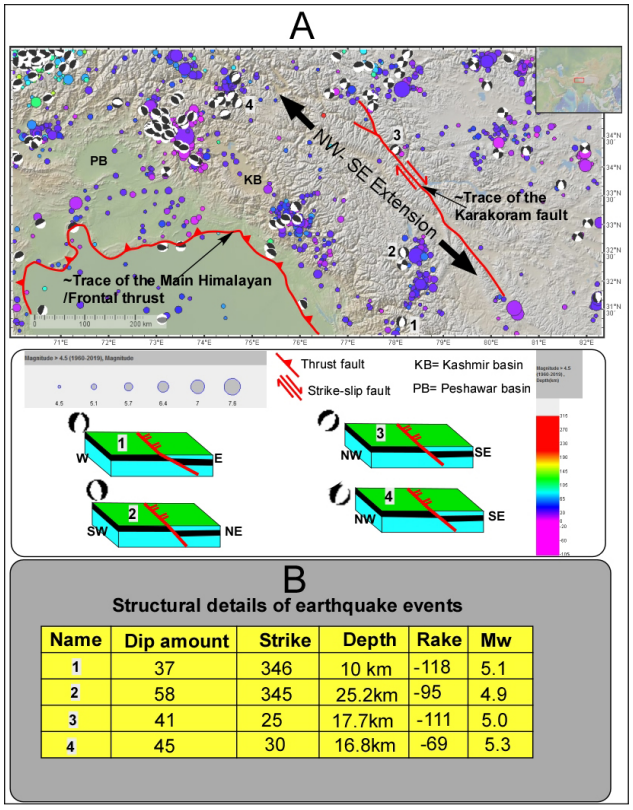

Name	Dip amount	Strike	Depth	Rake	Mw
1	37	346	10 km	-118	5.1
2	58	345	25.2km	-95	4.9
3	41	25	17.7km	-111	5.0
4	45	30	16.8km	-69	5.3

Figure 1: (A) Regional map showing the two major active faults system in NW Himalaya. The faults are in red, and the background satellite image is derived from the GeoMap App. The earthquake hypocenters (color filled circles and moment tensor solutions (earthquake beach balls)) are also plotted. The 3D-illustrations are based on the fault plane solutions that are labelled as numbers, and are interpreted as the best possible representative events of active normal faulting in the region. (B) The earthquake structural details that are used for the 3D-illustrations.

(http://www.geomapapp.org). and it covers data from January 1976 until July 2019 (Fig. 1). These data are used and correlated with our geomorphic mapping of tectonic landforms to interpret and understand the nature of faulting in the interior Himalayas.

3. Results and interpretation

3.1. Faulting

The geomorphic evidence of active normal faulting in the NW Himalayas is ubiquitous (Figs. 3 to 5). The > 60 km long and ~N-S trending normal fault is one of the most prominent looking geomorphic features in the region, and is located to the west of the Karakoram fault (Fig. 4). The ~N-S oriented elongated valley that is filled with Holocene sediments is a direct consequence of normal faulting, and it suggests a half graben geometry where the fault is dipping east (Fig. 4). The abrupt truncation of the ~NW-SE oriented ridge in front of the Tso Moriri Lake indicates faulting, which is consistent with the eastwards dipping fault plane (Fig. 4). Broadly, the region mapped here (e.g. Fig. 4) shows dominantly NW-SE, and NE-SW faults, which crosscut each other. The ridge

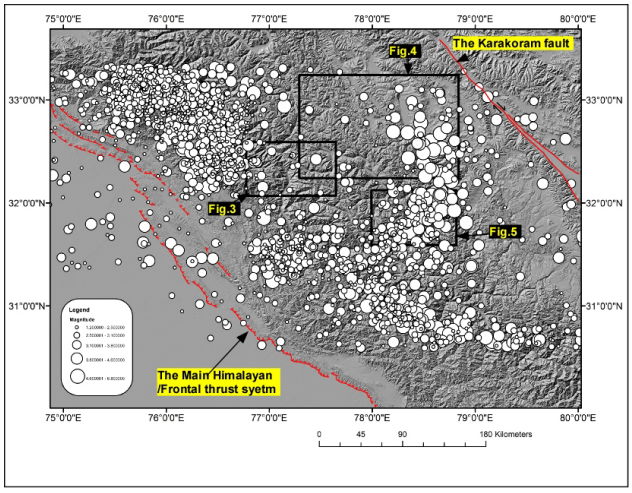

Figure 2: The shuttle radar topography (SRTM) with the regional seismicity. The major faults are shown in red, and the rectangular regions represent the areas that are studied in details (see Fig. 3 to 5).

crests are truncated by faults, triangular facets are widespread, and clear, and often Holocene filled glacial valleys are also cut by faults, which are narrow and spread across the region. This intersecting relationship of geological structures shows that ~NE-SW faults are older, and are truncated, and often cut by younger ~NW-SE faults. This suggests either the faults have formed together or, ~NW-SE trending faults are younger (see Discussion for details). Similar structures are observed in other areas (e.g. Fig. 3) where clear evidence for faults is observed, and a range of active tectonic features suggest active faulting. The entire region shows a consistent pattern of faults (Figs. 3 to 5) where a number of ~NW-SW and ~NE-SW trending normal faults are also mapped. Together all these faults show evidence of Holocene movement, and therefore these are active.

The abundance of topographic breaks that we have mapped in the region is mainly interpreted as normal faults because they are consistent with regional extension that has been observed in Tibet and Kashmir Himalaya (e.g. Shah et al., 2018). These faults are a direct consequence of the ongoing oblique convergence of India and Eurasia. The ~NW-SE major trending normal faults have displaced ~NE-SW trending normal faults, which indicate that it is younger, and our mapping shows that both are active, and interrelated to each other. Similarly, a large number of SE dipping normal faults are mapped (Figs. 3 to 5) and interpreted to have formed syn-tectonic with the oblique plate convergence that has also created the frontal thrust later in the Himalayan orogenesis. The topographic expresses of the mountains and valleys clearly show the faulting pattern, and the drainage system seems to have mirrored and followed the fault patterns. It is obvious that the entire region is split into

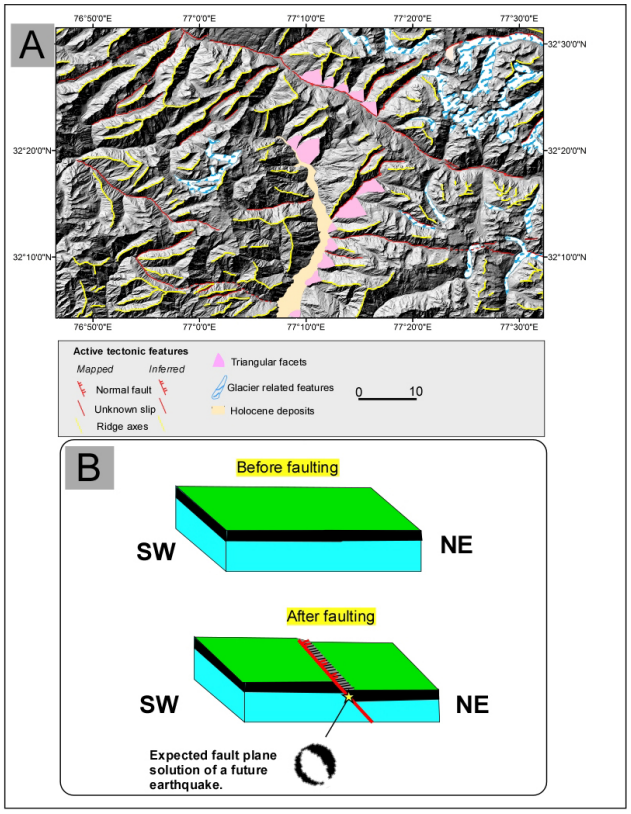

Figure 3: (A) Satellite image with interpreted tectonic and other geomorphic features. (B) 3D-illustrations before and after faulting. It is representative of one of the major normal fault systems that we have mapped here.

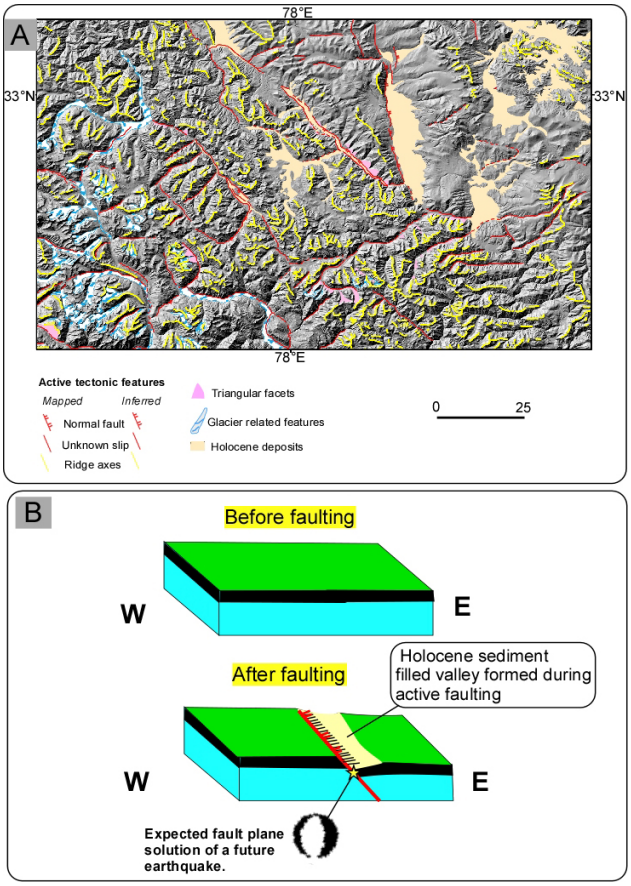

Figure 4: (A) Satellite image with interpreted tectonic and other geomorphic features. A number of syn-tectonic valleys are filled with Holocene sediments. (B) 3D illustrations before and after faulting. It is representative of one of the major normal fault systems that we have mapped here.

different ridges and valleys because of the progressive deformation that has formed these faults.

3.2. Earthquake moment tensor solutions

The distribution of earthquake hypocenters and examination of the available moment tensor solutions have corroborated with our mapping (Fig. 1A and 1B). The dominance of shallow focus earthquakes in the entire region is consistent with the brittle deformation of the interior portions. Some clusters are observed, which are mostly related to the major earthquakes events in the past. The ~NW-SE directed crustal extension that we have mapped above is also reflected from the moment tensor solutions, which show ~N-S and ~NE-SW trending normal faults. The instrumental earthquakes clearly show that normal faulting is active, and our mapping demonstrates the geomorphic and structural evidence of such events (Fig. 3 to 5). Figure 1B shows the structural parameters used to make the 3D-illustrations, which reflect the mapping of the geomorphic landform shown above.

4. Discussion

Shah et al. (2018) mapped the regional normal faults in the Kashmir Himalaya. They interpreted that ~NW-SE directed crustal extension is actively taking place in Kashmir Himalaya as well, and that it resembles the ~E-W extension that Tibet is undergoing (Fig. 6). The new mapping shown above further demonstrates that such faulting is ubiquitous throughout the west and southwest of the Karakoram fault. We have mainly observed orogen parallel faults, and ~NE-SW and ~N-S trending normal faults throughout the study area (Figs. 2 to 6). These normal faults are active, have ruptured and displaced Holocene deposits, and are morphologically similar to the normal faulting pattern that is observed in Tibet (Shah et al., 2018). The topographic expression of faulting is mainly shown by a number of faults and these are interpreted as normal faults, which have formed syn- or postgenetic to the formation of the Karakorum fault because we have observed dextral offset of normal faults at KF (Fig. 6D). The mapping further illustrates that ~NW-SE trending faults have truncated, and displaced the ~NE-SW trending faults (Figs. 2 to 5), which suggests the relative age relationship and confirms the earlier formation of ~NW-SE trending faults. The available earthquake moment tensor solutions (Fig. 1) strengthen our geomorphic mapping, and indicate the ~NW-SE to ~E-W directed crustal extension. This means on a regional scale that the ongoing lithospheric plate convergence is also absorbed by ~E-W extension, and that is strikingly similar to how Tibet is deforming

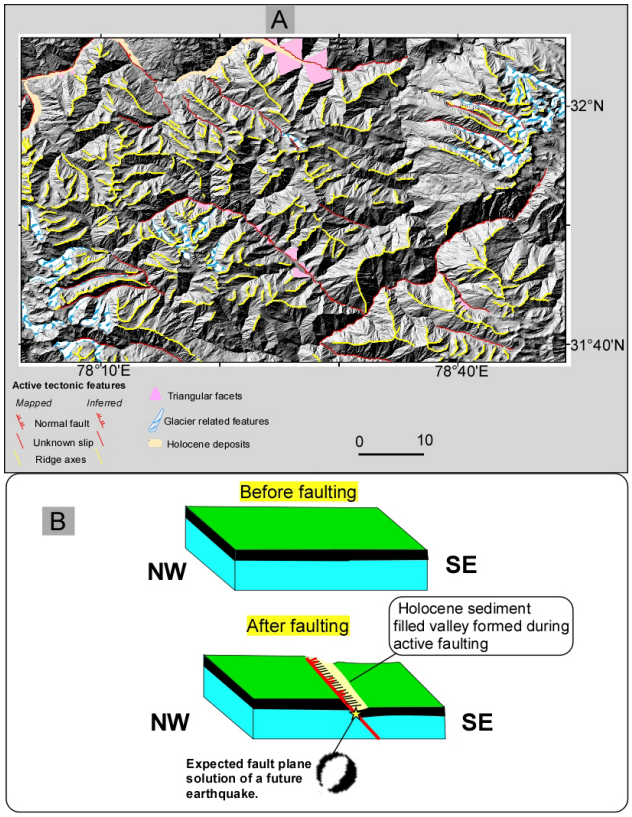

Figure 5: (A) Satellite image with interpreted tectonic and other geomorphic features. The rugged topography is dissected by glaciers, which often occupy tectonically controlled valleys. (B) 3D-illustrations before and after faulting. It is representative of one of the major normal fault systems that we have mapped here.

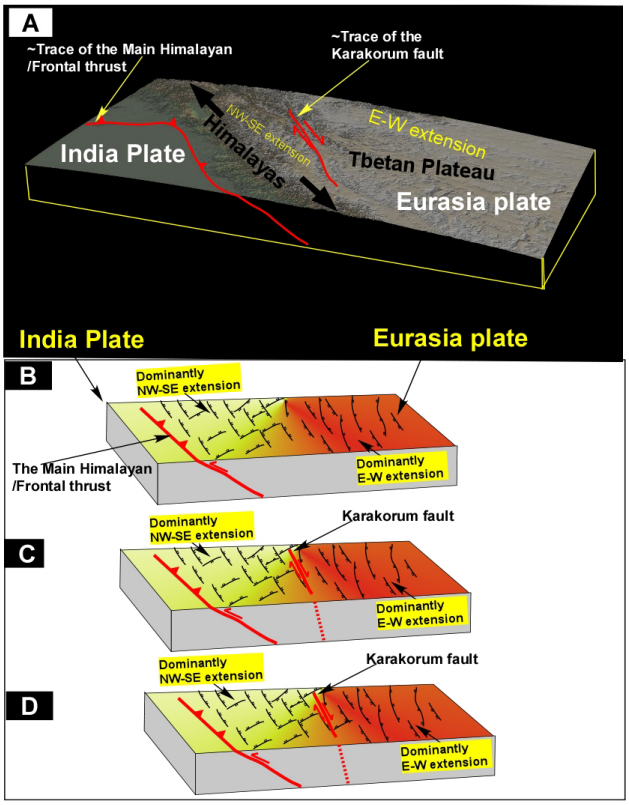

Figure 6: (A) 3-D view of the satellite image shows the two major active fault systems in the NW Himalaya that are reflective of the oblique tectonic convergence between India and Eurasia. The illustrations (B to D) summarize the formation and possible evolution of normal faulting in the studied region. (B) The normal faults could have formed earlier or syntectonic with the oblique plate convergence. (C) This could have later formed strike-slip faults, which have displaced normal faults. (D) This could mean that the Karakorum fault has formed later than normal faults. However, the regional oblique plate tectonic convergence could form both the fault systems together in the region with some time lag between their development history, which seems a normal procedure during the mountain building processes.

(McCaffrey and Nabelek 1998; Shah et al., 2018).

Further, the only major dextral strike-slip fault that exists in the NW Himalaya is the Karakoram fault (KF). The earthquake moment tensor solutions suggest (Fig. 1) that thrust faulting dominates at the frontal portions, which is consistent with the normal convergence of the two plates in convergence. However, north of Kashmir, the normal faulting predominates, and our mapping supports this with geomorphic evidence of normal faulting (Figs. 2 to 5). The faults east of KF are dominantly strike-slip and normal, and the ongoing deformation is consumed on these structures in the Tibetan plateau region (Yin and Harrison, 2000). Although the actual cause of this extension remains a controversial topic (e.g. Tapponnier and Molnar, 1977; Tapponnier et al., 1982; Yin and Harrison, 2000), our new mapping of the topographic landforms seems to suggest that regional oblique convergence can transport rocks on major strike-slip systems and could cause simultaneous extension (Fig. 6). Such a mechanism requires active and large systems of strike-slip movement in Tibet that are moving relatively faster compared to those in the east. The regional structures in NW Himalaya are broadly distributed in some restricted locations, and that suggests that frontal portions are dominated by ~NW-SE trending thrusts while interior regions are controlled by orogen parallel and orthogonal normal faulting and strike-slip faulting, where rocks are transported towards ~SE. This has been illustrated (Fig. 6) through a number of 3D illustrations (Fig. 6B–D) to discuss the evolution of normal faulting in the studied region. The faults were formed in response to the collision of lithospheric plates of India and Eurasia (Fig. 6B). This could have formed both, the normal and the strike-slip faults (Fig. 6C). However, the cross cutting relationship between normal and strike-slip faults suggest that some mapped normal faults are truncated by strike-slip faulting, which could indicate that Karakoram fault has formed later than normal faulting (Fig. 6D).

5. Conclusions

The geomorphic expression of faulting that is mapped here shows that ongoing regional deformation is actively contributing towards the ~NW-SE directed crustal extension in the interior of the Himalayas. This is similar to structures that have been mapped in Tibet and the Kashmir Himalayas. The

mapped faults are active and are interpreted to have formed in response to the tectonic convergence between the Indian and Eurasian plate. The active nature of deformation suggests distributed deformation in the NW Himalayan and confirms that a portion of tectonic convergence is compensated along regional scale normal faults. It shows that the presence of crustal extension in the interior Himalaya is mainly reflected by the regional normal faulting, which is in contrast to strike-slip and normal faulting in Tibet. The deformation in the interior portions during collisional mountain building processes seems to question the out-of-sequence faulting where such deformation is not a predictable mechanism to release crustal strain. The cause of extension could be related to the ongoing oblique plate convergence where active strike-slip faults transport rocks towards ~SE and we interpret that such faults are expected to slip more towards the east of KF, and less towards the west of it because of the dense network of linked transtensional structures (e.g. major strike-slip and normal faults). This is possibly the reason for low seismic activity on normal and strike slip faults in the Kashmir Himalayas.

6. References

Bilham, R. (2019). Himalayan earthquakes: a review of historical seismicity and early 21st century slip potential. Geological Society, London, Special Publications 483, 423–482. https://doi.org/10.1144/SP483.16.

Burg, J. P., and Bouilhol, P. (2019). Timeline of the South Tibet–Himalayan belt: the geochronological record of subduction, collision, and underthrusting from zircon and monazite U–Pb ages. Canadian Journal of Earth Sciences 56(12), 1318–1332. https://doi.org/10.1139/cjes-2018-0174.

McCaffrey, R., and Nabelek, J. (1998). Role of oblique convergence in the active deformation of the Himalayas and southern Tibet plateau. Geology 26(8), 691–694. https://doi.org/10.1130/0091-7613(1998)026<0691:ROOCIT>2.3.CO;2.

Malik, J.N. and Nakata, T (2003). Active faults and related Late Quaternary deformation along the northwestern Himalayan Frontal Zone. Indian Annals of Geophysics 46, 917–936. https://doi.org/10.4401/ag-3462.

Murphy, M. A., Yin, A., Kapp, P., Harrison, T. M., Manning, C. E., Ryerson, F. J., and Jinghui, G. (2002). Structural evolution of the Gurla Mandhata detachment system, southwest Tibet: Implications for the eastward extent of the Karakoram fault system. Geological Society of America Bulletin 114(4), 428–447. https://doi.org/10.1130/0016-7606(2002)114<0428:SEOTGM>2.0.CO;2.

Nakata, T. (1989). Active faults of the Himalaya of India and Nepal. Geological Society of America Special Publication 232, 243–264. https://doi.org/10.1130/SPE232-p243.

Sahoo, S. and Malik, J. N. (2017). Active fault topography along Kangra Valley Fault in the epicentral zone of 1905 Mw7. 8 earthquake NW Himalaya, India. Quaternary International 462, 90–108. https://doi.org/10.1016/j.quaint.2017.03.020.

Shah, A. (2016). The Kashmir Basin fault and its influence on fluvial flooding in the Kashmir Basin, NW Himalaya. Geological Society of America Special Paper 520, 321–334. https://doi.org/10.1130/2016.2520(28).

Shah, A. A., and Malik, J. N. (2017). Four major unknown active faults identified, using satellite data, in India and Pakistan portions of NW Himalaya. Natural Hazards 88(3), 1845–1865. https://doi.org/10.1007/s11069-017-2949-5.

Shah, A. A., Addly, A. A. B. M., and Samat, M. I. B. A. (2018). Geomorphic Mapping Reveals~ NW-SE Extension in NW Himalaya. In: Kallel A., Erguler, Z. A., Cui, Z.-D., Karrech, A. and Karakus, M. (eds) Recent Advances in Geo-Environmental Engineering, Geomechanics and Geotechnics, and Geohazards. Proceedings of the 1st Springer Conference of the Arabian Journal of Geosciences. Springer, Cham, 385–389. https://doi.org/10.1007/978-3-030-01665-4_89.

Shah, A. A. , Abd Manan, N., Aliudin, N. A. B., Cahyaningsih, C., Batmanathan, N. M. and Malik, J. N. (2020) Formation, Rotation, and Present-Day Configuration of Kashmir and Peshawar Basins in NW Himalaya. Frontiers in Earth Sciences 8:569771. https://doi.org/10.3389/feart.2020.569771.

Shah, A.A., (2013). Earthquake geology of Kashmir Basin and its implications for future large earthquakes. International Journal of Earth Sciences 102, 1957–1966. https://doi.org/10.1007/s00531-013-0874-8.

Stevens, V. L., and Avouac, J. P. (2015). Interseismic coupling on the main Himalayan thrust. Geophysical Research Letters 42(14), 5828-5837. https://doi.org/10.1002/2015GL064845.

Tapponnier, P., and Molnar, P. (1977). Active faulting and tectonics in China. Journal of Geophysical Research 82(20), 2905–2930. https://doi.org/10.1029/JB082i020p02905.

Tapponnier, P., Peltzer, G., Le Dain, A.Y., and Armijo, R. (1982). Propagating extrusion tectonics in Asia: New insights from simple experiments with plasticine. Geology 10, 611–616. https://doi.org/10.1130/0091-7613(1982)10<611:PETIAN>2.0.CO;2.

Yin, A. (2006). Mode of Cenozoic east-west extension in Tibet suggesting a common origin of rifts in Asia during the Indo-Asian collision. Journal of Geophysical Research: Solid Earth 105, 21745–21759. https://doi.org/10.1029/2000JB900168.

Yin, A., and Harrison, T.M. (2000). Geologic evolution of the Himalayan-Tibetan orogen. Annual Review of Earth and Planetary Sciences 28, 211–280. https://doi.org/10.1146/annurev.earth.28.1.211.

Zhao, L. S., and Xie, J. (1993). Lateral variations in compressional velocities beneath the Tibetan Plateau from P_n traveltime tomography. Geophysical Journal International 115(3), 1070–1084. https://doi.org/10.1111/j.1365-246X.1993.tb01510.x.

Application of Principal Component Analysis and Unsupervised Classification (ISODATA) to Estimate Arctic Sea Ice Extent Using ISRO's SCATSAT-1 Data

Nanaoba Khoisnam Singh[1,✉], Rajkumar Kamaljit Singh[2], Mamata Maisnam[1], Jayaprasad Pallipad[3], Saroj Maity[3]

[1] National Institute of Technology Manipur, Imphal-795004, Manipur, India;
[2] Manipur Technical University, Imphal-795004, Manipur, India;
[3] Space Application Centre- Indian Space Research Organisation (ISRO), Ahmedabad-380015, Gujarat, India
✉ meiteinanaoba@gmail.com

Keywords: Scatterometer, SCATSAT-1, ISODATA, Principal component analysis, Sea ice extent

1. Introduction

Sea ice plays an active role in ocean circulation, weather and regional climate as well as on the salinity of icy oceans. The insulating property of sea ice reduces evaporation of underlying water and heat loss to the atmosphere. The high albedo of 0.5 to 0.7 of sea ice reduces the global temperature (National Snow and Ice Data Center, 2020).

Expulsion of brine during the formation of sea ice increases salinity and density of surrounding ocean water in the polar regions (Lake and Lewis, 1970). In case of Antarctica, this dense water flows down to the continental shelf to form Antarctic Bottom Water (Dan and Robert, 2006) and in the Arctic, flows down to the ocean floor and moves to enter the Greenland and Norwegian Seas and forms Arctic Bottom Water (Glossary of American Meteorological Society, 2012). These waters lead to the formation of the thermohaline circulation, the largest ocean circulation.

Polar-orbiting satellite data are useful in observing and studying long term and seasonal changes of the Arctic sea ice extent (SIE). SIE is considered as a sensitive indicator of long-term global climate change (Budd, 1975). Estimation of SIE has been carried out using active remote sensing (Remund and Long, 2014) and passive remote sensing (Cavalieri and Parkinson, 2008; Comiso et al., 1996).

In this study, enhanced resolution SCATSAT-1 data are used to estimate the Arctic SIE. Image analysis technique of Principal Component Analysis (PCA) is applied to highlight different features within an image. After masking the land parts, discrimination between sea ice and ocean water is carried out using ISODATA classification. The results obtained are validated by comparing with 1) National Snow and Ice Data Centre (NSIDC) sea ice extent derived from 30 % sea ice concentration and 2) Ocean and Sea Ice Satellite Application Facility (OSI) sea ice edge. Statistical significance is calculated between the comparing data sets.

2. Data

The primary data of the study is SCATSAT-1 data. To validate the results of the SCATSAT-1 data, popular SIE data of NSIDC Sea ice concentration data and OSI sea ice-covered data are utilised.

2.1. SCATSAT-1

Though originally designed for the measurement of ocean winds, scatterometers have vast applications in other Earth observations. Likewise, Scatterometer Satellite-1 (SCATSAT-1), that measures near-surface ocean wind vectors, can be used to study different phenomena on Earth.

This active sensing satellite works at 13.515 GHz (Ku-band microwave). It was launched on 26 September 2016. Despite the gap of two and a half years (from February 2014 to September 2016) between the Oceansat-2 mission and SCATSAT-1, it is considered as the continuity mission of Oceansat-2. These two have similar functions and working principle. SCATSAT-1 data are archived at the Meteorological and Oceanographic Satellite Data Archival Centre, Space Applications Centre-ISRO, India (https://www.mosdac.gov.in).

This satellite gives three important parameters: backscattering coefficient (σ_0), incidence angle normalised backscattering coefficient or gamma nought (γ_0) and noise-derived brightness temperature (T_b). These parameters are measured in horizontal and vertical polarizations. Therefore, six datasets per day are available. Since it is a polar-orbiting satellite there are two passes, the ascending-pass (northward from the equator) and the descending-pass (southward from the equator). The data sets that we have used in this study are the ones obtained by combining these two daily passes, known as "both-pass". The spatial resolution of the data are the enhanced resolution of 2.25 x 2.25 km². More on these data sets are given by SCATAT-1 DP Team (2017).

DOI: 10.2312/yes19.21

Figure 1: Mask developed from SCATSAT-1.

2.2. NSIDC sea ice concentration

These data are generated from the brightness temperature data obtained from such sensors as the Scanning Multichannel Microwave Radiometer (SMMR) onboard Nimbus-7, Special Sensor Microwave/Imagers (SSM/I) onboard Defense Meteorological Satellite Program (DMSP)-F8, -F11 and -F13, and Special Sensor Microwave Imager/Sounder (SSMIS) on DMSP-F17 (Cavalieri et al., 1995).

The data are stored as a one-byte integer in 25 x 25 km² resolution pixels. The digital value for a pixel can range from 0 to 250. This value when divided by 2.50 will give us the sea ice concentration per pixel in percentage. For this study, a pixel with 30 % sea ice concentration is counted as a pixel of sea ice signature.

The data (data catalogue number NSIDC-0051) are archived at NSIDC and were downloaded from https://nsidc.org/data/nsidc-0051.

2.3. OSI sea ice concentration

The second validation data set is the sea ice concentration generated from both the passive satellites (SSM/Is, Advanced Microwave Scanning Radiometer 2/AMSR2 and Global Change Observation Mission-W1/GCOM-W1) and an active satellite (Advanced Scatterometer/ASCAT). Sea ice edge data of 10 x 10 km² resolution data is developed by combining the data of the active satellite and the passive satellites using the Bayesian method. The pixels of the data are assigned with one-byte integer 1, 2, 3 and -1 which represent No ice (less than 30% ice concentration), Open ice (30 to 70 % ice concentration), Closed ice (more than 70 % ice concentration) and Unclassified or Land, respectively. Open ice and Closed ice are considered as sea ice and OSI sea ice extent is derived by combining these types.

The data sets are produced by the OSI-SAF of EUMETSAT and were downloaded from www.osi-saf.org.

All the data used in this study are in polar stereographic projection but they have different grid sizes. The SCATSAT-1 data set has 4001 columns and 4001 rows (the total area in the projection is 9002.25 x 9002.25 km²); NSIDC has 304 columns and 448 rows (the total area in the projection is 7600 x 11200 km²) and OSI has 790 columns and 1120 rows (the total area in the projection is 7900 x 11200 km²). A primary mask (Fig. 1) is created for this study using SCATSAT-1 data in combination with a sectorial vector file used by Bliss and Anderson (2014) (obtained through personal communication).

3. Methodology

3.1. Principal Component Analysis

Principal component analysis (PCA) is a very useful technique in reducing correlation redundancy in the multi-spectral remotely sensed image data (Lillesand et al., 2008). The mechanism is to extract information from sample data and to transform it into a new set of orthogonal data (Abdi and Williams, 2010). As compared to other well-known transformation methods (e.g. Wavelet transformation), PCA has a drawback of higher distortion of the original spectral information. However, it can express spatial characteristics very well and provide an optimal expression of highly anisotropic edges and contours in images (Shi et al., 2010). PCA has been used in the study of sea ice in the Arctic by Wensnahan et al. (1993) and in Antarctica e. g. by Singh et al. (2018).

In this study, input data for PCA are the SCATSAT-1 data sets of the three parameters mentioned earlier in both polarisations (horizontal and vertical). Therefore, in total there are 6 image data. PCA has been performed in IITVIS ENVI 4.5 using Forward PC rotation transformation with the Correlation matrix. In our analysis, only the first three principal components (PC) are retained to produce the false-colour composite (1st PC, 2nd PC, and 3rd PC as Red, Green, and Blue channel, respectively).

This study covers the period from October 2016 to March 2018. PCA is performed on only three specific days of each month. The selected days are in the beginning, in the middle and in the end of each month. There are no days with missing data and lack of principal components (number of inputs is less than 6) in

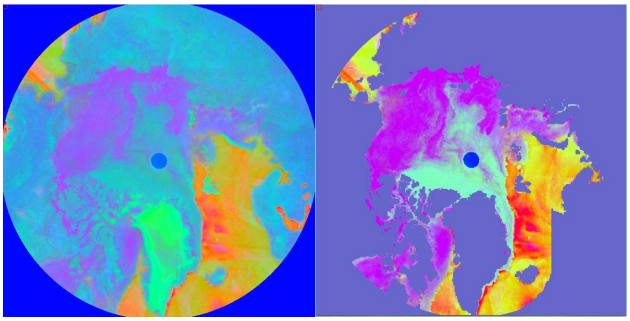

Figure 2: Unmasked image of PCA (left) and masked image of PCA (right).

the images picked for the study.

The result of an unmasked image after PCA and a masked image after PCA is shown side by side in Fig. 2. The unmasked and masked data are from the same day (1 January 2017). However, the colour of the two images is different. This is due to the increase in contrast to the masked image. There is no change in the data except the apparent colour. In the masked image, the violet part and the cyan part represent sea ice: the former representing first-year ice while the latter represents multi-year ice. Yellow, orange and red shades are possibly open oceans.

3.2. Unsupervised classification of image

As mentioned in the previous section, different features are visible in the PCA images. The false-colour composites formed using the first three principal components are then subjected to an unsupervised classification algorithm known as Iterative Self-Organizing Data Analysis Technique (ISODATA) to get a fair distinction between the open ocean and sea ice regions. Unsupervised ISODATA does not require a priori training data and classification proceeds by the formation of clusters using different cluster-means in the data space. Iteration is done with minimum distance technique and it reclassifies clusters and recalculates new means (Ball and Hall, 1965).

ESRI ArcGIS software is used for this classification. Application of PCA creates data sets in a range (standardised by mean = 0 and standard deviation = 1) and it is the requirement for ISODATA classification to yield a more accurate results. The number of output class is assigned to four, considering land (masked area), sea ice, open sea and central “pole hole”.

Iteration is performed until a threshold number of iteration (provided by software) is achieved. Four distinct classes were not obtained for some dates. The dates on which this problem was encountered are excluded from the analysis. Since the central pole hole is a sea ice area for the Arctic, this class is counted together with the surrounding sea ice class.

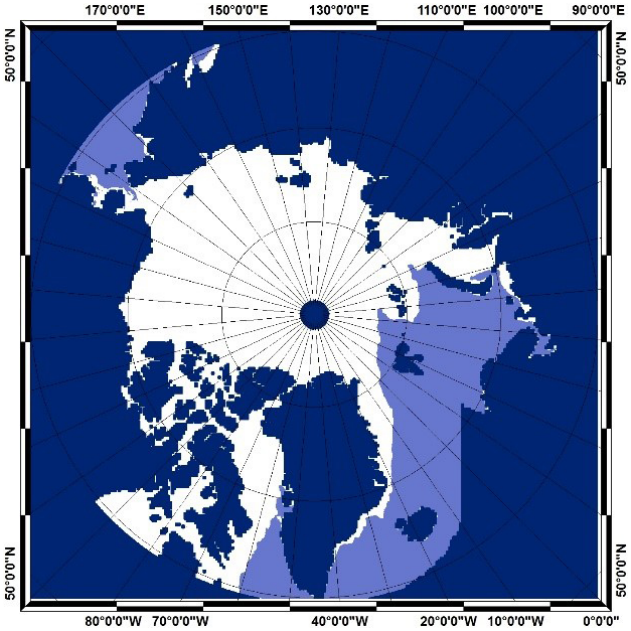

Figure 3: Sea ice extent obtained from the analysis.

4. Results

The sea ice extent map generated using PCA and unsupervised ISODATA classification from 1st of January 2017 is shown in Fig. 3. The white part of the map represents sea ice including the central hole, light blue represents the open sea and dark blue represents the masked part. A vast expansion of sea ice is also visible in the image. However further studies are needed to validate the method. Therefore, a comparison of sea ice extent was performed.

4.1. Qualitative comparison

Fifty-three days of SIE are available for comparison between the SCATSAT-1 and OSI data for the duration from October 2016 to March 2018. However, only 43 days of SIE are available for comparison between SCATSAT-1 and NSIDC during the duration from October 2016 to December 2017 due to unavailability of later NSIDC data at the time of this study.

SIEs of two selected days (1 January 2017 and 11 September 2017) derived from the above three sources are illustrated in Fig. 4. The month of January represents peak arctic winter while September represents peak summer melting season. Therefore, the growth and decay of sea ice should be visible in the figures.

The three derived SIE have shown a similar pattern in both summer and winter. However, in winter, NSIDC SIE is apparently more than SCATSAT-1 and OSI at the Bering Sea near Providence, Russia. However, at the Barents Sea along the coastline of Russia, the SIE is seen to be less in NSIDC < SACATSAT-1 < OSI.

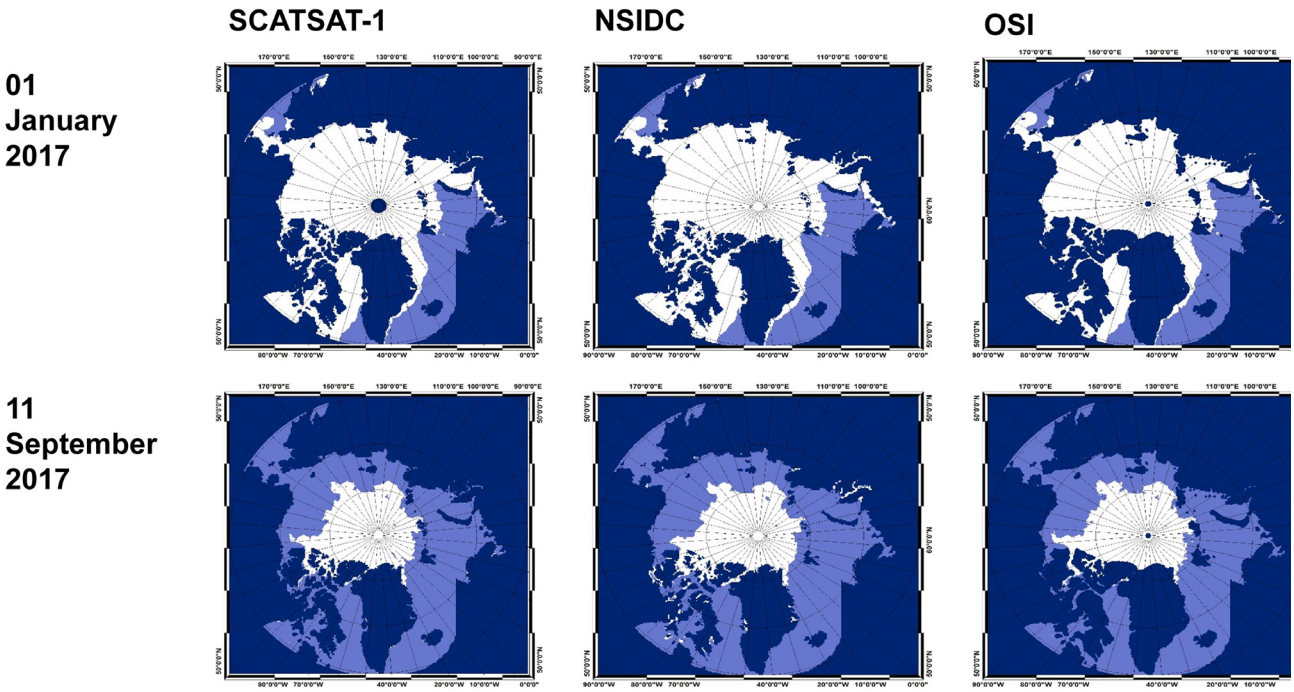

Figure 4: Qualitative comparison of SIEs.

During summer, in the NSIDC data some pixels along the coastlines of Greenland, the Canadian Archipelago and the Kara Sea are shown to be sea ice. But those are the open ocean in SCATSAT-1 and OSI.

4.2. Quantitative comparison

For quantitative comparison, SIEs inside the mask developed for this study are calculated for SCATSAT-1, NSIDC and OSI. For SCATSAT-1, the number of pixels classified as sea ice is counted and multiplied by 2.25 x 2.25 km^2 (resolution of the data) to calculate Arctic SIE. Similarly, the number of sea ice pixels are multiplied by 25 x 25 km^2 and 10 x 10 km^2 for NSIDC and OSI, respectively.

Temporal variations of three derived SIE are plotted in Fig. 5. A similar trend is observed despite the differences in these three extents. Our SCATSAT-1 SIE lies in between the NSIDC and OSI SIE curves. Thus, the observed SIE is in the order from large to small as NSIDC SIE, SCATSAT-1 SIE and OSI SIE.

The differences among the SIE are greatest in the period from January to April (winter to spring) and are the least during the period from August to October (summer to autumn). Between SCATSAT-1 and OSI SIE, the largest difference observed is ~$1.09 \cdot 10^6$ km^2 during the winter period while during the summer period, the largest difference observed is $0.57 \cdot 10^6$ km^2. These values for the SCATSAT-1 and NSIDC comparison are $0.91 \cdot 10^6$ km^2 and $0.66 \cdot 10^6$ km^2, respectively. Thus, the three estimations show convergence in summer rather than in winter. This should be investigated in our future work to understand why the difference smaller during summer than during winter.

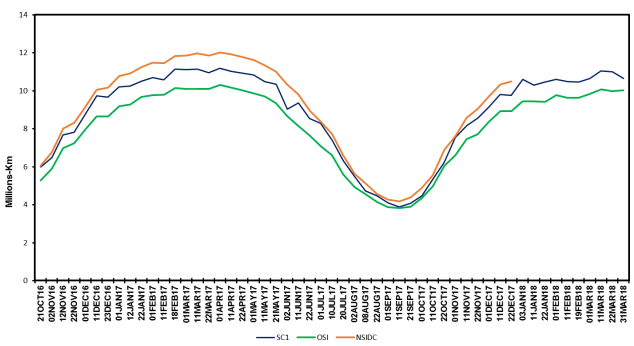

Figure 5: Temporal plot of SCATSAT-1 SIE, OSI SIE and NSIDC SIE.

A R^2 high value of 0.99 in the regression plot of Fig. 6 signifies the closeness between the data. It shows the similar variation of SCATSAT-1 SIE with NSIDC SIE and OSI SIE.

4.3. Student's t-test

We performed a statistical hypothesis test of comparing means of data samples, the null hypothesis (H_0) of which the samples have the same mean and variance (Kim, 2015).

Since data are unrelated, the independent type of a t-test is performed at a confidence level = 0.95 for both the SCATSAT-1/OSI comparison and SCATSAT-1/NSIDC.

The t-test parameters are shown in Table 1. We interpreted the result of this test using these parameters. If the obtained p-value is greater than present

Comparing datasets	Calculated t (t-stat)	Critical t (t-crit)	p-value
SCATSAT-1/OSI	1.8	1.983	0.07
SCATSAT-1/NSIDC	-0.97	1.988	0.33

Figure 1: Table 1: Result of t-test.

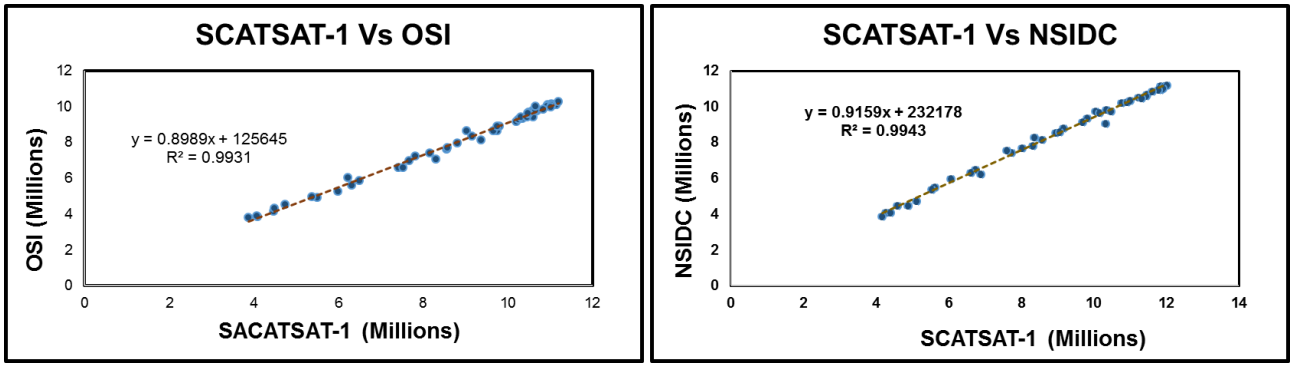

Figure 6: Regression plot between SCATSAT-1 SIE and OSI SIE (left) and SCATSAT-1 SIE and NSIDC SIE.

confidence level (95%), we have to accept the H_0 that the means that the data do not differ statistically. Another way is by considering the absolute value of the calculated t-value (t-stat). If it is less than t-crit (which is a standard value of the t value available in the standard table for given degrees of freedom and present confidence levels), we have to accept the null hypothesis.

In our comparison, we see that both the comparing data sets show statistically significant results.

5. Conclusion

An algorithm to estimate sea ice extent is developed for the Arctic region. High-resolution L4-data (2.25 km) of SCATSAT-1 data is used to produce the SIE. 54 days are selected to check the temporal variation of SIE and to compare with well-known SIE products.

The algorithm is developed by using an aesthetic combination of Principal Component Analysis (image redundancy reduction technique) and Unsupervised ISO classification (a popular image classification technique). SIE estimates from this method are found to be significantly comparable with the other popular data sets of SIE. Small differences may be attributed to the differences in techniques of estimations and the sensors employed. However, we will look further into this in our subsequent publications.

Comparisons between SIE derived from SCATSAT (1) versus derived SIE from NASA team sea ice concentration threshold at 30 % concentration provided by National Snow and Ice Data Centre (NSIDC), and (2) versus European Organisation for the Exploitation of Meteorological Satellites (EUMETSAT) SIE from Ocean and Sea Ice Satellite Application Facility (OSI-SAF) for the period October 2016 to March 2018 are performed. Comparison results show high correlation (R^2 ~ 0.99) at 95 % confidence level. Statistically, the comparing data sets show significant results.

Overall observations and comparisons confirmed the satisfactory of the estimation method. The SIE derived from the SCATSAT-1 will be useful to study the changes of arctic SIE throughout the life span of the SCATSAT-1 satellite. The method can also be applied to calibrated data of other scatterometer satellites with SCATSAT-1.

6. References

Abdi, H., and Williams, L. J., 2010. Principal component analysis. WIREs Computational Statistics 2, pp. 433–459. https://doi.org/10.1002/wics.101.

Ball, G. H., and Hall, D. J., 1965. ISODATA, A novel method of data analysis and pattern classification, Stanford Research Institute, Menlo Park.

Bliss, A. C., and Anderson, M. R., 2014, Daily Area of Snow Melt Onset on Arctic Sea Ice from Passive Microwave Satellite Observations 1979–2012. Remote Sensing. 6, pp. 11283-11314. https://doi.org/10.3390/rs61111283.

Budd, W. F., 1975. Antarctic sea-ice variations from satellite sensing in relation to climate: Journal of Glaciology 15, pp. 417–427. https://doi.org/10.3189/S0022143000034523.

Cavalieri, D. J., and C. L. Parkinson 2008. Antarctic sea ice variability and trends, 1979–2006. Journal of Geophysical Research Oceans 113, C07004. https://doi.org/10.1029/2007JC004564.

Cavalieri, D. J., Parkinson, C. L., Gloersen P., and Zwally, H. J., 1995, updated yearly. Sea ice concentration from Nimbus-7 SMMR and DMSP SSM/I-SSMIS passive microwave data Version-1, NASA National Snow and Ice Data Center Distributed Active Archive Center, Boulder, Colorado, USA . https://doi.org/10.5067/8GQ8LZQVL0VL.

Comiso, J. C., Cavalieri, D. J., Parkinson, C. L., and Gloersen P., 1996. Passive microwave algorithms for sea ice concentration: A comparison of two techniques. Remote Sensing of Environment 60, pp. 357–384. https://doi.org/10.1016/S0034-4257(96)00220-9.

Dan, L., and Robert, M., 2006. Polar remote sensing volume I: Atmosphere and Oceans. Springer, Berlin, 756 pp. https://doi.org/10.1007/3-540-30785-0.

Glossary of American Meteorological Society, Arctic bottom water, 2012. Available at http://glossary.ametsoc.org/wiki/Arctic_bottom_water [Accessed 20 January 2021]

Kim, T. K., 2015. T-test as parametric statistic. Korean Journal of Anesthesiology 68, pp. 540–546. https://doi.org/10.4097/kjae.2015.68.6.540.

Lake, R. A., and Lewis E. L., 1970. Salt Rejection by Sea Ice during Growth. Journal of Geophysical Research 75, pp. 583–597. https://doi.org/10.1029/JC075i003p00583.

Lillesand, T. M., Kiefer, R. W., and Chipman, J. W., 2008. Remote Sensing and Image Interpretation. 6th ed. Wiley, 756 pp.

National Snow and Ice Data Center, 2020. All About Sea Ice, Thermodynamics: Albedo. Available at https://nsidc.org/cryosphere/seaice/processes/albedo.html [Accessed 20 January 2021]

Remund, Q., and Long, D., 2014. A Decade of QuikSCAT Scatterometer Sea Ice Extent Data: IEEE Transactions on Geoscience and Remote Sensing 52, pp. 4281–4290. https://doi.org/10.1109/TGRS.2013.2281056.

Scatsat1 DP Team, 2017: SCATSAT-1 Level 4 Data Products Format Document, Microwave Data Processing Division/Sig-

nal and Image Processing Group, Space Applications Centre, Ahmedabad, ISRO Scientific Report- SC1/DP/L4FORMAT-DOC/V1.1/JUL2017. Available at ftp://ftp.mosdac.gov.in/docs/scatsat1_L4_data_products_formats_v1.1_jul_2017.pdf [Accessed 20.01.2021]

Shi, H., Tian, B., and Wang, Y., 2010. Fusion of Multispectral and Panchromatic Satellite Images using Principal Component Analysis and Nonsubsampled Contourlet Transform. In: 2010 Seventh International Conference on Fuzzy Systems and Knowledge Discovery. pp. 2312–2315. https://doi.org/10.1109/FSKD.2010.5569820.

Singh, R. K., Singh, N. K., Mamata, M., and Jayaprasad, P., 2018. Antarctic sea ice extent from ISRO's SCATSAT-1 using PCA and an unsupervised classification. Proceedings 2 (2nd International Electronic Conference on Remote Sensing), 340. https://doi.org/10.3390/ecrs-2-05153.

Wensnahan, M., Maykut, G. A., Grenfell, T. C., and Winebrenner, D. P., 1993. Passive Microwave Remote Sensing of Thin Sea Ice Using Principal Component Analysis. Journal of Geophysical Research 98, pp. 12453–12468. https://doi.org/10.1029/93JC00939.

Heritage Earth – Sustainable Resource Management

The Middle Atlas Domain of Morocco: Geoheritage Conservation Allowing Development in a Sustainable Manner

Souhail Mounir[1,✉], Naoufal Saoud[1], Kaoutar Mounir[2], Jaouad Choukrad[1], Abir Berbeche[3], Mohamed Charroud[1]

[1] Faculty of Sciences and Technologies Fez (FSTF), Fez, Morocco
[2] Faculty of Science Dhar El Mahraz Fez (FSDM), Fez, Morocco
[3] National School of Applied Sciences Fez (ENSAF), Fez, Morocco
✉ souhail022@gmail.com

Keywords: Geo-heritage, Georesources management, Conservation, Central Middle Atlas

1. Introduction

Many natural sites in Morocco are geologically rich, especially in the Atlasic area. The potential of these geosites with their geologically diverse and complex features has been recognized by geologists worldwide. Yet, studies in geotourism and the sustainable development of these sites are generally lacking. Sumanapala and Wolf (2020), who reviewed the field of geotourism, found that although geotourism clearly constitutes an emerging sub-sector of nature-based tourism with great potential, only 26 studies have been published in this field in peer reviewed journals to date. A lack of knowledge on how to assess the potential of geotourism sites has impeded their development as opportunities are not fully recognized. Assessments of the strength and weaknesses, along with opportunities and threats of geosites were recommended (Mounir, 2020).

Here we contribute to filling this gap by discussing the Middle Atlas in Morocco as a potential geotourism site. We evaluate the socio-economic, cultural and environmental conditions as they provide opportunities for development, and discuss the threats that impede such a development.

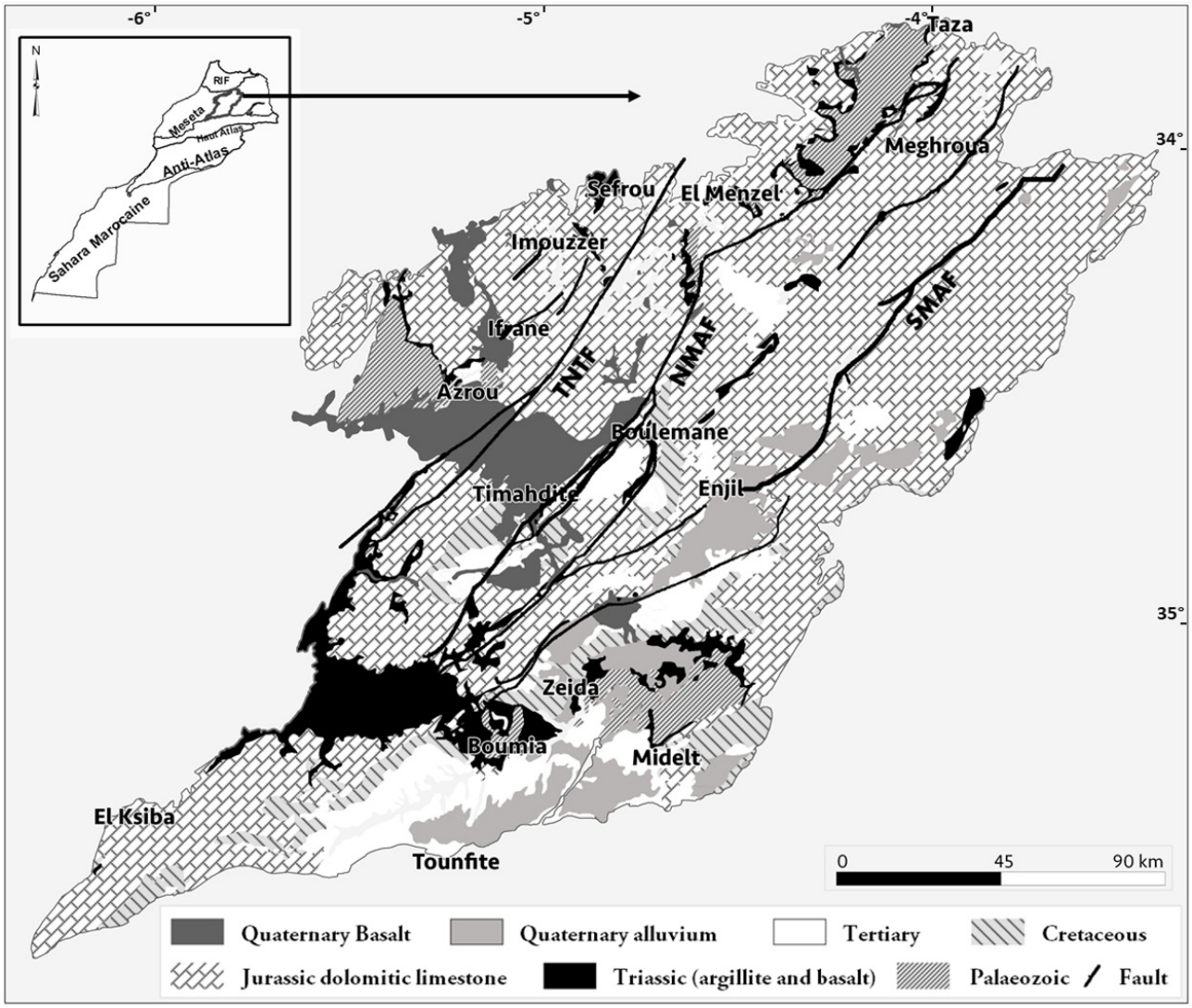

Figure 1: Geological Map of the Middle Atlas (after Mounir, 2020)

DOI: 10.2312/yes19.24

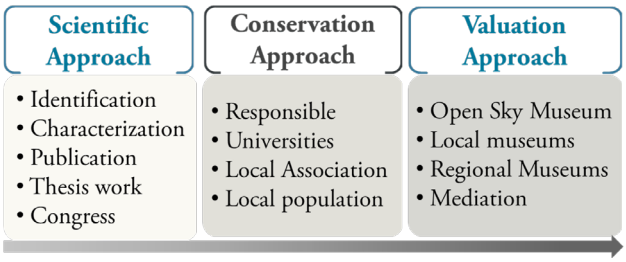

Figure 2: The main approaches, methods and interventions in the heritage industry process.

We highlight how the varied geomorphological and related elements of this geographic area showcase the geologically complex evolution of the Middle Atlas during the Meso-Cenozoic and the Quaternary. The rich portray of geological evolution lends itself to marketing and promotion of this site for geotourism.

2. Location and setting

The Middle Atlas (study area) is a part of the Atlasic domain. It is limited in the North by the South-Rifain corridor, in the East by the valley of the Middle Moulouya, in the South by the High Atlas of Beni Mellal, and in the West by the central land (Western Meseta).

The Middle Atlas is essentially represented by anticlinal rifts intruded by gabbroic formations, and with separate large synclinal basins that translate a complex geological history during the Meso-Cenozoic and the Quaternary (Termier, 1936; Choubert and Faure-Muret, 1962; Charroud, 1990; Michard et al., 2008, Hinaje et al., 2015, Mounir et al., 2019).

The mountainous region is formed by a juxtaposition of two major structural domains. The Tabular Middle Atlas (Middle Atlasic causse) formed essentially by the carbonate formations of the Lias in the form by layered plateaus. The North Middle Atlasic fault (NMAF) separates the tabular domain from the folded Middle Atlas. The latter is marked by a series of folds and faults forming ripples separated by synclines with marine and continental Dogger formations (Figure 1).

3. Geo-heritage process

The heritage process is subject to several stages of characterization, preservation, reclamation and geo-

Figure 3: Examples of geological sites of special interest in the Middle Atlas. a-b. The Middle Atlas Heritage Interpretation Centre. c. Guigou meander (Taferdoust Kasbah). d. The Sources Oum er-Rbia Waterfall. e. Aguelmam Azigza National Park. f. The bathonian Theropod Trackways of the Central Middle Atlas. g. Karst reliefs and landforms. h. Azurite and malachite. i-j. The Plio-Quaternary volcanism of the Middle Atlas.

logically remarkable trail display. It reflects the emergence of a specific mode of territorial development and ensures a holistic approach to geoconservation (Mounir et al., n. d.).

The main purpose of this work is to present a general perspective on geological heritage, focusing mainly on concepts, terminology and methods of identification and evaluation, to understand and give a general overview of the spatial and temporal evolution of the geological history of the Middle Atlas, thus bringing new scientific and socio-cultural approaches to the region (Figure 2).

4. The geological heritage of the Middle Atlas and its opportunities and strengths as a geotourism area

The Middle Atlas is a well-known outcrop set because of its stratigraphic relevance, which reflects the geodynamic history of the region. The diversity of these outcrops justifies the implementation of several strategies aimed at prioritizing geosites as a scientific place, educational, aesthetic and cultural interest. For this purpose, a systematic identification, characterization and evaluation of the geosites was carried out, taking into consideration the assessed interest, the rarity and the exceptional conservation status that the Middle Atlasic domain represents.

The geological heritage must be appreciated by the community; therefore the engagement with a large section of the society, through geotourism, may be an effective way to expand the importance of geological heritage as a valued part of the natural world (Sharples, 2002; Crofts and Gordon, 2015).

Consequently, after an analysis of the relationships between geological heritage and geotourism, Figure 3 illustrates several examples of the Middle Atlasic geoheritage in different geological contexts.

5. The threats and weaknesses of the Middle Atlas as a geotourism area

Geosciences are still poorly displayed in Morocco, or not at all concerned by administrative acts. The speech is strongly aimed to MEM ministries by geoscience scientists and researchers during the last national and international meetings.

However, Morocco still has no law for the protection of its geological heritage, especially its internationally important fossil sites of Paleo-Mesozoic age, which are very vulnerable and at risk of disappearing due to their over-exploitation as ornamental rocks and fossil sites (Mounir, 2020).

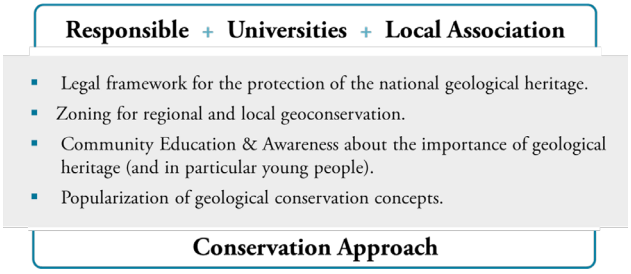

Figure 4: The key elements to ensure the protection, preservation and transmission of the natural wealth and heritage to future generations.

6. Concluding remarks about the future of the Middle Atlas as geotourism region

A positive development was noted recently in the creation of the 'Geology Direction' framework and the integration of a geological heritage service and museums in a national road framework for the development of geological and geothematic infrastructure for the period 2015–2025 (MEMEE, 2015; Mounir, 2020).

An exceptional area was identified as a project for a future geopark in the Middle Atlas of international interest under the premises of ensuring the protection, preservation and transmission of geoheritage wealth to future generations. Cooperation with international organizations, scientific institutions, and a non-governmental organization will significantly strengthen efforts in the field of conservation and the promotion of the geological heritage in Morocco (Figure 4).

7. References

Charroud, M. (1990). Evolution géodynamique de la partie sud-ouest du Moyen-Atlas durant le passage Jurassique - Crétacé, le Crétacé et le Paléogène: un exemple d'évolution intraplaque. PhD Thesis, Université Mohammed V, Rabat, 234 p.

Choubert, G., Faure-Muret, A. (1962). Evolution du domaine atlasique marocain depuis les temps paléozoïques. In : Durand-Delga, M. (ed.). Livre à la mémoire du Professeur Paul Fallot, consacré à l›évolution paléogéographique et structurale des domains méditerranéens et alpins d›Europe, 2 volumes. Societé Géologique de France, Paris, pp. 447–527.

Crofts, R., Gordon, J. E. (2015). Geoconservation in protected areas. In: Worboys, G. L., Lockwood, M., Kothari, A., Feary, S., Pulsford, I.(eds.). Protected Area Governance and Management. ANU Press, Canberra, pp. 531–568.

MEMEE (Ministry of Energy, Mines, Water and Environment) (2015). Feuille de Route Nationale pour le Développement des Infrastructures Géologiques et Géothématiques pour la période 2015-2025.

Michard, A., Sadiqi, O., Chalouane, A. (2008). Continental Evolution: The Geology of Morocco. Structure, Stratigraphy, and Tectonics of the Africa-Atlantic-Mediterranean Triple Junction. Springer, Berlin, Heidelberg, 426 p. https://doi.org/10.1007/978-3-540-77076-3.

Hinaje, S, Charroud, M., Ait Brahim, L., El Aarabi, H., Sabaoui, A. (2015). PALEOCONTRAINTES MESOZOIQUES, EVOLUTION TECTONIQUE ET PALEOGEOGRAPHIE DES BASSINS SEDIMENTAIRES MOYEN ATLASIQUE ET CENTRAL HAUT ATLASIQUE MAROCAINS, ScienceLib 7, 23 p.

Mounir, S. Saoud, N. Charroud, M. (n. d.). Valorisation du patrimoine géologique du Moyen Atlas 'Un Héritage riche e vue de Géoconservation'. La sixième Rencontre Internationale sur la Valorisation et la Préservation du Patrimoine Paléontologique '08 - 10 NOVEMBRE 2016- CASABLANCA – MAROC'.

Mounir, S., Saoud, N., Charroud, M., Mounir, K., Choukrad, J. (2019). The Middle Atlas Geological karsts forms: Towards Geosites characterization. Oil & Gas Science and Technology - Rev. IFP Energies nouvelles 74(17), 9 p. https://doi.org/10.2516/ogst/2018089.

Mounir, S. (2020). Le patrimoine géologique du Moyen Atlas et la Haute Moulouya: identification, caractérisation et valorisation. PhD Thesis, Université Sidi Mohammed Ben Abdellah, Fez, 350 p.

Sharples, C. (2002). Concepts and Principles of Geoconservation (version 3). Tasmanian Parks & Wildlife Service, Hobart, 79 pp.

Sumanapala, D., Wolf, I. D. (2020). Man-Made Impacts on Emerging Geoparks in the Asian Region. Geoheritage 12(3), 1–9. https://doi.org/10.1007/s12371-020-00493-0.

Termier H. (1936). Etudes géologiques sur le Maroc central et le Moyen Atlas septentrional, 4 volumes. Notes et mémoires (Morocco. Service des mines et de la carte géologique) 33, Imprimerie officielle, Rabat.

Cultural Practices and Sustainable Management of Wetlands in Nigeria

Emuobosa Akpo Orijemie[1,✉]

[1] Department of Archaeology and Anthropology, University of Ibadan, Nigeria
✉ Orijemie17@gmail.com

Keywords: Wetlands, Sustainability, Forest protection, Human-landscape interactions, Nigeria

1. Introduction

The goal of this paper is to provide historical data of Late Holocene human-environment interactions in the wetlands, specifically the mangrove swamp forests in the coastal region of Nigeria. The study locations are (i) Ahanve (6°25'55.020" N, 2°46'29.100" E) in Lagos State, (ii) Ikorigho (5°57'26.172" N, 4°55'51.492" E) in Ondo State, both are in south-western Nigeria, and (iii) the Okomu National Park (6°19'19" N 5°14'58" E) near Benin City, Edo State in southern Nigeria (Figure 1). Ahanve is a freshwater swamp while Ikorigho and Okomu are in the mangrove swamp forest.

Wetlands are naturally occurring distinct ecosystems that are flooded by water, either permanently or seasonally. They are characterized by unique vegetation types which grow in water bodies where oxygen-free conditions exist. The Ramsar Convention Secretariat (2007) defined wetlands as "areas of marsh, fen, peat-land or water, whether natural or artificial, permanent or temporary, with water that is static or flowing, fresh, brackish or salt, including areas of marine water, the depth of which at low tide does exceed 6 m" (Adekola et al., 2012: 666). Besides, the Ramsar Convention suggests that wetlands "may incorporate riparian and coastal zones adjacent to the wetlands, and island bodies of marine water deeper than six metres at low tide lying within wetlands". Consequently, most peatlands, freshwater swamps and mangrove forests are wetlands. In Nigeria, wetlands cover an estimated area of ~28,000 km^2; this is approximately 3 % of the 923,768 km^2 land surface area of the country (Adekola et al., 2012). The significance of wetlands includes water storage, processing of carbon and other nutrients, stabilization of shorelines, and support of a diverse array of endemic plants and animals (Bergkamp and Orlando, 1999). And more importantly, because early and indeed modern humans settle near wetlands and water bodies, they could serve as potential sources of human settlement history, human-environment interactions and palaeoenvironmental data. Therefore, data on wetlands are important because of their conservation value, cultural significance and importance in climate change policy frameworks.

Despite their importance it has been indicated that wetland systems are most affected by climate change and anthropogenic impact (Moomaw et al., 2018; Davidson et al., 2005; Erwin, 2009). Therefore, such knowledge could be employed by conservation experts and policy-makers in the management of wetlands. Bergkamp and Orlando (1999: 4) expressed concern that ''there has been little attention given so far by policy-makers to the relationship between climate change and the conservation and wise use of wetlands… as projected changes in climate are likely to affect wetlands significantly, in their spatial extent, distribution and function''. Similar sentiments were also recently echoed by Howard et al. (2017).

In Nigeria, several wetlands exist. However, the most significant is the mangrove swamp forests which are in the coastal states in Southern Nigeria such as Edo, Delta, Cross River, Rivers, Akwa-Ibom, Ogun, Ondo and Lagos. Are there policies aimed at the conservation, restoration, and sustainable use of these ecosystems in the face of climate change in Nigeria? Currently, there are no Nigerian laws which directly govern and/or regulate activities within wetlands. There are some laws such as the Forest Ordinance of 1901 and 1916, the Wild Animals Preservation Act of 1916, the Oil Pipelines Act of 1965, and the Fed-

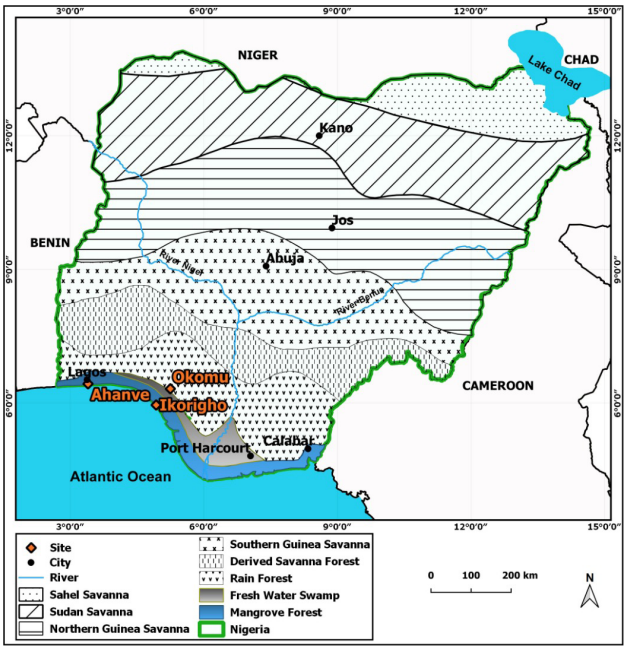

Figure 1: Map of Nigeria and the localities where sediment cores were retrieved.

DOI: 10.2312/yes19.10

eral Environmental Protection Agency (FEPA) Act of 1988, which have indirectly benefitted wetlands (Adekola et al., 2012). However, these laws have been ineffective in addressing threats to wetlands because of (i) their unspecific relations to wetlands, (ii) the lack of political will, and (iii) the culpability of the Nigerian Federal Government, whose main source of revenue, crude oil, is exploited within wetland ecosystems. Consequently, Adekola et al., (2012: 675) advocated for a National Wetland Policy which will ''tackle wetland degradation and its attendant social, ecological and economic implications''. Also, such a policy should be targeted towards addressing the potential anthropogenic and environmental challenges which arise from the destruction of wetlands. Furthermore, in formulating any wetland policy, there is a need to understand the palaeoenvironmental history and human-landscape interactions within wetlands from the past to the present. Such information about the palaeoecology of wetlands is important because of the major impact that humans can have on wetlands (Howard et al., 2017:42).

in this paper it is argued that, based on palaeoenvironmental data, anthropogenic activities particularly cultural practices, can contribute to the conservation or destruction of wetlands.

2. Environmental and anthropogenic history of Wetlands in Nigeria

This paper obtained data from palynology, sedimentology and historical sources (archaeology and oral tradition). Three localities with wetland vegetation, namely Ahanve (Lagos State), Ikorigho (Ondo State) and Okomu National Park (Edo State) (Figure 1) were drilled for sediment cores with lengths of 1.5 m (Lake 90 in Okomu National Park), 8 m in Ikorigho and 11 m in Ahanve. Ahanve is a freshwater swamp and Ikorigho a mangrove swamp forest, while Okomu is a National Park which consists of mangroves, freshwater, riverine forests and rainforests. The two major pantropical Late Holocene climatic upheavals which occurred from ca. 4,500 to 2,000 BP (ca. 2,500 to 0 BCE) and ca. 1,300 to 1,100 BP (ca. AD 600 to700) were registered in at least two of the three sediment cores. The Late Holocene Dry Phase of ca. 4500 to 2000 BP (ca. 2500 to 0 BCE) led to the decline and the subsequent complete disappearance of the mangroves from Ahanve at 3109 ± 26 BP (cal. 1440 to 1310 BCE, KIA-17574). The Ikorigho mangroves which were hitherto fairly abundant decreased at 1190 ± 30 BP (cal. 1240 to 1200 BP, Beta-296135), but they subsequently recovered and remained abundant in Ikorigho until today although they are currently being degraded by anthropogenic activities. In the sediment core of Lake 90 of the Okomu National Park, the mangrove swamp forest exhibited a pattern similar to that recorded at Ikorigho, which is approximately 45 km to its West. Hence, why did the mangrove swamp forest in Ahanve disappear in response to the Late Holocene environmental conditions compared to those in Ikorigho and Okomu?

3. Antiquity of Humans at the three wetland localities

3.1. Ahanve

A reconstruction of the vegetation history of Ahanve based on the palynological analysis of an 11 m core revealed that the rainforest and mangrove swamp forest vegetation was the most dominant vegetation from the Early to the Late Holocene (ca. 9000 to 4000 BP [ca. 7000 to 2000 BCE]) (Sowunmi, 2004). A marked reduction in the mangroves was noted from the Late Holocene until 3109 ± 26 BP (cal. 1440 to 1310 BCE, KIA-17574) when the mangrove swamp forest disappeared. The initial decrease in the mangroves was a result of natural climatic changes; but did humans played any role? The results of the archaeological excavations conducted at Ahanve indicated that there was continuity of human occupation in the area with two clear cultural phases, namely Phase I and Phase II (Orijemie, 2014). Phase I was pre-European, i.e. before the 15th century, while Phase II was post-15th century (cal. AD 1440 to 1640; Beta-296133) (Orijemie, 2013). These dates do not indicate that the present set of humans in Ahanve had any impact on the disappearance of the mangrove swamp forests. However, the antiquity of humans in the Badagry cultural area, where Ahanve is located, and the adjacent areas in the southern parts of the Republic of Bénin, a neighboring country to Nigeria, is between 2930 ± 130 BP and 2670 ± 90 BP to 2510 ± 120 BP (1060 to 540 BCE), respectively (Alabi, 1998). The associated artefacts include ground-stone axe and pottery, as well as charcoal particles and charred palm kernels (Oil palm, Elaeis guineensis). Alabi (1998) stated that the charred palm kernels and charcoal reflected slash-and-burn and clearing of the mangrove forest trees, while the ground-stone axe was presumably used to cut down the mangrove trees. Since the dates of human presence from the Ahanve area coincided with the disappearance of mangroves, it appears that the earliest humans may have contributed to the marked changes in the vegetation. Therefore, in situations where wetlands are negatively affected by natural environmental changes, cultural practices

such as uncontrolled deforestation could result in a devastating effect on wetlands. In extreme cases, it could lead to a complete disappearance of wetlands, such as the mangrove swamp forests, as noted during prehistoric times in Ahanve.

3.2. Ikorigho and Okomu National Park (ONP) near Benin City

Oral information gathered from Ikorigho (Ondo State) revealed that human occupation of the site is not more than 100 years old. Although this has not been tested archaeologically, the occurrence of plant pollen which are indicative of human disturbance at the topmost layer of the 8 m sediment core indicated that humans are a recent phenomenon in the area. The mangroves at Ikorigho were dominant until 1190 ± 30 BP (cal. 1240 to 1200 BP, Beta-296135), when they experienced a marked reduction. However, they recovered and have remained abundant afterwards. It is argued that the absence of humans or the existence of a small human population at Ikorigho ensured that the wetlands were not adversely affected, hence the almost immediate recovery of the mangrove swamp forest there.

In the Okomu National Park, the 1.5 m sediment core revealed an extensive mangrove swamp forest but significant decreases were noted at 1.4 m, 0.8 m and 0.4 m. The decrease at 1.4 m was natural as there were no pollen and spores associated with human impact; the converse was the case at 0.8 m and 0.4 m. There are currently no radiocarbon dates for the Okomu sediment core. However, the palynological sequence was correlated with that from archaeological excavations in the park. Human occupation of the Okomu National Park, based on charcoal samples recovered from archaeological trenches at depths of 20 cm and 20 to 28 cm was dated to 760 ± 50 BP (cal. 1177 to 1378 AD, Gif 10440), and 700 ± 60 BP (cal. AD 1230 to 1300, Gif 10441), respectively (White and Oates, 1999). Therefore, we could assume that the 13th to 14th centuries represent when humans had a significant impact on the wetlands in the Okomu National Park.

4. Cultural practices (Totems) and conservation of Wetlands in Nigeria

Despite the human interventions noted in Ikorigho and Okomu, the mangrove swamp forests have remained there till date. Although it has been established that human occupation in Ikorigho and the Okomu NP is comparatively recent compared to Ahanve, it is the cultural practice associated with the wetlands that have contributed to their continued existence in those areas. In Ikorigho and Okomu NP, both located within the Niger Delta, where the mangrove swamp forest is abundant, it is known to play critical roles in the people's well-being. It has been estimated that ca. 60 % of the near 30 millions local populations in the Niger Delta area of southern Nigeria rely on the mangrove swamp forest for survival (James et al., 2013). The mangrove swamp forest is viewed and venerated as spiritual heritage. Several legends and myths tell of the mystic and sacred nature of the forest, and the local people relive such stories from generations to generations. In addition, several animals (and in some cases plants) which are natural to the mangrove wetlands are considered deities, in the form of totems, and usually no one is permitted to hunt them. Such a traditional strategy helps instil fear in the community and hence acts as a means of conserving ecosystems (James et al., 2013), in this case, wetlands.

In the Niger Delta region in southern Nigeria where the mangrove wetlands are extensive, several animals, some of which are endemic to the region, have been attributed ''some theistic powers and attributes, which are considered responsible for their collective survival'' (Ikeke and Alumona, 2016: 88). One such animal is the West African Manatee (Trichechus senegalensis) which thrives in brackish and freshwater of West-Central Africa. It is referred to as the Sea goddess (Maame (Maami) Water) in folklore and myths. Although Maame Water is sometimes hunted and accidentally trapped in fishnets, it is respected as a symbol of wealth and beauty. Besides, it gets angry when its habitat is encroached and often flips over canoes. Hence it is venerated and its habitats are protected.

In several parts of the Niger Delta, particularly among the Urhobos and Itsekiris, it is the practice that persons who experience a 'bad death' such as (i) those who commit suicide, (ii) those who die from injuries sustained from falling from a tree or palm tree, and (iii) women who die during pregnancy or childbirth, are buried within the mangrove swamp forest (Rim-Rukeh et al., 2013). Such a practice is carried out to cleanse the community of 'evil spirits'. Similarly, the Binis and Ijos (Ijaw) in the same region venerate and enact regulations and customary laws regarding the protection of several animals and plants; such animals include the Nile crocodile (Crocodylus niloticus), the African Elephant (Loxodonta africana) and the African Python (Python sebae), while the plants are Newbouldia laevis and Cola acuminata. These regulatory practices check biodiversity and livelihood loss and enhance the conservation of wetlands (An-

wana, 2008).

In contrast, however, in the metropolitan cities such as Lagos, where isolated patches of mangrove wetlands still exist, cultural practices which could allow for the conservation of wetlands are nearly absent. This is partly a result of the adoption of Christianity and Islam, the principles and beliefs of which are sometimes at conflict with several African traditional principles. As stated above, some of these African traditional principles account for the sustenance of wetlands elsewhere. Consequently, several wetlands in metropolitan cities (such as Lagos) are 'desecrated' and destroyed without any concrete restoration plans (Obiefuna et al., 2013).

5. Conclusions

This paper has shown that certain cultural practices contribute to the conservation of wetlands in Nigeria, and these must be sustained. Therefore, given the importance of wetlands to the sustenance of humans and livelihoods, this paper advocates the following: (i) the establishment of a wetland policy, (ii) community engagement, and (iii) launching of a wetlands protection awareness campaign in the context of the wetland policy. Firstly, there is a need for national legislation for the conservation of wetlands. Such a policy will not only provide education to the citizens, particularly those living in the catchment areas of wetlands but will also engage them to adopt and sustain the right attitude towards wetlands. Secondly, the policy should incorporate into it the cultural practices of the people, particularly those relevant to the conservation of wetlands. This can easily be achieved by engaging community leaders and stating their clearly defined roles; the leaders must also be convinced of their roles as collaborators and stakeholders in the protection of wetlands. Thirdly and most fundamentally, there should be a medium such as a wetlands protection awareness campaign, which will function in enlightening the people, for instance, about the needless conflict between religion and the conservation of wetlands.

6. References

Adekola, O., Whanda, S. and Ogwu, F. 2012. Assessment of Policies and Legislation that affect Management of Wetlands in Nigeria. Wetlands 32:665–677. https://doi.org/10.1007/s13157-012-0299-3

Anwana, E.D. 2008. Forbidden (Sacred) Lakes and Conservation: the role of indigenous beliefs in the management of wetland resources in the Niger Delta, Nigeria. Unpublished PhD Thesis, University of Greenwich, London.

Alabi, R.A. 1998. An Environmental Archaeological study of the coastal region of southwestern Nigeria, with emphasis on the Badagry area. Unpublished PhD Thesis, University of Ibadan, Ibadan, Nigeria.

Bergkamp, G. and Orlando, B. 1999. Wetlands and Climate Change: Exploring collaboration between the Convention on Wetlands (Ramsar, Iran 1971) and the UN Framework Convention on Climate Change.

Davidson, N.C., D'Cruz, R. and Finlayson, C.M. 2005. Ecosystems and Human Well-being: Wetlands and Water Synthesis: a report of the Millennium Ecosystem Assessment. World Resources Institute, Washington, DC. 80 pp.

Erwin, K. L. 2009. Wetlands and global climate change: the role of wetland restoration in a changing world. Wetlands Ecology and Management 17:71–84. http://doi.org/10.1007/s11273-008-9119-1.

Howard, J., Sutton-Grier, A., Herr, D., Kleypas, J., Landis, E., Mcleod, E., Pidgeon, E., and Simpson, S. 2017. Clarifying the role of coastal and marine systems in climate mitigation. Frontiers in Ecology and the Environment 15(1):42–50. https://doi.org/10.1002/fee.1451.

Ikeke, M. O. and Alumona, N.O. 2016. Totemism and Sustainable Development in the Niger Delta. International Journal of Theology and Reformed Tradition 8:88–96. [online] Available at: https://academicexcellencesociety.com/totemism_and_sustainable_development_in_the_niger_delta.pdf [Accessed 29 September 2020].

James, G. K., Adegoke, J.O., Osagie, S., Ekechukwu, S., Nwilo, P. and Akinyede, J. 2013. Social valuation of mangroves in the Niger Delta region of Nigeria. International Journal of Biodiversity Science, Ecosystem Services and Management 9 (4):311-323. https://doi.org/10.1080/21513732.2013.842611.

Moomaw, W. R., Chmura, G. L., Davies, G. T., Finlayson, C. M., Middleton, B. A., Natali, S.M., Perry, J. E., Roulet, N., and Sutton-Grier, A. E. 2018. Wetlands in a Changing Climate: Science, Policy and Management. Wetlands 38:183–205. https://doi.org/10.1007/s13157-018-1023-8.

Obiefuna, J. N., Nwilo, P.C., Atagbaza, A.O.and Okolie C. 2013. Spatial Changes in the Wetlands of Lagos/Lekki Lagoons of Lagos, Nigeria. Journal of Sustainable Development 6 (7):123–133. https://doi.org/10.5539/jsd.v6n7p123.

Orijemie, E. A. 2013. A Palynological and Archaeological Investigation of the Environment and Human occupation of the Rainforest of South-Western Nigeria during the Late Holocene Period. Unpublished PhD Thesis, University of Ibadan, Ibadan, Nigeria.

Orijemie, E.A. 2014. Exploitation of Aquatic Resources in Ahanve, Badagry, south-western Nigeria. Internet Archaeology 37. http://dx.doi.org/10.11141/ia.37.8.

Ramsar Convention Secretariat, 2007. Wise use of wetlands: A Conceptual Framework for the wise use of wetlands. Ramsar handbooks for the wise use of wetlands, 3rd ed., vol. 1. Ramsar Convention Secretariat, Gland, Switzerland. [online] Available at: https://www.ramsar.org/sites/default/files/documents/library/hbk4-01.pdf [Accessed 29 September 2020].

Rim-Rukeh, A., Irerhievwie, G. and Agbozu, I. E. 2013. Traditional beliefs and conservation of natural resources: Evidences from selected communities in Delta State, Nigeria. International Journal of Biodiversity and Conservation 5 (7):426–432. [online] Available at: https://academicjournals.org/journal/IJBC/article-abstract/9B3B02C10727 [Accessed 29 September 2020].

Sowunmi, M.A. 2004 Aspects of Nigerian coastal vegetation in the Holocene: some recent insights. In: Past Climate Variability through Europe and Africa. Battarbee R.W., Gasse F., and Stickley C.E. (eds), Kluwer Academic Publishers, Dordrecht, the Netherlands, pp 199–218. https://doi.org/ 10.1007/978-1-4020-2121-3.

White, L.J.T and Oates, J. F. 1999. New Data on the History of the Plateau Forest of Okomu, Southern Nigeria: An Insight into How Human Disturbance has shaped the African Rain Forest. Global Ecology and Biogeography 8 (5):355–361. https://doi.org/10.1046/j.1365-2699.1999.00149.x.

Seismic and Petrophysical Analyses for Reservoir Evaluation of UKU Field, Offshore Niger Delta

Bright Chisom Osuagwu[1,✉], Olatunbosun Adedayo Alao[2], Saheed Ayodeji Adeosho[3]

[1] Platinum Geoservices, Nigeria;
[2] Obafemi Awolowo University, Ile-ife, Nigeria;
[3] MacBenuz Environs Limited and Technovate Nigeria
✉ just_bright@yahoo.com

Keywords: 3D-Seismic, Petrophysics, Distributary channel, Deltaic, Shallow marine, Reservoir evaluation

1. Introduction

The uncertainty in the quantification of hydrocarbon reserves due to inadequate and poor definitions of reservoir properties has been a challenge in the oil industry. From the exploration stage until the development and exploitation of hydrocarbon, well log analysis and 3D seismic interpretation are employed to provide information on oil fields reservoir characterization for economic viability and cost-effectiveness.

In recent times, the search for hydrocarbon has become more difficult. Geoscientists now have to look beyond conventional structural traps and are now giving attention to deposits that might be locked in structures controlled by stratigraphy, which in essence might hold the key to the future of the oil industry. However, the complexity in describing such reservoirs due to their inherent heterogeneity makes such an exercise very challenging for oil explorationists. Although much progress has been made for some oil fields having these trap features, there is still more to be achieved.

In the Niger Delta, growth faults and roll-over anticlinal structures have been documented to serve as structural traps for hydrocarbon accumulations (Merki, 1972; Orife and Avbovbo, 1982). The use of advanced technological tools in 3D seismic data interpretation and integration with other geological data has yielded great results in mapping such structural prospects as well as their stratigraphic counterparts (Srivastava et al., 2005).

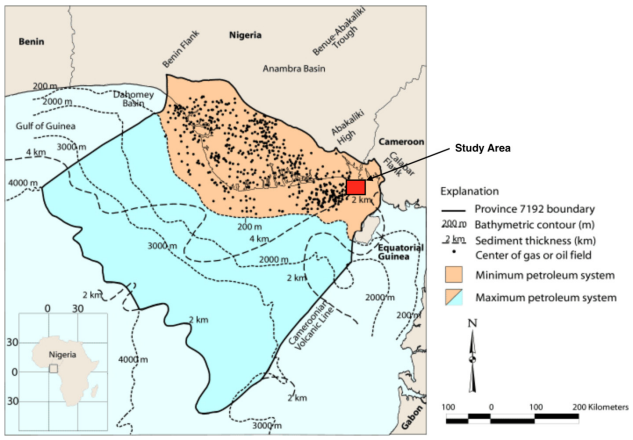

Figure 1: Location of the study area (modified from Tuttle et al., 1990).

The objective of this study is to determine the economic reservoir extent, quality, and structural architecture of the UKU field, offshore Niger Delta, and identify possible areas for further field development. In this study we have used an integrated approach, including well and seismic datasets, to create an optimized framework for siliciclastic reservoir properties.

2. Study Area

2.1. Geographical Location

The field under consideration, identified as UKU for this study is located 55 km offshore under 138 ft of water in the shallow offshore depobelt in the southeastern part of the Niger Delta (Fig. 1, Tuttle et al., 1990). Reservoirs of interest in this field are in the Pliocene D-1 sandstone deposits of the Paralic Agbada formation. The Niger Delta is situated within the Gulf of Guinea with extension throughout the Niger Delta Province (Klett et al., 1997). It is located in the southern part of Nigeria between 4° and 9° East and 4° and 6° North.

2.2. Geological Evolution

The UKU field is situated on the West African continental margin at the apex of the Gulf of Guinea, which formed the site of a triple junction during continental break-up in the Cretaceous (Doust and Omatsola, 1990). From the Eocene to the present, the delta has prograded southwestward, forming depobelts that represent the most active portion of the delta at each stage of its development (Doust and Omatsola, 1990). These depobelts form one of the largest regressive deltas in the world with an area of some 300,000 km^2 (Kulke, 1995).

2.3. Structural and Depositional Setting

Bruso et al. (2004) classified reservoir depositions into three major components along the southern Niger Delta/Equatorial Guinea axis. The authors explained that in the northerly updip section of the axis (Nigeria), shallow water delta-front sandstone depo-

Proceedings of the 5th International YES Congress
DOI: 10.2312/yes19.18

Well	GR	RES	NPHI	RHOB	SONIC	CALI	CHECKSHOT
UKU-1	*	*		*	*	*	*
UKU-2	*	*		*	*	*	*
UKU-6	*	*	*	*	*	*	*
UKU-4	*	*	*	*	*	*	*
UKU-8	*	*	*	*	*	*	*

Table 1: Well logs from vertical wells available on the study areas within UKU field and QC.

sition predominated along extensional deltaic growth faults that formed near the active margin shelf. In the mid-dip areas, slope shale and channel sand deposition predominated in the middle position of the compartment while it is translated basinward along its overpressured basal-detachment surface. The UKU field shares the features in the updip and mid-dip outlined in the author's work. Within the overall stratigraphic diagram of depositional features of Bruso et al., (2004), the reservoirs of interest are within the Qua Iboe member of the Pliocene part of the Agbada Formation.

2.4. Trapping Style

Doust and Omatsola (1990) described a variety of structural trapping elements (Supplementary Fig. 1). Most known traps in the Niger Delta fields are structural although stratigraphic traps are not uncommon. The structural traps developed during synsedimentary deformation of the Agbada paralic sequence (Evamy et al., 1978), while stratigraphic traps originated from palaeo-channel fills, regional sand pinch-outs, incised valleys, and low-stand fans as documented in Orife and Avbovbo (1982).

Structural complexity increases from the north (earlier formed depobelts) to the south (later formed depobelts) in response to the increasing instability of the under-compacted and overpressured shale.

3. Methodoloy

The methods used in this study include full prestack time migration (PSTM) seismic data comprising of 222 in-lines and 322 cross-lines, well log data from five vertical wells composed of gamma-ray (GR), density (RHOB), sonic, resistivity (RES), and caliper (CALI) logs for all wells with neutron (NPHI) log being available for UKU-4, 6, and 8 (Table 1) and checkshot data available for all wells.

3.1. Well log correlation

Well logs were interpreted and subjected to various petrophysical analyses. In addition, we carried out chrono-stratigraphic correlation across the wells in order to establish the distribution and features of the lithological units of interest across different well locations. Integration of well logs motifs allowed us to identify porous and permeable litho-units which are saturated with hydrocarbon and possess right qualities that distinct them as hydrocarbon reservoirs. In addition, other derivative reservoir parameters, such as reservoir thickness (ft), Net-To-Gross (NTG), volume of shale (Vsh) in the clastic reservoirs, effective porosity (ϕ_{eff}) in v/v, hydrocarbon saturation ($1 - S_w$; S_w = water saturation) in v/v, bulk volume water ($BVW = S_w \cdot \phi_{eff}$) and were derived from the well log data to evaluate the hydrocarbon potential of the UKU field.

3.2. Seismic to well-tie

Interpreting a seismic dataset involves the establishment of the relationship between seismic reflections and stratigraphy which is done via a synthetic seismogram (done by the convolution of Ricker wavelet with reflection coefficient). This seismogram shows the expected seismic response for comparison with the real seismic data followed by appropriate 2 ms time shifts and manual adjustments (Supplementary Fig. 2). The seismic amplitude ranges from -25 to +32 (· 10000 AU).

3.3. Seismic Interpretation

Interpretation of seismic sections was done interactively in Petrel software for which two sand units were mapped, superimposed from well log interpretation with correction for seismic data pull down due to gas effect (Supplementary Fig. 3). Various indicator maps such as structural, isopach, isochron and amplitude maps were generated from results of the horizons mapping. This information is useful in determining appropriate locations for drilling exploratory, appraisal or development wells within a prospect.

3.4. Fault Interpretation

Coherence cubes of the seismic data were generated with the chaos, variance edge, and ant tracking attributes. The variance edge time slice (Supplementary Fig. 4) showed the highest fault-delineation advantage; hence it was used to guide the fault-mapping process.

3.5. Velocity Model/Map Generation

Time structure maps were generated from the derived horizon surface maps by inserting the fault polygons of delineated major faults and subsequently converted to depth structure maps using the layer cake velocity model with the aid of sonic calibrated check-shot data. The resultant depth structure map was used to generate the gross volume of the reservoir rock (GRV). The top and base of the reservoirs

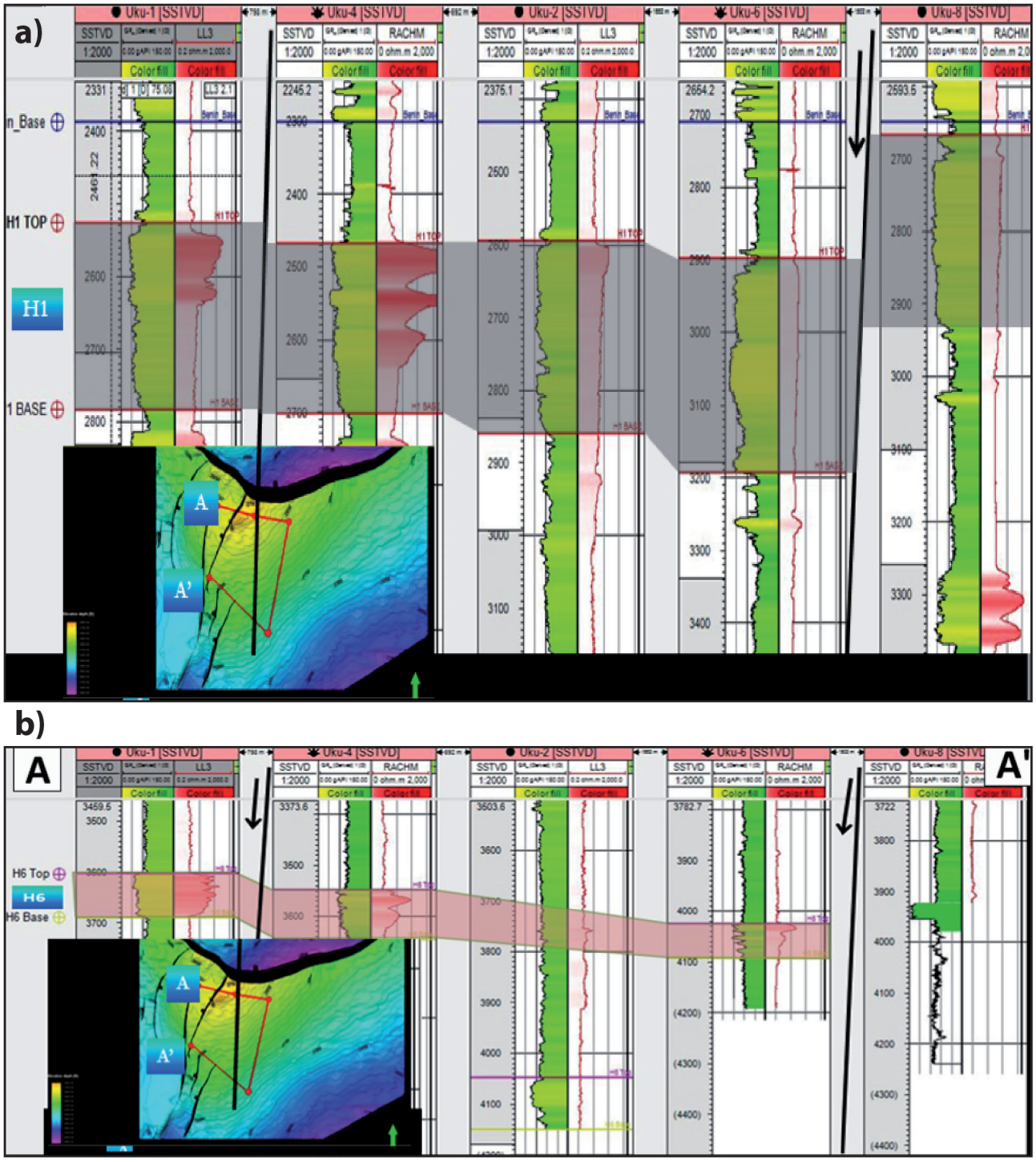

Figure 2: Well correlation of the H-1 and H-6 sands and the lateral discontinuity of the H-6 sands.

were mapped and subsequently used to generate the isochron and isopach maps via arithmetic operations in Petrel mapping software.

3.6. Volumetric Calculations

Reserves were calculated using the map-based volume calculation module available in Petrel 2013 software. Inputs to the process include: depth maps delineating reservoir intervals (GRV), fluid contacts as well as saturation values derived from petrophysical logs and formation volume factor (FVF)

4. Results and discussion

4.1. Well Log Interpretation

In evaluating the hydrocarbon potentials of the UKU field, it is essential to obtain a good picture of the subsurface stratigraphy to establish reservoir consistency (Fig. 2). H1 and H6 have been identified as reservoirs. H1 exhibits lateral continuity across all wells and occurs at a depth range from 2470 to 3200 ft. H6 shows lateral discontinuity and exist between 3600 and 4100 ft with stacked channels and ponded lobes. Seven surface boundaries, three maximum flood-

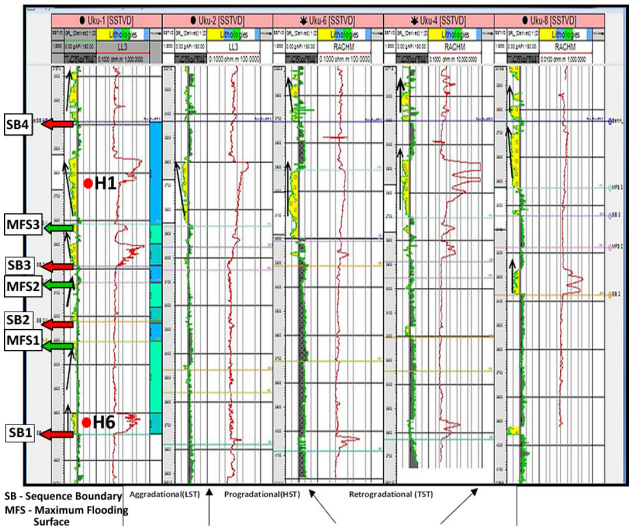

Figure 3: Chronostratigraphic correlation and stacking patterns.

ing surfaces and four sequence boundaries, were identified as peaks and troughs of seismic onsets, respectively. Well log signatures of both reservoirs reveal a funnel-shaped motif which is an indication of a coarsening-up succession. This can be interpreted as a deltaic progradation or a shallow marine progradation in a high energy depositional environment (Highstand system tract – HST). In the absence of biostratigraphic data, a combination of gamma-ray and resistivity log curve signatures was used to deduce the depositional environments based on their characteristic pattern mainly from well UKU-1. With this in mind, the deposition environment was inferred from log motifs to indicate deposits of fluvial, deltaic, and shallow marine origin (Fig. 3).

4.2. Seismic Interpretation

The variance edge attribute was used to aid the interpretation of the faults as it is effective for detecting edge effects, channels, discontinuous features and to measure the continuity between seismic traces in a specified window along a picked horizon (Supplementary Fig. 5).

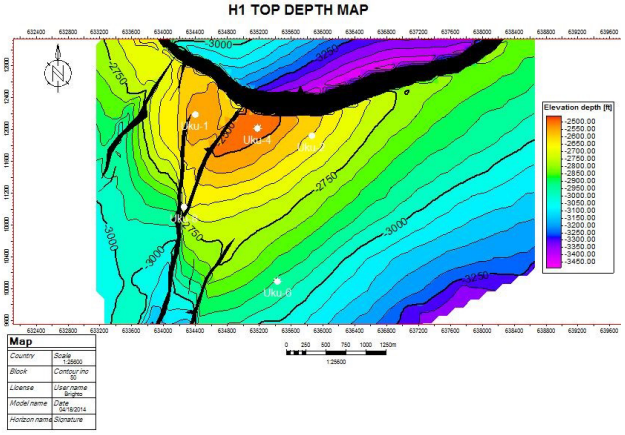

Figure 5: H1 Top depth map.

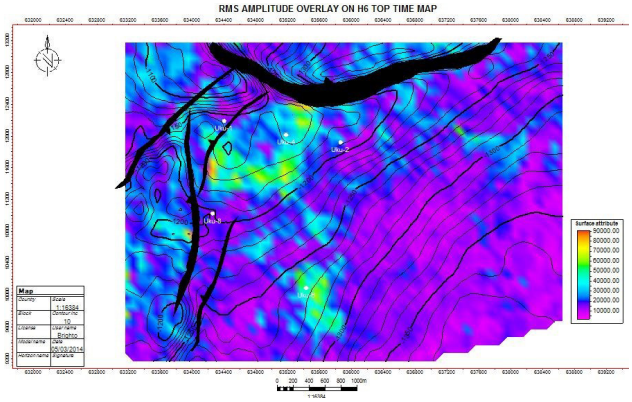

Figure 4: RMS amplitude overlay on H6. Time map@10 ms window.

A total of fourteen faults were mapped on seismic sections. Seven faults intersected the horizons of interest as shown in Supplementary Fig. 5; five west-dipping faults (synthetic), one east-dipping fault (antithetic), and a major structure building a northward dipping fault (antithetic to the dominant structural fault trend in the Niger Delta). These faults show a structural trend that agrees with the principles that emphasize the influence of the ratio of sedimentation to subsidence rates.

4.3. Amplitude maps

The amplitude maps were generated for the mapped horizons to aid structural trap interpretation. RMS amplitude maps show discontinuity of trapped hydrocarbons in H1 and H6 reservoir better than other attribute maps. Hart et al. (1996) mentioned the concentration of high amplitude towards the crest of anticlines. Therefore, conformance of high amplitude to fault delineation and map contours was used to further describe trap definitions in the process. Figure 4 shows the root mean square amplitude map of H6 to apprehend the geological framework. The high amplitude zones seen on the map are constrained to the red to yellow color band while the medium to low amplitude are constrained to the blue to pink color bands. The high-amplitude values are indicative of hydrocarbon-rich sands and thus delineate the pos-

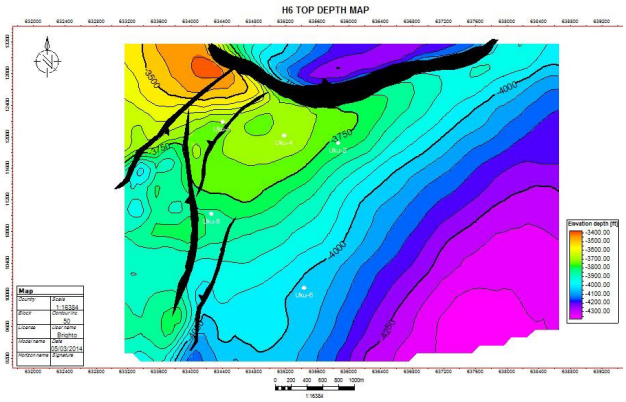

Figure 6: H6 Top depth map.

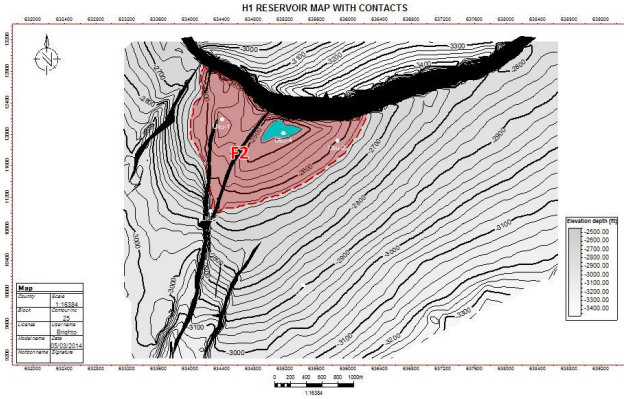

Figure 7: Reservoir Description and contacts for H1 top sand. FB1, OWC = -2640 ft, FB2, GOC = -2470 ft and OWC = -2640 ft; red: oil; green: gas.

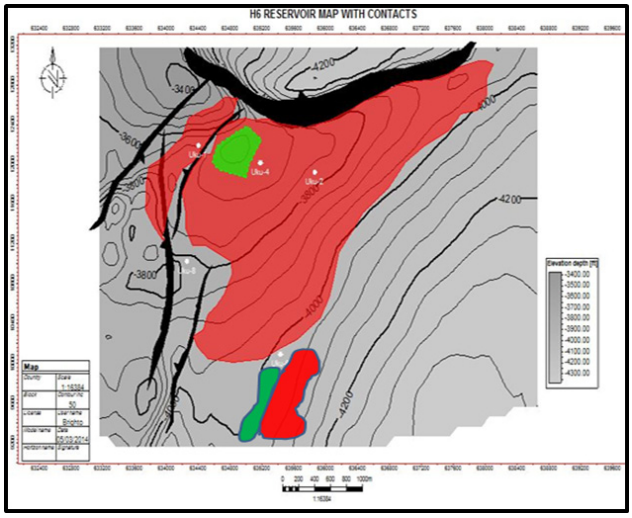

Figure 8: Reservoir description and contacts for H6 top sand. FBW, strat-trap = -3683 ft; FB Central = -3584 ft (gas) oil-strat-trap, South lobe GOC = -4048.8 ft oil-strat-trap; red: oil; green: gas.

sible extent of the prospect, which in turn is supported by oil shows in the wells. Interestingly, on the seismic sections, these zones have been observed as bright spots. The Amplitude map of H1 displayed similar features. Distinct on the attribute maps for H6 (Fig. 4) is the high amplitude on an isolated geological structure appearing as lobes in the southern part of the map. The high amplitude trend was interpreted to be a high porosity trend and it is interchanged with the low amplitude zone which was interpreted to come from lateral lithofacies changes. The bright spot observed within the upper central part of the map validates the results on the depth maps.

4.4. Time and Depth Structural Maps

Time and depth structural contour maps were produced for the two horizons defined on top of sand bodies, namely H1 and H6. The time and depth structure contour maps show a system of differently oriented growth faults (Figs. 5 and 6). A major curvy shaped growth fault, dipping NW-ward, extends over about 85 % of the mapped area. The two faults on the map give a fault dependent structure favorable for hydrocarbon accumulation, which is somewhat uniform westward across the field but better developed towards the main structure-building fault. The trap type that developed for H1 is fault assisted while the trap type for H6 is a combination of structural and stratigraphic trap components (Figs. 5 and 6). Depth maps were generated via velocity modeling. Wells were drilled in areas that have low velocity, which supports the idea that hydrocarbons generally have low seismic velocity in addition to the fact that the top of the anticlinal structures are less compacted. Generated isochron maps for H1 and H6 show that deposition of reservoir material is NW-SE oriented. The outward building trend is more obvious in Supplementary Fig. 6 while the well logs for H6 in Figure 2 show that the reservoirs fines towards UKU-6 which is in the spatially distal part of the reservoir; thereby confirming depositional direction of reservoir sediments.

4.5. Reservoir Properties

Hydrocarbon potentials of the delineated sands were revealed in their Petrophysical properties. Table 2 shows reservoir properties that were calculated for H1 and H6 from UKU-1, UKU-4, and UKU-6. Sands are well sorted with low values of water saturation (S_w). Effective porosities (greater than 0.3 or 30 % porosity units) are satisfactory for a reservoir to be adjudged a producible reservoir (Shell, 2002). In these wells, all the reservoir sands have MHI values lower than 0.7; hence hydrocarbons were moved during invasion.

A buckle plot of water saturation (S_w) against po-

Well	Zones	Top [ft]	Base [ft]	Gross [ft]	Net [ft]	NTG	Vsh [v/v]	PhiE [v/v]	Sw [v/v]	Sxo [v/v]	BVW	MHI	MOS	ROS
Uku-1	H1_Oil	2534.7	2636.9	102.30	98.50	0.96	0.04	0.37	0.26	0.76	0.10	0.34	0.50	0.24
Uku-1	H6_Oil	3599.5	3683.3	83.81	82.84	0.99	0.01	0.36	0.20	0.72	0.07	0.27	0.53	0.28
Uku-4	H1_Gas	2464.9	2469.7	4.76	3.70	0.78	0.02	0.34	0.27	0.77	0.09	0.35	0.50	0.23
Uku-4	H1_Oil	2469.7	2636.5	167.20	164.70	0.99	0.08	0.33	0.22	0.74	0.07	0.29	0.52	0.26
Uku-4	H2_Gas	3547.6	3583.4	35.77	32.37	0.91	0.04	0.37	0.22	0.74	0.08	0.30	0.52	0.26
Uku-4	H2_Oil	3583.4	3624.0	40.66	37.63	0.93	0.16	0.33	0.37	0.82	0.12	0.46	0.45	0.18
Uku-6	H6_Gas	4023.3	4040.8	17.50	16.83	0.96	0.08	0.353	0.25	0.76	0.09	0.33	0.51	0.24
Uku-6	H6_Oil	4040.4	4058.5	17.67	10.17	0.58	0.17	0.33	0.51	0.87	0.17	0.59	0.36	0.13

Table 2: Petrophysical parameters of the reservoir sands.

rosity in H1 shows general non-conformance with the Bulk Volume Water (BVW) hyperbolic curves. Similarly, the buckle plot for H6 has a perpendicular trend with respect to the buckle trend lines. In both cases, the reservoirs trend away and are not at irreducible water saturation, indicating that production from both reservoirs will yield water with hydrocarbon during depletion (Supplementary Fig. 7).

Based on the seismic amplitude maps and petrophysical analyses of resistivity, neutron, and density logs, reservoir maps indicative of fluid contacts were generated and labeled with green and red colors (Figs. 7 and 8). Fault F2 compartmentalizes the study area giving rise to contrast in fluid contacts across the field as evidenced by inferred variations in well log readings across the fault. Reservoir limits were defined by the oil/water contact derived from well logs (UKU-1, UKU-4, UKU-6). Among these wells, UKU-1 falls within the first fault block FB1 (downthrown side of F2) while the other wells fall within the second fault block FB2 (upthrown side of F2). Well logs within the latter block show that H1 has a gas-oil contact (GOC) of -2470 ft and an oil-water contact (OWC) of -2640 ft while the H6 has a GOC at about -3584 ft (at UKU-4 structural trap component) and -4048.8 ft (at UKU-6 stratigraphic trap component). Within FB1, H6 has oil-down-to (ODT) -3683 ft while H1 has an ODT at -2636.9 ft (Table 2).

4.6. Volumetrics

Using a volumetric approach, the stock tank oil in place and gas initially in place was estimated as shown in Supplementary Tables 1, 2a, 2b). Calculations of original hydrocarbon in place were done using the following standard volumetric estimation formula (Eq. 1),

$$STOIIP/GIIP = GRV \cdot NTG \cdot \phi \cdot \frac{1 - S_W}{FVF} \qquad (Eq.\ 1)$$

where FVF is the formation volume factor estimated from production data, ϕ is porosity, NTG is net to gross ratio, Sw is water saturation, GRV is the gross rock volume, STOIIP is stock tank oil initially in place, and GIIP is gas initially in place. Recoverable reserve (N) is calculated according to eq. 2,

$$N = STOIIP \cdot RF \qquad (Eq.\ 2)$$

where RF is the recovery factor, which depends on drive mechanism, permeability, reservoir depth, and hydrocarbon viscosity.

The present proven reserves were estimated at 49 million barrels of oil (MMBO) and 0.29 million standard cubic feet (MSCF) of gas in H1, and 27 MMBO, 14 MSCF for H6, assuming a recovery factor of 51 % and a water drive mechanism for the reservoirs.

5. Conclusions

In this study, the integration of seismic data with well logs was successful in defining the subsurface geometry, stratigraphy, and hydrocarbon trapping potential of the UKU field. The UKU field is a faulted three-way structural closure against a large down-to-the-north normal fault with deeper reservoirs having stratigraphic components. The oil-bearing sandstones in the field are the shallow marine sandstones of the D-member and the deepwater channelized deposits of the Qua Iboe, both of which are believed to lie within the Biafra Member of the Agbada formation and are of Pliocene age, with reservoir units belonging to the highstand system tract. Isochron maps show thicker sediments in the central and northern parts of the field. Based on this study the results suggest more development opportunities in the field and could also guide the placement of production and injection wells for optimum recovery.

More rigorous stratigraphic framework should be built to integrate more data to develop the prospect. 4D seismic survey and AVO analysis can be done pre-drilling in order to reduce the risk of hydrocarbon type and distribution, compliment the amplitude support in the study areas and locate bypassed oils due to stratigraphic controls on the field.

6. Supplementary material

Supplementary data to this article can be found online at https://doi.org/10.2312/yes19.18.

7. References

Asquith, G. and Krygowski, D. (2005), Basic Well Log Analysis. AAPG Methods in Exploration Series 16. TheAmerican Association of Petroleum Geologists, Tulsa, Oklahoma, USA. 224 p.

Bruso, J. M., Getz, S. L., and Wallace, B. (2004), Gulf of Guinea Geology. Oil and Gas Journal, Feb. 16th. 7 p.

Doust, H. and Omatsola, O. (1990), Niger Delta, In: Edwards J. D. and Santoyiossi, P. A. (eds.), Divergent and `Passive Margin Basin. American Association of Petroleum Geologists Memoir 48, pp. 201–238.

Evamy, B.D., Haremboure J., Kamerling, P., Knaap, W.A., Molloy, F.A., and Rowlands, P.H. (1978), Hydrocarbon habitat of tertiary Niger Delta, American Association of Petroleum Geologists Bulletin 62, pp. 1–39. https://doi.org/10.1306/C1EA47ED-16C9-11D7-8645000102C1865D.

Hart, S., Sibley, D. M., and Flemings, P. B. (1996), Reservoir Compartmentalization by Depositional Features in a Pleistocene Shelf Margin (Lowstand) Delta Complex, Eugene Island Block 330 Field, Louisiana Offshore. In: Weimer, P., and Davis, T. L. (eds), AAPG Studies in Geology No. 42 and SEG Geophysical Developments Series No. 5. American Association of Petroleum Geologists/Society of Exploration Geophysicists, Tulsa, Oklahoma, USA, pp. 21–26. https://doi.org/10.1306/St42605C3.

Klett, T.R., Ahlbrandt, T.S, Schmoker, J.W and Dolton, J. L. (1997), Ranking of the world's oil and gas provinces by known petroleum volumes. US Geological Survey Open-file Report 97-463. https://doi.org/10.3133/ofr97463.

Kulke, H. (1995), Regional Petroleum Geology of the World. Part II: Africa, America, Australia and Antarctica. Beiträge zur regionalen Geologie der Erde 22, Borntraeger, Berlin, 729 p.

Merki, P. J. (1972), Structural Geology of the Cenozoic Niger Delta. In: Dessauvagie, T. F. J. and Whiteman, A. J. (eds), African Geology, University of Ibadan Press, Nigeria, pp. 635–646.
Orife, J.M and Avbovbo, A.A (1982), Stratigraphic and unconformity traps in the Niger Delta; the deliberate search for the subtle traps. American Association of Petroleum Geologist Memoir 32, pp. 251–265. https://doi.org/10.1306/M32427C17.
Shell (2002), An Introduction to the Basics of Log Evaluation.
Srivastava, A. Singh, V., Vijayakumar, V., Singh, B., and Gupta, S. (2005), Identification and delineation of subtle stratigraphic prospects by advanced interpretation tools: A case study. The Leading Edge 24, pp. 792–798. http://dx.doi.org/10.1190/1.2032250.
Tuttle, M.L.W., Charpentier, R.R., and Brownfield, M.E. (1990), The Niger Delta petroleum system; Niger Delta Province, Nigeria, Cameroon, and equatorial Guinea, Africa. US Geological Survey Open-file Report 99-50-H. https://doi.org/10.3133/ofr9950H.

Assessing Anthropogenic Impacts in Coastal Areas Through Landuse and Land Cover Changes from 1980 to 2019 Using Remote Sensing and GIS Techniques: A Case Study of Southern Coastal Gujarat, India

Ritika Prasad[1,✉]

[1] University of Lucknow, India
✉ prasad.ritika24@gmail.com

Keywords: land use, land cover, coastal areas, degradation, human impact

1. Introduction

Coastal regions are areas that offer vital ecosystem services to mankind in direct and indirect ways. These areas are valuable environments, which signify a very important resource base for society, economy, and human culture. These significant resources have gathered huge population and development activities around coastal regions that have imposed stresses on the coastal environment, inducing wide-ranging and rapid changes.

Coastal regions accommodate more than 60 % of the world's population in less than 15 % of the earth's land surface (Kubiszewski and Cleveland, 2012). It is projected that by 2025 this number could climb up to 75 % of humanity living on coastal areas and most of the world's coastal ecosystems will possibly be threatened by unsustainable development activities (EEA, 1999). In the current situation, this threat continues and even accelerates because of the lack of planning and management.

Human pressures on coastal regions are varied and consist of the manufacturing sector, the residential development sector, leisure and recreation, the transport sector, agriculture, and fishing (Mimura, 2008). The degree of impact of human actions in coastal areas and communities is different, subject to local conditions. The distinguishing factors that cause pressure on coastal zones are demographic change, socio-economic development, and land use policy. Among these, population growth and economic development are considered the utmost dominant cause of pressure on coastal regions (Clark, 1982, Jaiswal et al., 1999, Chilar, 2000, Yuan et al., 2005, Joshi et al., 2011, Rawat et al., 2013). India is one such example in the world where the population is centralized in coastal areas.

The southern coastal region of Gujarat, India, is an area that faces stresses from various human activities that have been occurring for a long time (Misra and Balaji, 2015). Land alteration is not in accordance with the objective of sustainable development and gives pressure to both biophysical conditions and the community that depends on the coastal resources. As land use is not compatible with the carrying capacity of the land, this causes the degradation of coastal ecosystems and results in adverse impacts such as coastal erosion, increased relative sea-level rise, and marine pollution. Relative sea-level rise is one of the impacts that accelerates pressure and affects coastal destruction. Lack of appropriate management and guidelines aggravates the current scenario of coastal degradation which requires urgent spatial planning on resource utilization in such areas.

To back up the coastal management, access to land cover information is essential (Dahdouh-Guebas, 2002). The land cover turns out to be a core indicator because the processes of human activity development directly impact its changing conditions. Besides, land cover change can be used as an indicator to define the extent of pressure from human activities and development in coastal zones, and what form of management could be undertaken to achieve stable future conditions.

2. Statement of the Problem

Coastal areas are regions that have huge prospects of environmental services and resources related to social, economic, and cultural activities. The concern nowadays is that human activities and physical development in coastal areas haphazardly increase without control. They expand and change the existing coastal ecosystem without considering the suitability and capacity of the coastal land.

Coastal areas of southern Gujarat are subject to development pressure that will have lasting effects for a long time (Chauhan and Nayak, 2005). The pressures are aggravated by sea-level rise that can be seen as a primary factor in coastal degradation. This situation poses a risk to the resilience of both human and environmental coastal systems. One of the impacts can be seen in land cover change conditions in coastal areas. Dealing with the above problem, this study will analyse land cover change in coastal areas and identify changing trends.

Coastal planning processes are conducted with a consensus-building that depends on local knowledge

DOI: 10.2312/yes19.05

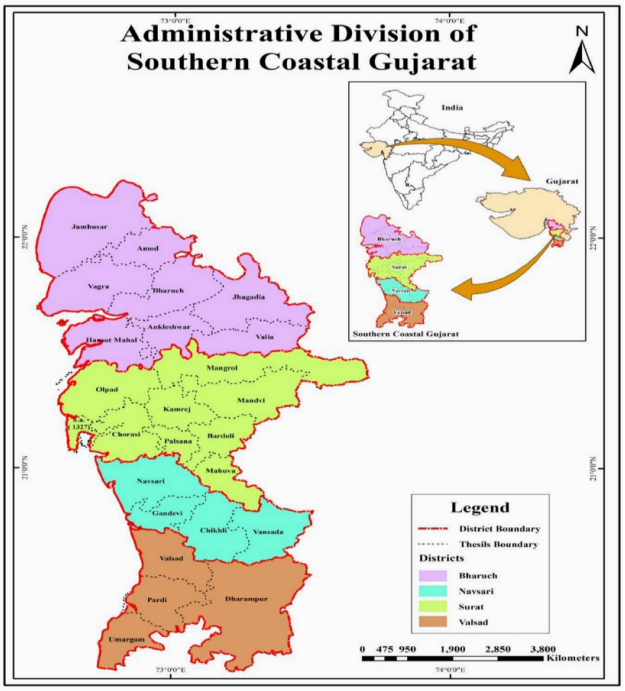

Figure 1: Administrative divisions of Southern Gujarat.

and stakeholder preferences to make informed choices about equitable resource allocation. Coastal planning and management in Gujarat is constrained by a dearth of data about interaction between development activities and coastal environment conditions. Information relating to causes of land use change will allow more cautious preparation and organisation in the area. It will provide us with an understanding of cause and effect relationships between interacting social, economic, and environmental components.

3. Study Area

The coastline of about 200 km in South Gujarat, forming a part of four districts of Gujarat such as Bharuch, Surat, Navsari, and Valsad, has been investigated in the present study (Fig. 1).

The geographical area extends from 20°49' N to 21°41' N in latitudes and 73°01' E to 73°3' E in longitudes. The coastline of the study area is comparatively uniform and broken by a few indentions. Sandy beaches are present along most of the coast of the study area. Mudflats, marsh, and mangrove vegetation are also found along the coast of the study area. The major rivers of the area are Damanganga, Kolak, Par, Purna, Auranga, Ambica and Mindhola, etc which are comparatively smaller and rise within the boundaries of the state from the eastern highlands.

The Bharuch district has a population of 1,550,822 in the southern part of the Gujarat peninsula on the west coast of the state of Gujarat (Census of India, 2011a). The Narmada River flows into the Gulf of Khambat through its lands. The district of Surat with a total population of 6,079,231 covers an area of 7657 km² and is bordered by the districts of Bharuch and Narmada in the North, Navsari and Dangs in the South and the Gulf of Khambat in the West (Census of India, 2011b). The town of Hazira is located in this district, which is an important transhipment port and is popularly known as the "industrial hub" of India due to the presence of major industrial facilities. The district of Navsari covers an area of 2211 km² with a population of 1,329,672 and is bordered by the districts of Surat in the North, and Dangs in the East (Census of India, 2011c). The district of Valsad is surrounded by the district of Navsari in the North, Dang in the East, and Maharashtra in the South. The population of Valsad is 1,705,678 persons for an area of 3034 km². (Census of India, 2011d).

4. Objectives

- To identify the changes in land use and land cover that influence the coastal zone in southern Gujarat from 1980 to 2019.
- To determine the causes which affect the change of land use in the study area.

5. Data Sources and Methodology

The study uses both primary information and secondary information available at various levels. Multitemporal analysis has been done in this study by us-

Data Source: https://earthexplorer.usgs.gov/

S. No.	Sensor	Year	Date of Passing	Resolution
1	Landsat - 3	1980	08.04.1980	30 Meter
2	Landsat - 5	1990	25.03.1990	30 Meter
4	Landsat - 7	2000	23.11.2000	30 Meter
5	Landsat – 5 (Landsat 7 images after 2002 black spot and liner so does not useable)	2010	12.05.2010	30 Meter
5	Landsat – 8	2019	28.05.2019	30 Meter

Software :
1. ArcGIS 10.1
2. ERDAS 2014

Method:
Supervised Classification (ERDAS)

Figure 2: Description of satellite images used in the study.

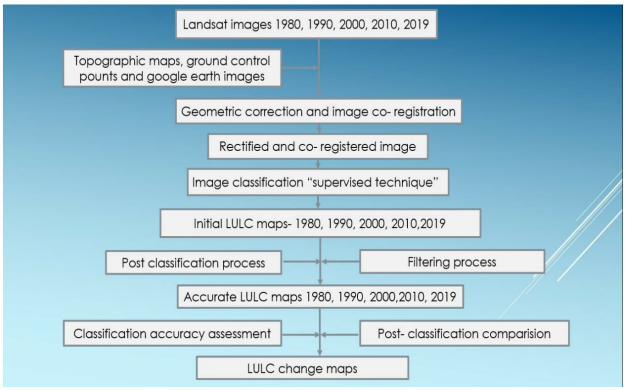

Figure 3: Datasource and methodology,

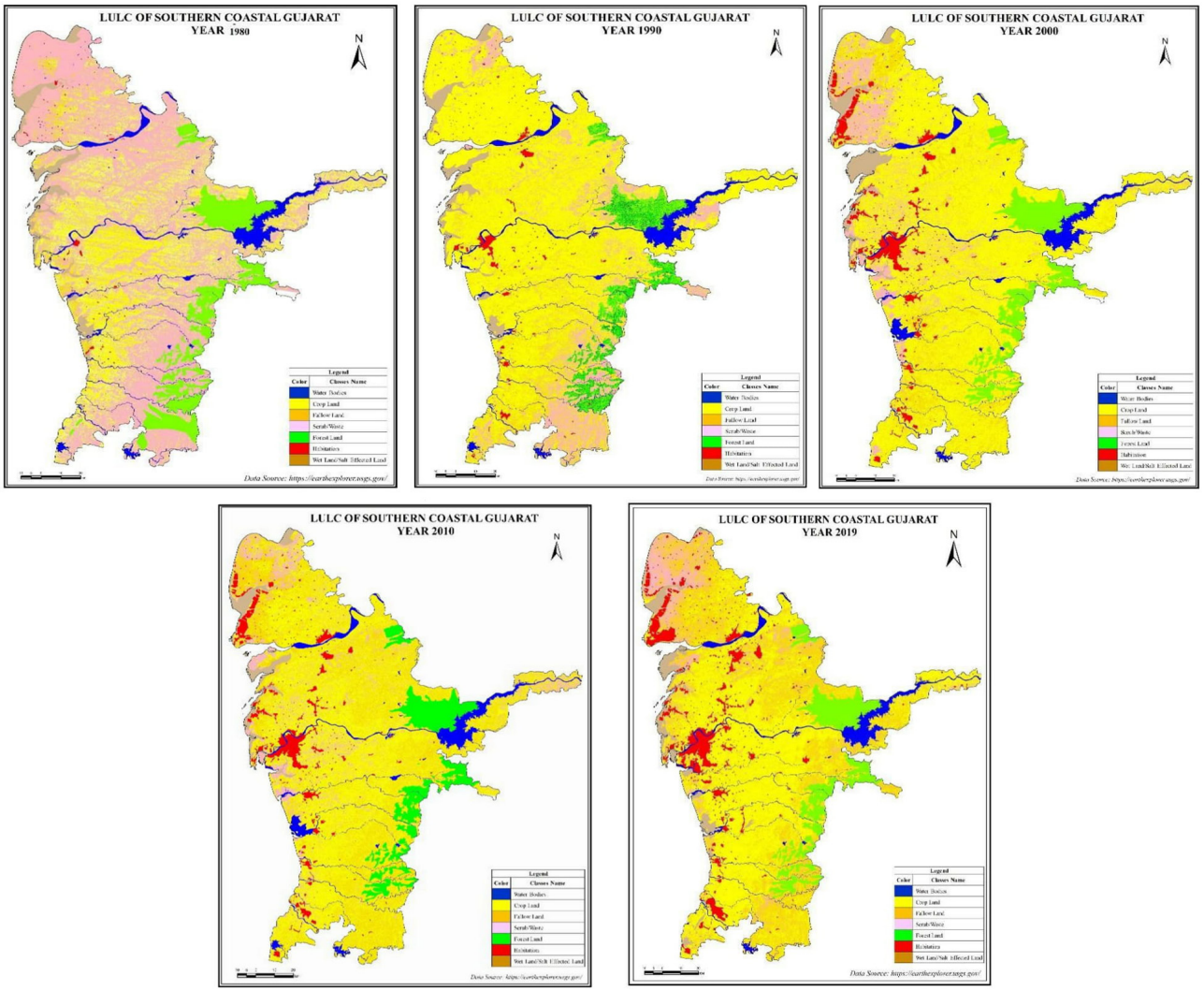

Figure 4: Maps showing land use and land cover from 1980 to 2019.

ing Landsat images from 1980 to 2019 (Fig. 2). To obtain land cover data, each image is classified by using supervised classification. Change detection of land cover in the study area is done in five stages from 1980 to 1990, 1990 to 2000, 2000 to 2001, 2001 to 2010, and 2010 to 2019 (Fig. 3).

6. Results and Discussion

In the study, the images are classified based on the land conditions of the area. According to the classification, the following categories could be identified: forest land, crop land, fallow land, scrub land, habitation and water bodies, and rivers.

Based on the findings, land use changes in 1980, 1990, 2000, 2010, and 2019 (Fig. 4), the fallow land has experienced the most significant increase, followed by urban areas. Agricultural area and wasteland tend to decrease over time. Rivers, wetlands, and forest land remained more stable during the 1980-2019 periods.

The primary factors influencing the coastal areas are mainly human activities which include economic development, population growth, demographic growth, infrastructure development policy, topography, and climate change. In this study, the primary factors are determined by interpreting the interaction between the social-economic and ecological systems in the area and their relevance to the coastal degradation.

As it has already been noted that there has been a significant increase in urban areas, the population is the most important underlying factor because with population growth there is the corresponding need for urban land. The growth of population increases various human activities in the area, including resi-

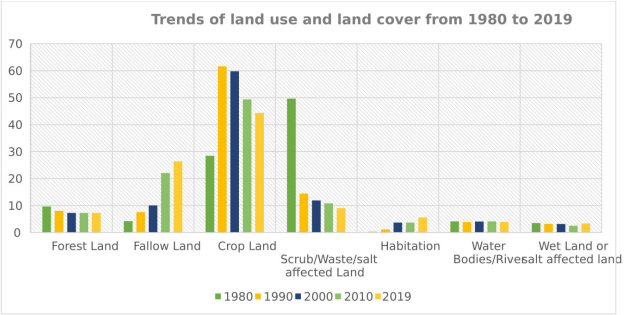

Figure 5: Trends of land use and land cover changes from 1980 to 2019.

dential, industrial, and commercial development, and aquaculture development. With the rising demand for residential, industrial, and commercial growth and the limit of land availability, land use change occurs in this area. The early development process of urban built-up area in this location is influenced by river and coastline patterns, including Narmada River and Tapti River. These patterns relate to the general livelihood of the community that correlates with fisheries and agriculture. Rivers are amongst the major contributors to the pattern of urban built-up area expansion because fisherman communities use the river for transportation from their house to the sea. This results in emerging urban development patterns along the river and coastline.

The increase in fallow land can be attributed to the growing population that has placed a great deal of stress on the topsoil resources of this region. Much of the land used for agriculture is decreasing in the state. The increase in fallow land can be due to land getting affected by salinity in the region.

On the other hand, there is a decline in the crop land which is mainly due to the scarcity of water and declining water quality. Since the study area is also dominated by industrial activities migration of the human population to urban centres is also leading to a decline in agriculture.

Wasteland is also on decline mainly because of expansion in urban activities like an increase in commercial and residential buildings (Fig. 5).

6.1. Impact of land use changes

In southern Gujarat, the development of activities along the coastal area does not consider the physical condition of the existing land. Consequently, this area is incapable to accommodate all of these activities and causes various impacts. Impacts describe the effects of changes in coastal states on measures of ecosystem function.

In southern Gujarat the impacts of these uncontrolled activities could be seen in recent years, including relative sea-level rise. In addition, it has also been noted through the primary survey that the intensity of floods over the years has risen especially in the monsoon season. The degradation of coastal zones is the main impact of land use conversion that is caused by the pressures in this area. This phenomenon is mainly caused by land utilization that is incompatible with the capacity and suitability of land. Along with the degradation of the coastal zone, other impacts emerge in the study area, including coastal flooding and decreasing productivity in many sectors such as agriculture and aquaculture fisheries. Over the next few years, it could lead to the socio-economic impoverishment of the coastal community.

7. Conclusions

This study is conducted to examine the land use change in the coastal zone of southern Gujarat and the primary factors that underlie these changes can be taken into consideration to assess the future land use configuration in the coastal zone. Information about land use change is particularly important to understand the behaviour of land uses related to human activities in the study area. Moreover, information on future land use change and distribution obtained from this research can be used in supporting the arrangement of coastal zone management plan, charting future activities, and guiding the steps required to achieve coastal planning aims. Appropriate coastal land use planning to attain a sustainable future is important in the coastal zone because the region still encounters several problems, including the implementation of regulations and the arrangement process of a coastal management plan.

Land use/land cover (LULC) maps demonstrate that the study area covers a fragile ecosystem including mudflats, and salt marshes, and hence future environmental degradation along this coast could disrupt the natural functioning of the environment. Therefore, improved remote sensing tools (high-resolution data) and GIS accompanied by field surveys and numerical modelling can enable a better understanding of these regions to develop a sound strategy for the conservation and restorations of these natural systems. Finally, the present research pertaining to the mapping of LULC will enable decision-makers to identify the susceptible zones and find better solutions to the existing coast problems in these locations.

8. REFERENCES:

Census of India 2011a, Gujarat: District Census Handbook Bharuch: Village and Town Directory. Series 25, Part-XII-A. Directorate of Census Operations Gujarat. 372 pp. [Online] https://censusindia.gov.in/2011census/dchb/DCHB_A/24/2421_PART_A_DCHB_BHARUCH.pdf [Accessed 22.08.2020].

Census of India 2011b, Gujarat: District Census Handbook Surat: Village and Town Directory. Series 25, Part-XII-A. Directorate of Census Operations Gujarat. 372 pp. [Online] https://censusindia.gov.in/2011census/dchb/DCHB_A/24/2425_PART_A_DCHB_SURAT.pdf [Accessed 22.08.2020].

Census of India 2011c, Gujarat: District Census Handbook Navsari: Village and Town Directory. Series 25, Part-XII-A. Directorate of Census Operations Gujarat. 372 pp. [Online] https://censusindia.gov.in/2011census/dchb/DCHB_A/24/2423_PART_A_DCHB_NAVSARI.pdf [Accessed 22.08.2020].

Census of India 2011d, Gujarat: District Census Handbook Valsad: Village and Town Directory. Series 25, Part-XII-A. Directorate of Census Operations Gujarat. 372 pp. [Online] https://censusindia.gov.in/2011census/dchb/DCHB_A/24/2424_PART_A_DCHB_VALSAD.pdf [Accessed 22.08.2020].

Chauhan, H.B., Nayak, S. 2005. Land use/land cover changes

near HAzira Region, Gujarat using remote sensing satellite data. Journal of the Indian Society of Remote Sensing 33, 413–420. https://doi.org/10.1007/BF02990012

Chilar, J. 2000. Land cover mapping of large areas from satellites: status and research priorities. International Journal of Remote Sensing. 21(67). pp. 1093–1114. https://doi.org/10.1080/014311600210092

Clark, D. 1982. Urban Geography: an Introductory Guide, Croom Helm, London. 231 pp.

Dahdouh-Guebas, F. 2002. The use of remote sensing and GIS in the sustainable management of tropical coastal ecosystems. Environment, Development and Sustainability. 4. pp. 93–112. https://doi.org/10.1023/A:1020887204285

Kristensen, P., Anderson, Ö., Denisov, N., 1999. A checklist for state of environment reporting. Technical report No. 15. European Evironmental Agency, Copenhagen. 24 pp. [Online] https://www.eea.europa.eu/publications/TEC15/ [Accessed 22.08.2020].

Kubiszewski, I., Cleveland, C. (2012). United Nations Conference on Environment and Development (UNCED), Rio de Janeiro, Brazil. [Online] http://editors.eol.org/eoearth/wiki/United_Nations_Conference_on_Environment_and_Development_(UNCED),_Rio_de_Janeiro,_Brazil [Accessed 22.08.2020].

Jaiswal, R. K., Saxena,R., Mukherjee, S. 1999. Application of remote sensing technology for land use/land cover change analysis Journal of the Indian Society of Remote Sensing. 27(2). pp. 123–128. https://doi.org/10.1007/BF02990808

Joshi, R.R., Warthe, M., Dwivedi, S., Vijay, R., Chakrabarty, T. 2011. Monitoring changes in land use land cover of Yamuna riverbed in Delhi: a multi temporal analysis. International Journal of Remote Sensing. 32(24). pp. 9547–9558. https://doi.org/10.1080/01431161.2011.565377

Mimura, N. 2008. Conclusions: The Rapidly Changing Environment of the Asia and Pacific Region and its Implications for Sustainability of the Coastal Zones. In: Mimura, N. (ed.), Asia-Pacific Coasts and Their Management. States of Environment. Springer, Amsterdam. pp. 345–358. https://doi.org/10.1007/978-1-4020-3625-5_6

Misra A, Balaji R. 2015. Decadal changes in the land use/land cover and shoreline along the coastal districts of southern Gujarat. India. Environmental Monitoring and Assessment. 187(7). 461. https://doi.org/10.1007/s10661-015-4684-2

Rawat, J.S., Biswas, V., Kumar, M. 2013. Changes in land use/cover using geospatial techniques: a case study of Ramnagar town area, district Nainital, Uttarakhand, India. Egyptian Journal of Remote Sensing and Space Sciences. 16. pp. 111–117. https://doi.org/10.1016/j.ejrs.2013.04.002

Yuan, F., Sawaya, K. E., Loeffelholz, B. C., Bauer, M. E. 2005. Land cover classification and change analysis of the twin cities (Minnesota) metropolitan area by multi temporal Landsat remote sensing. Remote Sensing of Environment. 98. pp. 317–328. https://doi.org/10.1016/j.rse.2005.08.006

Geo-Spatial Mapping of Sustainable Geo-Resource Management: A Case Study of Ranthambore Tiger Reserve, India

Bhanwar Vishvendra Raj Singh[1,✉]

[1] Department of Geography, Faculty of Earth Sciences, Mohanlal Sukhadia University, Udaipur, India
✉ bhanwarsa28@gmail.com

Keywords: Geo-resource Management, Tiger conservation, Climate change, Geo spatial mapping

1. Introduction

Natural georesources are the foundation of the human lifecycle. We are using these varied natural resources in different ways to satisfy our needs and deeds. However, natural resources are not substantially available for human consumption and both non-renewable and renewable resources are limited. Therefore people should be economical with their natural resources in a sustainable manner.

In many parts of the world, we are using natural resources in an unsustainable manner and creating a huge gap between demand and supply and then we talk about security, after we discuss on security, which is an unsuitable way. The degradation and destruction of natural resources are mainly due to overuse or a non-adapted use of these resources (Förch and Schütt 2005).

The connection between man and the environment has been established in early history itself. Human beings live in the realm of nature and interact with it continuously. The effect of nature is in the form of the air we breathe, the water we drink, the food we eat, and the flow of energy and information. Any alteration in the ecosystem cannot only result in devastating effects but can also pose a threat to the human species.

Meanwhile “geo-resources” denotes all geological capitals that are used by humankind, such as groundwater, mineral resources, energy production, underground space for construction and storage, and the surface geology and landscape. In this space, humankind continuously encroaches resources from top to bottom, which affects the whole environment ecosystem, because they are directly and indirectly connected.

Sustainable environment conservation can lead to a better development of ecosystem services as well as community development (Armiatage 2005). The ecosystem services are defiantly mitigated for climate change such as conserving the habitat, water quality, quality of life, global carbon cycle, economic growth, demographics, agriculture, and forest products, regional and planning policies through tiger conservation practices.

The Ranthambhore Tiger Reserve has more than 60 tigers and about 0.5 million people directly or indirectly interdependent on tiger ecosystem services. Tiger conservation practices influence both environmental quality and the quality of life of native people. Alterations in habitat, water and air quality would contribute to the environmental, social and economic aspects of local communities.

In biodiversity, tigers play pivotal roles in regulating and maintaining ecological equilibriums. In India, tiger species are living in high mountains, semiarid areas, mangrove swamps, and grasslands; these are the main habitats for a thriving population of tigers. In the present context, global climate change has an indirect consequence of tiger species and their habitat.

It is seen that a healthy number of tiger species means automatic conservation of biodiversity. There is a growing need to take prominent initiatives towards conservation of tiger species and other wild species as there are every day man-tiger conflicts, unnatural death of tigers, water scarcity in protected areas and other wildlife issues. The sustainable ecosystem services are provided a valuable framework for analyzing and acting on the linkages between local to global communities and their man-environment relationships, so that it will be more fruitful and sustainable for human well-being and the future Earth.

Therefore, my focus is on community development through biodiversity conservation and a climate change mitigation approach, possible through a capacity building program, maximum public participation, development of an indigenous community, as well as restoration of the corridor, corridor planning etc. (Leach et al. 1999). Therefore my concept is based on the community development model of geo-resource management (Kellert et al. 2000).

Hence, it will prepare one consensus and vision for sustainable development which is more holistic, inclusive and ecological in its approach (Grimble and Wellard 1997). The main outcomes of ecosystem services provide a valuable framework for analyzing and acting on the linkages between local to global scales and their man-environment relationships so that it is more fruitful for human well-being and the future Earth.

Proceedings of the 5th International YES Congress
DOI: 10.2312/yes19.03

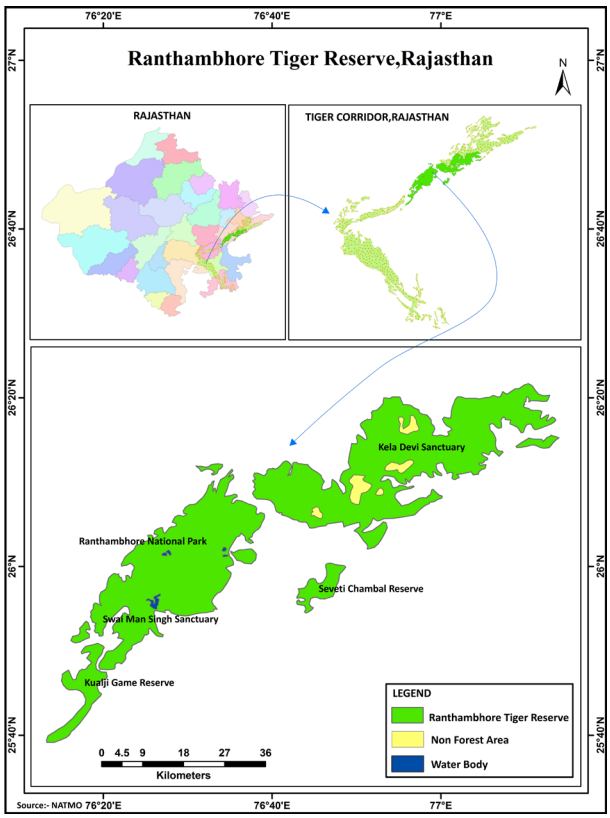

Figure 1: Location Map of Ranthambhore Tiger Reserve

2. Study Area

In India, the Tiger corridor of Ranthambhore is located amid latitudes 25°52'071" N to 26 33'713" N to longitudes 75 85'84.0" E to 77 02'48.0" E at the intersection of the Aravalis and Vindhyan mountains (Fig. 1). The corridor ensures a tiger habitat in an area of 6741.73 km^2 and it is home to over 60 tigers. Especially the core area of the corridor is well known in Ranthambhore, of which the habitat is 1113.36 km^2 and the buffer area is 297.92 km^2 (Fig. 1). It is a total geographical area of 1411.28 km^2. The Ranthambore is a hotspot of tiger population and marks the transition zone between the real deserts and seasonally wet peninsular India. It is connecting from Keoladeo, Van Vihar, Ranthambhore, Sawai Mansingh, Ramgarh, Jawahar Sagar, and Dara sanctuaries. As per the biogeography classification (Rodgers & Panwar, 1988), it falls in 4 B (Semiarid zone and Gujarat-Rajwara biotic province).

3. Research Methodology

The research methodology is summarized in Fig. 2.

4. Results and Discussion

The geo-resources of the Ranthambhore Tiger Reserve provide an abundance of natural and cultural services. Land, water, soil, plants and animals, with particular natural resources affect the quality of life for both present and future generations of Ranthambhore. Geo-resource management deals with the many ways in which people and natural landscapes are connected (Holling and Meffe 1996). It brings together land-use planning, water management, biodiversity conservation, and the future sustainability of geo-industries. Geo-resource management issues are complex as they involve the geological cycle, ecological cycles, hydrological cycles, climate, human beings, animals, plants and biogeography etc. In this paper, numerous approaches are included such as Top-down, Bottom-Up, Adaptive management and Precautionary approach. Finally, all approaches are integrated within a sustainable manner framework.

Ranthambhore tiger reserve consists of two parts, viz., 'a core or critical tiger habitat' and 'a buffer or peripheral area'. Section 38V 4(i) of the Wildlife (Protection) Act, 1972 (hereinafter referred to as WPA, 1972) explains Core or Critical Tiger Habitats (CTH), identified based on scientific and objective criteria (Fig. 3), as "areas of National Parks and Sanctuaries to be kept inviolate for tiger conservation, without affecting the rights of the Scheduled Tribes and Other Traditional Forest Dwellers". It is notified as such by the State Government, in consultation with an Expert Committee constituted for the purpose (Fig. 3).

Section 38V 4(ii) of the WPA, 1972 explains 'buffer' or 'peripheral area' as "consisting of the area peripheral to the critical tiger habitat or core area, where a lesser degree of habitat protection is required to ensure the integrity of the critical tiger habitat, providing supplementary habitat for dispersing tigers, besides offering scope for the coexistence of human activity (Prain 2006)."

The map of relief and slope of Ranthambhore is showing mostly rugged, hilly and rough land topography area. The formation of the ground is intimately related to the Great Boundary Fault. The hills to the NW of this fault are typical for Gwalior and lower Vindhyans and are considered by ridges on one side and a gentle slope on the other side (Fig. 4).

Gwalior and the lower Vidhyan tract are highly undulant except for a few small plateaus like Salwata ki Dang, Rann ki Dang and Mandook, and some small valleys like Kachida, Anatpura, Berda, Lakeda and Malik Talab. The climatic map shows semi-arid climatic conditions and is characterized by a sub-tropical dry climate with distinct cold from November to February, hot climate from March to June, and rainy season from July to September. October is a conversion period. The highest temperature (around 47 °C) is recorded from May to June and the lowest (around 2 °C) in December to January. The diurnal variation of

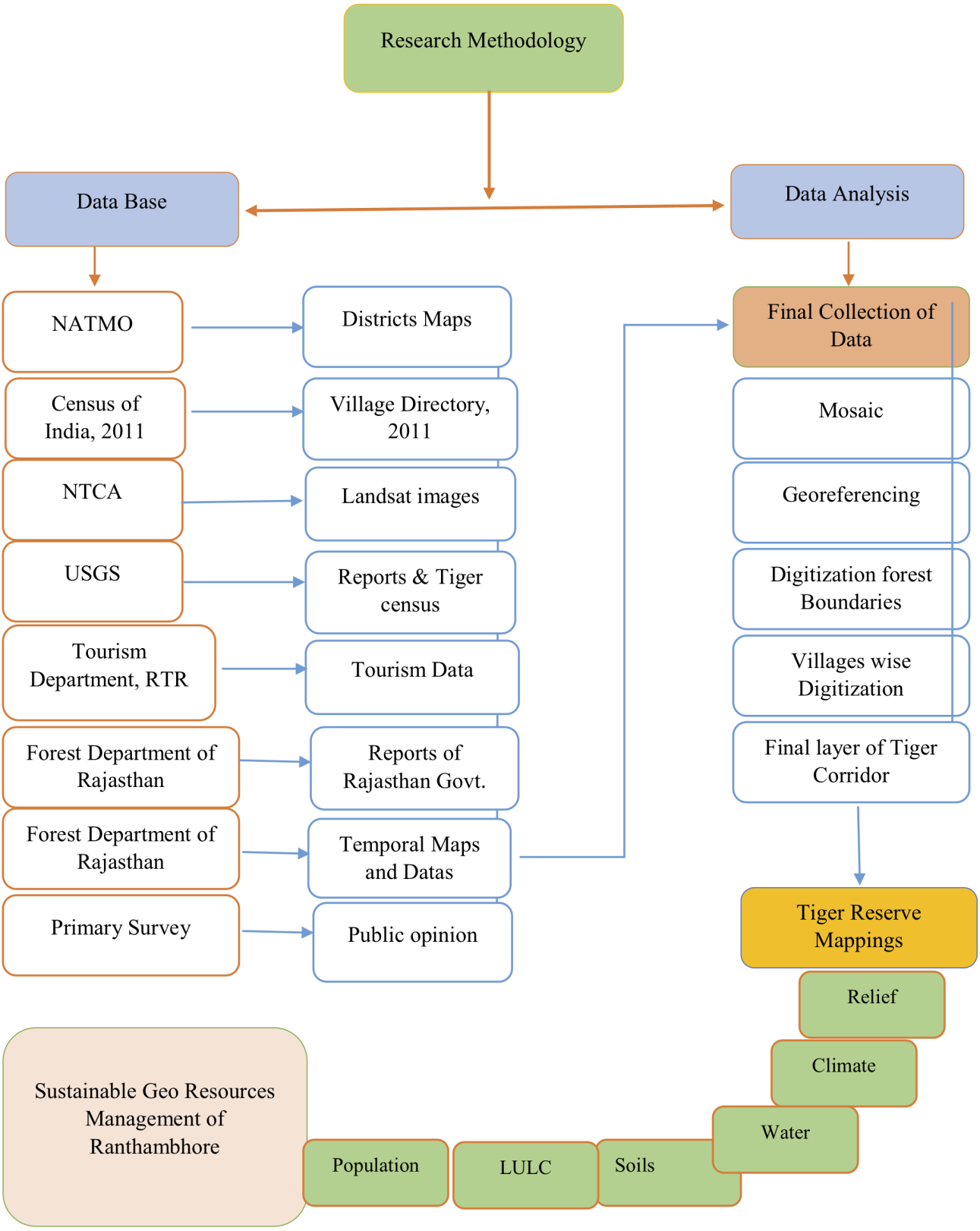

Figure 2: Research Methodology Chart (Database and Data Analysis)

temperature is high. Relative humidity on an average is 30 to 34 %. Strong wind in summer is called “Loo” (Fig. 4).

In Ranthambhore, geomorphologic characteristics have a unique pattern. In this area, there is much topography such as rocky, forest, ravine, rivers, reservoirs, and sandy areas. These landforms are a composite of numerous rocks and minerals. Ranthambhore Tiger Reserve terrain is mostly formed by Pre-Cambrian metamorphic, igneous, and sedimentary rocks belonging to pre-Aravali Vindhyas. Pre-Aravali rocks units, quartzites, micashocts geneuses, and migmatites cover the north-eastern part of the tiger reserve between Lalsot and Karauli. The rocks of the Vindhyas super group are characterized by the Kaimur, Rewa and Bhander group, and consist

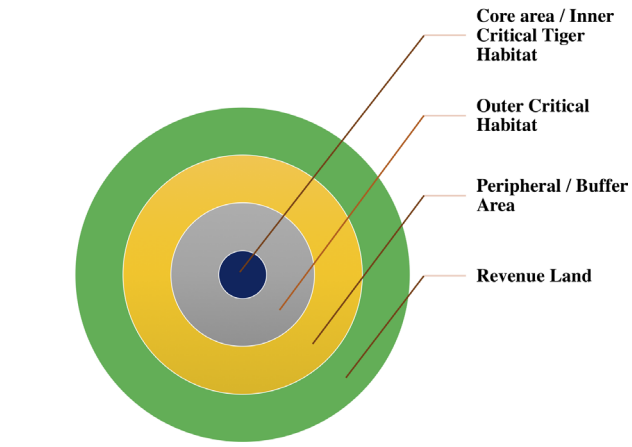

Figure 3: Administrative Division of Ranthambhore Tiger Reserve

mainly of various types of sandstones, and limestones. The geologic structure of the Ranthambhore Tiger Reserve area has a strong influence on the soil types, which in turn also determines the vegetation type. In these particular areas where quartzite forms the uppermost strata, the soil is impoverished and unhealthy for agricultural land. These areas have a very thin layer of coarse-grained soil in the slate and shale areas of Gwalior areas and the soils are fine clayey and shallow. Ranthambhore soils have very little fertility due to numerous physical and man-made

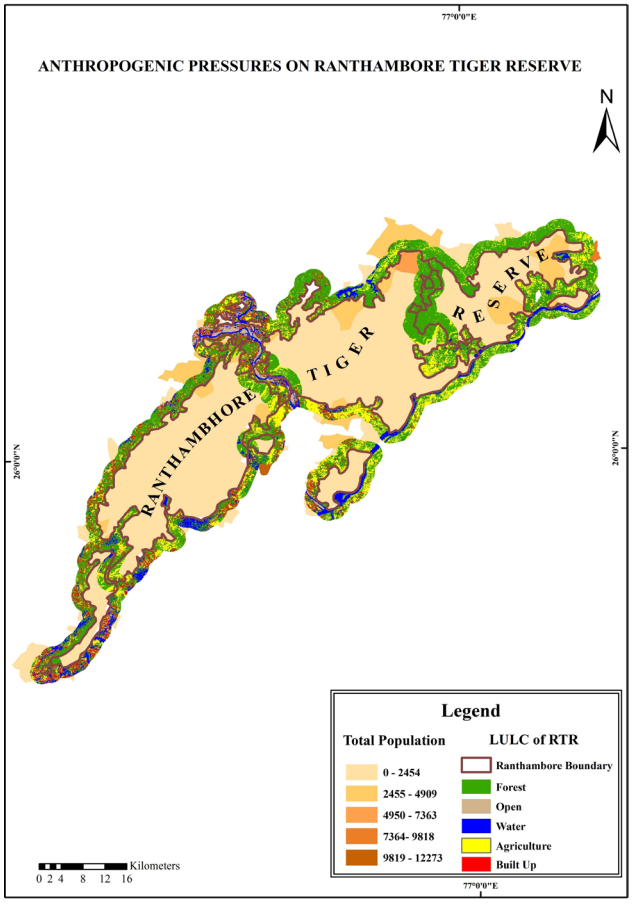

Figure 4: Anthropogenic Pressures on Ranthambore Tiger Reserve.

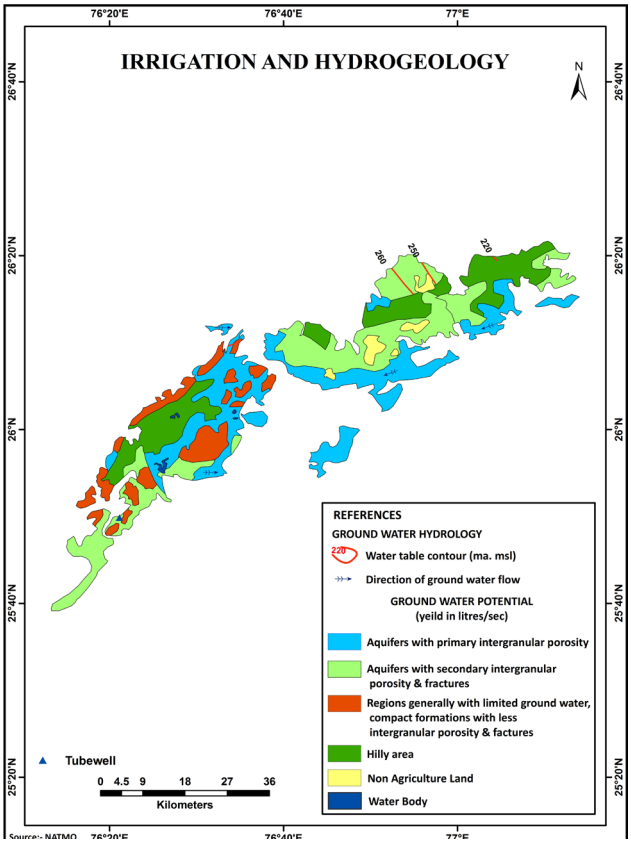

Figure 5: Map of Irrigations & Hydrology of Ranthambhore Tiger Reserve.

causes.

Ranthambhore area has good water availability due to the mountain region and unique topography as well as a forest ecosystem. But at some locations governments and forest staff created artificial pond structures through water conservation methods, which are very fruitful for wild animals, plants and groundwater ecosystems (Fig. 5).

The Ranthambhore area has natural assets as well as cultural assets that are conserved through sustainability. It has a UNESCO cultural site, archaeological sites, Tiger Safari, Rural Tourism and other recreational sites. They are all sites attractive for tourism, which contributed much in comparison to other services in Ranthambhore areas (Fig. 6). However, geo-resources are used too much and encroachment by human intervention is unhealthy for the ecosystem. Numerous challenges of the Ranthambhore area, with a lot of people surrounding the tiger by safari and forest cutting. Grass cutting is not allowed in the areas reserved for “No Go Zone Area” or Eco-Sensitive Zone. Therefore local people cannot build own houses and development activities in such zones, a limitation of development activities that may harm quality of life. Other areas are reserved to prevent forest wildlife and creating a start-up for geo-resources management (Fig. 7).

IMAGES OF CULTURAL RESOURCES OF RTR

UNESCO Cultural site

ASI Historical Site

Clean Tiger School

Wildlife painting at SWM Railway Station

Figure 6: Images of Cultural Resource, Ranthambhore Tiger Reserve.

5. Conclusions

Conservation of the tiger habitat is very important for the sustainable development of the Ranthambhore areas. The area is a reserve for tiger breeding and flourishing as well as for other wild animals. But nowadays, we are devoting millions of dollars for the tiger conservation program because the tiger is an umbrella species. Its conservation automatically ensures the conversation of flora and fauna and the entire ecosystem. The strength of the Ranthambhore Tiger Reserve is in its iconic natural capital, biodiversity and attractive beauty, therefore the region can

CHALLENGES OF RTR

Tourism Pressure

Old Ocupation

Movement of Local people

Condition of House in Core areas.

Figure 7: Challenges and Issues of Ranthambhore Tiger Reserve)

provide a wide range of ecosystem services in terms of supporting, provisioning, regulating and cultural services (Soni 1999).

Cultural services are strongest among all of them. At present, the growing demand for these services has put an immense burden on the ecosystem of Ranthambhore, as well as other tiger landscapes that are significantly undervalued in national and global agendas. As a result, degradation, fragmentation, human-wildlife conflicts and loss of natural habitats, depletion of prey animals, and poaching to supply a large illegal global trade in their body parts have pushed wild tigers and their landscapes to the brink of extinction (Karanth et al. 2004). These threats are alarming for biodiversity and human wellbeing.

Therefore, we should work on sustainable development of tiger landscapes, because the ecosystem services defiantly mitigate for climate change such as conservation of habitat, water quality, quality of life, global carbon cycle, economic growth, demographics, agriculture, forest products, regional and planning policies through sustainable practices.

Eventually, “saving tigers is our test, if we pass, we get to keep the planet” (Marjorie Stoneman Douglas). Tiger conservation is contributing to the increase of carbon storage and sequestration (Velmourougane et al. 2014), poverty alleviation, watershed protection, natural hazard regulation, sustaining food security and agriculture services of Ranthambhore areas. That is possible through maximum public participation, to the community development program, and the development of a holistic, inclusive, and sustainable method, which is sustainable for all stakeholders.

6. References

Armitage, D., 2005. Adaptive capacity and community-based natural resource management. Environmental Management 35(6), 703–715. https://doi.org/10.1007/s00267-004-0076-z.

Förch, G. and Schütt, B., 2005. Watershed management–an introduction. In Förch, G. and Thiemann, S. (Eds.). Lake Abaya Research Symposium 2004 Proceedings: Catchment and Lake Research. Universität Siegen, FWU Water Resources Publications 4. pp. 119–133. [online] Available at: https://www.uni-siegen.de/zew/publikationen/fwu_water_resources/volume0405/f%C3%B6rch.pdf [Accessed 29 September 2020]

Kellert, S.R., Mehta, J.N., Ebbin, S.A., and Lichtenfeld, L.L., 2000. Community natural resource management: promise, rhetoric, and reality. Society & Natural Resources 13(8), 705–715. https://doi.org/10.1080/089419200750035575.

Karanth, U.K., Nichols, J.D., Kumar, N.S., Link, W.A., and Hines, J.E.. 2004. Tigers and their prey: Predicting carnivore densities from prey abundance. Proceedings of Natural American Society 101(14), 4854–4858. https://doi.org/10.1073/pnas.0306210101.

Grimble, R., and Wellard, K., 1997. Stakeholder methodologies in natural resource management: a review of principles, contexts, experiences and opportunities. Agricultural systems 55(2), 173–193. https://doi.org/10.1016/S0308-521X(97)00006-1.

Holling, C.S., and Meffe, G.K., 1996. Command and control and the pathology of natural resource management. Conservation biology 10(2), 328–337. https://doi.org/10.1046/j.1523-1739.1996.10020328.x.

Leach, M., Mearns, R., and Scoones, I., 1999. Environmental entitlements: dynamics and institutions in community-based natural resource management. World development 27(2), 225–247. https://doi.org/10.1057/9781137271631_16.

Prain, G. 2006 Urban harvest: A CGIAR Global Program on Urban and Peri-urban Agriculture. Extension Bulletin 575, Food and Fertilizer Technology Centre, Taiwan.

Rodgers, W.A., and Panwar, H.S., 1988. Planning a wildlife protected area network in India. Field document 9. FAO, Wildlife Institute of India, Dehradun, 2 vol.

Soni, R.G. 1999. Tiger returns to Rajasthan. Report on tiger conservation programme three years and beyond. Worldwide Fund for Nature India, New Delhi.

Simmons, A.M., Buxbaum, R.C. and Mirin, M.P., 1993. Perception of complex sounds by the green treefrog, Hyla cinerea: envelope and fine-structure cues. Journal of Comparative Physiology A 173(3), 321–327. https://doi.org/10.1007/BF00212696.

Velmourougane, K., Venugopalan, M.V., Bhattacharyya, T., Sarkar, D., Pal, D.K., Sahu, A., Chandran, P., Ray, S.K., Mandal, C., Nair, K.M., and Prasad, J., 2014. Microbial Biomass Carbon Status in Agro- Ecological Sub Regions of Black Soils in India. Proceedings of the National Academy of Sciences, India Section B: Biological Sciences 84(3), 519–529. https://doi.org/10.1007/s40011-013-0238-y.

Coastal Management Strategies: An Overview of Integrated Coastal Zone Management and Namibian Case Study Outlining Challenges and Successes of Its Implementation

Denzel Joseph Van Wyk[1,✉]

[1] University of Namibia, Namibia
✉ denzeljosephvanwyk@gmail.com

Keywords: Integrated Coastal Zone Management, re-evaluation, monitoring, indicators, challenges

1. Introduction

Coastal areas offer opportunities for economic and social development, which is evident in the increasing concentration of the human population near coasts (Crossland et al., 2006). Part of the reason for this development is the general coastal richness and diversity in resources. Often the increasing concentration of the human population and the utilization of resources come with impacts on these areas. The impacts are mostly negative, with environmental issues like pollution and physical or biological alterations by economic activities or mere settlement development.

The term Coastal Zone in this context refers to a zone or area in which significant physical, chemical, and biological exchanges take place between land and a large body of water (Lundgren, 1999). Lundgren (1999) further defines it for open ocean coasts as the belt of land and water that extends from the edge of the continental shelf inland across coastal plains or sea cliff regions. The land forming part of this belt includes areas up to 75 km from the coastline. Thus, it is not only coastal towns or settlements with an impact on coastal systems, but also those situated within this ranged distance from the coastline.

Due to coastal systems being open systems, energy and matter can enter and leave them. Coastal systems function with the principle of dynamic equilibrium in which it would respond to a disturbance by achieving a new equilibrium. Disturbances to the coastal systems can be both natural and anthropogenic. Typically, the anthropogenic disturbances accompanied by large, sudden, or continuous increasing impact put these systems under stress, and make returning to its equilibrium state difficult. The longer these systems are away from equilibrium, the more severe and prolonged consequences might arise, as it struggles to reach a newer or earlier equilibrium. The consequences are mostly only realised and felt when life in coastal ecosystems is affected. Thus, the aim of this extended abstract is to provide a brief general overview of Coastal Management Strategies and to highlight the Namibia Coast Conservation and Management Project (NACOMA) as a case study to give an example of partly successful and partly unsuccessful Coastal Management.

2. Overview of Integrated Coastal Zone Management

In order to avoid severe and prolonged consequences at an early stage, Coastal Zone Management was introduced and given formal status in the United States in 1972. It was seen as an effort to incorporate scientific understanding and economic analyses to ensure that biological resources were maintained and that each use of the coastal zone was guided to minimize adverse effects (Lundgren, 1999).

The Coastal zone faces many diverse problems which, in turn, have brought many different organisations with an interest in its management. These may be local, regional, national, and international administrative authorities, such as councils and governments, environmental and conservation organisations, and other groups that may represent residents, tourists and industrial interests (Haslett, 2000).

However, it is only when all these organisations can work together that coastal zone management is believed to be most effective. And it was for this reason that the concept of Integrated Coastal Zone Management (ICZM) was born during the Earth Summit of Rio de Janeiro in 1992. Integrated Coastal Zone Management is a dynamic process in which a coordinated strategy is developed and implemented for the allocation of environmental, socio-cultural and institutional resources to achieve the conservation and sustainable, multi-purpose use of the coastal zone. The idea behind it is to maximise the use of resources without having to damage or destroy the area and ecosystems that make those resources available through development planning (Burbridge, 2012).

Kay and Alder (1999) outlined a continuum of coastal management integration consisting of five stages. These are:

1. Fragmented stage, which refers to many little organizations operating independently with little communication.

DOI: 10.2312/yes19.06

2. Communication stage, where there is regular but occasional communication between different organizations.
3. Coordination stage, which involves the different organizations in close communication and synchronising their work.
4. Harmonisation stage, where the different groups synchronise their work along universally-agreed policy guidelines.
5. And lastly, the Integration stage, which refers to complete synchronisation and formal mechanisms along which work must be carried out, and therefore, independence of individual organizations are lost and fully integrated coastal management is achieved.

As noted by Haslett (2000), the movement towards the integration stage along this continuum shows that there is usually a high degree of legislation that allocates management responsibility to one particular organization. This organization may often be referred to as the coastal manager.

In instances where individual organizations have not been lost and the final stages are at arm's length, a lead agency is often chosen. Its aim would then be to organise dialogues between different sectors or organisations to show how a more integrated approach might reduce negative economic effects and allow them to meet their mandate in a more effective manner (Burbridge, 2012).

Due to Integrated Coastal Zone Management being a complex and broad form of management it operates at many different levels and scales. Two of its distinctive levels are namely the Intimate level and Policy level. The Intimate level refers to a lower level at which carefully managed activities scheduled at different periods of time at the same place can be carried out for the benefit of different economic and social groups without degradation. The later, Policy level, refers to a higher level at which a set of principles or guidelines are established for strengthened development planning (Burbridge, 2012). The different scales at which ICZM can be implemented are local, regional, national, and international scales. It is often the level of sense of responsibility, availability of financial resources, and understanding of the strategic value of these zones that determine the level and scale at which ICZM is employed.

Reaching ICZM from a fragmented stage of organizations at the beginning of the outlined continuum is a continuous process not easily achieved over a small period of 5 to 10 years (Burbridge, 2012). And as a result, monitoring and evaluation are essential process steps to determine the progress made in both reaching complete integration of coastal management organizations and their impact. This is only possible if measurable indicators and quantitative targets have been defined for this purpose.

In Table 1, I summarize some of the most important indicators for reducing the rapidity of anthropogenic disturbances on coastal environments (Dronkers, 2019). Table 1 shows that ICZM goals may possibly require coordinated efforts from individual organizations contributing towards the management of coastal zones. To ensure that beaches are clean and that coastal waters are unpolluted, coordinated management efforts from local authorities, operating oil corporations and scientific studies from scientists are required. Moreover, to ensure natural resources are wisely used, fishing companies and water distributing corporations would also be required to engage in the management of coastal zones.

3. Namibia Coast Conservation and Management Project

In an effort to manage its coastal resources offered by its 1572 km long coastal zone, the Ministry of Environment and Tourism in Namibia launched the Namibia Coast Conservation and Management Project (NACOMA) in 2006. It aimed to facilitate and coordinate the participation and inputs from various stakeholders. These stakeholders included the line ministries, regional councils, local authorities, civil society, sectoral stakeholders, and support organisations. The project relied heavily on the co-operation of partner projects and utilized the services and advice of local and international experts and scientists.

As part of its strategy, NACOMA held regular consultative forums to discuss topics of interest and the measuring and re-evaluation of indicators. The forums included representatives from regional councils, the Ministry of Fisheries and Marine Resources, law enforcement officials, and others. With an objective to have an Integrated Coastal Zone Management Bill enacted, the project operated in a number of steps: a) creation of a road map of the coast, b) facilitation process, c) compilation of the green and white papers, d) adoption of an Integrated Coastal Zone Management Policy which was gazetted in 2010, e) creation of an ICZM draft bill.

Although the project reached the final step of drafting an ICZM bill, its enactment was unsuccessful due to several challenges faced. The challenges faced by the project were;

- Slow process of enabling legislation, at the beginning for essential institutional and process focus of the project,

Goals	Indicators	Measurements
To control further development of the coast as appropriate.	1. Demand for property on the coast	1.1 Size, density and proportion of the population living on the coast
		1.2 Value of residential property
	2. Area of built-up land	2.1 Percentage of built-up land by distance from coastline
	3. Rate of development of previously undeveloped land	3.1 Area converted from non-developed to developed land uses
	4. Demand for road travel on the coast	4.1 Volume of traffic on coastal motorways and major roads
	5. Pressure for coastal and marine recreation	5.1 Number of berths and moorings for recreational boating
	6. Land taken up by intensive agriculture	6.1 Portion of agricultural land formed intensively
To ensure that beaches are clean and that coastal waters are unpolluted.	7. Quality of bathing water	7.1 Percentage of bathing waters compliant with the guide value of Bathing Water Directives
	8. Amount of coastal, estuarine and marine litter	8.1 Volume of litter collected per given length of shoreline
	9. Concentration of nutrients in coastal waters	9.1 Riverine and direct inputs of nitrogen and phosphorous in inshore waters
	10. Amount of oil pollution	10.1 Volume of accidental oil spills
		10.2 Number of observed oil slicks from aerial surveillance
To use natural resources wisely	11. Fish stocks and fish landings	11.1 State of main fish stocks by species and sea area
		11.2 Recruitment and spawning stock biomass by species
		11.3 Landings and fish mortality by species
		11.4 Value of landings by port and species
	12. Water Consumption	12.1 Number of days of reduced supply

Table 1: Possible targets or goals and measurable indicators for ICZM (compilated from Dronkers, 2019).

- Limited number of staff availed by the Ministry of Environment and Tourism,
- Limited financial resources for monitoring and assessment of the state of the coast and for restoration measures,
- Short term interests from local authorities,
- Short political cycles that caused changes in ministers (Kandjii, 2019).

Despite the challenges encountered, the project had a tremendous positive impact on the coastal zone in terms of awareness creation, contributions to the conservation of coastal biodiversity, and involvement in development planning. The project also directly supported the proclamation of three national parks: Sperrebiet, Namibian Islands Marine Protected Areas, and the Dorob National Park. Also, it improved the governance of coastal areas through the preparation of management and contingency plans, training, monitoring and evaluation, and matching grants in park infrastructure.

NACOMA was rated satisfactory in an Implementation Completion Report (ICR) compiled and released by the Independent Evaluation Group (IEG) of the World Bank in 2017 when it was closed (World Bank, 2017). In a recent interview, Kandjii (2019) noted that the rating was satisfactory to the ministry and project staff, although the enactment of the ICZM Bill would have been “the cherry on the cake”.

Often when the lead agency or coastal manager is appointed within a project, its time-span is limited as funding only lasts for an indented period. As much as this would not be advisable to do, developing countries should be commended for efforts and noticeable improvements because most funding is received through grants or possibly loans. Kandjii (2019) also noted that the establishment of the project instead of a coastal managing authority was mostly due to the limited funding that was made available. He further suggests that a coastal managing authority should preferably be located in a coastal town and established as a branch of the ministry with similar objectives as NACOMA, should funds become available in the future.

Currently, the absence of the project is being felt despite the efforts of the ministry. This is especially the case in terms of awareness creation and coordination between stakeholders, which creates platforms for discussions of management issues such as the recently proposed phosphate mining in the coastal zone.

4. Conclusion

In summary, successful integrated coastal zone management requires stronger analytical founda-

tions, extensive consultations, and transparency amongst stakeholders. Although transparency is generally not easy to achieve, stakeholders should keep in mind that it is the wellbeing of the richest resource providers that is at stake. In addition, attention should also be paid to institutional arrangements, government commitment, capacity building and awareness-raising in order to achieve a balance between biodiversity and sustainable utilisation of natural resources offered by our coastal zones worldwide.

5. Acknowledgements

Firstly, I would like to thank the Almighty God for giving the knowledge and seeing me through the journey of my research. I would like to thank all the reviewers both from the University of Namibia and YES Network who guided me in my writing. And also a special thank you goes to Ms. Monique Clarice Clarke of sharing about the YES Network and 5th Young Earth Scientists Congress in the beginning of 2019 with me. Last but most importantly, I would like to thank all the sponsors who made it possible to both carry out my research and present it in Germany at the 5th Young Earth Scientists Congress held under theme “Rocking Earths Future”. These are: Air Namibia, Enkehaus Medical Centre (Namibia), Namibia Desert Diamonds (Pty) Ltd, YES Network Namibia and the University of Namibia, who played an important role too by paying my registration fee to the congress in Germany.

6. References

Burbridge P.R. 2012. Dr. Peter Burbridge & Integrated Coastal Zone Management. Interviewed by Erkki Siirila . [video online] Available at: <https://www.youtube.com/watch?v=g3uD-m6D-Pcc> [Accessed 01 September 2020]

Crossland, C.J., Kremer, H.H., Lindeboom, H., Crossland, J.I.M. and Le Tissier, M.D. (Eds), 2005. Coastal fluxes in the Anthropocene: the land-ocean interactions in the coastal zone project of the International Geosphere-Biosphere Programme. Springer, Berlin, Heidelberg, 232 pp. https://doi.org/10.1007/3-540-27851-6.

Dronkers J. 2019. Integrated Coastal Zone Management . [online] Available at: <http://www.coastalwiki.org/wiki/Integrated_Coastal_Zone_Management_(ICZM)> [Accessed 30 August 2020]

Haslett, S. 2000.Coastal systems. Routledge, London. 218 pp.

Kandjii C. 2019. The engagements of Namibia Coast Conservation and Management Project. Personal interview.

Kay, R., Alder, J. 1999. Coastal Planning and Management. CRC Press, London, 400 pp. https://doi.org/10.4324/9780203010174.

Lundgren L.W. 1999. Environmental Geology. 2nd ed. Prentice Hall, London, 511 pp.

World Bank. 2017. Namibia - Coast Conservation and Management Project (English). Washington, D.C.: World Bank Group. Available at: <http://documents.worldbank.org/curated/en/602121485210052624/pdf/ICRR-Disclosable-P070885-01-23-2017-1485210039750.pdf> [Accessed 15 August 2019]

Society at Risk – Impacting Earth Phenomena

Erodibility Problems and Land Instabilities in the Wayimirya Valley: Environment, Geotechnics and Tectonics

Pacifique S. Mukandala[1,✉], Lisette G. Menomavuya[2,✉]

[1] Université Officielle de Ruwenzori, Democratic Republic of the Congo
[2] Institut des Batiments et des Travaux Publics, Democratic Republic of the Congo
✉ pmukandala@uor-rdc.net, lisettemenomavuya@gmail.com

Keywords: Instabilities, Soils, Geotechnical, Tectonism, Cartography.

1. Introduction

Urbanization, as a social phenomenon and a physical transformation of landscapes is the most powerful, irreversible and visible of human transformations on earth. Rapid urbanization around the world will be one of the great challenges of human well-being and a healthy living environment (Redman and Jones, 2004). The spatial organization of African cities is most often characterized by a superposition of two contradictory models: the so-called colonial model and the indigenous African models (Coquery in Antoine, 1991, cited by Wouters & Wolff, 2010). Here we focus on environmental changes in relation to such a city in the Wayimirya Valley, located in Mususa Municipality, Butembo City, and North Kivu Province in the Democratic Republic of the Congo.

The waterproofing of large tracts of land following a rapid spatial expansion of the city has created environmental problems that affect the urban structure. The city, in fact, faces diversified hydrological risks. The gradual and regressive gullies are constantly increasing and influencing the availability of water. The urban area has been struggling in recent years with floods perceived locally as exceptional. We are currently witnessing the remobilization of old landslides, which locally generate desolation following the caused damage. Butembo City has an area of 158.95 km^2. In 2008, its population was estimated at 581449 inhabitants (Sahani, 2012). Based on recent rural exodus due to growing insecurity in the countryside, the entire city of Butembo is on the verge of overcrowding. Thus several anarchic constructions have spread, even in the study area.

The Wayimirya Valley experiences several field instabilities: landslides, erosion and land subsidence. Apart from these events, also floods occur during rainy periods and a great insalubrity. These instabilities cause destruction and sinking of structures, causing human and material losses.

Roose (1984) explained the causes and factors of water erosion in tropical climates. He talked about the wind, the water in the groundwater and the drains, ravines and tunnels. He also added that plant cover, slope, soil resistance to erosion and anti-erosion techniques are the factors for managing erosion.

The water erosion is further accentuated in the Wayimirya Valley during floods. The floods could spread to all flat valley bottoms in the future if left unchecked. The landslides are active and are in the creep phase. Eleven of the sixteen listed landslides are partially co-generated by earthquakes. The rain is not the basis of the accentuation of the environmental problems, which disturb the urban structure of Butembo, but urbanization is the main cause (Sahani, 2011). Sambola and Vuillet (2015) also characterized the floods during their research. To study erosion, it is also necessary to describe the soils (Maignien, 1980). The Wayimirya Valley has no sewage pipeline. The ground is bare, sometimes with steep slopes. It is less resistant due to its low particle cohesion power. It's black with the presence of the remains of plant debris interspersed. This valley was part of the swamps of Butembo City a few years ago. The soil was characterized by the geotechnical laboratory of the North Kivu Roads Office. At a conference, Desmet (2014) outlined some techniques for preventing and managing crises during landslides and subsidence, indicating it is important to take into account the permanent danger of these instabilities in the human environment. Lateltin, (1997) insisted on the need to take into account the dangers due to ground movements in the context of spatial planning activities. He also insisted on hazard mapping for the action planning. This mapping involved identification, hazard assessment, and planning. It included a topographic map, geological map, geotechnical map, ground map and aerial photographs. It ended with a consequent development plan. This approach was also supported by Fares et al. (1994) in their work entitled "Methodical test of natural risks relative to ground movements cartography". In disaster reduction, we move on to the identification and study of natural hazards that can be hydro-meteorological (floods, mudslides and debris, etc.), geological (earthquakes, volcanism, landslides, mass movements, surface collapses, geological fault activities, etc.) or biological (contagion by plants or animals, extensive infestations, etc.) (Benson and

Proceedings of the 5th International YES Congress
DOI: 10.2312/yes19.23

Figure 1: View of some environmental forms in the Wayimirya Valley.

Figure 2: The Wayimirya Valley is a waste deposit site.

Twigg, 2007)

The ground movements are a topical subject covered by several authors (Chang and Zhang, 2010; Cuomo and Della Sola, 2015; Desodt et al., 2017; Garnier et al., 2011; Kukemilks and Saks, 2013; Larsen et al., 2010; Lissak, 2012; Maurizot and Lafoy, 2001; Raetzo and Loup 2016; Rodriguez et al. 2003; Stieltjes, 2004). These authors also proposed some ways to manage ground movements.

There is a logical link between erosion, geology, tectonics and the various types of ground movements (Graveleau, 2008). Sahani (2011) presents the physical framework of the Butembo city. It should be noted that this city is located in the western branch of the East African rift system and is crossed by faults. It is built on hills and is in an equatorial climate. It is drained by several streams, of which the Kimemi and Wayimirya flows are the most dominant.

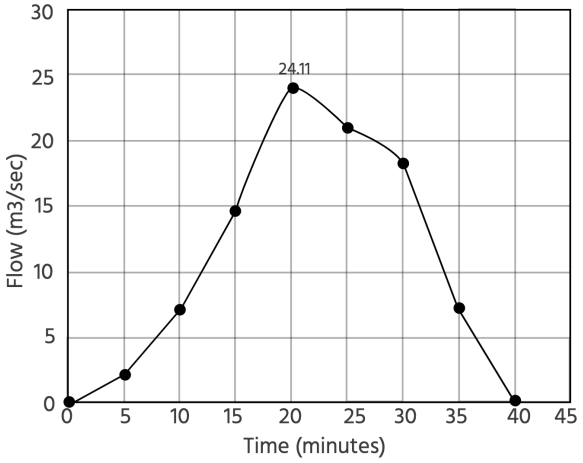

Figure 3: Project hydrograph at the confluence of the Wayimirya and Kimemi flows.

2. Observations

Butembo city comprises four main types of Kibarian geological formations, namely the base complex of Luhule-Mobisio (with meta basalts, dolerites, diorites and islets of quartzites), the sedimentary base of Luhule-Mobisio (with shales, quartzites with intercalations limestones), the ortho-gneissic complex (with stratified and retromorphized granites and granodiorites, sometimes ortho-gneiss and homogeneous migmatites) and the Lubero series (micaschists with granitic intrusions, phyllites, schists, sandstones and quartzites).

Butembo City has fewer cartographic references on the morphological, hydrological, geological, tectonic, and geotechnical levels. This is a major challenge this city faces during its urbanization process. The insufficient data are from the colonial era and require updating. With this in mind, we set ourselves the goal

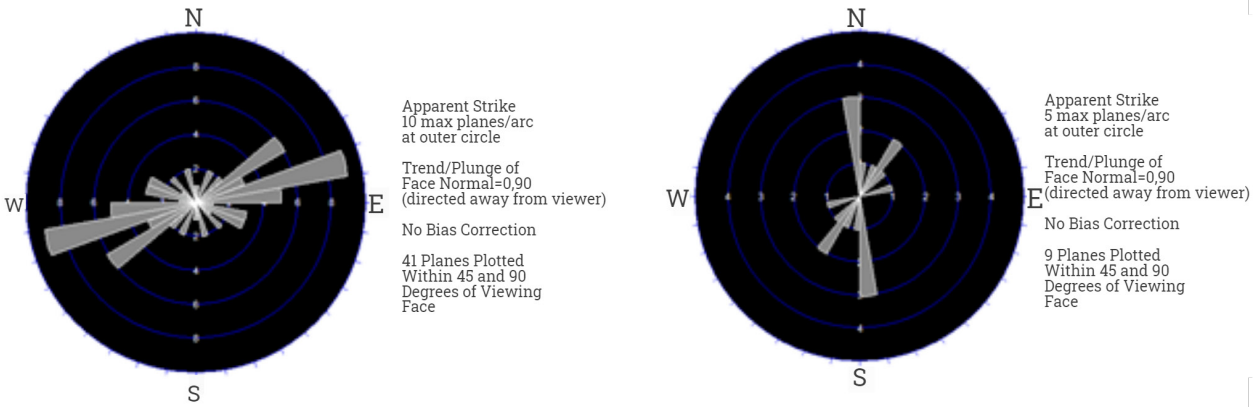

Figure 4: Frequency rosette orientation of fractures (left) and schistosity (right).

Nature of Materials	Clay Soil
Origin	Wayimirya valley
Depth	6,5 m
Water natural content	14 %
Granulometry	
Maximum	8 mm
Afnor fines	38 %
Proctor	
W optm	-12 %
Maximum dry density	1,99 t/m^3
Bearing	
Dry density at 95% opm	1,89 t/m^3
CBR at 95% opm	2,10 %
Atterberg limits	
Liquidity limit	42 %
Plasticity limit	32 %
Plasticity index	10 %
Classification	
NRC	s1c
H.R.B.	a-5 (1)

Table 1: Synthesis of laboratory analysis results.

of contributing to the characterization of environmental risks and their impact. In future research, we aim to carry out their complete mapping and thereafter, our work may be extended to the whole city.

During this research, we used descriptive and analytical methods. We started with the observation of landscapes, took standard samples of the soil, carried out a structural study on visible outcrop breaks, processed structural data with Dips and Win Tensor software (Delvaux et al., 2012; Delvaux and Barth, 2009), and performed data analysis and interpretation.

The Wayimirya Stream has its source in the Vulema-Vuhika Hills. It crosses moderate slopes but its low water flow measured at its mouth is large enough to reach 144 l/s with a total length of 2990.27 m. It pours into the Kimemi flow. It should be noted that the slope of this flow becomes increasingly weaker from upstream to downstream.

The perimeter is around 10,240 m, the total altitude is 67 m, the length of the equivalent rectangle is 4369.9 m and its width 750.08 m. Tthe length of the watercourse is 2990.27 m, the Gravellius coefficient is 3.56, the average percentage slope is 1.5 and the hydraulic length is 4182.17 m. The total area is 3.27 km^2. Most of the Wayimirya catchment area is urbanized, and the accommodation is generally of medium standing. The tertiary roads are made of compact earth. It is the same for those of the Bulema Hills because of water transport. The instabilities (landslides, erosions, collapses, etc.) of the land are remarkable (Figure 1). Beyond the natural causes, this situation appears to be caused by human survival activities (extraction of sand and gravel) and by the mode of urbanization observed on the spot (houses, gardens, poor management of domestic water, etc.) in the valley itself, even just in the banks of the flow.

The Wayimirya Valley serves as an illegal bin for the population (Figure 2). Consequently, the flows are accompanied by several degradable and non-degradable solid wastes, which pose a health hazard. To control the soil deformation problem, we carried out an experimental study on undisturbed samples. The standard instrument for studying soil compressibility is the Terzaghi odometer.

The specific density is 2.65, and the dry density is 2.21. The wet density is 2.55, the density of the solid component is 1.52 at the depth of 6.5 m and the density of natural water is 14 %. Table 1 presents the summary of laboratory work.

We estimate it is a mixture of of 38 % fine particles and 62 % large particles. The soil is silty with 4 % gravel. In view of the Atterberg limits (Table 1), the soil has a mediocre bearing capacity. The consistency index is 2.8. With the plasticity index of 10, the percentage of fine particles is less than 30.

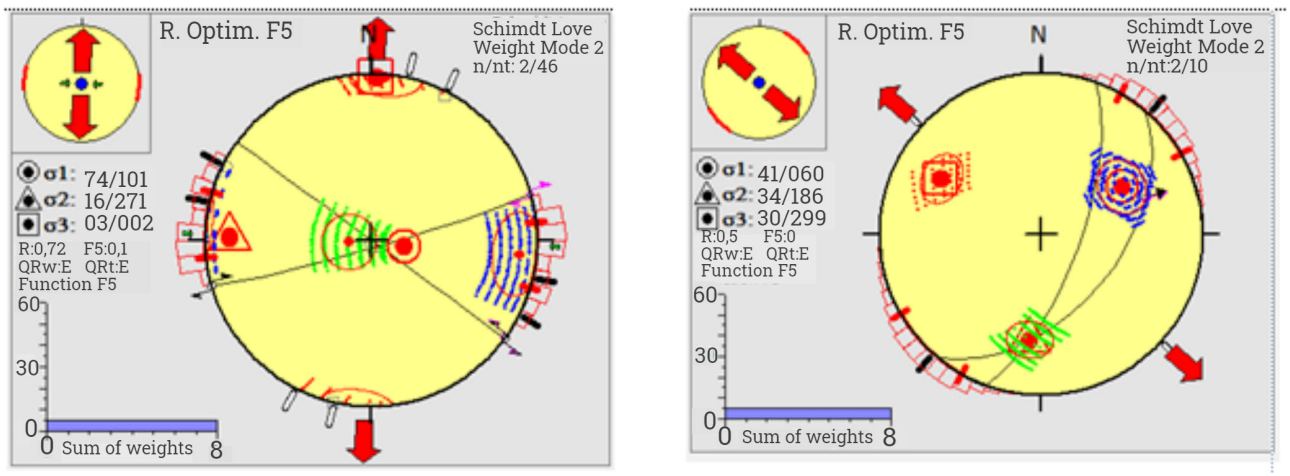

Figure 5: Stress tensor orientation of fractures (left) and schistosity (right).

Site	Permeability tests		Penetrometer tests: Resistance
	Dt (min)	Dh (cm)	
1	1	26,5	204 MPa
	5	24	
	8	22,6	
	10	21,9	
4	5	26	188 MPa and 320 MPa
	10	24,5	
	15	23	
	20	22	
6	5	5,9	180 MPa
	10	5,85	
	15	5,8	
7	5	12	580 MPa
	10	11	
	15	20	
	20	8	

Table 2: Results of the permeability and in situ penetrometer test.

The urban area of the Wayimirya Valley has an estimated waterproofing rate of 80 %. The runoff hydrogram, which shows the evolution of the flow, is shown in Figure 3. It was calculated based on the surfaces of the sub-basins and the values of various runoff coefficients. Since we have a uniform flow in the section, Table 2 shows how the speed and the tension vary according to the flow. After calculations, the width of the stable section was estimated at 1251.497 m. Hydraulic structures are needed to stabilize the Wayimirya flow bed.

The values of the field penetrometer test are summarized in Table 2. From a petrographic and structural point of view, the Wayimirya Field is based on granitic and metamorphic formations, susceptible to tectonic deformation. The orientations of the open fractures and shale planes form the two geological structures encountered on the ground are presented in Figure 4. The opened ruptures are generally oriented in the first and second quadrants. There are others oriented in the third and fourth quadrants, but are less important. The schistosity planes are mainly oriented in the third and fourth quadrants.

The materialization of the stress is presented in Figure 5. The stress tensor (Figure 5, left) shows the maximum stress σ_1 acting in the field in the direction N101/74. The average stress σ_2 acts on the ground in a direction N271/16 and the minimum stress σ_3 acts on the ground in a direction N02/03. The compression forces of σ_2 create an extension along the plane σ_1-σ_3. The two fracture planes are preferably oriented N-S and NW-SE, with a compressive force acting along the σ_2 plane. According to the stress tensor (Figure 5, right), the σ_1 maximum stress acts on the ground in a direction N60/41. The average stress σ_2 acts on the ground in a direction N186/34 and the minimum stress σ_3 acts on the ground in a direction N299/30. The compression forces of σ_2 create an extension along the plane σ_1-σ_3. The two fracture planes are preferably oriented NE-SW and NW-SE, with a compressive force acting along the plane of σ_2.

With the low dip values, there is always a probability of an overlapping field. According to the Mohr circle (Figure 6), the formations have a brittle behavior and are therefore favorable to ruptures.

3. Discussion and conclusion

Several authors have dealt with ground movements. These movements have harmful effects on the daily human life, and the Wayimirya Valley in Butembo City is no exception. It experiences landslides, erosions, and land subsidence. According to the results of this research, these instabilities have a natural origin (rifting). They are accentuated by the unanticipated population explosion in Butembo City. It should also be noted that the city does not have an urbanization plan.

This research is the beginning of a contribution to the management of ground movements. We aim to extend it later to the city of Butembo.

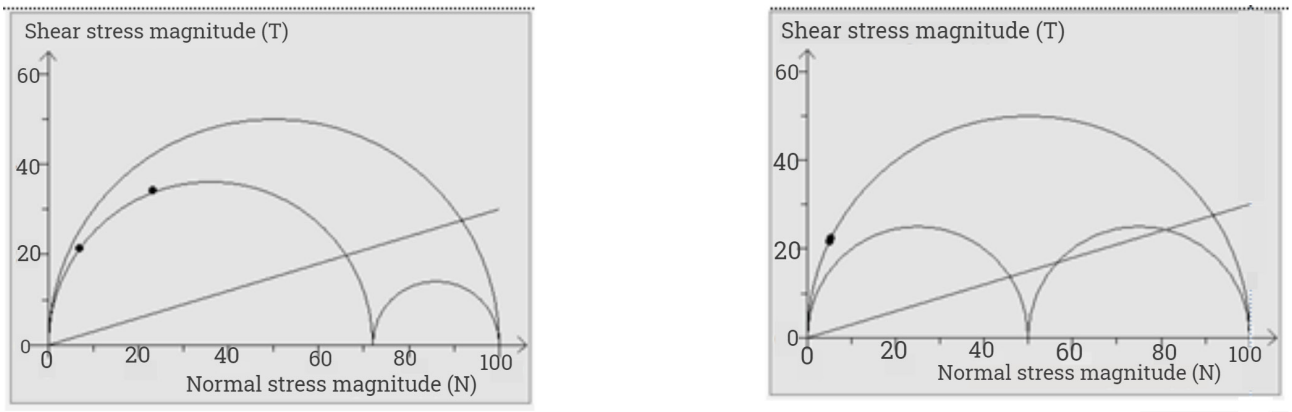

Figure 6: Mohr circle of open fractures (left) and of schistosity (right).

4. References

Benson, C and Twigg, J., 2007, Outils d'intégration de la réduction des risques de catastrophes, Fédération internationale des Sociétés de la Croix-Rouge et du Croissant-Rouge/consortium ProVention. [online] Available at https://www.preventionweb.net/files/1066_toolsformainstreamingDRRfr1.pdf [Accessed 18 April 2021]

Chang, D. S. and Zhang, L. M., 2010, Simulation of the erosion process of landslide dams due to overtopping considering variations in soil erodibility along depth, Department of Civil and Environmental Engineering, Hong Kong University of Science and Technology, Clear Water Bay, Hong Kong, 14 pp. https://doi.org/10.5194/nhess-10-933-2010.

Cuomo, S. and Della Sola, M., 2015, Large-area Analysis of Soil Erosion and Landslides Induced by Rainfall: A case of unsaturated Shallow Deposits, Journals of Mountain Science 12 (4), pp. 783–796. https://doi.org/10.1007/S11629-014-3242-7.

Delvaux, D., Kervyn, F., Macheyekib, A. S., Temu, E. B., 2012, Geodynamic significance of the TRM segment in the East African Rift (W-Tanzania): Active tectonics and paleostress in the Ufipa plateau and Rukwa basin. Journal of Structural Geology 37, pp. 161–180. https://doi.org/10.1016/j.jsg.2012.01.008.

Delvaux, D. and Barth, A., 2009, African stress pattern from formal inversion of focal mechanism data. Tectonophysics 482, pp. 105–128. https://doi.org/10.1016/j.tecto.2009.05.009.

Desmet, B., 2014, Effondrements et affaissements du sol, Direction Générale Opérationnelle de l'Agriculture, des Ressources naturelles et de l'environnement, 29 pp. [online] Available at http://geologie.wallonie.be/files/events/Effondrements2014/11-DESMET.pdf [Accessed 18 April 2021]

Desodt ,C., Launay, J. and Horsin, M. H., (2017), Les glissements de terrain, modélisation et prévision, Ecole Normale Supérieure, Paris, 18 pp.

Graveleau, F., 2008, Interactions Tectonique, Erosion, Sédimentation dans les avant-pays de chaînes : Modélisation analogique et étude des piémonts de l'est du Tian Shan (Asie centrale). PhD thesis, Université Montpellier II - Sciences et Techniques du Languedoc, Montpellier, 486 pp. [online] Available at https://tel.archives-ouvertes.fr/tel-00339145v2 [Accessed 18 April 2021]

Fares, A., Rollet, M., and Broquet, R., 1994, Méthodologie de la cartographie des risques naturels liés aux mouvements de terrain, Révue Française de Géotechnique W6, pp. 63-72.

Garnier, P., Moles, O., Caimi, A., Gandreau, D. and Hofmann, M., 2011, Aléas naturels, catastrophes et développement local. CRAterre éditions, 59 pp. [online] Available at https://hal.archives-ouvertes.fr/hal-00837774 [Accessed 18 April 2021]

Larsen, I. J., Montgomery, D. R., and Korup, O., 2010, Landslide erosion controlled by hillslope material, Nature Geoscience 3, pp. 247–251. https://doi.org/10.1038/ngeo776

Kukemilks, K. and Saks, T., 2013, Landslides and gully slope erosion on the banks of the Gauja River between the towns of Sigulda and Līgatne, Estonian Journal of Earth Sciences 62(4), pp. 231–243. https://doi.org/10.3176/earth.2013.17.

Lateltin, O., 1997, Prise en compte des dangers dus aux mouvements de terrain dans le cadre des activités de l'aménagement du territoire, 42 pp. [online] Available at https://www.planat.ch/fileadmin/PLANAT/planat_pdf/alle_2012/1996-2000/Lateltin_1997_-_Prise_en_compte_des_dangers.pdf [Accessed 18 April 2021]

Lissak, C., 2012, Les glissements de terrain des versants côtiers du Pays d'Auge (Calvados) : Morphologie, fonctionnement et gestion du risque. Université de Caen, Paris, 317 pp.

Maignien, R., 1980, Manuel pour la description des sols sur le terrain, O.R.S.T.O.M., Paris, 145 pp.

Maurizot, P., and Lafoy, Y., 2001, Cartographie des formations superficielles et des aléas mouvements de terrain en Nouvelle–Calédonie – Zone de Touho - Poindimié, Rap. BRGM/R P 50846-FR, 44 pp.

Raetzo, H. and Loup, B., 2016, Protection contre les dangers dus aux mouvements de terrain, Office fédéral de l'environnement (OFEV) Suisse, Ittigen, 100 pp.

Redman, C. L., and Jones, N. S., 2004, The environmental, social and health dimensions of urban expansion. Produced for Population-Environment research Network cyberseminar, 29 November – 15 December 2004, 12 pp. https://doi.org/10.1007/s11111-005-0010-1.

Rodriguez, F., Andrieau, H., Creutinb, J. D., 2003. Surface runoff in urban catchments: morphological identification of unit hydrographs from urban databanks. Journal of Hydrology 283, pp. 146–168. https://doi.org/10.1016/S0022-1694(03)00246-4.

Roose, E., 1984, Causes et facteurs de l'érosion hydrique sous climat tropical conséquences sur les méthodes antiérosives, Machinisme Agricole Tropical 87, ORSTOM-IRD (Office de la Recherche Scientifique et Technique Outre Mer-Institut de recherche pour le développement), Marseilles, 16 pp.

Sahani, M., 2011, Le contexte urbain et climatique des risques hydrologiques en ville de Butembo. PhD thesis, Université de Liège, Liège, 300 pp.

Sambola, S. and Vuillet, M., 2015, Impact des inondations sur les infrastructures et réseaux techniques et solutions d'amélioration de la résilience des systèmes urbains, École des ingénieurs, Paris, 109 pp.

Stieltjes, L., 2004, Evaluation du risque mouvements de terrain-Etat de l'art sur l'aléa mouvements de terrain-Analyse du risque mouvements de terrain, Geosciences pour une Terre durable, B.R.G.M./RP-53005-FR, 61 pp.

Wouters, T. and Wolff, E., 2010, Contribution à l'analyse de l'érosion intra-urbaine à Kinshasa (R.D.C.), Belgeo 3, pp. 293–314. https://doi.org/10.4000/belgeo.6477.

Vadose Zone Hydro Geophysical Studies in Urban Environment

Sepiso Shawin Mushe[1,✉]

[1] UNAM, Namibia
✉ sepisomushe20@gmail.com

Keywords: Groundwater, Vadose Zone, Geophysical methods, Challenges, Applications

1. Introduction

Namibia is a country located in SW Africa. The aridity of this country is caused by two surrounding deserts: the Kalahari Desert located on the E border with Botswana, and the Namib Desert located in the SW of Namibia. The Namib Desert's mean annual rainfall is mostly below 50 mm and less than 20 mm in some places, while large parts of the Kalahari Desert are a semi-desert, coupled with a mean annual rainfall in the 150 to 350 mm range (Namibia Water Corporation, 2019). Namibia has a current population of approximately 2.6 million, growing at a steady rate of 4.2 % per year, and 48.9 % of this population is urban (CIA World Factbook, 2021). Rapid urbanization and an ever increasing number of young people moving from rural areas to large settlements, towns, and cities requires well developed water management strategies to secure even basic living standards for Namibia's growing population. The capital city of Windhoek is the main focus of urbanization, even though all of the country's urban centers are increasing in size (Pendleton, Crush and Nickanor, 2014). The percentage of the total national and total urban population within the city is 16 % (raised from 14 % in 2001) and 36 %, respectively (Pendleton, Crush and Nickanor, 2014).

While urban livelihoods in Namibia have been frequent subjects of research over the years, its effects on groundwater quality has been a neglected topic. However, there is an obvious relationship between an increasing population and contamination of groundwater: as the urban population increases so does the contamination. Namibia does not base its water supply on rainfall due to its scarcity and uneven pattern, and therefore groundwater is its main hydric source. The biggest advantage of using groundwater sources in Namibia is that it enables water supply to isolated communities and for economic activities such as mining, industry and agriculture over nearly 80 % of the country (Christelis and Struckmeier, 2011). Thus the need to develop sustainable water resources for an increasing population, agriculture and energy needs, and the threat of climate and land use change on ecosystems motivates an improved understanding of flow and transport processes in the shallow subsurface (Hubbard & Linde, 2011).

This paper focuses on filling the gap of vadose zone research literature in Namibia by highlighting the importance of the vadose zone and providing applications of some hydrogeophysical methods that investigate processes in the subsurface. Vadose zone contamination serves as a continued "source" of contamination for groundwater and analogous receptors at almost all environmentally contaminated sites (Wellman et al., 2012) and therefore it is also important to study the different processes that lead to the contamination of the vadose zone, such as leaching. Geophysical surface based electrical methods, such as direct current resistivity and induced polarization (DC/IP), are principally convenient for investigations at large contaminated sites, where several boreholes would be required to obtain a satisfactory high sampling density (Balbarini et al., 2018). The DC resistivity method does not allow a distinction between high salinity of groundwater and formations with a low resistivity while the induced polarization method gives information on both the bulk and surface conduction/polarization, which can aid in differentiating changes in salinity from those due to lithology (Balbarini et al., 2018).

2. Vadose Zone

The vadose zone refers to the partially saturated part of the subsurface between the land surface and the underground water (Fig. 1). The shallow subsurface is a highly crucial geological zone that provides, supports and influences our water resources, agriculture and climate. It also serves as the storehouse for our contaminants (Hubbard & Linde, 2011). The vadose zone can be described by its thickness and chemistry. The thickness helps to determine how long water takes to reach the saturated zone while its chemistry acts as a natural purifier. Contaminants are leached from the solid waste as water seeps through the landfill, thus producing what is termed as leachate. This leachate extracts contaminants into the liquid phase, and forms moisture content that is sufficiently high enough to begin liquid flow (Kamboj and Choudhary, 2013).

Proceedings of the 5th International YES Congress
DOI: 10.2312/yes19.25

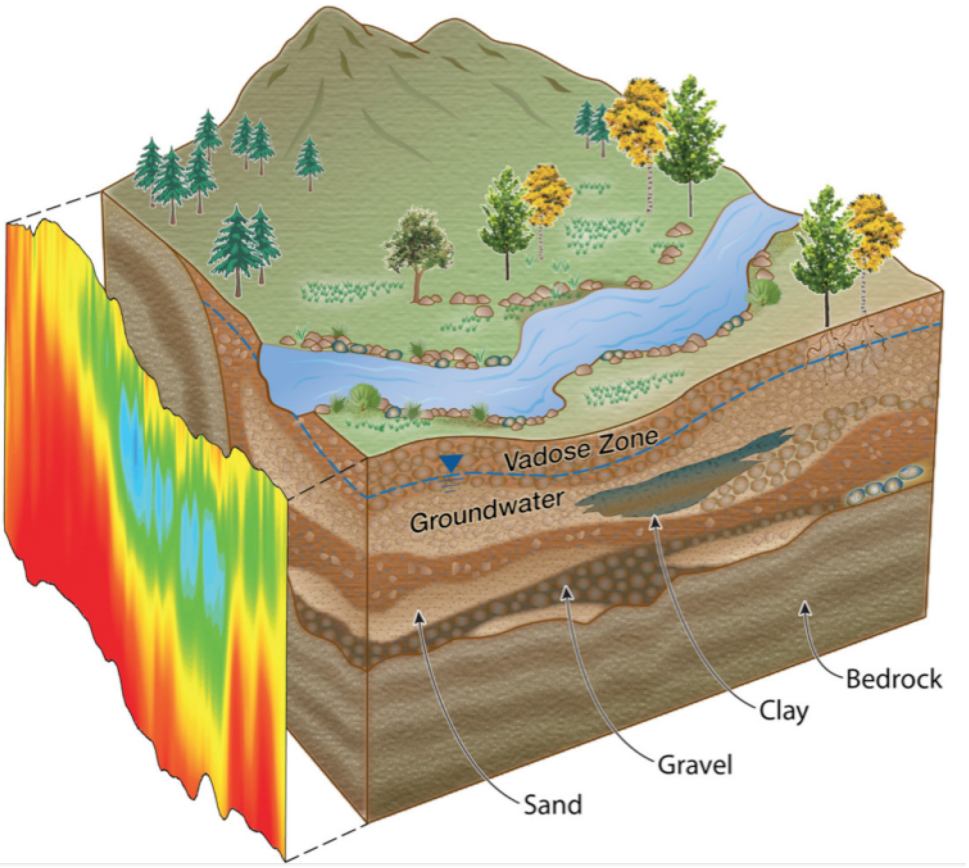

Figure 1: Example of how geophysical methods are often used to portray the subsurface. The signals show a change in color as a result of the different layering of earth materials below the surface. (Binley et al., 2015; figure licensed under CC-BY-NC-ND 4.0)

However, the vadose zone can become increasingly contaminated and hence the degree of purification decreases. Urban environments are a source of numerous contaminants such as cattle dung, salinization contamination, dumping and irrigation that negatively impacts the water quality, thus posing new challenges to monitoring and treatment schemes. The contaminant mass discharge method is frequently used to evaluate the environmental effect of contaminated sites on groundwater quality (Cai et al., 2011; Guilbeault et al., 2005; Kubert & Finkel, 2006; Trold-borg et al., 2010, 2012). Moreover, at large contaminated sites, portrayed by high source diversity such as landfills, it is often not economically practicable to install the number of multilevel wells required to establish an adequately dense sampling grid (Troldborg et al., 2010). The difficulties of access and low dynamics show significant challenges for deep vadose zone reclamation, even though the techniques for reducing the flux of contaminants within the deep vadose zone are effectively the same as those applicable to shallow vadose zone or groundwater remediation (Wellman et al., 2012). Monitoring methods for complicated subsurface environments, such as deep vadose zones, are currently not well developed and are critical constituents of reclamation strategies, including those for flux-based methods (Bunn et al., 2012). Nonetheless, methods incorporating geophysical data in the evaluation of contaminant mass discharge have not been developed yet (Balbarini et al., 2018).

3. Hydrogeophysics

In recent years the field of hydrogeophysics has emerged to examine the potential that geophysical methods hold for improving the quantification of subsurface properties and processes important for hydrological investigations (Hubbard & Linde, 2011). One of the main aims of applying hydrogeophysical methods in Namibia is the identification of water reservoirs below the Earth's surface to target borehole drilling. Electrical resistivity is probably the method that has been used most often for groundwater studies, compared to any other geophysical method. Resistivity is defined as a measure of the potential to resist electrical current flow through materials; it implies the inverse of electrical conductivity and is an intrinsic property of the material. Electrical resistivity methods generally involve a low frequency (< 1 Hz) current that is instilled into the ground between two current electrodes, whilst the electrical potential differences are measured by one or more pairs of potential electrodes (Hubbard and Linde, 2011). Moreover, most resistivity surveys make use of a four-electrode measurement approach. Two potential electrodes are

placed at some distance from the current electrodes, and the difference in electrical potential or voltage is measured. The value attained from this measurement is for subsurface resistivity. This measurement, together with the instilled current and the geometric factor that is a function of the particular electrode configuration and spacing, may be used to determine resistivity for uniform subsurface conditions following Ohm's law (Hubbard and Linde, 2011). The direct current (DC) and induced polarization (IP) methods are used to examine the spatial distribution of the electrical resistivity and the polarization of the subsurface. The IP signal can be measured either in the frequency sphere, as frequency-dependent complex resistance, or in the time sphere, as a voltage decay response during which the medium is excited by a square current pulse (Balbarini et al., 2018). The merged resistivity and polarization properties of a medium can be expressed in the frequency sphere in terms of a complex conductivity (σ^*) as the sum of two current paths (Lesmes & Frye, 2001). The first one is the electrolytic bulk conduction (σ_{bulk}), which involves the conduction that takes place through the fluid that fills the interconnected pore spaces, and the other is the complex surface conduction (σ^*_{surf}), which includes both the surface conduction and the surface polarization of the electrical double layer created at solid-fluid interface (Balbarini et al., 2018).

In addition to resistivity methods, water samples can be gathered at landfill sites from all screens, and analyzed for major cations and anions, sulfonamides, and barbiturates. The samples are then filtered (0.45 µm) and stored on dry ice in the field until analysis. Information provided by DC/IP should involve interpolation of the chemical concentration data using regression kriging, which thus serves as a benefit from these geophysics-based methods (Balbarini et al., 2018). This kriging method is used when the estimated variable such as the contaminant concentration, sampled at few locations, corresponds to an auxiliary variable such as the imaged bulk conductivity from DC/IP, sampled at many locations (Hengl, 2009; Hengl et al., 2007; Matheron, 1973; McBratney et al., 2003; Odeh et al., 1995). According to Balbarini et al. (2018) the geophysical-based method is less reliant on the number of water samples and their location, and thus the method is suitable for large contaminated sites and/or deep plumes. In such places, the number of water samples is frequently too low for determining the extension of the contaminant plume and estimating the contaminant mass discharge. The major advantage of using geophysical data over conventional measurements is that geophysical methods can provide spatially extensive information about the subsurface in a nominally invasive manner at a provisionally high resolution (Hubbard and Linde, 2011). However, the greatest disadvantage is that the geophysical methods only provide indirect information about subsurface hydrological properties as well as processes relevant to subsurface flow and transport (Hubbard and Linde, 2011). This means that the data recorded requires dedicated and potentially time-consuming interpretation in order to obtain an indication of the location to drill for groundwater.

4. Discussion/Conclusion

While the multitude of challenges facing rapidly growing migrant cities (e.g. employment, housing, and service provision) is well-recognized in Namibia, vadose zone studies and contamination is not. It is important to highlight to the Namibian population and industries such as the Ministry of Lands, Geological Survey of Namibia, Namwater, and several other consultants on the importance of vadose zone studies carried out. The population can benefit from vadose zone studies since they promote environmental sustainability. As more people become aware of how contamination can negatively affect the groundwater quality, they can build towards the use of more environmentally safe strategies such as planting trees. One of the ways of having an effective study of the vadose zone is through collaboration; developers of geophysical equipment should have effective communication with users of the equipment. This can help in finding out what possible improvements could be made on the instruments.

5. Acknowledgements

The author would like to extend thanks to Namibia Desert Diamonds (Pty) Ltd (NAMDIA) for the sponsorship to present the review in Germany at the 5th Young Earth's Scientist Congress, YES Network Namibia and the University of Namibia for the involvement and guidance. The author would also like to thank the reviewers who provided feedback and insightful comments.

6. References

Balbarini, N., Rønde, V., Maurya, P., Fiandaca, G., Møller, I., Klint, K. E., et al., 2018. Geophysics-Based Contaminant Mass Discharge Quantification Downgradient of a Landfill and a Former Pharmaceutical Factory, Water Resources Research 54, pp. 5436–5456. https://doi.org/10.1029/2017WR021855.

Binley, A., Hubbard, S. S., Huisman, J. A., Revil, A., Robinson, D. A., Singha, K., and Slater, L. D., 2015. The emergence of hydrogeophysics for improved understanding of subsurface processes over multiple scales, Water Resources Research 51, pp. 3837–3866. https://doi.org/10.1002/2015WR017016.

Bunn, A. L., Wellman, D. M., Deeb, R. A., Hawley, E. L., Truex, M. J., Peterson, M., Freshley, M. D., Pierce, E. M., McCord, J., Young, M. H., Gilmore, T. J., Miller, R., Miracle, A. L., Kaback, D., Eddy-Dilek, C., Rossabi, J., Lee, M. H., Bush, R. P., Beam, P., Chamberlain, G. M., Marble, J., Whitehurst, L., Gerdes, K. D., and Collazo, Y., 2012. Scientific Opportunities for Monitoring at Environmental Remediation Sites (SOMERS): Integrated Systems-Based Approaches to Monitoring. PNNL-21379. Pacific Northwest National Lab. (PNNL), Richland, WA (United States). https://doi.org/10.2172/1046328.

Cai, Z., Wilson, R.D., Cardiff, M.A. and Kitanidis, P.K., 2010. Increasing Confidence in Mass Discharge Estimates Using Geostatistical Methods, Ground water 49, pp. 197–208. https://doi.org/10.1111/j.1745-6584.2010.00709.x.

Christelis, G. and Struckmeier, W. F. (Eds.), 2011. Groundwater in Namibia: an explanation to the Hydrogeological Map – Unrevised 2nd edition of Technical Cooperation Project «HYMNAM», Windhoek, 128 p. [Online] Available at: <https://www.bgr.bund.de/EN/Themen/Wasser/Projekte/abgeschlossen/TZ/Namibia/groundwater_namibia.html> [Accessed 17 July 2021].

CIA 2021. The World factbook: Namibia. [Online] Available at: <https://www.cia.gov/the-world-factbook/countries/namibia> [Accessed: 17 July 2021].

Guilbeault, M. A., Parker, B. L. and Cherry, J. A., 2005. Mass and flux distributions from DNAPL zones in sandy aquifers, Groundwater 43(1), pp. 70–86. https://doi.org/10.1111/j.1745-6584.2005.tb02287.x.

Hengl, T., 2009. A practical guide to geostatistical mapping, 270 p.[Online] Available at: <http://spatial-analyst.net/book/system/files/Hengl_2009_GEOSTATe2c1w.pdf> [Accessed 20 July 2021].

Hengl, T., Heuvelink, G. B. M. and Rossiter, D. G., 2007. About regression-kriging: From equations to case studies, Spatial Analysis 33(10), pp. 1301–1315. https://doi.org/10.1016/j.cageo.2007.05.001.

Hubbard, S. and Linde, N., 2011. Hydrogeophysics, 106 p. [Online] Available at: <https://escholarship.org/uc/item/11c8s8d4> [Accessed 17 July 2021].

Kamboj, N. and Choudhary, M., 2013. Impact of solid waste disposal on ground water quality near Gazipur dumping, Journal of applied and natural science 5(2), pp. 306–312. https://doi.org/10.31018/jans.v5i2.322.

Kübert, M. and Finkel, M., 2006. Contaminant mass discharge estimation in groundwater based on multi-level point measurements: A numerical evaluation of expected errors, Journal of Contaminant Hydrology 84(1), pp. 55–80. https://doi.org/10.1016/j.jconhyd.2005.12.003.

Lesmes, D. P. and Frye, K. M., 2001. Influence of pore fluid chemistry on the complex conductivity and induced polarization responses of Berea sandstone, Journal of Geophysical Research: Solid Earth 106(B3), pp. 4079–4090. https://doi.org/10.1029/2000JB900392.

Matheron, G., 1973. The intrinsic random functions and their applications, Advances in Applied Probability 5(3), pp. 439–468. https://doi.org/10.2307/1425829.

McBratney, A. B., Mendonça Santos, M. L. and Minasny, B., 2003. On digital soil mapping, Geoderma 117(1), pp. 3–52. https://doi.org/10.1016/S0016-7061(03)00223-4.

Namibia Water Corporation, 2019. Hydrological Services. [Online] Available at: <https://www.namwater.com.na/index.php/services/56-hydrological-services?showall=1> [Accessed 17 July 2021].

Odeh, I. O. A., McBratney, A. B. and Chittleborough, D. J., 1995. Further results on prediction of soil properties from terrain attributes: heterotopic cokriging and regression-kriging, Geoderma 67(3), pp. 215–226. https://doi.org/10.1016/0016-7061(95)00007-B.

Pendleton, W., Crush, J. and Nickanor, N., 2014. Migrant Windhoek: Rural-Urban Migration and Food Security in Namibia, Urban Forum 25(2), pp. 191–205. https://doi.org/10.1007/s12132-014-9220-x.

Troldborg, M., Nowak, W., Lange, I. V., Santos, M. C., Binning, P. J., and Bjerg, P. L., 2012. Application of Bayesian geostatistics for evaluation of mass discharge uncertainty at contaminated sites, Water Resources Research 48(9). https://doi.org/10.1029/2011WR011785.

Troldborg, M., Nowak, W., Tuxen, N., Bjerg, P. L., Helmig, R., and Binning, P. J., 2010. Uncertainty evaluation of mass discharge estimates from a contaminated site using a fully Bayesian framework, Water Resources Research 46(12). https://doi.org/10.1029/2010WR009227.

Wellman, D.M., Freshley, M.D., Johnson, T.C. and Miracle, A.L., 2012. Contaminants in Vadose Zone Environments, Vadose Zone Journal 11(4), vzj2012.0159. https://doi.org/10.2136/vzj2012.0159.

Intensification of the Built-Up Zone in the Riparian Area of Bukavu City: Impact on Population Vulnerability in the Context of Urban Natural Hazards

Jean-Robert Nshokano Mweze[1,✉], Mireille Muhigwa[2]

[1] Université Paris 8, France
[2] Université d'Ottawa, Canada

✉ nshokano@gmail.com

Keywords: Riparian zone, vulnerability, Landslides, urbanization, Bukavu

1. Introduction

D. Dodman et al. (2017) shows that "the extensive urban growth and development anticipated in sub-Saharan Africa also offer considerable opportunity to address vulnerability and disaster risk before or as it emerges". In many cities of the Democratic Republic of Congo (DRC), the urbanization rate and population growth seem to be two of the explanatory factors that increase the population vulnerabilities. Developing countries have a high rate of poverty where internal migration accentuates and increases the city precariousness. Instead of these two reasons, G. O'Hare and S. Rivas (2005) consider rural exodus as the main reason. This cause is also considered by F. Leone and F. Vinet (2004) as an element of growth and transfer of poverty from rural areas to urban areas.

Located on the shores of Lake Kivu (Fig. 1), the city of Bukavu is located in a seismically active region. N. D'Oreye et al. (2011) show that the vulnerability of the Bukavu area is high due to potential larger earthquakes in neighboring basins.

The region of the Lake Kivu basin is mountainous and characterized by several faults. According to L. Ilunga (1977), the city of Bukavu is located along the faults, between the Alberta direction and the Tanganyika direction. Observations show that there has been in recent decades an increase in natural disasters (flooding and landslide) in the Kivu-Rwanda-Burundi region in general and in South Kivu in particular (I. Vandecasteele et al. 2009 cited in S. Ndynabo 2010). The seismic activity, the very rugged terrain and the altered soil make many parts of the city unstable and sensitive to landslides. The rainfall and the beds of the major rivers that cross the city increase the risk of floods during the wet season.

Since 1970, the city of Bukavu and its surroundings experienced several landslides and floodings. In addition, the South Kivu province is impacted by wars and conflicts, which have contributed to a rural exodus of populations into the urban environment.

B. T. Mugaruka et al. (2017) show that most inhabitants are unaware about the presence of landslides for instance in the areas they settle in. E. Monsieurs et al. (2018) state that the occurrences of reported landslides during a year correlate with the rainfall pattern. Landslide events are more abundant in more densely populated areas and in areas that have been estimated to be moderately to highly susceptible for landslides. For E. Monsieurs et al. (2018), the most important factor for landslides after rain is demographic pressure. With respect to the African population growth projections, the importance of this factor must not be underestimated.

C. Kalikone et al. (2017) showed that "ground deformations in Bukavu are the environmental constraints that should be taken into account for risk management and urban planning". Although large landslides may appear to be stabilized and on the whole be affected only by movements of relatively small magnitude and speed, a large-scale triggering event such as a strong earthquake could cause fairly substantial sudden displacements that could affect larger areas, especially if this occurs during the rainy season when lands are more susceptible to instability (M. S. Kulimushi et al. 2017).

The combination of permanent and active natural hazards with social vulnerability is crucial to disturb the urban balance. For J.-C. Thouret and R. D'Ercole

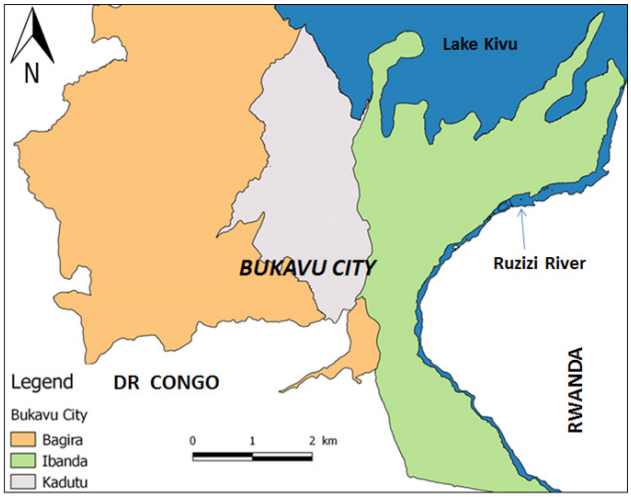

Figure 1: The Bukavu City with its three municipalities (data from the GeoRiskA project of the Royal Museum for Central Africa, *MRAC).*

Proceedings of the 5th International YES Congress
DOI: 10.2312/yes19.26

(1996), the social vulnerability is crucial in the study of natural risk in the context of growing cities and urbanization patterns. In the case of Bukavu, the increase of the built-up zone particularly in the riparian area of Bukavu has not received a particular focus of research, especially from the relation between land use and the population vulnerability, while it is a geographical space with a remarkable degree of risk exposure.

2. Study Area

The city of Bukavu, capital of the South Kivu province, is located in the eastern part of the Democratic Republic of Congo, between 2° 33.1' and 2° 28.3' S and 28° 48.4' and 28° 53.6' E. It is separated from Rwanda by Lake Kivu (1460 m above sea level) and the Ruzizi River. Administratively, the city of Bukavu is subdivided into three municipalities Ibanda, Bagira, and Kadutu (Fig. 1). Bukavu has a humid tropical climate moderated by altitude, with alternating seasons. The rainy season lasts 9 months, from September to May, while the dry season lasts only 3 months, from June to August.

The city is crossed by the tributaries of the Ruzizi River: Nyamuhinga, Bwindi, Wesha, Tshula, Nyakaliba, Mukukwe and Kahwa. These rivers flow into Lake Kivu with very variable discharge rates and carry large masses of soil from erosion. Most of Bukavu is built on basaltic rocks, which can be accessed in several places of the city due to quarrying.

This study focuses on the impact of urban growth and population vulnerability. To reach this aim, the three riparian sites Muhanzi, Bassin du Collège and Panzi (Fig. 2) were chosen for a comparative approach according to the following criteria: Location in the Bukavu riparian area (on the shore of Lake Kivu and the Ruzizi River), presence of landslides, landslide scars or soil deformation zones, presence of slope and drainage networks as indicators of topographic constraints and hydrographic dynamics, and presence of exposed elements like buildings, infrastructure, and socio-economic activities.

Muhanzi and Bassin du Collège are located in the ground deformation zones identified by A. Nobile et al. (2018) with Differential Synthetic Aperture Radar Interferometry. Muhanzi is in their zones I and II, which indicate important deformation rates with a principally eastward directed slope movement in some parts and moderate to high ground deformation rates in the others. Bassin du Collège is in zone III of A. Nobile et al. (2018), indicating a nearly vertical subsidence.

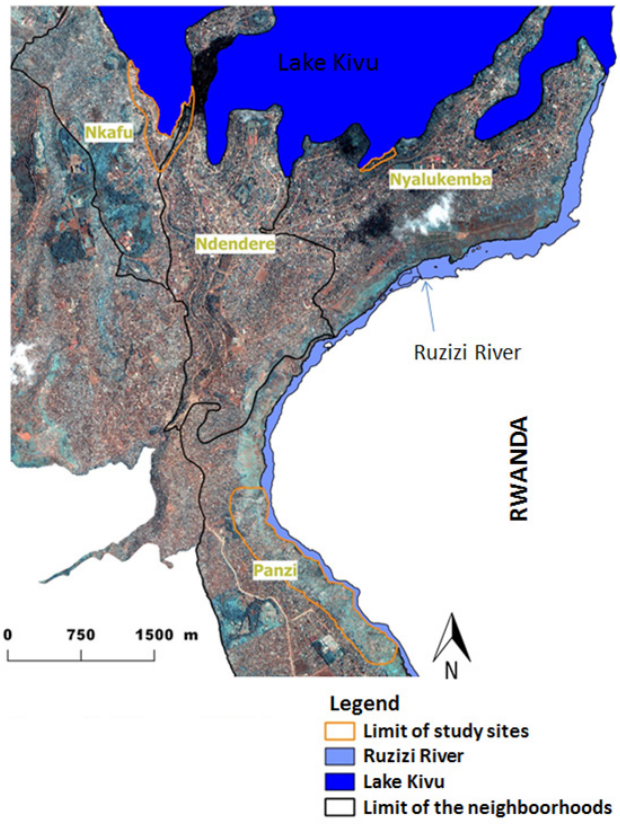

Figure 2: Location of study areas in the riparian space of Bukavu (background map: GeoRiskA project of the Royal Museum for Central Africa, *MRAC).*

3. Materials and Methods

Work in this study is primarily based on the exploration of bibliographic sources concerning the intensification of the built-up zone in the riparian area and its impact on population vulnerability concerning natural hazards. We compared GoogleEarth satellite images of the riparian built-up zone of Bukavu between 2004 and 2021 to establish a diachronic analysis. This work allows to understand the urban growth and the exposure of the built-up zone to risks in the riparian area of Bukavu.

The overall objective is to describe and understand the spatial organization of the built-up zone and its impact on the vulnerability of the population in the three study sites. The specific objective is to see how the built-up zone has evolved especially in the riparian area of Bukavu.

A follow-up investigation will characterize the land use of this geographical area to better understand the urban sprawl of the riparian area of Bukavu. To reach this aim, a double analysis approach will be applied: A first approach will analyze the evolution of the urban area and the patterns of land use with respect to landslides hazards. Subsequently, the nexus between urban planning and the state of the current urban fabric will be examined.

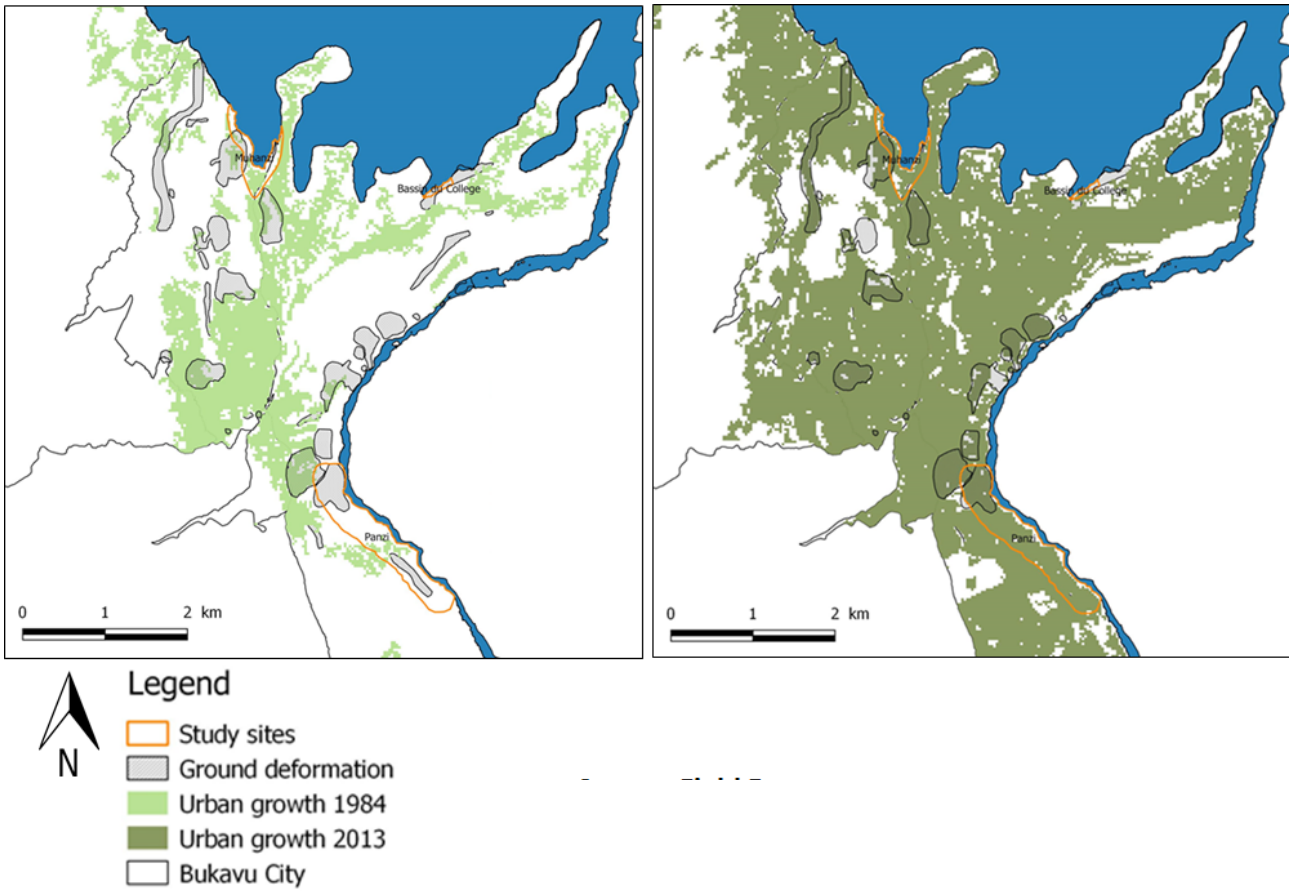

Figure 3: Map of ground deformation (C. Kalikone et al. 2017) and urban growth evolution between 1984 and 2013 (data from the GeoRiskA project of the Royal Museum for Central Africa, *MRAC).*

4. Results and Discussion

F. Grecu (2011) shows that the risks associated with the development of contemporary cities lead to factors of vulnerability to hazards. Among them, the following ones are applicable to our study sites:

- Urban growth: e. g. the vulnerability to hazards of large populations is high;
- Urban extensions in dangerous areas: e. g. the riparian zone is characterized by steep slopes and torrential rain falls;
- Development as an indicator and risk factor: Poverty, low socioeconomic levels and restricted access to goods and services, low quality of housing;
- The development of buildings horizontally (in surface) and vertically (in height).

Urban growth in sub-Saharan Africa and particularly in the DR Congo is developing slums due to the absence of clear and practical urban policies. These slums occupy a major part of the urban growth areas and they are often associated with areas that are precarious and sensitive to risks in general. Superposition of the urban growth map (1984-2013) and the ground deformation zones established by C. Kalikone et al. (2017) (Fig. 3) reveal especially in the riparian areas significant areas of overlap. These results are a strong indicator for a susceptibility of the riparian zone to natural risks.

The study of C. Balegamire et al. (2017) indicate that there is a high presence of persons with low incomes that live in slums or precarious houses, which were erected during the post-conflict period 2005 to 2010 because of the displacement of rural people: some were searching for employment in the city while others were fleeing from abuses of armed groups in their villages (some located in remote areas and other surrounding the city of Bukavu). The diachronic comparison of GoogleEarth satellite images from 2004 and 2021 show the progression of the built-up area in the riparian area of Bukavu (Fig. 4). Figure 4 shows that in 2004 there were very few built-up houses on the study sites. In 2021, a strong land use is visible that continues until today.

In 2004, the riparian zone was made by non-built plots and sometimes reserved land for green space. This area is increasingly invaded by spontaneous constructions. This new configuration has entailed natural risks with associated consequences. This partly reflects one of the conclusions of O. Dewitte et al. (2021) that thousands of highly diverse surface processes are connected to both natural and human-induced evolution of the landscape.

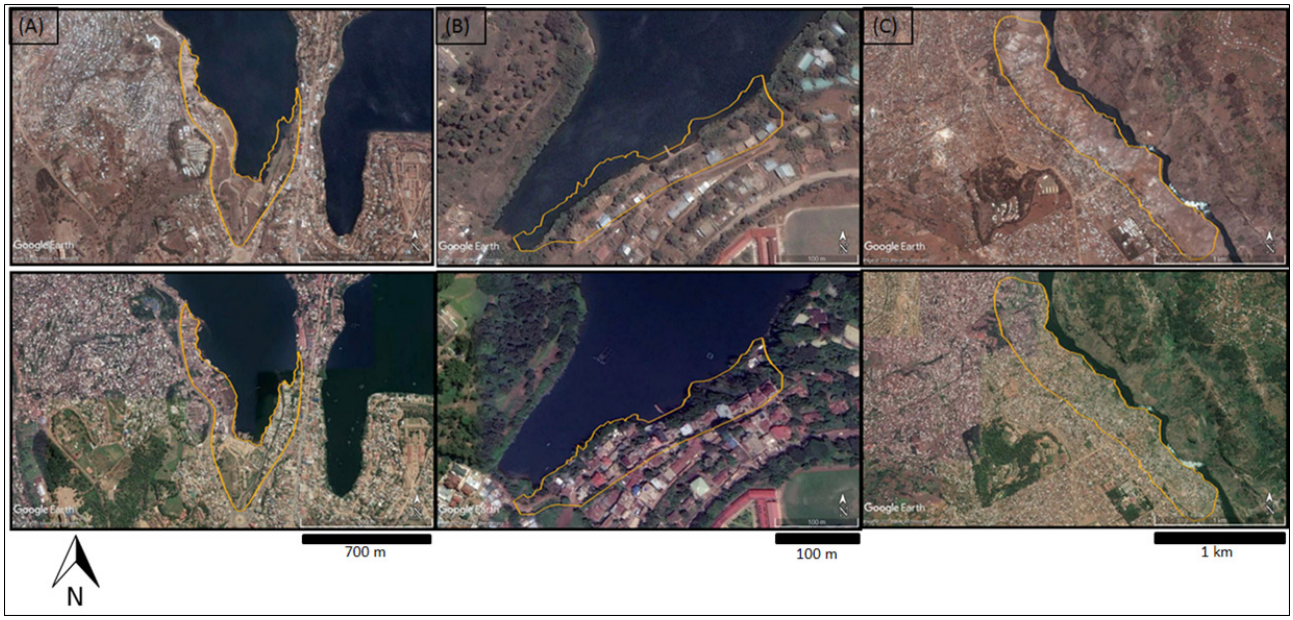

Figure 4: Google Earth satellite images (upper row: 2004, lower row: 2021) showing evolution of the built-up zone in the riparian area in Bukavu Muhanzi (A), Bassin du Collège (B) and Panzi (C).

5. Conclusions

We see a strong urban growth in the city of Bukavu which gained momentum between 2005 and today. This urban growth is not only linked to internal growth but also to rural exodus, which is significantly intensified by the insecurity that reigns in the rural environment. As in most cities in sub-Saharan Africa, the rate of urban growth is increasing every year. Unfortunately, this urban growth in Bukavu has not followed an adequate development. Rural migration or rural exodus leads to the populating of outskirts and increases urban vulnerability. This vulnerability varies from one point to another in the urban environment. C. Michellier et al. (2020) show that social ecological system thinking is consistent with the necessity to integrate the capacity of human societies to transform their environment to understand disasters.

The development of the city of Bukavu intensified on the riparian zone informally and spontaneously. Because of this development, B. T. Mugaruka et al. (2017) suggested that the knowledge of natural and anthropogenic factors of landslides is an important element for the best management of territories affected by landslide hazards. This situation is at the same time the cause of the precariousness of the neighborhoods located in this zone. It may also increase the vulnerability of the population in the face of natural hazards in the riparian area of Bukavu.

6. References

Balegamire, C., Michellier, C., Muhigwa, J-B., Delvaux, D., Imani, G., and Dewitte, O. (2017). Vulnérabilité du bâti face aux glissements de terrain: analyse spatio-temporelle à Bukavu (RD Congo). Geo-Eco-Trop 41(2), pp. 263–278. [Online] Available at: <http://www.geoecotrop.be/uploads/publications/pub_412_08.pdf> [Accessed 4 August 2021].

Dewitte, O., Dille, A., Depicker, A., Kubwimana, D., Maki Mateso, J. C., Mugaruka Bibentyo, T., Uwihirwe, J., and Monsieurs, E. (2021). Constraining landslide timing in a data-scarce context: from recent to very old processes in the tropical environment of the North Tanganyika-Kivu Rift region. *Landslides 18*(1), pp. 161–177. https://doi.org/10.1007/s10346-020-01452-0.

Dodman, D., Hayley, L., Rusca, M., and Colenbrander, S. (2017). African urbanisation and urbanism: Implications for risk accumulation and reduction. International Journal of Disaster Risk Reduction 26, pp. 7–15. https://doi.org/10.1016/j.ijdrr.2017.06.029.

D'Oreye, N., González, P. J., Shuler, A., Oth, A., Bagalwa, L., Ekström, G., Kavotha, D., Kervyn, F., Lucas, C., Lukaya, F., and Osodundu, E. (2011). Source parameters of the 2008 Bukavu-Cyangugu earthquake estimated from InSAR and teleseismic data. Geophysical Journal International 184(2), pp. 934–948. https://doi.org/10.1111/j.1365-246X.2010.04899.x.

Grecu, F. (2011). Concernant la notion de risque naturel urbain, Analele Universitatii Bucuresti, Seria Geografie LX, pp. 105–116.

Ilunga, L. (1977). L'érosion dans la ville de Bukavu. Antennes du Centre de Recherches Universitaires du Kivu (CERUKI) 2, pp. 277–299.

Kalikone, C., Teganyi, F., Dewitte, O., and Michellier, C. (2017). Impact des déformations du sol sur la vulnérabilité des réseaux de distribution d'eau et d'électricité à Bukavu (RD Congo). Geo-Eco-Trop 41(2), pp. 279–292. [Online] Available at: <http://www.geoecotrop.be/uploads/publications/pub_412_09.pdf> [Accessed 4 August 2021].

Kulimushi, M. S., Mugaruka, B. T., Muhindo, S. W., Michellier, C., and Dewitte, O. (2017). Landslides and elements at risk in the Wesha watershed (Bukavu, DR Congo). Geo-Eco-Trop 41(2), pp. 233–248. [Online] Available at: <http://www.geoecotrop.be/uploads/publications/pub_412_06.pdf> [Accessed 4 August 2021].

Leone, F., and Vinet, F. (2005). La Vulnérabilité, un concept fondamental au cœur des méthodes d'évaluation des risques naturels. In: Leone, F., and Vinet, F. (eds.), La vulnérabilité des Sociétés et des Territoires face aux menaces naturelles: Analyses géographiques. Géorisques 1, Université Paul Valery-Montpellier 3, pp. 9–26. [Online] Available at: <http://www.univ-montp3.fr/gcrn/images/stories/Documents_pdf/georisques_1_lv_part1.pdf> [Accessed 4 August 2021].

Michellier, C., Pigeon, P., Paillet, A., Trefon, T., Dewitte, O., and Kervyn, F. (2020). The Challenging Place of Natural Hazards in Disaster Risk Reduction Conceptual Models: Insights from Central Africa and the European Alps. International Journal of Disaster Risk Science 11, pp. 316–332. https://doi.org/10.1007/s13753-020-00273-y.

Mugaruka, B. T., Kulimushi, M. S., Muhindo, S. W., and Dewitte, O. (2017). Anatomy of Nyakavogo landslide (Bukavu, DR Congo):

interplay between natural and anthropogenic factors. Geo-Eco-Trop 41(2), pp. 249–261. [Online] Available at: <http://www.geo-ecotrop.be/uploads/publications/pub_412_07.pdf> [Accessed 4 August 2021].

Ndynabo, S., Vandecasteele, I., Moeyersons, J., Ozer, A., Ozer, P., Kalegamire, T., and Bahati, C. (2010). Développement de la ville de Bukavu et cartographie des vulnérabilités, R.D. Congo, Annales des Sciences et Sciences Appliquées de l'Université Officielle de Bukavu 2, pp. 120–127.

Nobile, A., Dille, A., Monsieurs, E., Basimike, J., Bibentyo, T. M., D'Oreye, N., Kervyn, F., and Dewitte, O. (2018). Multi-Temporal DInSAR to Characterise Landslide Ground Deformations in a Tropical Urban Environment: Focus on Bukavu (DR Congo). *Remote Sensing* 10(4), 626. https://doi.org/10.3390/rs10040626.

O'Hare, G., and Rivas, S., (2005). The landslide hazard and human vulnerability in La Paz City, Bolivia. The Geographical Journal 171(3), pp. 239–258. [Online] Available at: <www.jstor.org/stable/3451554> [Accessed 4 August 2021].

Thouret, J.-C., and D'Ercole, R. (1996). Vulnérabilité aux risques naturels en milieu urbain: effets, facteurs et réponses sociales. Cahiers des sciences humaines 32 (2), pp.407–422. [Online] Available at: <https://hal.archives-ouvertes.fr/hal-01180445> [Accessed 4 August 2021].

Detection and Attribution of Climate Change in Extreme Precipitation Using Optimal Fingerprinting (Case Study: Southwestern Iran)

Tofigh Saadi[1,✉], Bohloul Alijani[2], Ali Reza Massah Bavani[3], Mehry Akbary[2], Mojtaba Noury[4], Soad Saeidi[5]

[1] Alborz Regional Water Authority, Iran
[2] Kharazmi University, Tehran, Iran
[3] Department of Irrigation and Drainage Engineering, University of Tehran, Tehran, Iran
[4] Iran Water Resources Management Company, Tehran, Iran
[5] Shahid Chamran University, Ahwaz, Iran

✉ tofigh_sadi@yahoo.com

Keywords: attribution, optimal fingerprint method, extreme precipitation, APHRODITE

1. Introduction

Determining regional vulnerability of a basin is one of the issues which have attracted scientists and researchers attentions in recent years. In discussions on climate change, the issue of extreme precipitations is significant because those extreme events are closely related to the increase in temperature of the troposphere and resulting effects of various climatic influences in form of hazards such as flood precipitations (Mondal and Mujumdar, 2015). The effect of global warming on precipitation can be explained by the Clausius-Clapeyron relationship and the associated physical evidence (Allen and Ingram 2002), Due to the fact that the relative humidity in the lower troposphere layer remains constant, the moisture capacity increases about 6 to 7 % per degree Celsius (Willett et al., 2007). Arid regions, where those values are reduced, are no exception (O'Gorman and Muller, 2010). As the Earth's temperature rises, factors such as changes in continental runoff, tropospheric water vapor, large-scale rotational patterns, ice mass balance, evaporation, and evapotranspiration can affect changes in extreme precipitations (Huntington, 2006). According to the literature, extreme precipitations have changed significantly on the global scale (Westra et al., 2013; Fischer and Knutti, 2014). These studies confirm the harmonization of temperature increase with extreme precipitations. Although these studies differ in terms of the definition of extreme events, methods of analysis, and databases, the sensitivity of extreme precipitations to the temperature rise seems not to be similar to the same in smaller spatial and temporal scales (Wasko and Sharma, 2014) because it is assumed that various dynamic and thermodynamic processes are affected by the relationship between precipitation data and atmospheric temperatures (Westra et al., 2013). Recently, extensive research has been conducted to detect changes in trends of hydroclimatic variables and to attribute changes to climate variables caused by anthropogenic forces in different parts of the planet. However, there are few studies in this area on a regional scale.

According to the definition presented by Intergovernmental Panel on Climate Change (IPCC), detection is the process of demonstrating that climate has changed in some defined statistical sense, without providing a reason for that change, while attribution of causes of climate change is the process of establishing the most likely causes for the detected change with some defined level of confidence. Hence, the process of attribution is a more complex one than detection. The reason may be due to the combination of various statistical analyses with the physical understanding (Hegerl and Zwiers, 2011).

Detection and attribution via the fingerprint method which uses modified empirical models is a formal way of understanding the relationship between global warming affected by anthropogenic forcing and observational variables such as extreme precipitation (Hegerl et al, 1996). It is currently the most common detection and attribution way (Zhang et al. 2013; Ribes and Terray, 2013). In a study done by Min et al. (2011) on extreme precipitation, the simulation signals of climate change models caused by anthropogenic forcing were investigated based on the observations of maximum daily precipitation (Rx1day) and the five-day maximum precipitation (Rx5day) of the northern hemisphere (on a semi-international scale). On a regional scale, however, these signals can be more difficult to detect because the signal-to-noise ratio decreases (Karoly and Wu, 2005; Stott et al., 2010). In addition, the extreme precipitations are rare considering their definition and the analysis of extreme precipitations in regional and basin scales is a major challenge in terms of extreme temperature and precipitation fluctuations.

In spite of the challenges of detection and attribution in small and regional scales, in the 5th assessment report of the IPCC (AR5), the approach to moving towards smaller-scale studies has been encouraged and motivated. In addition, due to the novelty of de-

DOI: 10.2312/yes19.14

Station	Station type	Lon.	Lat.	Height (m)
Ahwaz	Synoptic	48.40° E	31.20° N	22.5
Dezful	Synoptic	48.23° E	32.24° N	143
Emamzadeh Gheis	Climatology	51.30° E	31.75° N	2285
Polzaman Khan	Climatology	50.90° E	32.50° N	1885

Table 1: Specifications of the selected stations

tection and attribution via the fingerprint method, especially in Iran (Saadi et al., 2016a,b), and also the importance of the study on extreme precipitation, the present study aims to apply the fingerprint method to external effects of climate change on extreme precipitation in southwestern Iran.

2. Materials and methods

In this study, two data sets of the selected stations (Tab. 1) and APHRODITE (Asian Precipitation - Highly-Resolved Observational Data Integration Towards Evaluation) daily gridded data (Yatagai et al., 2012) at 0.25° resolution during a period of 55 years (1951-2005) were used as precipitation data. Also the NorESM1-M model of the CMIP5 model series was employed for calculation of the region's internal climate change and to simulate climate responses to various forces. The responses addressed in this study include anthropogenic plus natural external forces (ALL), anthropogenic forces alone (ANT), natural forces alone (NAT) and the effects of greenhouse gases forces alone (GHG). In addition, 500-year-old daily precipitation simulation data before the industrial revolution, called control run (Rypdal et al., 2015), was used to simulate the regional climate change and also to provide another independent noise sample for estimating the uncertainty intervals. Figures 1 and 2 shows the methodology in this research and the study area, respectively. We compare observed changes to model simulations with a standard optimal fingerprinting method (Allen and Tett, 1999). This method assumes that the observations Y are expressed as the sum of scaled fingerprints X plus internal variability.

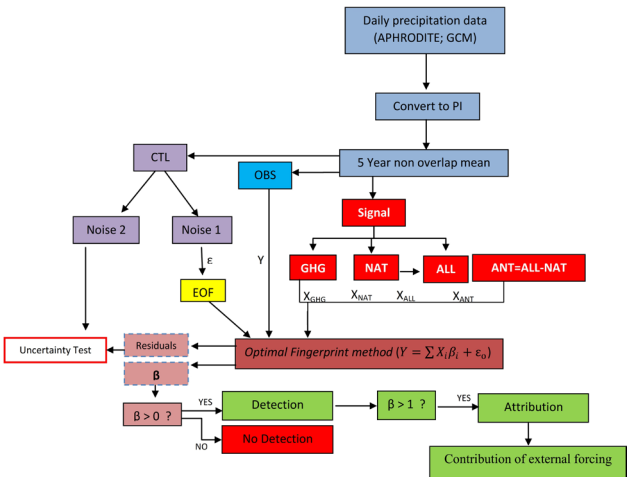

Figure 1: Flowchart of the methodology.

3. Results and discussion

The results of fingerprinting various forces on the 55-year Rx1day and Rx5day time series generated by the OLS algorithm are illustrated in Figure 3. The results obtained from fitting observation data and simulations of the NorESM1-M model show that the scaling factor associated with optimal fingerprinting, the anthropogenic plus natural external forces (ALL), greenhouse gases forcing (GHG) and the human forces alone (ANT) is significantly bigger than zero. Thus, we can say that the Rx1day of the study area during the statistical period of 55 years (1951-2005) has a significant trend and the trend change has been detected. Moreover, the confidence intervals for all detected scaling factors are also larger than one, which means that the simulated changes in the Rx1day under the above signals are consistent with changes in the maximum daily precipitation observed in the Great Karun Basin. Furthermore, the results also show that, changes in the observations can be attributed to the aforementioned forces or signals. Comparison of the results of the intervals indicates a higher uncertainty in the ANT signal fingerprint than those of the GHG and ALL. According to Figure 3a, the natural forces alone (NAT) have no significance, consistent with the change in the significant trend of maximum daily precipitation in southwestern Iran. The confidence intervals for fingerprint coefficients related to the NAT signal include negative values which are not detected. This finding reinforces the results of the effects and contribution of external factors of climate change (GHG, ANT) and confirms these results.

Optimal fingerprint analysis of the investigated forces for the Rx5day time series is similar to the results

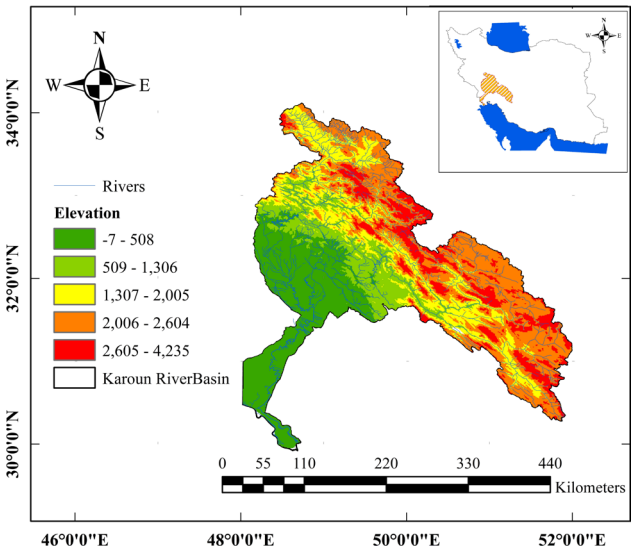

Figure 2: Study area.

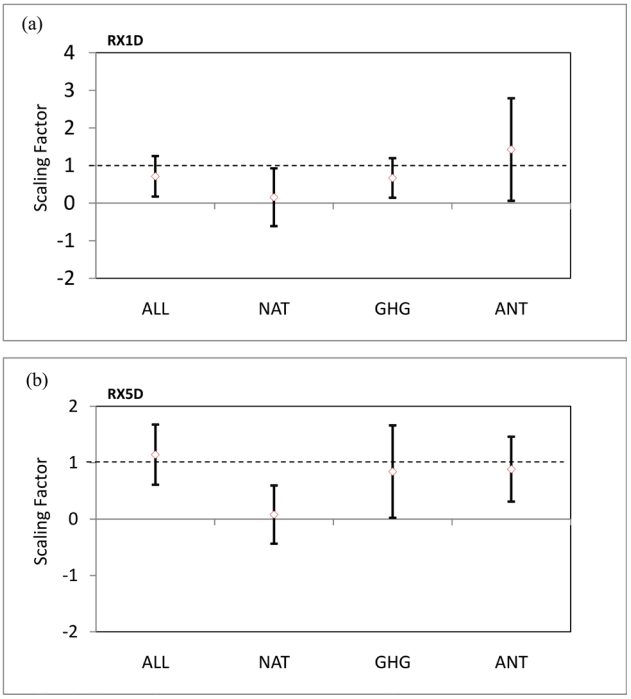

Figure 3: Optimal fingerprint analysis of various forces contributing to the (a) Rx1day and (b) Rx5day changes in southwestern Iran between 1951 and 2005.

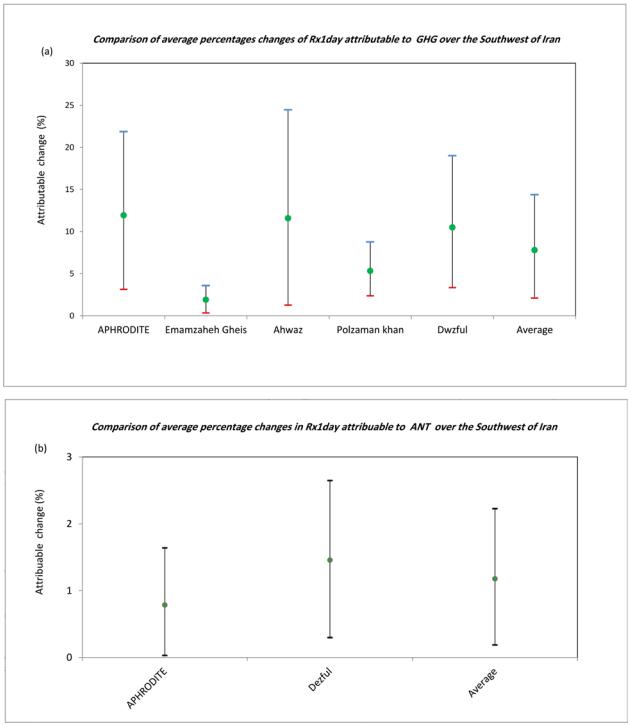

Figure 4: Comparison of the average percentages changes of maximum daily precipitation attributed to the (a) GHG and (b) ANT.

of the maximum daily precipitation index. As shown in Figure 3b, the Rx5day changes in southwestern Iran during the study period have a significant trend and these changes can be attributed to the ALL, GHG, and ANT signals. In other words, the Rx5day simulations extracted from the NorESM-1-1 model are consistent with the five-day maximum observation time series. In addition, the NAT signals were identified to be triggered undetectable and attributable, thus changes in the trend of recent decades have been outside the range of natural fluctuations in the climate.

The results show that, after applying the optimal fingerprinting method, and determining the percentages of changes in the Probability Index (PI) and changes in the median extreme precipitation, the contribution of the effects of climate change signals including ANT and GHGs can be achieved in the study area. To this end, the average percentage of changes in the median precipitation for the whole region was first calculated via previous results. To do this separately, for the ANT and GHG signals, the average of all percentage changes in the median can be calculated and considered as the percentage changes in the basin.

The figures 4a and 4b show the comparison graphs of the mean of the total percentage changes of the Rx1day time series of the Great Karun Basin for GHG and the ANT, respectively. The figures 5a and 5b are the corresponding diagrams for the Rx5day time series. As observed in Figure 4a, the Emamzadeh Gheis Station has the lowest percentage changes in the median, and the Polzaman Khan and Dezful stations have the least estimated percentage changes. The 4x4 degree APHRODITE cell dataset depicted with the letter A and Ahwaz station have similar attributable percentage changes, with the difference that the uncertainty intervals related to the percentage changes attributable to APHRODITE datasets are smaller. The average of all of these percentage changes, each of which is a member of the entire region, is calculated and indicated in the last column of figure 4a. The average median percent change attributable to the ANT, as shown in Figure 4b, is derived

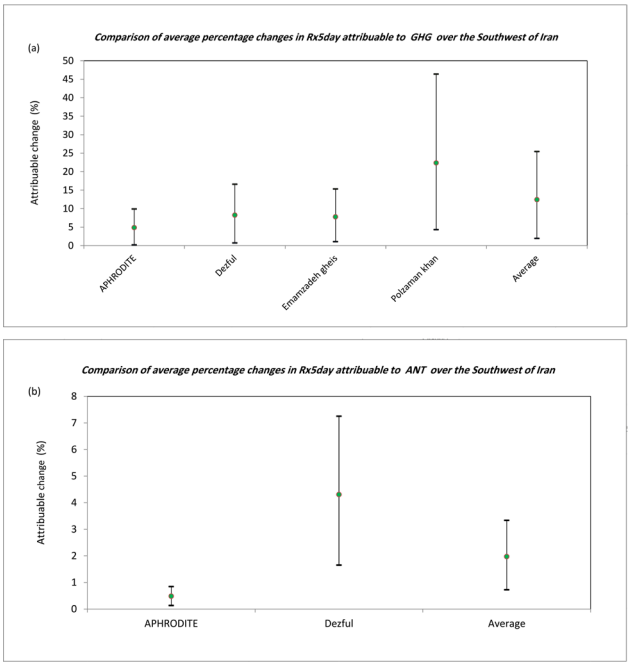

Figure 5: Comparison of the averages of the median percent changes of the Rx5day in southwestern Iran attributable to the (a) GHG and (b) ANT.

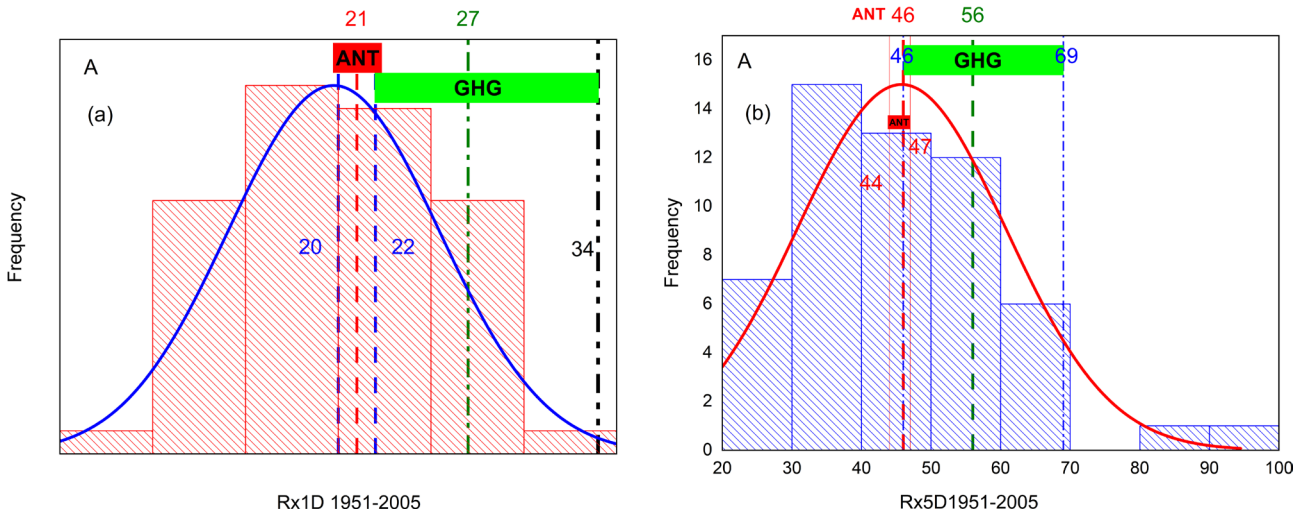

Figure 6: The range of the GHG and ANT effects on the frequency of (a) Rx1day and (b) Rx5day in the frequency histogram between 1951 and 2005.

from averaging two Dezful stations and the APHRODITE datasets. The median percent change at the Dezful station is bigger than that of the APHRODITE dataset.

According to the basin averages which are taken as the percentage change in the basin, the extreme precipitation rate attributed to the GHG and ANT were calculated for all datasets including the APHRODITE data and the four sample stations. Figure 6a illustrates the range of the GHG and ANT forces on the histogram of the maximum daily precipitation rate during 1951 to 2005. As observed, the average daily precipitation has values about 21 mm and higher on a scale, and in other part of area A (averaged APHODITE), it was detected by the ANT. The uncertainty range related to the contribution of the ANT to the maximum daily precipitation is very small including one millimeter difference on both sides and values 20 and 22 mm of maximum daily precipitation. The contributions of GHG are colored with green in the figure including 27 mm maximum daily precipitation and more. In terms of uncertainty in the results of the GHG signal, this value is 22 mm in the lower limit (that is, it corresponds to the high limit of the ANT uncertainty) and 34 mm in the upper limit. The contribution of climate change effects on the Rx5day in southwestern Iran, as indicated in the Figure 6b, shows that in all the results the ANT is close to the median and is about 44 mm average regional precipitation of the Rx5day, and its contribution is confirmed to be larger than the median. Furthermore, the GHG is about 46 mm of Rx5day (area average) immediately after the uncertainty boundary of the upper limit of the ANT, i.e. about in the threshold and its uncertainty intervals are bigger than the uncertainties of the ANT. Although the above values are calculated on the basis of certain mathematical equations, it should be kept in mind that given the available uncertainties and including data especially from global models, it cannot be expected to specify certain values for sharing of climate change. It can be concluded from the results that the GHG effects are within the range of extreme precipitation, while other components of the ANT have had a less severe effect on values close to median. In addition, the starting point of the range attributable to the ANT are much shorter and the uncertainty of the results is low, while the uncertainty range of results related to the GHG is very long and covers the range close to the extreme precipitation up to the most extreme precipitation values.

4. Conclusions

The present research aimed to examine various forces which affect Earth's climate system including human forces at the regional scale. Therefore, the standard fingerprint method was employed and the effects of different forces on the Rx1day and Rx5day for the statistical period of 1951-2005 in southwestern Iran were investigated. According to the results, the extreme precipitation of the study area during 1951-2005 had a significant rise. These findings are consistent with previous studies (for example, Zhang et al., 2013) and with the general model derived from global scales. This is confirmed by the relevant mechanism between global warming and increase in relative humidity of the atmosphere and increase in the probability of extreme precipitation by average global temperature rise. The NorESM1-M model reacted significantly to the ALL, and the simulation of the signal was compatible with the observed changes in the studied indices. In other words, the changes of the significant trend of extreme precipitation of the study area was attributed to the ALL signal. The contribution of ANT and GHG have been confirmed

as forces of the climate change phenomenon on regional extreme precipitation changes in past periods. The NAT including the effects of solar radiation and volcanic eruptions did not interfere with the changes in the precipitation trend in southwestern Iran. These results reinforce the existence of non-natural factors in past change and increase the probability of regional climate vulnerability to the effects of climate change. The GHG forces include extreme precipitation to some extent, while other components of the NAT have affected values close to the median and with lower intensity. Moreover, the starting point of the range attributable to the ANT are much shorter, and the uncertainty of the results is low, while the uncertainty range of the results is associated to the GHG, and covers the range close to the median of the maximum precipitation up to the biggest values of extreme precipitation.

5. References

Allen, M.R. and Tett, S.F., 1999. Checking for model consistency in optimal fingerprinting. Climate Dynamics 15(6), pp. 419–434. https://doi.org/10.1007/s003820050291.

Allen, M.R. and Ingram, W.J., 2002. Constraints on future changes in climate and the hydrologic cycle. Nature 419(6903), pp. 228–232. https://doi.org/10.1038/nature01092.

Fischer, E.M. and Knutti, R., 2014. Detection of spatially aggregated changes in temperature and precipitation extremes. Geophysical Research Letters 41(2), pp. 547–554. https://doi.org/10.1002/2013GL058499.

Hegerl, G. and Zwiers, F., 2011. Use of models in detection and attribution of climate change. Wiley interdisciplinary reviews: climate change 2(4), pp. 570–591. https://doi.org/10.1002/wcc.121.

Hegerl, G.C., Von Storch, H., Hasselmann, K., Santer, B.D., Cubasch, U. and Jones, P.D., 1996. Detecting greenhouse-gas-induced climate change with an optimal fingerprint method. Journal of Climate 9(10), pp. 2281–2306. https://doi.org/10.1175/1520-0442(1996)009<2281:DGGICC>2.0.CO;2.

Huntington, T.G., 2006. Evidence for intensification of the global water cycle: review and synthesis. Journal of Hydrology 319(1-4), pp. 83–95. https://doi.org/10.1016/j.jhydrol.2005.07.003.

Karoly, D.J. and Wu, Q., 2005. Detection of regional surface temperature trends. Journal of Climate 18(21), pp. 4337–4343. https://doi.org/10.1175/JCLI3565.1.

Min, S.K., Zhang, X., Zwiers, F.W. and Hegerl, G.C., 2011. Human contribution to more-intense precipitation extremes. Nature 470(7334), pp. 378–381. https://doi.org/10.1038/nature09763.

Mondal, A. and Mujumdar, P.P., 2015. On the detection of human influence in extreme precipitation over India. Journal of Hydrology 529, pp. 1161–1172. https://doi.org/10.1016/j.jhydrol.2015.09.030

O'Gorman, P.A. and Muller, C.J., 2010. How closely do changes in surface and column water vapor follow Clausius–Clapeyron scaling in climate change simulations?. Environmental Research Letters 5(2), 025207. https://doi.org/10.1088/1748-9326/5/2/025207.

Stott, P.A., Gillett, N.P., Hegerl, G.C., Karoly, D.J., Stone, D.A., Zhang, X. and Zwiers, F., 2010. Detection and attribution of climate change: a regional perspective. Wiley Interdisciplinary Reviews: Climate Change 1(2), pp. 192–211. https://doi.org/10.1002/wcc.34.

Ribes, A. and Terray, L., 2013. Application of regularised optimal fingerprinting to attribution. Part II: application to global near-surface temperature. Climate dynamics 41(11-12), pp. 2837–2853. https://doi.org/10.1007/s00382-013-1736-6.

Rypdal, K., Rypdal, M., and Fredriksen, H. B., 2015. Spatiotemporal long-range persistence in Earth's temperature field: Analysis of stochastic–diffusive Energy balance models. Journal of Climate 28(21), 8379–8395. https://doi.org/10.1175/JCLI-D-15-0183.1.

Saadi, T., Alijani, B., Massah Bavani, A.R. and Akbary, M., 2016a. Detection of extreme precipitation changes and attribution to climate change using standard optimal fingerprinting (Case study: The Southwest of Iran). Journal of Spatial Analysis Environmental hazarts 3(3), pp. 65–80. https://doi.org/10.18869/acadpub.jsaeh.3.3.65.

Saadi, T. Alijani, B., Massah Bavani, A. R., and Akbary, M. 2016b. Detection of extreme precipitation and attribution to climate change (Case study: The Great Karun river basin); unpublished PhD thesis, Kharazmi University, Tehran, Iran.

Wasko, C. and Sharma, A., 2014. Quantile regression for investigating scaling of extreme precipitation with temperature. Water Resources Research 50(4), pp. 3608–3614. https://doi.org/10.1002/2013WR015194.

Westra, S., Alexander, L.V. and Zwiers, F.W., 2013. Global increasing trends in annual maximum daily precipitation. Journal of Climate 26(11), pp. 3904–3918. https://doi.org/10.1175/JCLI-D-12-00502.1.

Willett, K.M., Gillett, N.P., Jones, P.D. and Thorne, P.W., 2007. Attribution of observed surface humidity changes to human influence. Nature 449(7163), pp. 710–712. https://doi.org/10.1038/nature06207.

Yatagai, A., Kamiguchi, K., Arakawa, O., Hamada, A., Yasutomi, N. and Kitoh, A., 2012. APHRODITE: Constructing a long-term daily gridded precipitation dataset for Asia based on a dense network of rain gauges. Bulletin of the American Meteorological Society 93(9), pp. 1401–1415. https://doi.org/10.1175/BAMS-D-11-00122.1.

Zhang, X., Wan, H., Zwiers, F.W., Hegerl, G.C. and Min, S.K., 2013. Attributing intensification of precipitation extremes to human influence. Geophysical Research Letters 40(19), pp. 5252–5257. https://doi.org/10.1002/grl.51010.

Adaptation or Decline? Consequences of Climate Change in Iran

Babak Shaikh Baikloo Islam[1,✉], Tahmineh Sokhansefat[2]

[1] Department of History and Archaeology, Science and Research Branch, Islamic Azad University, Tehran, Iran.
[2] Department of New Sciences and Technologies, University of Tehran, Tehran, Iran.
✉ babak.bagloo@srbiau.ac.ir

Keywords: Iran, Holocene climate change, global warming, extreme weather events, drought, adaptation, renewable energy

1. Introduction

Human health, subsistence, and culture have always been influenced by climate change, from hunter-gatherer communities in the Pleistocene to food producer societies in the Holocene (DeMenocal, 2001; Prentice, 2009; Weiss, 2000). Climatic conditions have been constantly fluctuating at different temporal and spatial scales for a variety of reasons (Berger, 2013; Clark et al., 2002; Shindell et al., 2003). Abrupt climatic changes have caused severe tensions and pressures on the nature and subsistence patterns of human societies and played an important role in the cultural transitions (Anderson et al., 2007; Dalfes et al., 2013; Danti, 2010; Gupta, 2004; Staubwasser and Weiss, 2006; Weiss, 1997). Thus, the adaptation or decline of human societies is directly dependent on the extent of the vulnerability, the public's perception of the importance of climate change, and the effective actions of statesmen to mitigate this phenomenon (Semenza et al., 2008).

The intensification of global warming and increasing extreme weather events, especially floods and droughts, have imposed heavy losses and damages to the industrial and agricultural sectors in Iran over the past fifteen years. Two major problems in Iran are the concentration of power in Tehran (located in North Central Iran) and the ignorance/denial of many officials about the possible consequences of climate change. This led us to recount the Holocene climatic events and their effects on human societies from the Neolithic to the Iron Age (with a case study of the North Central Iran region), as well as propose some possible methods of adaptation and resilience to climate change. The main question is, if this situation continues, to what extent will Iran be able to withstand the consequences of climate change? This country, due to its historical and archeological background, and as one of the most vulnerable countries in the world in terms of environmental conditions and water resources, needs to take greater steps to adapt to the current global warming; otherwise it will soon face severe social and political risks (Madani, 2014).

2. Climate change

Although the general temperature trend in the late Holocene epoch, according to the paleoclimate research of a Greenland ice core (GISP2), indicates cooling (Alley, 2004), due to intense human activities and population growth over the last two hundred years, Earth's temperature has been rising at an accelerating rate. The effects of this climate change on nature include the rising and acidification of ocean water, the melting of glaciers, the rise of El Niño events, and extreme weather events such as heat waves, cold spells, severe storms, flooding, droughts, dust storms, and wildfires which disrupt the life of several species. These effects can also have devastating consequences for human health, not only as direct threats to human lives, but also as a cause of internal and external social conflicts (especially water wars), widespread migrations, the spread of fatal diseases, and increased mortality (Pachauri et al., 2014). While the global warming crisis is on the rise, the increasing population will undoubtedly increase the risks.

3. Holocene Climate Change in the Middle East

Climatic archives around the world show that during the Holocene, abrupt climate change has occurred repeatedly (Alley et al., 2003; Bond et al., 1997; Mayewski et al., 2004). Climate change has had devastating effects on many human cultures and civilizations. For example, during the 8.2 ka BP climatic event, a severe cooling period (less severe than Younger Dryas) occurred in the northern hemisphere, which caused severe droughts in the Middle East by weakening Indian monsoons and the Mediterranean and Sudanese precipitation systems (Alley and Ágústsdóttir, 2005; Dixit et al., 2014; Rohling and Pälike, 2005). Most Neolithic cultures in southwest Asia were disrupted in the second half of the 7th millennium BC. The event also triggered the spread of early farmers, by different routes, out of West Asia and the Near East into Greece and Bulgaria (Budja, 2007; Weninger et al., 2006). Historical studies of the last two thousand years show that cooling periods have been directly related to the prevalence of fatal infectious

DOI: 10.2312/yes19.22

epidemics, such as plague and cholera (McMichael, 2012). Therefore, the presence of cooling events has likely led to population decline during this period. Also, during the 5.2, 4.2, and 3.2 ka BP events, the occurrence of severe droughts (in the Northern Hemisphere) caused the decline of many Middle Eastern cultures and civilizations through famine, war, mass migration, sand and dust storms, and possibly the spread of epidemics. The collapse of the developed Uruk culture in Mesopotamia is likely to be justified by the 5.2 ka BP dry event (Danti, 2010; Postgate, 1986; Weiss, 2003), and the 4.2 ka BP Megadrought event appears to be the root cause of the decline for almost all Middle East civilizations of that time: the collapse of the Akkad dynasty, the First Intermediate period in Egypt, and the post-urbanization period in the Indus Valley (Hassan, 1997; Possehl, 1997; Staubwasser et al., 2003; Weiss et al., 1993; Weiss, 2016; Welc and Marks, 2014). Also, the period of wars, civil conflicts, migrations, and the collapse of powerful civilizations such as the Kassites (the Middle Babylonian dynasty in Mesopotamia), the Hittites (in Anatolia), Ugarit (in Syria), and the weakening of the Egyptian kingdom between 1200 and 900 BC has been synchronous with the 3.2 ka BP drought event (Kaniewski et al., 2015, 2019).

4. Iran's vulnerability to climate change

Iran lies between latitudes 24° and 40° N and longitudes 44° and 64° E, and due to its proximity to the subtropical region, generally has a semi-arid to arid climate and desert nature. Therefore, the country has been severely vulnerable to drought periods. For example, during the severe drought of the years 1870 to 1872, over one million people across Iran died from famine and starvation (Melville, 1988; Okazaki, 1986). Furthermore, Iran is not easily able to supply the water needed for 83 million people in the agricultural, industrial, and domestic sectors because of limited water reserves and inefficient management of water resources. Therefore, population growth (more than 100 million people by 2050) in parallel with global warming, without the necessary infrastructure and facilities, can have adverse consequences for the livelihood of the people and the security of the country.

Drought periods damage the agricultural and industrial sectors, which can lead to increased unemployment, poverty, public discontent, and, consequently, civil conflicts. Given that several industrialized and densely populated provinces of Iran such as Tehran (the capital city with 10 million inhabitants), Qazvin, Alborz, and Markazi are located in the semi-arid parts of North Central Iran, the occurrence of insecurity (as a result of drought) in this key region can have extremely risky consequences for the whole country. Besides, prolonged droughts lead to the drying up of lakes, wetlands, and the abandonment of agricultural lands, turning them into dust hotspots. Not only is this a threat to people's health, but it also disrupts their daily activities. This phenomenon has created a critical situation in recent years, especially in the Elam, Khuzestan, Sistan, and Baluchistan provinces.

Another important climatic hazard in Iran is flooding. The floods in March 2019 caused heavy damage in the western, southwestern, and northern parts of Iran. The main causes of these tragic events were torrential rains, inefficient urban management, and lack of coordination between academics and government officials (Abbasi et al., 2017; Kardan et al., 2017; Manavipour et al., 2017; Mehdinasab et al., 2014; Roknoddin Eftekhari et al., 2010). Many people were killed and displaced in these events.

5. Impacts of Holocene dry events in North Central Iran

As mentioned, North Central Iran is currently an important region in the country. Therefore, mentioning the effects of Holocene climatic events on the ancient communities of this region can be useful in clarifying the potential consequences of current climate change in Iran.

Archaeological data shows that the region was almost uninhabited during the 8.2 ka BP cold event between ca. 6500 and 6000 BC (Shaikh Baikloo et al., 2018). This event coincides with the end of the Pre-Pottery Neolithic. Evidence of the 8.2 ka BP event can be observed in high-resolution climate proxies in Iran (Fig. 1). It seems that the dry climatic conditions in the continuation of this event lasted until about 5400 BC. Since then, irrigation agriculture in the Near East has flourished. The end of the Pottery Neolithic coincided with the 6.2 ka BP dry event, which occurred between about 4300 and 4000 BC (Shaikh Baikloo et al., 2019). During the Chalcolithic period (4300 – 3000 BC) several dry periods occurred and evidence of the occurrence of floods belonging to the middle and late of this millennium has been found from some ancient sites in North Central Iran; floods that caused long-term abandonment of some areas (Chaychi Amirkhiz and Shaikh Baikloo, 2020). Finally, under the influence of the 5.2 ka BP dry event, this period was also over. Many people in the region appear to have perished during the 5.2 ka BP event due to drought and famine and some communities have also migrated to the southeastern plains of the Caspian Sea through passages of the Alborz mountains

in North Semnan to survive. At that time, this area has been a good place for rural communities due to the more favorable climate (Shaikh Baikloo et al., 2020). The Bronze Age in North Central Iran is considered a period of cultural decline because the number of settlements has decreased significantly (Shaikh Baikloo et al., 2016). Probably the main cause was the 4.2 ka BP dry event and other droughts during the third millennium BC. Paleoclimate studies of Gol-e-Zard (Yellow Flower) Cave in the northeast of Tehran province show two very dry periods in 4.51 – 4.4 and 4.26 – 3.97 ka BP (Carolin et al., 2019). The occurrence of these droughts can explain the sharp decline in population in this region during the third millennium BC. The unfavorable climatic and environmental conditions of this period may have changed the subsistence system of some farming communities in North Central Iran to pastoral-nomadism (Shaikh Baikloo and Chaychi Amirkhiz, 2020). The end of the Bronze Age overlapped with a dry period between ca. 1700 and 1600 BC. Then, in the early Iron Age, a humid climate prevailed, but the occurrence of the 3.2 ka BP dry event has brought intense tension to the Iranian plateau (Fig. 1). Most of the sites belonging to Iron Age I and II (1500 – 900 BC) are cemeteries without evidence of permanent settlement. This dry period has also caused an influx of nomadic groups from the north, whether via the Caucasus or Central Asia (Potts, 2014).

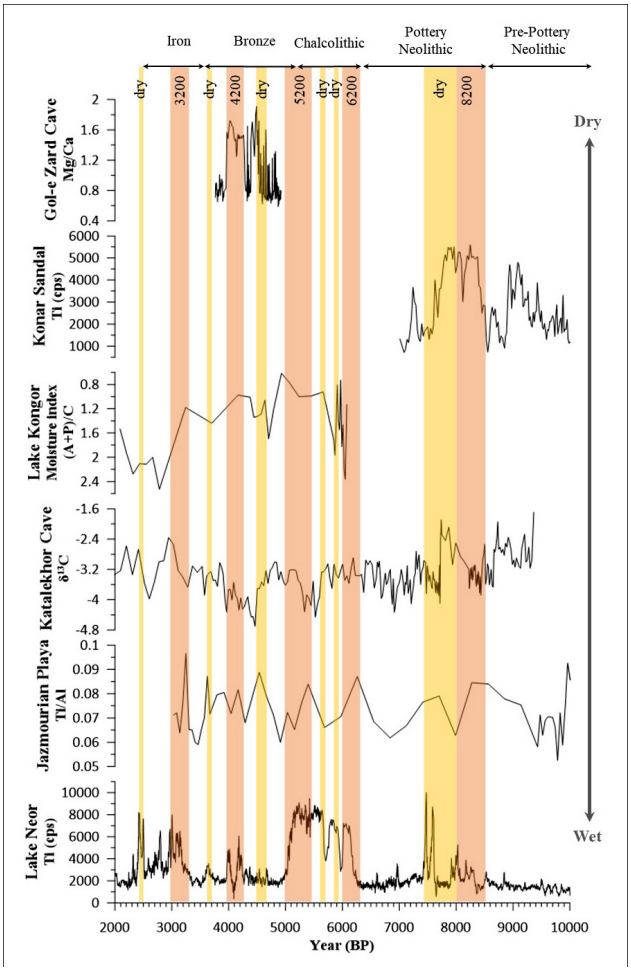

Figure 1: Dry events and dry periods in Iran from 10000 to 2000 BP. Red bands indicate dry events known in the paleoclimate literature (the 6200 BP event is introduced by the first author), and yellow bands illustrate dry climatic periods identified from the results of paleoclimate research in Iran. Lake Neor in Ardebil (Sharifi et al., 2015), Jazmourian Playa in Kerman (Vaezi et al., 2019), Katalekhor Cave in Zanjan (Andrews et al., 2020), Lake Kongor in Gorgan Plain (Shumilovskikh et al., 2016), Konar Sandal in Kerman (Safaierad et al., 2020) and Gol-e Zard Cave (Carolin et al., 2019).

6. Adaptation, resilience and mitigation strategies related to climate change

We propose some methods to deal with the consequences of climate change in Iran. Some of these methods are easily possible, but others require fundamental changes in the country's management strategies. First of all, it is recommended that government decisions are related to academic scientific outputs. One of the main tasks of both government and academia is to raise public awareness about climate change through mass media. This should be done regularly and frequently to institutionalize the culture of dealing with this phenomenon in society. Unfortunately, the majority of people and even the officials are still not aware of the depth of the tragedy.

The potential for renewable energy (solar, wind, and hydro) in Iran is widely available (Bahrami and Abbaszadeh, 2013; Hosseini et al., 2013). According to a study, constructing a solar power plant with an area of 2100 km^2 in the Lut desert (SE Iran) can supply electricity to the whole of Iran (Shaikh Baikloo and Sokhansefat, 2019). Changing the fuel of cars produced in Iran to non-fossil (such as electric and hybrid) can also be effective in the mitigation of global warming and reducing air pollution in large and industrial cities.

In Iran, only 35 to 40 % of water consumption is optimal. In the agricultural sector, mainly due to the use of traditional and inefficient methods of water transfer, more than 70 % of water either penetrates into the ground or evaporates (Haghiri and Karimkoshteh, 2004). Therefore, it is necessary to correct this situation as well.

Encouraging more non-meat foods can be one way to adapt to climate change. Global livestock production emits about 18 % of greenhouse gases (Moran and Wall, 2011). Also, 15.415 liters of water is used to produce one kilogram of beef and 8.763 liters for one kilogram of sheep/goat meat (Mekonnen and Hoekstra, 2012). In Iran, due to religious restrictions and general taste, there is no consumption of some foods, and in the current situation, it is necessary to make

reforms in this regard.

Avoiding international tensions is of great importance for Iran. Over the past four decades, a series of sanctions imposed on Iran has put great pressure on the people's livelihood economy. Inflation and unemployment have risen to unprecedented levels, especially in the last decade (Islam, 2019). These conditions undoubtedly reduce the government's economic power to implement adaptation, resilience, and mitigation strategies related to climate change.

7. Conclusion

Archaeological and paleoclimate studies of Iran clearly show the impact of climatic events on human subsistence patterns. The current trend of anthropogenic global warming is not like the natural climate change in the past, which stopped and decreased after a while. The consequences of climate change for human societies can be migration, disease, unemployment, recession, civil unrest, war, and insecurity. Given the intensification of droughts and torrential rains due to increased global warming, it is necessary to implement adaptation, resilience, and mitigation strategies related to climate change in Iran (and the world). Apart from having an arid environment, Iran also suffers from numerous infrastructure and management (especially water) deficiencies that need to be reformed. Droughts can lead to regional desertification in large parts of Iran, and the occurrence of frequent floods causes heavy damage and losses. The combination of these consequences increases public dissatisfaction and has the potential for unrest and insecurity. Therefore, public understanding of climate change, optimal resource management, and the widespread use of renewable energy instead of fossil fuels in Iran is necessary to reduce the destructive effects of current global warming. Unfortunately, economic sanctions against Iran, in addition to the spread of unemployment and poverty, have led to a sharp decline in the government's economic ability to deal with climate change. Thus, Iran is at considerable risk of socio-economic collapse due to its high environmental vulnerability, inadequate infrastructure, dark international politics, severe economic weakness, and civil conflicts.

8. References

Abbasi, H., Sharafi, S. and Maryakji, Z., 2017. Geomorphological hazards threatening the spatial analysis of urban living complex in Lorestan province. Journal of Spatial Analysis Environmental Hazards 4(2), pp. 107–125. (in Persian). [online] Available at: http://jsaeh.khu.ac.ir/article-1-2719-en.html [Accessed 17 June 2021]

Bahrami, M. and Abbaszadeh, P., 2013. An overview of renewable energies in Iran. Renewable and Sustainable Energy Reviews 24, pp. 198–208. https://doi.org/10.1016/j.rser.2013.03.043.

Alley, R.B., Marotzke, J., Nordhaus, W.D., Overpeck, J.T., Peteet, D.M., Pielke, R.A., Pierrehumbert, R.T., Rhines, P.B., Stocker, T.F., Talley, L.D. and Wallace, J.M., 2003. Abrupt climate change. Science 299(5615), pp. 2005–2010. https://doi.org/10.1126/science.1081056.

Alley, R.B., 2004. GISP2 Ice Core Temperature and Accumulation Data NOAA. ftp://ftp.ncdc.noaa.gov/pub/data/paleo/icecore/greenland/summit/gisp2/isotopes/gisp2_temp_accum_alley2000.txt.

Alley, R.B. and Ágústsdóttir, A.M., 2005. The 8k event: cause and consequences of a major Holocene abrupt climate change. Quaternary Science Reviews 24(10-11), pp. 1123–1149. https://doi.org/10.1016/j.quascirev.2004.12.004.

Anderson, D.G., Maasch, K.A., Sandweiss, D.H. and Mayewski, P.A., 2007. Climate and culture change: exploring Holocene transitions. In: Anderson, D.G., Maasch, K.A., and Sandweiss, D.H. (Eds.), Climate Change and Cultural Dynamics. Academic Press., Amsterdam, pp. 1–23. https://doi.org/10.1016/B978-012088390-5.50006-6.

Andrews, J.E., Carolin, S.A., Peckover, E.N., Marca, A., Al-Omari, S. and Rowe, P.J., 2020. Holocene stable isotope record of insolation and rapid climate change in a stalagmite from the Zagros of Iran. Quaternary Science Reviews 241, 106433. https://doi.org/10.1016/j.quascirev.2020.106433.

Berger, A., 2013. Milankovitch and climate: understanding the response to astronomical forcing. Springer, Dordrecht, 377 pp.

Bond, G., Showers, W., Cheseby, M., Lotti, R., Almasi, P., DeMenocal, P., Priore, P., Cullen, H., Hajdas, I. and Bonani, G., 1997. A pervasive millennial-scale cycle in North Atlantic Holocene and glacial climates. Science 278, pp. 1257–1266. https://doi.org/10.1126/science.278.5341.1257.

Budja, M., 2007. The 8200 calBP 'climate event' and the process of Neolithisation in south-eastern Europe. Documenta Praehistorica 34, pp. 191–201. https://doi.org/10.4312/dp.34.13.

Carolin, S.A., Walker, R.T., Day, C.C., Ersek, V., Sloan, R.A., Dee, M.W., Talebian, M. and Henderson, G.M., 2019. Precise timing of abrupt increase in dust activity in the Middle East coincident with 4.2 ka social change. Proceedings of the National Academy of Sciences 116(1), pp. 67–72. https://doi.org/10.1073/pnas.1808103115.

Chaychi Amirkhiz A. and Shaikh Baikloo Islam, B., 2020. Climatic Hazards of Fourth Millennium BC and Cultural Responses of Human Societies. Case Study: Tehran Plain and Qomroud-Gharachay Basin. Journal of Research on Archaeometry 6(1), pp. 67–80. (in Persian).

Clark, P.U., Pisias, N.G., Stocker, T.F. and Weaver, A.J., 2002. The role of the thermohaline circulation in abrupt climate change. Nature 415(6874), pp. 863–869. https://doi.org/10.1038/415863a.

Danti, M.D., 2010. Late Middle Holocene Climate and Northern Mesopotamia: Varying Cultural Responses to the 5.2 and 4.2 ka Aridification Events. In: Mainwaring, A.B., Giegengack, R. and Vita-Finzi, C. (Eds.), Climate Crises in Human History. American Philosophical Society, Philadelphia, pp. 139–172.

DeMenocal, P.B., 2001. Cultural responses to climate change during the late Holocene. Science 292(5517), pp. 667–673. https://doi.org/10.1126/science.1059287.

Dixit, Y., Hodell, D.A., Sinha, R. and Petrie, C.A., 2014. Abrupt weakening of the Indian summer monsoon at 8.2 kyr BP. Earth and Planetary Science Letters 391, pp. 16–23. https://doi.org/10.1016/j.epsl.2014.01.026.

Gupta, A.K., 2004. Origin of agriculture and domestication of plants and animals linked to early Holocene climate amelioration. Current Science 87, pp. 54–59. www.jstor.org/stable/24107979.

Haghiri, M. and Karimkoshteh, M., 2004. Water-Reform Strategies in Iran's Agricultural Sector. Perspectives on Global Development and Technology 3(3), pp. 327–346. https://doi.org/10.1163/1569150042442511.

Hassan, F.A., 1997. The dynamics of a riverine civilization: a geoarchaeological perspective on the Nile Valley, Egypt. World Archaeology 29(1), pp. 51–74. https://doi.org/10.1080/00438243.1997.9980363.

Hosseini, S.E., Andwari, A.M., Wahid, M.A. and Bagheri, G., 2013. A review on green energy potentials in Iran. Renewable and Sustainable Energy Reviews 27, pp. 533–545. https://doi.org/10.1016/j.rser.2013.07.015.

Islam, L.S., 2019. US Imposed Sanction on Iran: Analysing The Aftermaths. PhD thesis, Bangladesh University of Professionals, 47 pp.
Kaniewski, D., Guiot, J. and Van Campo, E., 2015. Drought and societal collapse 3200 years ago in the Eastern Mediterranean: a review. Wiley Interdisciplinary Reviews: Climate Change 6(4), pp. 369–382. https://doi.org/10.1002/wcc.345.
Kaniewski, D., Marriner, N., Bretschneider, J., Jans, G., Morhange, C., Cheddadi, R., Otto, T., Luce, F. and Van Campo, E., 2019. 300-year drought frames Late Bronze Age to Early Iron Age transition in the Near East: new palaeoecological data from Cyprus and Syria. Regional Environmental Change 19(8), pp. 2287–2297. https://doi.org/10.1007/s10113-018-01460-w.
Kardan, N., Hassanzadeh, Y. and Arzanlou, A., 2017. 2D Numerical Simulation of Urban Floods Using CCHE2D (Case Study: Aghghala City). Iranian Journal of Marine Technology 4(4), pp. 25–36. (in Persian).
Madani, K., 2014. Water management in Iran: what is causing the looming crisis? Journal of Environmental Studies and Sciences 4(4), pp. 315–328. https://doi.org/10.1007/s13412-014-0182-z.
Manavipour, K., Shiravand, H. and Shah Hosseini, M., 2017. Zoning and monitoring of atmospheric and climatic disasters in Lorestan province. New research in geographical sciences, architecture and urban planning 1(5), pp. 47–68. (in Persian).
Mayewski, P.A., Rohling, E.E., Stager, J.C., Karlén, W., Maasch, K.A., Meeker, L.D., Meyerson, E.A., Gasse, F., van Kreveld, S., Holmgren, K. and Lee-Thorp, J., 2004. Holocene climate variability. Quaternary Research 62(3), pp. 243–255. https://doi.org/10.1016/j.yqres.2004.07.001.
McMichael, A.J., 2012. Insights from past millennia into climatic impacts on human health and survival. Proceedings of the National Academy of Sciences 109(13), pp. 4730–4737. https://doi.org/10.1073/pnas.1120177109.
Mekonnen, M.M. and Hoekstra, A.Y., 2012. A global assessment of the water footprint of farm animal products. Ecosystems 15(3), pp. 401–415. https://doi.org/10.1007/s10021-011-9517-8.
Mehdinasab, M., Tavoosi, T., and Mirzaei, R., 2014. Prediction Probable Flood and Maximum Precipitation Using Poldukhtar Basin Suffered Partial Series. Natural Ecosystems of Iran 5(1), pp. 97–109. (in Persian)
Melville, C., 1988. The Persian Famine of 1870–1872: Prices and Politics. Disasters 12(4), pp. 309–325. https://doi.org/10.1111/j.1467-7717.1988.tb00685.x.
Moran, D. and Wall, E., 2011. Livestock production and greenhouse gas emissions: Defining the problem and specifying solutions. Animal Frontiers 1(1), pp. 19–25. https://dx.doi.org/10.2527/af.2011-0012.
Okazaki, S., 1986. The great Persian famine of 1870–71. Bulletin of the School of Oriental and African Studies 49(1), pp. 183–192. https://doi.org/10.1017/S0041977X00042609.
Pachauri, R.K., Allen, M.R., Barros, V.R., Broome, J., Cramer, W., Christ, R., Church, J.A., Clarke, L., Dahe, Q., Dasgupta, P. and Dubash, N.K., 2014. Climate change 2014: Synthesis Report. Contribution of Working Groups I, II and III to the Fifth Assessment Report of the Intergovernmental Panel on Climate Change. Geneva, Switzerland, 151 pp. http://hdl.handle.net/10013/epic.45156.d001.
Possehl, G.L., 1997. Climate and the eclipse of the ancient cities of the Indus. In: Dalfes, H.N., Kukla, G. and Weiss, H. (Eds.), Third millennium BC climate change and old world collapse. Nato ASI Series I: Global Environmental Change, vol. 49. Springer, Berlin, pp. 193–243. https://doi.org/10.1007/978-3-642-60616-8_8.
Postgate, J.N., 1986. The transition from Uruk to Early Dynastic: continuities and discontinuities in the record of settlement. In: Finkbeiner, U., Röllig, W. (Eds.), Ğamdat Naṣr: period or regional style?: papers given at a symposium held in Tübingen, November 1983, Reichert, Wiesbaden, pp. 90–106.
Potts, D.T., 2014. Nomadism in Iran: from antiquity to the modern era. Oxford University Press, New York, 592 pp. https://doi.org/10.1186/s13570-018-0114-8.
Prentice, R., 2009. Cultural responses to climate change in the Holocene. Anthós 1(1), p. 3. https://doi.org/10.15760/anthos.2009.41.
Rohling, E.J. and Pälike, H., 2005. Centennial-scale climate cooling with a sudden cold event around 8,200 years ago. Nature 434(7036), pp. 975–979. https://doi.org/10.1038/nature03421.
Roknoddin Eftekhari, A., Sadeghloo, T., Ahmadabadi, A. and Sojasi Qidari, H., 2010. Zoning of Rural Regions in Flood Hazard with Use of HEC-GeoRAS Model in GIS Sphere (Case study: flooded villages of Gorganrud Basin). Community Development (Rural and Urban Communities) 1(1), pp. 157–182. (in Persian).
Safaierad, R., Mohtadi, M., Zolitschka, B., Yokoyama, Y., Vogt, C. and Schefuß, E., 2020. Elevated dust depositions in West Asia linked to ocean–atmosphere shifts during North Atlantic cold events. Proceedings of the National Academy of Sciences 117(31), pp. 18272–18277. https://doi.org/10.1073/pnas.2004071117.
Semenza, J.C., Hall, D.E., Wilson, D.J., Bontempo, B.D., Sailor, D.J. and George, L.A., 2008. Public perception of climate change: voluntary mitigation and barriers to behavior change. American Journal of Preventive Medicine 35(5), pp. 479–487. https://doi.org/10.1016/j.amepre.2008.08.020.
Shaikh Baikloo Islam, B., Chaychi Amirzhiz, A. and Valipour, H., 2016. On the Possible Correlation between the Collapse of Sialk IV and Climatological Events during the Middle–Late Holocene. Iranian Journal of Archaeological Studies 6(1), pp. 42–52.
Shaikh Baikloo Islam, B., Chaychi Amirzhiz, A. and Valipour, H., 2018. The Impact of the Mid-Holocene Climate Changes on the Genesis and Development of the early Settlements in North Central Iran. Parseh Journal of Archaeological Studies 2(4), pp. 7–22. (in Persian).
Shaikh Baikloo Islam, B., Chaychi Amirzhiz, A. and Valipour, H., 2019. Cultural Responses of Prehistoric Societies in North Central Iran to Holocene Climate Change, pazhoheshha-ye Bastan shenasi Iran 8(19), pp. 7–26. (in Persian).
Shaikh Baikloo Islam, B. and Chaychi Amirkhiz, A., 2020. Adaptations of the Bronze and Iron Ages Societies of North Central Iran to the Holocene Climatic Events. Climate Change Research 1(2), pp. 39–54. (in Persian). https://dx.doi.org/10.30488/ccr.2020.111121.
Shaikh Baikloo Islam, B., Chaychi Amirkhiz, A., and Niknami, K., 2020. Late Holocene Climatic Events, the Main Factor of the Cultural Decline in North Central Iran During the Bronze Age. Documenta Praehistorica 47, pp. 446–460. https://doi.org/10.4312/dp.47.25.
Shaikh Baikloo Islam, B. and Sokhansefat, T., 2019. A case study on the potential of solar PV power plants as an adaptive solution to climate change issue. In: 14th Congress of the Geographical Association of Iran, University of Shahid Beheshti, Tehran, pp. 908–926. (in Persian).
Sharifi, A., Pourmand, A., Canuel, E.A., Ferer-Tyler, E., Peterson, L.C., Aichner, B., Feakins, S.J., Daryaee, T., Djamali, M., Beni, A.N. and Lahijani, H.A., 2015. Abrupt climate variability since the last deglaciation based on a high-resolution, multi-proxy peat record from NW Iran: The hand that rocked the Cradle of Civilization? Quaternary Science Reviews 123, pp. 215–230. https://doi.org/10.1016/j.quascirev.2015.07.006.
Shindell, D.T., Schmidt, G.A., Miller, R.L. and Mann, M.E., 2003. Volcanic and solar forcing of climate change during the preindustrial era. Journal of Climate 16(24), pp. 4094–4107. https://doi.org/10.1175/1520-0442(2003)016<4094:VASFOC>2.0.CO;2.
Shumilovskikh, L.S., Hopper, K., Djamali, M., Ponel, P., Demory, F., Rostek, F., Tachikawa, K., Bittmann, F., Golyeva, A., Guibal, F., and Talon, B., 2016. Landscape evolution and agro-sylvo-pastoral activities on the Gorgan Plain (NE Iran) in the last 6000 years. The Holocene 26(10), pp. 1676–1691. https://doi.org/10.1177/0959683616646841.
Staubwasser, M., Sirocko, F., Grootes, P. M., and Segl, M. 2003. Climate change at the 4.2 ka BP termination of the Indus valley civilization and Holocene South Asian monsoon variability. Geophysical Research Letters 30(8), pp. 1–7. https://doi.org/10.1029/2002GL016822.
Staubwasser, M., and Weiss, H., 2006. Holocene climate and cultural evolution in late prehistoric–early historic West Asia. Quaternary Research 66(3), pp. 372–387. https://doi.org/10.1016/j.yqres.2006.09.001.
Vaezi, A., Ghazban, F., Tavakoli, V., Routh, J., Beni, A.N., Bianchi, T.S., Curtis, J.H., and Kylin, H., 2019. A Late Pleistocene-Holocene multi-proxy record of climate variability in the Jazmurian playa, southeastern Iran. Palaeogeography, Palaeoclimatology, Palaeoecology 514, pp. 754–767. https://doi.org/10.1016/j.palaeo.2018.09.026.
Weiss, H., 1997. Late third millennium abrupt climate change and social collapse in West Asia and Egypt. In: Dalfes, H.N., Kukla,

G. and Weiss, H. (Eds.), Third millennium BC climate change and old world collapse. Nato ASI Series I: Global Environmental Change, vol. 49. Springer, Berlin, pp. 711–723. https://doi.org/10.1007/978-3-642-60616-8.

Weiss, H., 2000. Beyond the Younger Dryas, Collapse as adaptation to abrupt climate change in ancient West Asia and the Eastern Mediterranean. In: Reycraft, R.M. and Bawden, G. (eds.), Environmental disaster and the archaeology of human response. Anthropological Papers (Maxwell Museum of Anthropology), vol. 7, University of New Mexico. Albuquerque, pp.75-98.

Weiss, H., 2003. Ninevite 5 periods and processes. In: Rova, E.,Weiss, H. (Eds.), The Origins of North Mesopotamian Civilization. Subartu IX, Brepols, Turnhout, pp. 593–624.

Weiss, H., 2016. Global megadrought, societal collapse and resilience at 4.2–3.9 ka BP across the Mediterranean and west Asia. PAGES 24, pp. 62–63.

Weiss, H., Courty, M.A., Wetterstrom, W., Guichard, F., Senior, L., Meadow, R. and Curnow, A., 1993. The genesis and collapse of third millennium north Mesopotamian civilization. Science 261(5124), pp. 995–1004. https://doi.org/10.1126/science.261.5124.995.

Welc, F. and Marks, L., 2014. Climate change at the end of the Old Kingdom in Egypt around 4200 BP: New geoarchaeological evidence. Quaternary International 324, pp. 124–133. https://doi.org/10.1016/j.quaint.2013.07.035.

Weninger, B., Alram-Stern, E., Bauer, E., Clare, L., Danzeglocke, U., Jöris, O., Kubatzki, C., Rollefson, G., Todorova, H. and van Andel, T., 2006. Climate forcing due to the 8200 cal yr BP event observed at Early Neolithic sites in the eastern Mediterranean. Quaternary Research 66(3), pp. 401–420. https://doi.org/10.1016/j.yqres.2006.06.009.

Trace and Major Elements in Iranian Bottled Mineral Water: Effect of Geology and Compliance with National and International Standards

Mahsa Tashakor[1,✉], Soroush Modabberi[2]

[1] Researcher, School of Geology, College of Science, University of Tehran, Tehran, Iran

[2] Associate professor, School of Geology, College of Science, University of Tehran, Tehran, Iran

✉ mahsa.tashakor@ut.ac.ir

Keywords: Mineral bottled water, anions, cations, geological units, Iran

1. Introduction

Mineral bottled water, as a safe source of drinking water, has gained a universal popularity in the last few decades (Cidu et al., 2011). Mineral water is the most common type of bottled water (Doria, 2006), which contains essential element cations and anions derived from lithological sources (Biddau et al., 2019). As many studies on bottled mineral water have shown, trace elements, above certain levels, can be detrimental to human health (Güler et al., 2002; Birke et al., 2010a; Bityukova et al., 2010; Cicchella, et al. 2010; Frengstad et al., 2010; Petrović, et al., 2010; Reimann and Birke, 2010; Smedley, 2010; Banks et al., 2015). Due to the fact that mineral water has its origin from groundwater resources, the influence of regional and in particular aquifer geology on their chemical composition is expected (Brenčič, et al. 2010; Platikanov et al., 2013). Chemical composition of groundwater reflects the local geology of spring source area and the geochemistry of the rocks in contact with the water (Daniele et al., 2019). Groundwater in aquifers may interact with various minerals and become enriched or depleted in some elements (Peh et al., 2010). In Iran, the demand for bottled mineral water consumption has been growing extremely fast in the last few years. However, the detailed chemistry of this vulnerable resource has hitherto received little attention (Samadi et al., 2009; Miranzadeh et al., 2015; Kermanshahi et al., 2010; Salehi et al., 2014). To determine the quality of Iranian bottled mineral water in relation to the contribution of various lithological units, we studied 36 best-selling brands of bottled mineral water throughout the country, and compared the results with the threshold limit values.

2. Methods and Materials

2.1. Characteristics of water sources

The bottled mineral water samples were selected from eighteen provinces located in four different lithological units of Iran, namely Zagros, Alborz, Central Iran and Kopet Dagh (Fig. 1). Groundwater from the spring sources in Chahar Mahal Bakhtiari, Ilam, Kermanshah, Fars and Kohgilouyeh provinces is thought to be influenced by Zagros sedimentary rocks. This unit is dominantly composed of carbonate rocks with interlayers of shale, sandstone, chert, anhydrite and gypsum. The brands of bottled mineral water, sold in the markets of Tehran, Alborz, Ardebil, Zanjan, Golestan, Guilan and Mazandaran provinces, pass through several structural subdivisions of Alborz with different lithological components of sedimentary rocks as well as andesitic to basaltic volcanic rocks (Stöcklin, 1968). Even though Central Iran is dominated by metamorphic and magmatic host rocks, the selected Kerman water has its source in Oligo-Miocene carbonates of this unit. The source of the bottled mineral water produced in Khorasan Razavi province is located in a thick sequence of limestone and dolomite of Kopet Dagh basin in north-eastern Iran.

The number of studied samples per geological unit is proportional to the number of producers in each

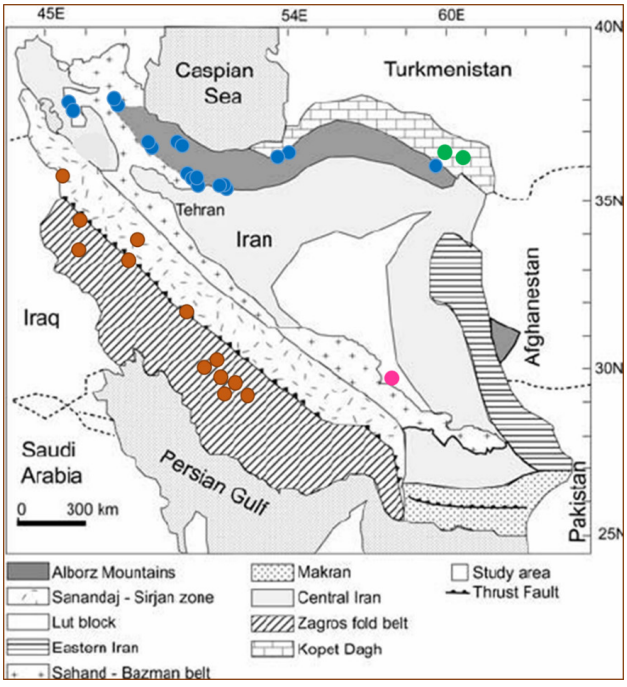

Figure 1: The location of water samples on the map of structural zones of Iran (Stöcklin 1968). Red circle = samples from the Zagros orogeny (folded Zagros and Sanandaj-Sirjan), blue circle = samples from Alborz Mountain and its extension, green circle = samples from Kopet-Dagh, and pink circle = samples from Central Iran unit.

Proceedings of the 5th International YES Congress
DOI: 10.2312/yes19.11

	Unit	Techn.	D.L.	Mean	Median	Std. Dev	Min	Max	25ile	50ile	75ile	Spread	ISIRI	WHO
pH	-	-	0,01	7,81	7,86	0,2	7,27	8,12	7,72	7,86	7,93	1,12	6.5–9	
EC	µS/cm	-	1	366	347	137	95	742	265	347	419	8		
TDS	mg/l	-		238	226	89	62	482	172	226	272	7,8	1500	
TH		-		167	162	71	33	325	125	161	217	9,8	500	
Macro Elements														
Ca	mg/l	ICP-OES	0,1	47,1	46,2	20,8	0,1	95,2	36,4	46,2	59,1	952	300	
K	mg/l	ICP-OES	0,1	0,7	0,7	0,5	0,1	3	0,4	0,7	0,8	30		
Mg	mg/l	ICP-OES	0,01	12,05	9,89	7,97	0,04	36,5	6,66	9,89	17,85	912		
Na	mg/l	ICP-OES	0,1	13,3	8,6	13,8	0,7	59,7	4,4	8,6	19,5	85	200	50
Mn	µg/L	ICP-MS	0,01	0,1	0,05	0,12	0,01	0,54	0,03	0,05	0,14	54	400	
SiO_2	mg/l	ICP-OES	0,1	10,7	9,1	6,9	0,1	33,7	6,2	9,1	14,1	337		
Sr	mg/l	ICP-OES	0,001	0,427	0,339	0,361	<0.001	1,85	0,234	0,339	0,502	3700		
Br	mg/l	IC	0,003	0,023	0,017	0,042	0,003	0,251	0,005	0,017	0,028	83		
Cl	mg/l	IC	0,01	13,31	7,6	14,76	0,86	59,4	2,52	7,6	23,72	69	400	5
F	mg/l	IC	0,01	0,157	0,128	0,122	0,003	0,696	0,091	0,128	0,217	232	4	1,5
HCO_3	mg/l	Titration	0,1	172	172	74	3	322	140	172	214	107		
NH_4	mg/l	Photometry	0,01	<0.01	<0.01	-	<0.01	<0.01	<0.01	<0.01	<0.01	-		
NO_2	mg/l	IC	0,003	<0.003	<0.003	<0.003	<0.003	0,01	<0.003	<0.003	<0.003	-	20	3
NO_3	mg/l	IC	0,001	9,34	5,78	8,68	0,16	36,2	3,7	5,78	12,68	226	50	50
PO_4	mg/l	ICP-OES	0,03	0,02	<0.01	0,16	<0.01	0,87	<0.01	<0.01	<0.01	-		
SO_4	mg/l	IC	0,01	24,66	14,6	31,9	0,66	130	6,93	14,6	29,35	197	400	
Micro and Trace Elements														
Al	µg/l	ICP-MS	0,01	1,5	0,9	1,5	0,1	5,5	0,5	0,9	1,7	55		200
As	µg/L	ICP-MS	0,01	1,98	0,32	9,59	0,01	57,92	0,21	0,32	0,44	5792	10	10
B	µg/L	ICP-MS	0,01	64,1	20,1	138,2	4,8	692	11,2	20,1	52,9	144		2400
Ba	µg/L	ICP-MS	0,01	29,5	16,28	40,71	0,02	237,34	8,68	16,28	39,98	11867	700	700
Cd	µg/L	ICP-MS	0,001	<0.001	<0.001	0,01	<0.001	0,03	<0.001	<0.001	<0.001	60	3	3
Co	µg/L	ICP-MS	0,001	0,017	0,014	0,009	0,006	0,05	0,011	0,014	0,02	8,3		
Cr	µg/L	ICP-MS	0,01	0,96	0,59	1,24	0,02	6,7	0,35	0,59	1,05	335	50	50
Cu	µg/L	ICP-MS	0,01	5,54	0,23	0,79	0,01	3,01	0,08	0,23	0,65	301	2000	2000
Fe	µg/l	ICP-MS	0,1	0,3	0,2	0,3	<0.1	1,6	0,1	0,2	0,3	32		
Hg	µg/L	ICP-MS	0,01	<0.01	<0.01	0,01	<0.01	0,02	<0.01	<0.01	0,01	4	1	6
I	µg/L	ICP-MS	0,1	6,3	4,5	5,6	0,2	22	2,9	4,5	6,4	110		
Li	µg/L	ICP-MS	0,1	5,4	2,7	9,5	0,1	56,7	1	2,7	6,1	567		
Mo	µg/L	ICP-MS	0,01	1,01	0,75	0,95	0,01	3,83	0,29	0,75	1,37	383		
Ni	µg/L	ICP-MS	0,01	0,26	0,16	0,3	0,07	1,71	0,13	0,16	0,21	24	70	70
Pb	µg/L	ICP-MS	0,01	0,04	0,01	0,08	<0.01	0,4	<0.01	0,01	0,03	80	10	10
Rb	µg/L	ICP-MS	0,01	0,42	0,26	0,8	0,02	4,71	0,1	0,26	0,39	235		
Sb	µg/L	ICP-MS	0,001	0,329	0,243	0,201	0,141	0,988	0,186	0,243	0,463	7	5	20
Se	µg/L	ICP-MS	0,01	0,49	0,29	0,59	<0.01	2,64	0,16	0,29	0,53	528	50	40
V	µg/L	ICP-MS	0,01	2,2	1,42	2,3	<0.01	11,98	0,8	1,42	2,92	2396		
Zn	µg/L	ICP-MS	0,01	17,09	1,5	40,4	<0.01	207,1	0,4	1,5	12,4	41420		

Table 1: An overview of general statistics of parameters determined in the analyzed bottled waters (n=36) together with guideline values established by Iranian legislation for drinking water (ISIRI, 1997) and by the WHO (2017).

region. Because of an uneven distribution of annual precipitation, the number and quality of commercially exploited aquifers vary across the country. Accordingly, the majority of samples were taken from the Zagros and Alborz units.

2.2. Bottled water preparation

Among a large number of different brands of mineral bottled water in Iran, 36 of the well-known and top-selling brands were purchased from randomly selected local supermarkets from all over the country. The selected samples were gas-free mineral waters of the same production date and were stored in 0.5 l polyethylene terephthalate (PET) plastic bottles. The bottled mineral waters were purchased in duplicate for quality control purposes and stored in the refrigerator prior to analysis.

2.3. Bottled water analysis

The purchased bottled mineral water samples were analysed at the Federal Institute for Geosciences and Natural Resources (BGR) in Hannover, Germany with the procedures described by Birke et al. (2010a,b), and Reimann and Birke (2010). Chemical elements, ions, and parameters were analysed using the following techniques: inductively coupled plasma optical emission spectrometry for major elements of Ca, Mg, K, Na, PO_4, SiO_2 and Sr; ion chromatography for major anions and cations of Br, Cl, F, NO_2, NO_3 and SO_4; inductively coupled plasma mass spectrom-

etry for 54 trace elements; titration method for HCO_3; photometric method for NH_4; potentiometric method for pH, and conductometric method for electrical conductivity (EC).

3. Results

3.1. Physical parameters and major elements

The pH values of bottled mineral water vary from 7.27 to 8.12, with a median of 7.81, which fall in the range of near neutral to slightly alkaline water. The median value of EC of all samples is 347 µS/cm (ranging from 95 to 742 µS/cm). Total dissolved solids (TDS) varies between 62 and 482 mg/l (median: 226 mg/l). Total hardness (TH) varies from 33 to 325 mg/l, with a median of 162 mg/l.

Bicarbonate is dominant in 30 of the bottled water samples with the median and maximum values of 172 mg/l and 322 mg/l, respectively (Tab. 1). Zagros bottled mineral samples have the highest bicarbonate concentration at 322 mg/l. The content of sulphate in the mineral water samples is generally low except for four brands with SO_4 higher than 40 mg/l. The analysed bottled mineral water samples are characterized by low concentrations of chloride (median: 7.60 mg/l) and fluoride (median: 0.128 mg/l). The highest chloride value (59.4 mg/l) was measured in one brand from Kerman province, Central Iran. Bottled mineral water samples contain various levels of nitrate ranging from 0.16 to 36.2 mg/l. Nitrite yielded values below 0.01 mg/l. Ammonium ion and ammonia were not detected in the analysed bottled mineral water samples. Calcium (median: 46.2 mg/l), sodium (median: 8.6 mg/l) and potassium (median: 0.65 mg/l) are present in concentrations that progressively decrease in the order listed. Magnesium has a wide concentration range, varying from 0.04 to 36.5 mg/l with a median of 9.89 mg/l.

3.2. Trace elements

The median value for most trace elements (As, Cd, Co, Cs, Cu, Fe, Hg, Ni, Pb, Rb, Sb, Sc, Se, Zr) is less than 0.5 µg/l in all of the studied bottled mineral water samples (Tab. 1). The elements Ag, Be, Bi, Br, Ce, Dy, Er, Eu, Ga, Gd, Ge, Hf, Ho, La, Lu, Nb, Nd, Pr, Sm, Ta, Tb, Te, Th, Ti, Tl, Tm, W, Y and Yb occur in very low concentrations and mostly below their detection limits. Bottled mineral water yielded concentrations of Al (0.06 to 5.51 µg/l), Fe (0.04 to 1.56 µg/l) and Mn (0.01 to 0.54 µg/l). The greatest variability (maximum value divided by minimum value) was observed for As, Ba, Cr, Cu, I, Li, Mo, Se, V and Zn where the concentrations differ by several orders of magnitude. The concentration of As is significantly high (58 µg/l) in one sample collected from Kerman province, while the amount of As in the other bottled mineral water samples vary between 0.01 to 1 µg/l. The maximum permissible value of As is 10 µg/l (WHO, 2017; ISIRI, 1997). Furthermore, this sample together with one from Zanjan contains considerable amounts of boron at 522 µg/l and 692 µg/l, respectively. Concentration of boron in the other samples range between 4 and 132 µg/l. The WHO standard (2017) suggests a permissible value of 2400 µg/l for boron.

4. Discussion

The pH value range in bottled mineral water samples is in accordance with the statutory range of Iranian standards for potable water (pH 6.5 to 9.0). All bottled mineral water samples are within the optimal European Commission limits for bottled mineral water (Birke et al., 2010b), and thus reflect adequate content in TDS.

Concentration of most major ions complies with recommendations by ISIRI (1997) and WHO (2017). Based on piper diagrams, thirty out of the 36 analysed bottled mineral water samples are of Ca-HCO_3 hydrogeochemical type. No health-based guideline is proposed for HCO_3. The taste limit for calcium is between 100 and 300 mg/l (Van der Aa, 2003). Hydrochemical types of bottled mineral water samples do not change over the four structural units of Iran, but presents a relatively broader variation in samples drawn from different subdivisions of the Alborz unit. Five of the analysed bottled mineral waters, from Alborz, Ardebil, Tehran (two samples) and Zanjan provinces, are of Na-HCO_3, Ca-SO_4, Ca-Cl, Mg-SO_4 and Na-SO_4 types, respectively.

Concentration of sulphate in samples is relatively low (median: 14.60 mg/l) and within the safe standard limit of 400 mg/l proposed by ISIRI (1997). Regarding NO_3, concentrations of up to 9 mg/l could be considered to be naturally occurring in groundwater (WHO, 2017). Samples with higher contents of NO_3 can be related to the influence of agricultural fertilizers. Chlorine and F^- contents are below the permissible values proposed by WHO (2017), i.e. 5 mg Cl-/l and 1.5 mg F-/l. Based on the Stuyfzand (1989) classification, 32 of the bottled mineral water samples from this study have a chloride content of less than 30 mg/l, and fall into the very oligohaline (< 5 mg/l Cl^-) and oligohaline (5 to 30 mg/l Cl^-) classes. Based on the European Commission classification for bottled mineral water types, as discussed by Birke et al. (2010b), none of the studied samples contain values in excess, i.e.

HCO_3 > 600 mg/l), SO_4 > 200 mg/l, Cl > 200 mg/l, Ca > 150 mg/l, Mg > 50 mg/l, F > 1 mg/l, and Na > 200 mg/l). Due to the very low sodium content of the bottled mineral water samples they mostly fit into the "suitable for low sodium diets" (Na < 20 mg/l).

Trace elements have very low concentrations in bottled mineral water samples and comply with the limits set by national and international standards. Nevertheless, the amount of arsenic and boron is remarkably high in one brand of bottled mineral water sourced in the Central Iran lithological zone. Further research is recommended to elaborate the specific lithological factors causing this anomaly.

The difference between the elemental contents of the analysed bottled mineral water samples, based on their origin in variety of geological and structural units of Iran was verified. The null hypothesis for this test is that the natural concentrations of elements in water samples are not influenced by local geology. This hypothesis rejects when the attained significance level (p) is less than or equal to 0.05. The Kruskal-Wallis test revealed significant differences for boron (p-value = 0.028), nickel (p-value = 0.017), potassium (p-value = 0.031), strontium (p-value = 0.008), bromine (p-value = 0.050) and sulphate (p-value = 0.016). The rest of the components showed no difference in various lithological units (p-value > 0.05).

In general, cations cannot be regarded as an impression of the impact of regional geology because the essential cations of Ca and Mg are originated from both, calcareous and volcanic rocks. Anions are better indicators for revealing such correlation. Samples taken from Zagros contain high bicarbonate concentrations indicating karstic spring sources. Elevated amounts of sulphate in four of the samples can be attributed to: i) the black shale of the Jurassic Shemshak Formation underlying the source rock limestone in an Alborz sample; ii) the marl and evaporate units of the Upper Red Formation underlying the alluvium in Zanjan sample in Alborz Zone; iii) impact of the evaporate unit beneath the volcanic rocks in Kopet-Dagh; iv) the evaporate units underlying the limestone in Central Iran sample.

5. Conclusion

The bottled mineral water samples used in this study represent the top 36 selling brands in Iran. The quality of these water samples generally complies with Iranian (ISIRI, 1997) and WHO (2017) standards for drinking water. Nevertheless, one brand seems not to be suitable for consumption due to containing exceeding amounts of arsenic. This brand of bottled mineral water has its source in Oligo-Miocene carbonates of Central Iran unit. However, we are not certain which lithological factors are responsible for this anomaly. Chemical differences between the bottled mineral water samples in four Iranian geological units are mainly reflected in the content of anions such as carbonate and sulphate. In addition to water-rock interactions, climatic parameters may have contributed to the contents of the studied bottled mineral water samples.

6. References

Banks, D., Birke, M., Flem, B. and Reimann, C., 2015. Inorganic chemical quality of European tap-water: 1. Distribution of parameters and regulatory compliance. Applied Geochemistry 59, 200–210. https://doi.org/10.1016/j.apgeochem.2014.10.016.

Biddau, R., Cidu, R., Da Pelo, S., Carletti, A., Ghiglieri, G. and Pittalis, D., 2019. Source and fate of nitrate in contaminated groundwater systems: Assessing spatial and temporal variations by hydrogeochemistry and multiple stable isotope tools. Science of the Total Environment 647, 1121–1136. https://doi.org/10.1016/j.scitotenv.2018.08.007.

Birke, M., Reimann, C., Demetriades, A., Rauch, U., Lorenz, H., Harazim, B. and Glatte, W., 2010a. Determination of major and trace elements in European bottled mineral water—analytical methods. In: Birke, M., Demetriades, A., De Vivo, B. (Guest Eds.), Mineral Waters of Europe. Special issue, Journal of Geochemical Exploration 107(3), 217–226. https://doi.org/10.1016/j.gexplo.2010.05.005.

Birke, M., Rauch, U., Harazim, B., Lorenz, H. and Glatte, W., 2010b. Major and trace elements in German bottled water, their regional distribution, and accordance with national and international standards. In: Birke, M., Demetriades, A., De Vivo, B. (Guest Eds.), Mineral Waters of Europe. Special issue. Journal of Geochemical Exploration 107(3), 245–271. https://doi.org/10.1016/j.gexplo.2010.06.002.

Bityukova, L. and Petersell, V., 2010. Chemical composition of bottled mineral waters in Estonia. In: Birke, M., Demetriades, A., De Vivo, B. (Guest Eds.), Mineral Waters of Europe. Special issue, Journal of Geochemical Exploration 107(3), 238–244. https://doi.org/10.1016/j.gexplo.2010.07.006.

Brenčič, M., Ferjan, T. and Gosar, M., 2010. Geochemical survey of Slovenian bottled waters. In: Birke, M., Demetriades, A., De Vivo, B. (Guest Eds.), Mineral Waters of Europe. Special issue. Journal of Geochemical Exploration 107(3), 400–409. https://doi.org/10.1016/j.gexplo.2010.09.007.

Cicchella, D., Albanese, S., De Vivo, B., Dinelli, E., Giaccio, L., Lima, A. and Valera, P., 2010. Trace elements and ions in Italian bottled mineral waters: identification of anomalous values and human health related effects. In: Birke, M., Demetriades, A., De Vivo, B. (Guest Eds.), Mineral Waters of Europe. Special issue. Journal of Geochemical Exploration 107(3), 336–349. https://doi.org/10.1016/j.gexplo.2010.04.004.

Cidu, R., Frau, F. and Tore, P., 2011. Drinking water quality: Comparing inorganic components in bottled water and Italian tap water. Journal of Food Composition and Analysis 24(2), 184–193. https://doi.org/10.1016/j.jfca.2010.08.005.

Daniele, L., Cannatelli, C., Buscher, J.T. and Bonatici, G., 2019. Chemical composition of Chilean bottled waters: Anomalous values and possible effects on human health. Science of the Total Environment 689, 526–533. https://doi.org/10.1016/j.scitotenv.2019.06.165.

Doria, M.F., 2006. Bottled water versus tap water: understanding consumers' preferences. Journal of Water and Health 4(2), 271–276. https://doi.org/10.2166/wh.2006.0023.

Frengstad, B.S., Lax, K., Tarvainen, T., Jæger, Ø. and Wigum, B.J., 2010. The chemistry of bottled mineral and spring waters from Norway, Sweden, Finland and Iceland. In: Birke, M., Demetriades, A., De Vivo, B. (Guest Eds.), Mineral Waters of Europe. Special issue. Journal of Geochemical Exploration 107(3), 350–361. https://doi.org/10.1016/j.gexplo.2010.07.001.

Güler, C., Thyne, G.D., McCray, J.E. and Turner, K.A., 2002. Evaluation of graphical and multivariate statistical methods for clas-

sification of water chemistry data. Hydrogeology journal 10(4), 455–474. https://doi.org/10.1007/s10040-002-0196-6.
ISIRI, 1997. Drinking water physical and chemical specifications. Institute of Standards and Industrial Research of Iran. 5th edition. Standard No. 1053.
Kermanshahi, K.Y., Tabaraki, R., Karimi, H., Nikorazm, M. and Abbasi, S., 2010. Classification of Iranian bottled waters as indicated by manufacturer's labellings. Food Chemistry 120(4), 1218–1223. https://doi.org/10.1016/j.foodchem.2009.11.067.
Miranzadeh M.B, Hoseinidoost Gh.R., Marzaleh M.A. 2015. Assessing the Chemical Components of some Iranian Brands of Bottled Water. International Archives of Health Sciences 2(3), 125–128. [online] Available at: http://oldiahs.kaums.ac.ir/article-1-49-en.html [Accessed 29 September 2020]
Peh, Z., Šorša, A. and Halamić, J., 2010. Composition and variation of major and trace elements in Croatian bottled waters. In: Birke, M., Demetriades, A., De Vivo, B. (Guest Eds.), Mineral Waters of Europe. Special issue. Journal of Geochemical Exploration 107(3), 227–237. https://doi.org/10.1016/j.gexplo.2010.02.002.
Petrović, T., Zlokolica-Mandić, M., Veljković, N. and Vidojević, D., 2010. Hydrogeological conditions for the forming and quality of mineral waters in Serbia. In: Birke, M., Demetriades, A., De Vivo, B. (Guest Eds.), Mineral Waters of Europe. Special issue. Journal of Geochemical Exploration 107(3), 373–381. https://doi.org/10.1016/j.gexplo.2010.07.009.
Platikanov, S., Garcia, V., Fonseca, I., Rullán, E., Devesa, R. and Tauler, R., 2013. Influence of minerals on the taste of bottled and tap water: A chemometric approach. Water Research 47(2), 693–704. https://doi.org/10.1016/j.watres.2012.10.040.
Reimann. C. and Birke, M. (Eds), 2010. Geochemistry of European Bottled Water. Borntraeger Science Publishers, Stuttgart, 268 pp.
Salehi, I., Ghiasi, M., Rahmani, A.R., Sepehr, M.N., Kiamanesh, M. and Rafati, L., 2014. Evaluation of microbial and physico-chemical quality of bottled water produced in Hamadan province of Iran. Journal of Food Quality and Hazards Control 1(1), 21–24. [online] Available at: http://jfqhc.ssu.ac.ir/article-1-48-en.html [Accessed 29 September 2020]
Samadi, M.T., Rahmani, A.R., Sedehi, M. and Sonboli, N., 2009. Evaluation of chemical quality in 17 brands of Iranian bottled drinking waters. Journal of Research in Health Sciences 9(2), 25–31. [online] Available at: http://jrhs.umsha.ac.ir/index.php/JRHS/article/view/245/html_26 [Accessed 29 September 2020]
Smedley, P.L., 2010. A survey of the inorganic chemistry of bottled mineral waters from the British Isles. Applied Geochemistry 25(12), 1872–1888. https://doi.org/10.1016/j.apgeochem.2010.10.003.
Stöcklin, J. 1968. Structural history and tectonics of Iran: a review. AAPG Bulletin 52(7), 1229–1258. https://doi.org/10.1306/5D25C4A5-16C1-11D7-8645000102C1865D.
Stuyfzand, P.J., 1989. A new hydrochemical classification of water types with examples of application to The Netherlands. In: Ragone, S.E. (Ed.) Regional characterization of water quality. IAHS Publication 182. International Association of Hydrological Sciences, Wallingford, Oxfordshire, 89–98. [online] Available at: https://iahs.info/uploads/dms/7868.89-98-182-Stuyfzand.pdf [Accessed 29 September 2020]
Van der Aa, M., 2003. Classification of mineral water types and comparison with drinking water standards. Environmental Geology 44(5), 554–563. https://doi.org/10.1007/s00254-003-0791-4.
WHO 2017. Guidelines for drinking-water quality. 4th Edition. World Health Organization, Geneva. [online] Available at: https://www.who.int/water_sanitation_health/publications/drinking-water-quality-guidelines-4-including-1st-addendum/en/ [Accessed 29 September 2020]

Brave New World – Advanced Technologies in Earth Sciences

Global Near Real-Time Flood Mapping Using a Fully Automated Sentinel-1-Based Processing Chain

Christian Böhnke[1]✉, Sandro Martinis[1], Michael Nolde[1], Stefan Schlaffer[1,2], Torsten Riedlinger[1]

[1] Deutsches Zentrum für Luft- und Raumfahrt (DLR), Germany;
[2] Department of Geodesy and Geoinformation, Vienna University of Technology
✉ christian.boehnke@dlr.de

Keywords: flood, SAR, flood mapping, processing chain

1. Introduction

Fast-growing population numbers and climate change as a driving force for extreme meteorological events lead to an increasing impact of natural disasters on the environment in general and human life in particular. Concurrently, technical developments strongly enable a better spacecraft-driven earth observation resulting in an increasing demand for rapid crisis mapping products (Voigt, et al., 2016).

Of all globally monitored natural disasters floods occurred with a frequency of 39 % in the period from 1980 to 2015 (Munich RE, 2016). This number emphasizes the need for a global time-independent flood monitoring followed by information about the spatial distribution of flooded areas. This information directly serves as an input for end users, e.g. rescue forces in the field, insurance companies, planners of infrastructure, etc.

In this article, we demonstrate an automated processing chain automatically deriving flood information from globally acquired Sentinel-1 data. We first describe the data used and further elaborate on the methodology in more detail. The processing chain has been designed to compute global data and currently operates on different areas of interest all over the world. However, we apply the methodology to a single-use case in Kerala, India, and discuss the benefits and disadvantages of a radar-based flood detection system. We conclude this article with the further use of the results in the form of a web-based presentation as well as crisis mapping products.

2. Data

The processing chain derives flood information from Sentinel-1 data. Due to its physical properties, Sentinel-1 as a radar satellite operates independently from cloud cover or illumination. This makes it an ideal tool for full-time flood observation during extreme meteorological events which are usually accompanied by a dense cloud cover and therefore often limit optical remote sensing methods.

Sentinel-1 describes a pair of two satellites Sentinel-1A and Sentinel-1B, orbiting the earth in the same orbital plane 180° apart. Both satellites carry a C-band SAR instrument. Each satellite has a repeat cycle of 12 days (Supplementary Fig. 1). The acquisition frequency highly depends on the region. As a European satellite mission within the Copernicus program, the acquisition frequency for mainland Europe is 6 days.

By default, Sentinel-1 acquires data in VV polarization mode (vertical emit and vertical receive). The polarization mode VH (vertical emit and horizontal receive) is widely available but not always provided (Supplementary Fig. 2).

3. Methodology

We use an automated processing chain written in the high-level programming language Python to compute the flood extent from radar data. The processing chain was originally developed for TerraSAR-X data (Martinis, Twele and Voigt, 2009; Martinis, Kersten and Twele, 2015) and has been extended to also include Sentinel-1 data (Twele, et al., 2016). The workflow is depicted in Fig. 1 and describes the major steps from retrieving the raw data through the main processing procedure where water masks are generated. This happens by computing a threshold, separating the radar image into the thematic classes water and non-water. By targeting two thematic classes as output we require a bimodal backscatter distribution. Therefore, we do not compute the threshold on the entire radar image but on selected image tiles fulfilling the requirement of a bimodal distribution. In a final step, we integrate a fuzzy logic approach to refine the classification result. This step is followed by a region growing implementation to include or exclude further locations not covered by the last steps. The final product is a binary water mask with the information if a pixel holds water or non-water. We distribute the results through an in-house web client to be available for researchers and project partners.

3.1. Data Ingestion

We use ground range detected (GRD) Sentinel-1 data in the VV polarization, acquired in the interferometric wide swath mode (IW). The use of VV polarization is preferred over VH, as dual-

DOI: 10.2312/yes19.01

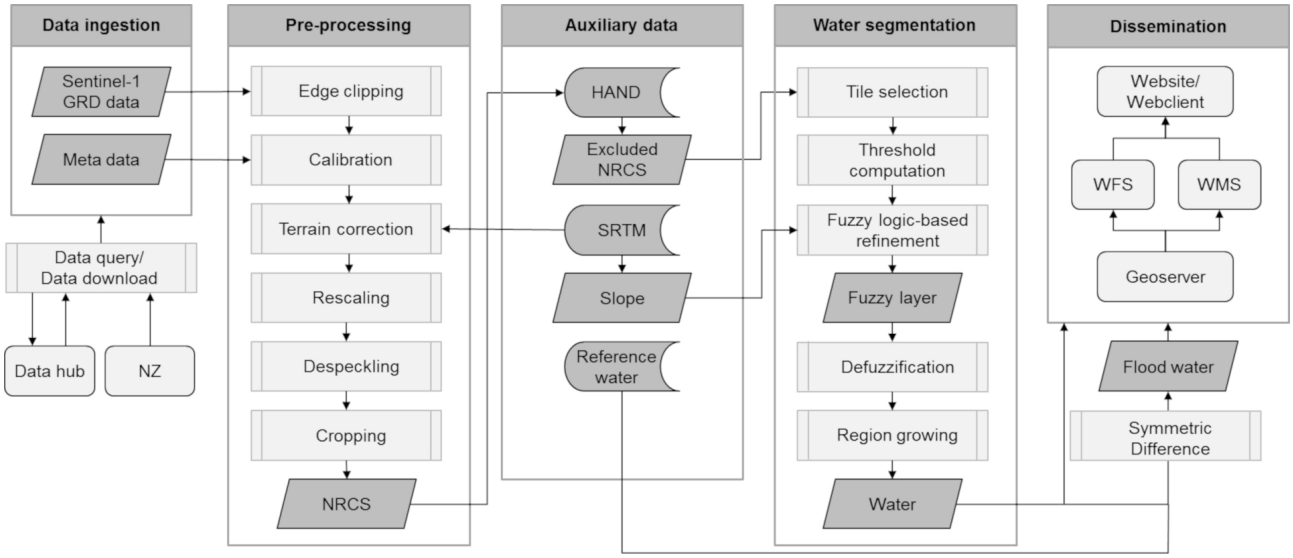

Figure 1: Workflow of the automated Sentinel-1 processing chain.

polarized data dominantly accounts for volume scattering, e.g. over tree canopies. This scattering mechanism is currently not investigated and would add a substantial processing load.

Data is retrieved either through constantly requesting new data from the Sentinel-1 Data Hub of the European Space Agency (ESA) or through data ingestion directly from one of the facilities of the German Aerospace Center (DLR) in Neustrelitz, receiving data directly via an antenna. The entire processing chain is event-driven, i.e. the computation starts as soon as new data is available.

3.2. Pre-processing

Pre-processing requires a radiometric calibration to sigma naught, thus, converting the digital numbers of the input image to physical units, decibels (dB). In a second step, we apply a Range-Doppler terrain correction on the basis of data from the Shuttle Radar Topography Mission (SRTM). All of these steps are performed through the software *snappy*, a Python wrapper around ESA's Sentinel Application Platform SNAP (ESA 2020). The image output of this step is the normalized radar cross section (NRCS) giving information about the radar backscatter in dB for each image pixel.

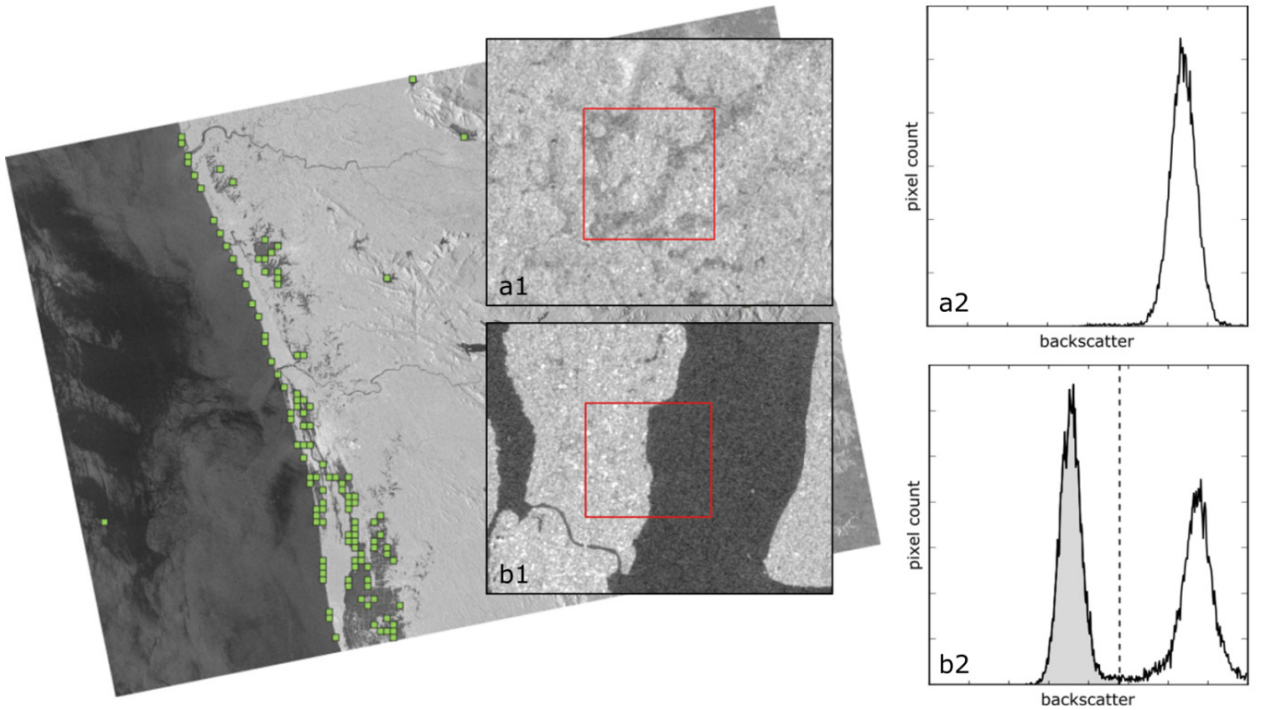

Figure 2: Selected tiles (green) have a low mean backscatter value and a high standard deviation of children mean backscatter values. Two subsets show the effect of these conditions. Subset a1 has a high mean backscatter value and a unimodal backscatter distribution a2, not allowing to separate the histogram into two classes. In contrast to that, subset b1 has a low mean backscatter value and also shows two distinct brightness regimes as can also be seen in the bimodal backscatter distribution b2. Therefore, subset b1 serves as a suitable candidate for threshold computation. The separating threshold is marked with a dashed line.

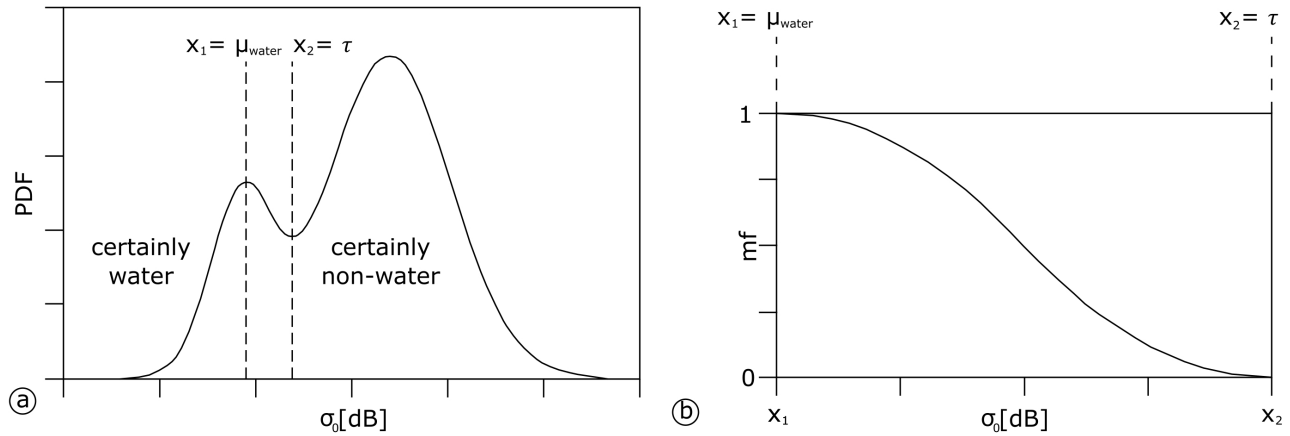

Figure 3: (a) The threshold τ is computed from the backscatter distribution and marks the class break between water and non-water. When applying the threshold to the entire scene μ_{water} describes the mean backscatter value in the water regime. (b) The mean of all water pixels μ_{water} describes locations with a high classification certainty whereas the threshold τ describes locations with a low classification certainty. This is due to the fact that pixel values close to τ may also be misclassified as the underlying backscatter value is caused both by the presence of water and non-water.

3.3. Tiling

After finishing the pre-processing step, the resulting NRCS serves as an input dataset for the following thematic processing task. However, not all areas in the NRCS are suitable for water processing. Nobre, et al. (2011) produced the HAND layer (height above the nearest drainage) to exclude any location with a certain vertical distance from the next drainage. These areas are mainly subject to direct runoff and unlikely to hold enough water for a long period of time. Thus, these areas are to be excluded from the calculation.

In a further step, we divide the NRCS image into quadratic non-overlapping parent tiles and only keep tiles with more than 50 % valid pixels where non-valid pixels are a byproduct of the HAND based exclusion. We then sub-divide each remaining parent tile into 4 quadratic non-overlapping child tiles and record the mean pixel value for each of the sub-tiles. Only tiles with a low mean backscatter value on the parent level as well as a high standard deviation of all means on child-level are suitable for threshold computation (Fig. 2). Requiring a low mean backscatter value corresponds with the physical property of radar data where smooth surfaces like water result in a low backscatter value. Requiring a high standard deviation of the children means ensures to have a bimodal backscatter distribution and thus, a higher probability of having both water and non-water in one tile.

3.4. Thresholding & fuzzy logic

Martinis, et al. (2009) have discussed major image segmentation techniques to extract water information from radar backscatter. In Twele, et al. (2016) they concluded that the algorithm of Kittler and Illingworth (1986) gives the best results. The algorithm computes a cost function and separates the radar backscatter information for each tile into two distinct classes, i.e. water and non-water in the case of our application. The goal is to decrease the effort to separate these classes on the basis of the histogram of the backscatter values. Thus, the separation optimum marks a threshold τ in the unit of the specific pixel value (Fig. 3a).

The threshold is applied to the entire scene and splits the radar image into the two thematic classes. However, the class break is naturally rather imprecise. We, therefore, use a fuzzy logic approach to analyze the membership of any pixel between the computed threshold τ and the mean value of all water pixels μ_{water} (Fig. 3b).

Pixels with a value close to μ_{water} are assigned with a high degree of membership to the class water as they plot well in the class' regime. Pixel values with a greater distance to μ_{water} towards the threshold τ share a higher uncertainty of being classified correctly and are therefore assigned with a low degree of membership to the class water, respectively with a high degree of membership to the class non-water.

Based on that information the first classification result is refined to exclude certain locations with a weak membership to the class water.

The final image is a binary water mask and will be presented in the next section.

4. Use case

In August 2018 the south-Indian state Kerala was affected by unusual monsoon rainfall resulting in the severest flood in decades. The Government of India (2018) reported a deviation in precipitation of 164 % for August 2018 and stated the entire state of Kerala to be affected. The event triggered the International Charter "Space and Major Disasters" for immediate

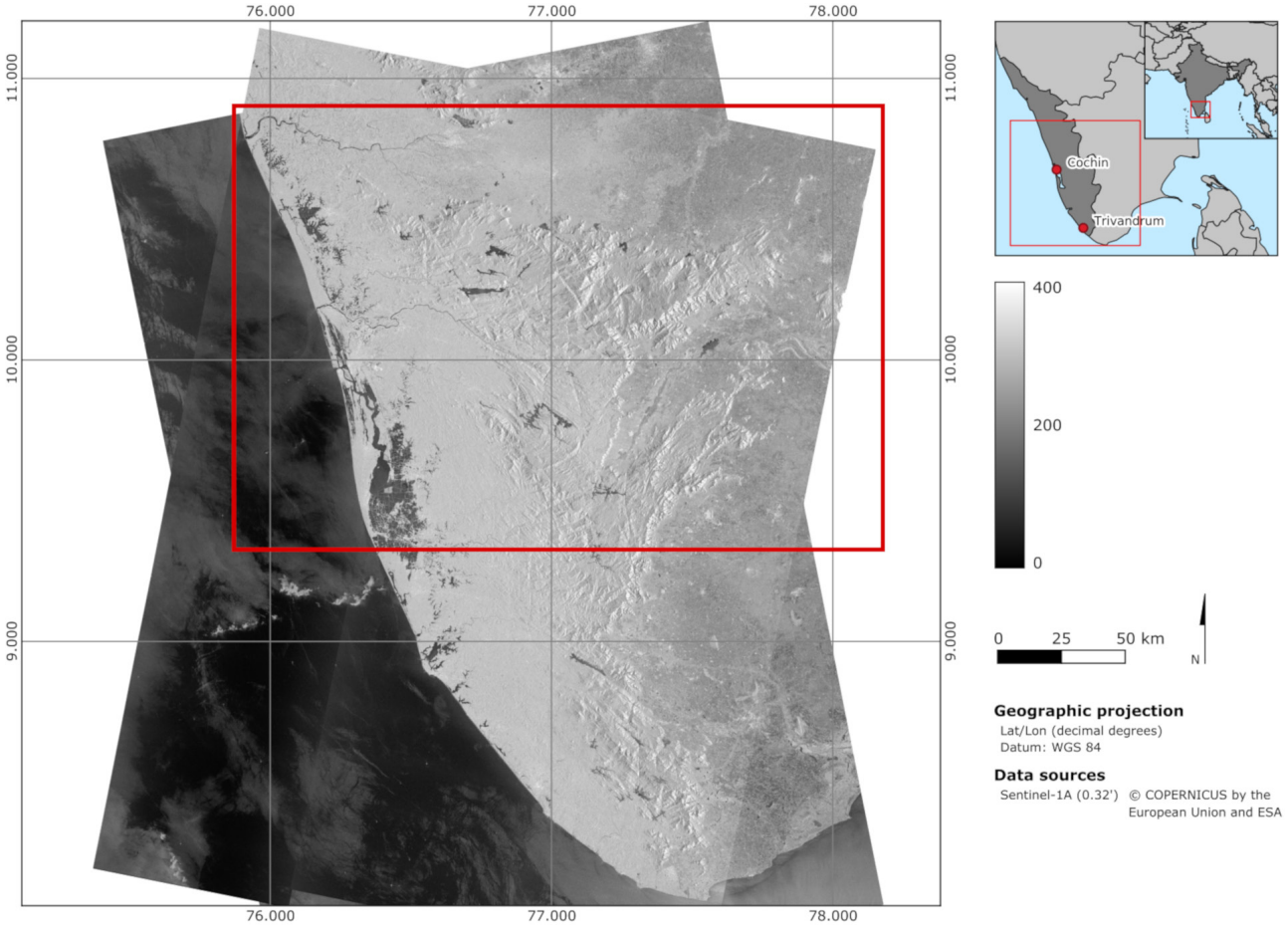

Figure 4: Overview of the study area. Background: 4 Sentinel-1A scenes from descending and ascending path (2 each), acquired on 21 August 2018, VV polarization (© Copernicus data/ESA 2018).

crisis information on the basis of satellite imagery. We took advantage of this situation to check the accuracy of the processing chain and promote further thematic development.

Due to the event, the ESA tasked Sentinel-1 not only to record on the descending path but to also acquire data on the ascending path. We present the output of our processing chain based on the initial

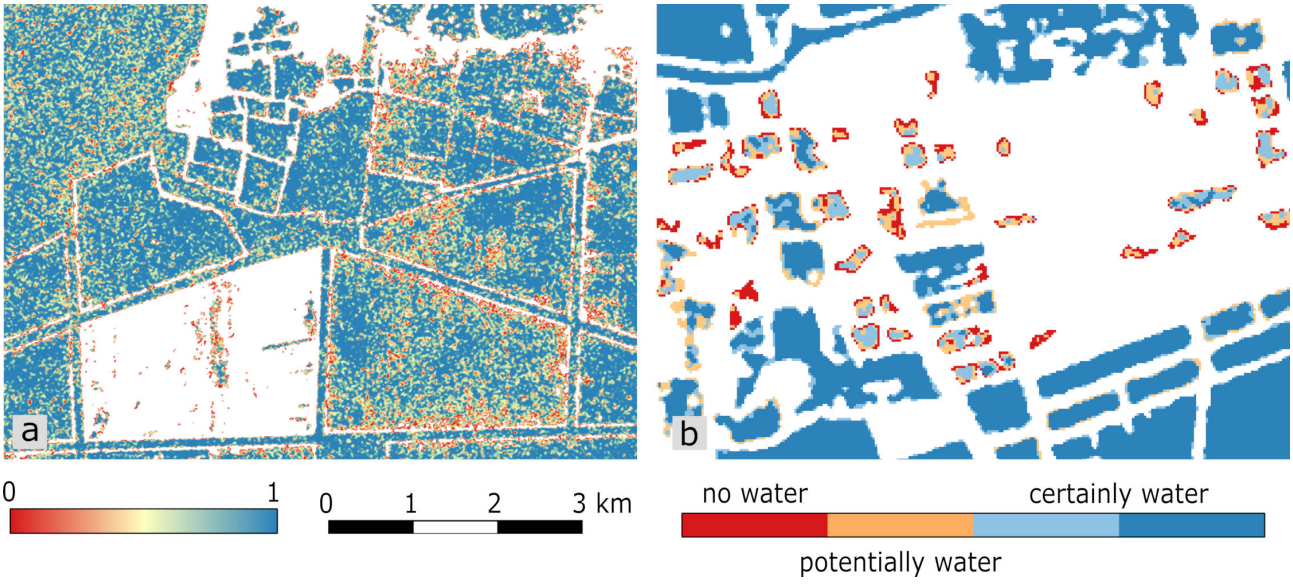

Figure 5: (a) Fuzzy logic-based refinement of NRCS values. Locations with a higher backscatter value are assigned with a low membership degree and thus, a low fuzzy value (close to 0). Locations with lower backscatter are assigned with a high fuzzy value (close to 1). Low fuzzy values mostly plot along edges and are likely to be water-lookalikes. Lower and medium fuzzy values in the center of potentially water patches are usually caused by rough water surfaces, e.g. from wind-induced waves resulting in higher backscatter values. (b) Categorical result of the fuzzy logic-based refinement. Locations with a certain fuzzy value are likely to be water whereas locations with very low fuzzy values are unlikely to be water. Those areas are to be excluded. Locations with medium fuzzy values are subject to region growing and may be re-included.

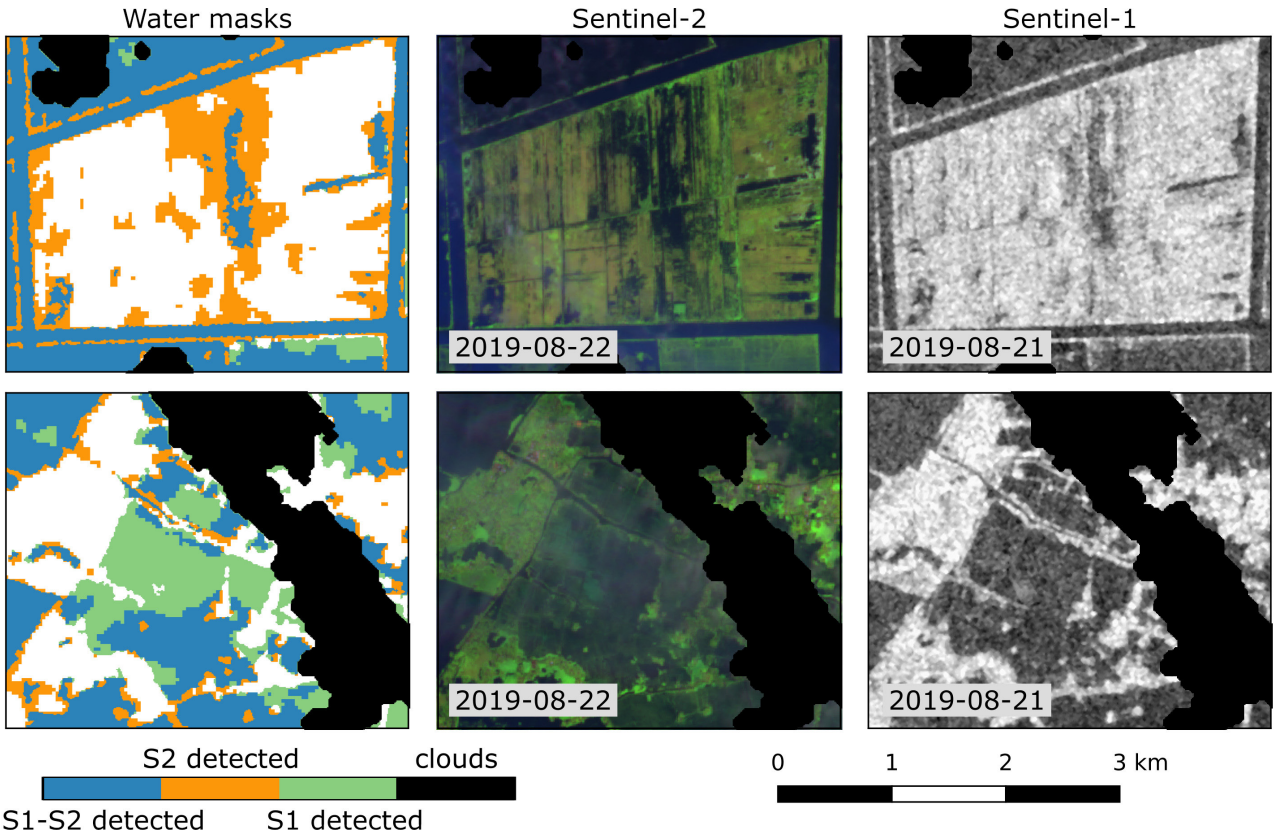

Figure 6: (left) water either detected by Sentinel-1, Sentinel-2, or both. Further subsets show the corresponding Sentinel-2 patch (middle) and Sentinel-1 patch (right). The upper row clearly shows the limitation of radar systems being sensitive to higher surface roughness resulting in non-detected water areas. In contrast to that, the lower row shows the limitation of optical systems where areas are not specifically cloud-covered (see black cloud mask). However, the occurrence of very fine clouds in the center of the path results in a significant change of the spectral signature and thus non-detected water areas.

data and focus on a Sentinel-1 scene in the northern part of the study area (Fig. 4).

Based on the tiling procedure and the thresholding algorithm we get information about water locations. Through the fuzzy logic-based refinement we further exclude location with low certainties of being water (Fig. 5).

5. Discussion

Like every derived dataset, the resulting water masks are not without errors and are highly dependent on the in-situ situation.

The following conditions are likely to cause misclassifications: wind-induced waves roughening the surface and non-water objects with similar backscatter patterns like water, e.g. sand surfaces.

Fig. 5a shows that water bodies are slightly disturbed rather than perfectly smooth, whereas the latter is the ideal behavior.

Wind-induced waves are a common source for misclassifications, especially during extreme meteorological events which are also responsible for floodings. As water surfaces are usually smooth compared to the surrounding area, an increase in surface roughness has a significant impact on the final threshold value. Rough areas within water bodies actually being water by ground truth can have a low fuzzy value, thus, a decreasing certainty for a correct classification.

Water-lookalikes such as sandy features and dunes tend to have similar surface geometries compared to water. Thus, the signal return of water and sand features is nearly the same, challenging the distinction of these classes. Problems arise when observing water objects adjacent to sandy features. In this case, the transition is rather fuzzy and both features may not be differentiated properly. It is also not unlikely to misidentify sand features as water since their fuzzy logic values tend to be similar.

These points underline the fact, that the use of fuzzy logic as an intermediate step helps to refine the initial classification but should not be used solely as a tool for error classification.

In order to solve these challenges, we developed a second processor analyzing Sentinel-2 optical data (Wieland, 2019a; Wieland, 2019b). Sentinel-2, as an optical sensor, has the advantage of being less sensitive to surface disturbances compared to Sentinel-1, as water bodies are detected based on their spectral signature. However, a limitation of the optical system is their sensitivity to cloud cover.

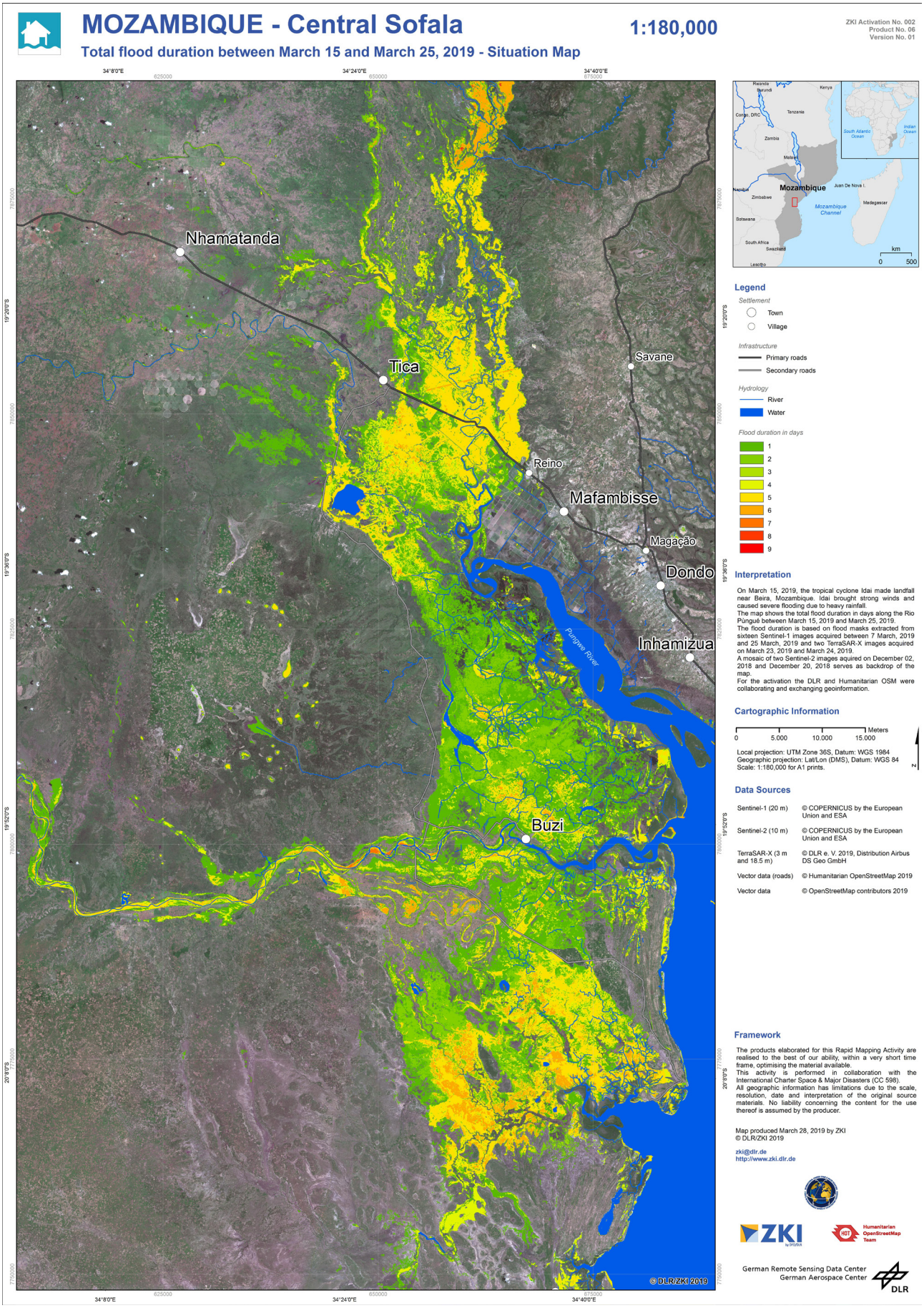

Figure 1: Flood duration map for the area around Buzi, Mozambique. In March 2019 the cyclone Idai made landfall on the east coast of Mozambique resulting in severe floods. Colors of red depict locations with flood duration up to 9 days.

Fig. 6 shows a comparison of Sentinel-1 and Sentinel-2 water masks. Both systems have their benefits and disadvantages, which are highlighted in the subsets.

Further accuracy can be added through the exploitation of VH polarized data, being a frequent effect over tree canopies. By that, flooded vegetation could be detected as well which is to the current state not sufficiently mapped with VV data solely.

6. Conclusions

In connection with extreme meteorological events causing flooding, SAR sensors have proven to give good results. By using an automated system we are able to reduce human interaction and provide a 24/7 data production service. We further distribute the results of the processing through a web client, which is automatically equipped with the latest results whenever available. In the current stage, this web client is not publicly exposed but available to project partners and users of the Center for Satellite Based Crisis Information (ZKI) of the DLR.

A direct use of the results is as input for the computation of flood frequency and flood duration maps (Fig. 7). This information is especially useful for the evaluation of infrastructure as well as which areas were flooded for the longest time and may be sensitive to outbreaks of flood-related diseases.

However, radar sensors have certain physical limitations. Our goal is to enhance the pre-existing processing chain to also include optical data, thus eliminating the disadvantages of both sensor systems.

7. Supplementary material

Supplementary data to this article can be found online at http://doi.org/10.2312/yes19.01.

8. References

Martinis, S., J. Kersten, and A. Twele, 2015. A Fully Automated TerraSAR-X Based Flood Service. ISPRS Journal of Photogrammetry and Remote Sensing 104, 203–212. https://doi.org/10.1016/j.isprsjprs.2014.07.014.

Martinis, S., A. Twele, and S. Voigt, 2009. Towards Operational near Real-Time Flood Detection Using a Split-Based Automatic Thresholding Procedure on High Resolution TerraSAR-X data. Natural Hazards and Earth System Sciences 9, 303–314. https://doi.org/ 10.5194/nhess-9-303-2009.

Government of India, 2018. Study Report: Kerala flood of August 2018. Hydrological Studies Organisation, Central Water Commission, New Delhi, 46 pp. [online] Available at: https://reliefweb.int/report/india/study-report-kerala-floods-august-2018-september-2018 [Accessed 14 August 2020].

Kittler, J. and Illingworth, J. 1986. Minimum error thresholding. Pattern Recognition 19, 41–47. https://doi.org/10.1016/0031-3203(86)90030-0.

Münchener Rückversicherungs-Gesellschaft, 2016. NatCatSERVICE: Loss events worldwide 1980 – 2015, [online] Available at: https://reliefweb.int/report/world/natcatservice-loss-events-worldwide-1980-2015 [Accessed 13 August 2020].

Nobre, A., Cuartas, L., Hodnett, M., Rennó, C., Rodrigues, G., Silveira, A., Waterloo, M. and Saleska, S. 2011. Height Above the Nearest Drainage – a hydrologically relevant new terrain model. Journal of Hydrology 404, 13–29. https://doi.org/10.1016/j.jhydrol.2011.03.051.

European Space Agency, 2020: Sentinel Application Platform, [online] Available at: https://github.com/senbox-org/snap-engine [Accessed 13 August 2020]

Twele, A., Cao, W., Plank, S. and Martinis, S. 2016. Sentinel-1-based flood mapping: a fully automated processing chain. International Journal of Remote Sensing 37, 2990–3004. https://doi.org/10.1080/01431161.2016.1192304.

Voigt, S., Giulio Tonolo, F., Lyons, J., Kucera, J., Jones, B., Schneiderhan, T., Platzeck, G., Kaku, K., Hazarika, M., Czaran, L., Li, S., Pedersen, W., James, G., Proy, C., Macharia, D., Bequignon, J., Guha-Sapir, D., 2016. Global trends in satellite-based emergency mapping. *Science* 353, 247-252. https://doi.org/10.1126/science.aad8728.

Wieland, Marc und Martinis, Sandro (2019a) A modular processing chain for automated flood monitoring from multi-spectral satellite data. Remote Sensing 11, 2330. https://doi.org/10.3390/rs11192330.

Wieland, Marc und Yu, Li und Martinis, Sandro (2019b) Multi-sensor cloud and cloud shadow segmentation with a convolutional neural network. Remote Sensing of Environment 230, 111203. https://doi.org/10.1016/j.rse.2019.05.022.

Land Surface Temperature Volatilities with the Recent Forest Cover Changes in Wilpattu Forest Complex, Sri Lanka

M. M. G. S. Dilini[1,✉], A. K. Wickramasooriya[2,✉]

[1] *Postgraduate Institute of Agriculture, University of Peradeniya, Peradeniya, Sri Lanka*
[2] *Department of Geography, University of Peradeniya, Peradeniya, Sri Lanka*
✉ sathyadilini8@gmail.com; ashvin@pdn.ac.lk

Keywords: Forest Cover Change, Land Surface Temperature, Micro-climatic, Spatiotemporal, Wilpattu Forest

1. Introduction

Forests play an important role in regulating background climatic condition. In order to realize the statement, the study was conducted in and around the area of Wilpattu forest complex. Inherently, the effect of forests on the temperature has a gradient distribution from cooling to warming from the equator towards polar region (Li et al., 2016; Peng et al., 2014). Condition may change due to land cover changes as well as resultant impacts of climatic volatilities. Distribution of Land Surface Temperature (LST) in the tropical region areas shows phenomenal increase for the high built-up areas and decrease for the low built-up, grassland, forested areas, and areas covered by water bodies (Hua et al., 2018). Alleged deforestation of the Wilpattu National Park (WNP) has been focussed in recent past in Sri Lanka. Therefore, the selected area was ideal to check whether there is a land cover change and any causative impact on micro-climatic conditions in the area.

2. Objectives of the Study

The focal objective of the study was to check whether the recent forest cover changes have an observable impact on LST in Wilpattu forest complex. Possible causative factors and measures to mitigate the situation have been examined as minor objectives of the study.

3. Study Area

The Wilpattu forest complex consists of nine adjacent forest reserves (Fig. 1). The boundaries of the forest complex extend over the administrative divisions of Mannar, Puttalam, Anuradhapura and Vavuniya districts. WNP is a well-known forest within this forest complex as it is the largest national park in Sri Lanka and also is important as a Ramsar declared site.

4. Materials and Methods

Using the historical image series of Google Earth Pro from the years 1984 to 2018, remarkable forest cover clearing was identified during recent past. Accordingly, LST maps were prepared using high spatio-temporal resolution Landsat 8 OLI and TIRS bands recorded on the 18th December 2013 at 13:25:41 UTC + 5.30 time and on the 10th of January 2018 at 13:10:15 UTC + 5.30 time.

ERDAS IMAGINE 2014 and ArcMap10.5.1 software applications were used for the preparation of the maps and the analysis of thematic maps and satellite images in this study. After the radiometric corrections, bands were converted to top of atmosphere (TOA) radiance using the radiance rescaling factors (Eq. 1).

$$L_\lambda = M_L \cdot Q_{cal} + A_L \quad \textit{(Eq. 1)}$$

$$M_L = RADIANCE\_MULT\_BAND\_10 = 3.342 \cdot 10^{-4}$$

$$A_L = RADIANCE\_ADD\_BAND\_10 = 0.1$$

Then it was converted to TOA brightness temperature using the thermal constants (Eq. 2).

$$TB = \frac{K_2}{In\left(\frac{K_1}{L_\lambda}+1\right)} - 273.15 \quad \textit{(Eq. 2)}$$

$$K_1 = CONSTANT_{BAND_{10}} = 774.8853$$

$$K_2 = CONSTANT_{BAND_{10}} = 1321.0789$$

The atmospheric brightness temperature was converted to the land surface temperature (Eq. 3).

$$T = \frac{TB}{\left[1 + \left(\lambda \cdot \frac{TB}{c_2}\right) \cdot \ln(e)\right]} \quad \textit{(Eq. 3)}$$

$$e = 0.004 \cdot P_v + 0.986$$

Vegetation fraction (P_V) was estimated preparing Normalized Difference Vegetation Index (NDVI) images for the area (Eq. 4).

$$Pv = \left(\frac{NDVI - NDVI_{min}}{NDVI_{max} - NDVI_{min}}\right)^2 \quad \textit{(Eq. 4)}$$

$$NDVI = \frac{NIR - Red}{NIR + Red}$$

NDVI images were used to clarify the changing nature of forest cover in the study area. Created LST maps were used to compare the effects of forests on LST through the comparison between forests and nearby open lands. Possible reasons for the spatio-temporal changes were uncovered through the Key Informant Interviews (KII) and literature sources. KIIs were conducted with relevant stakeholders like environmental of-

DOI: 10.2312/yes19.17

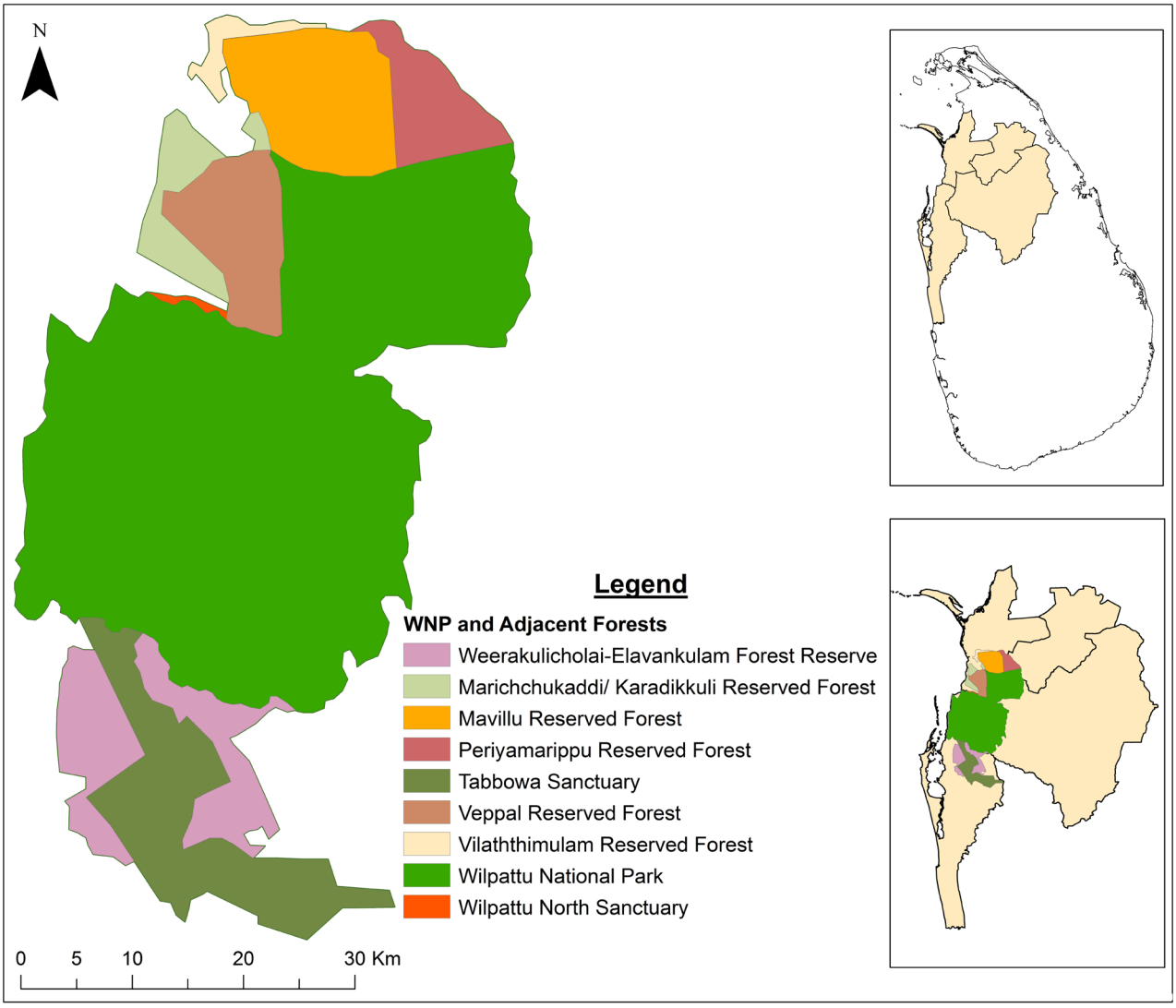

Figure 1: The Study Area.

ficers, range forest officers, public officials relevant government officers and residents in the area.

5. Results and Discussion

LST over the WNP and adjacent forested areas have extensively increased over time (Fig 2). Marichchukaddi/Karadikkuli reserved forest, Vilaththimulam reserved forest, Weerakulicholai-Elavankulam forest reserve and some areas of the northern part of the WNP and the eastern edges of the WNP were remarkable for the higher LST distribution in December 2013. In January 2018, situation got dramatically worse in these areas, especially for the Eastern part of the WNP in the areas adjoining to the Anuradhapura district such as Dematamalgama, Nelumvila, Kukulkatuwa, and Hunuwilgama. LST has gradually spread into the WNP from its eastern edge while highest LST values remain closer to the edge. The south-western part of the WNP remains with a lower LST increase throughout the period. The major supported factor to appointed by the central government, other the lower LST is the existence of dense forest cover in this part of the study area. Mullikkulam, Karadikkuli, Marichchukaddi and Palalikuli areas, which are adjoining to Mannar district from Northern and Western edges of the forest reserve, also indicate extensive LST increases in the year 2018 compared to the year 2013. Total forest cover in WNP and adjacent forested areas has reduced from 204708 ha in 2013 to 197849 ha in 2018 (Fig 3). The total change in forested area due to various uses in the study area during this period is a loss of 6859 ha. It is visible that areas with a higher increase in the LST are associated with high forest clearance areas (Fig. 3).

It is noted that the highest LST value remains around 31 °C over the area throughout the period. However, the lowest LST values varies from 18 °C to 29 °C. When compared to the LST values in areas nearby open lands outside the forest areas higher LST values are recorded and are extended up to 36 °C. This implies that the forest is still dominating

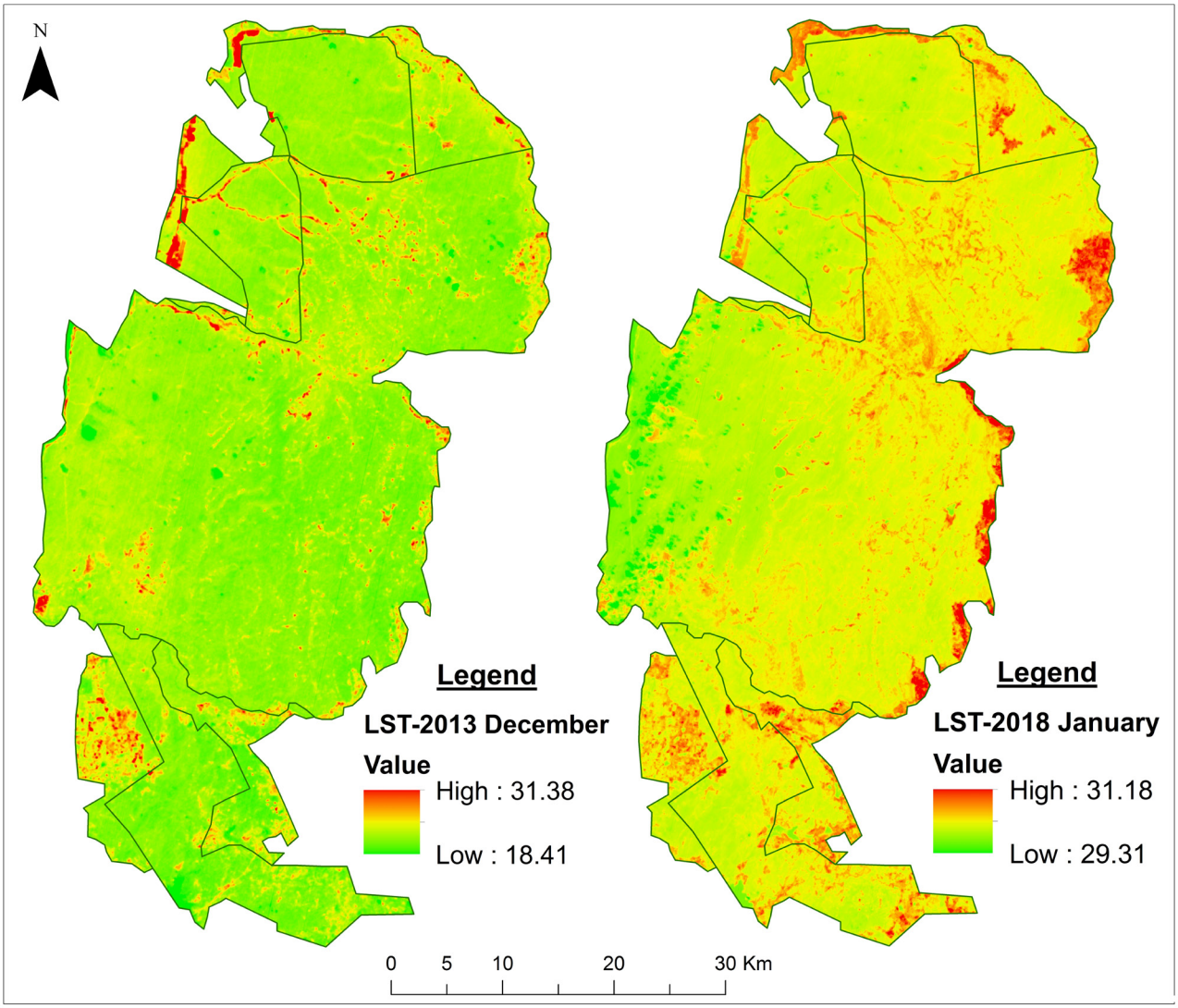

Figure 2: Land Surface Temperature Distribution over Wilpattu Forest Complex.

in its function of regulating micro-climatic conditions.

It could be identified that anthropogenic interventions are involved in the increase of the LST, especially at the buffer areas of the WNP and reserved forests. However, there is still a debate on the issue as residents claim these cleared vegetative areas as their native lands. According to the habitants, Wilpattu communities have left their native lands due to the civil war and they were not allowed to return until the peace treaty in 2009. After the migrants were allowed to return, the Marichchukaddi/Karadikkuli reserved forest areas are facing serious problems as more anthropogenic interventions came into practice.

When considering this issue it was noted that areas in Marichchukaddi/Karadikkuli reserved forest was not deforested before or during the civil war period. To compare the total extension of forested areas when the civil war had started in 1983 and very recent, 1984 satellite images and recent satellite images are used. It was noted that the vegetated areas has remained unchanged until road development activities were taken into operation. Just after these activities begun, the surrounding area was cleared as land plots for settlements during 2010 to 2012. Analysis of Google Earth Pro image series shows that these developments accelerated since 2013.

However, it is true that there have been settlements in Periyamarippu reserved forest area even before the civil war. According to the KIIs, population increased over the time and demand for houses and other buildings also increased. Accordingly, settlements and infrastructure facilities have been expanded in these areas. Areas adjacent to WNP from its eastern edges such as Kukulkatuwa have encroached even during the civil war period.

Given that there already has been a deficiency in the context of nature conservation activities in these areas, WNP as a declared national park should be open for the public only for aesthetic viewing and scientific purposes. However, the outcomes of this study show that the LST has increased along the forest boundary and even towards its inside. This is a

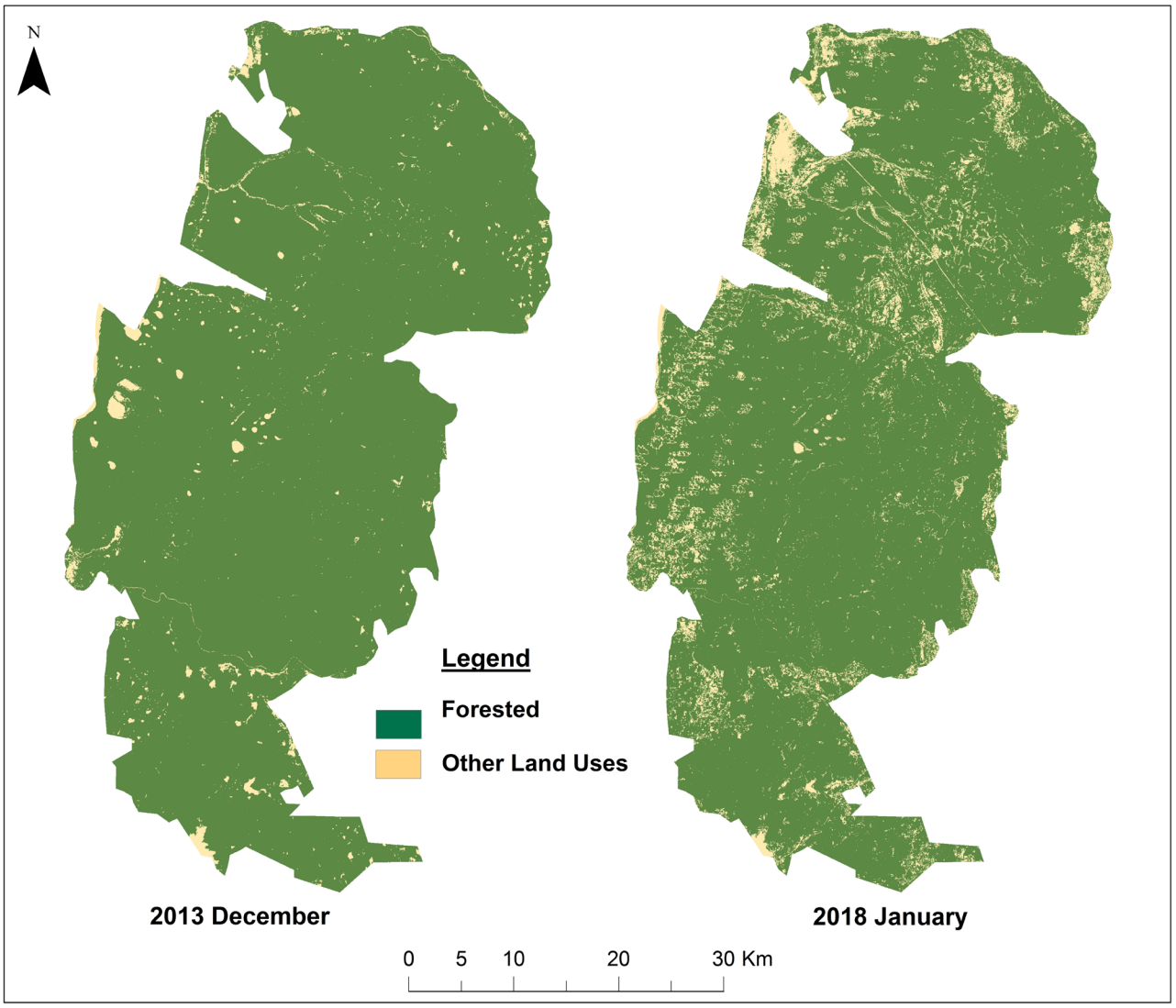

Figure 3: Forest Distribution in the Study Area in 2013 and 2018.

critical issue not only for the degradation of vegetation healthiness but it also impacts the degradation of biodiversity, especially of thermal sensitive flora and fauna species.

6. Conclusions and Recommendations

This study proves that forests play an important role in regulating LST conditions within the context of Sri Lanka. The higher LST distribution area has increased over the period as a response to the reduction of vegetation cover. WNP, Periyamarippu reserved forest, Tabbowa sanctuary and Weerakulicholai-Elavankulam forest reserve areas can be considered as newly emerged LST extended areas within the Wilpattu forest complex. Since the healthiness of the forests affects the LST, forest protection strategies must be implemented to maintain favorable environmental conditions necessary for humans and faunal species in the area. To maintain this task, destruction of trees is not allowed since 2015 and reforestation programs are already implemented in the area. However, illegal activities within these forested areas are contributing to the reduction of forested areas and the rise of the LST. Hence, it is more important to direct people's attitudes through awareness and capacity building. Also reinforcements of rules and regulations are vital in this sense.

7. References

Hua, A.K. and Ping, O.W., 2018. The Influence of Land-Use/Land-Cover Changes on Land Surface Temperature: A Case Study of Kuala Lumpur Metropolitan City. European Journal of Remote Sensing 51(1), 1049–1069. https://doi.org/10.1080/22797254.2018.1542976.

Li, Y., Zhao, M., Mildrexler, D.J., Motesharrei, S., Mu, Q., Kalnay, E., Zhao, F., Li, S. and Wang, K., 2016. Potential and Actual Impacts of Deforestation and Afforestation on Land Surface Temperature. Journal of Geophysical Research Atmospheres 121, 14372–14386. https://doi.org/10.1002/2016JD024969.

Peng, S.S., Piao, S., Zeng, Z., Ciais, P., Zhou, L., Li, L.Z.X., Myneni, R.B., Yin, Y. and Zeng, H., 2014. Afforestation in China Cools Local Land Surface Temperature. Proceedings of the National Academy of Sciences of the United States of America 111, 2915–2919. https://doi.org/10.1073/pnas.1315126111.

The Study of Land Cover Changes in Iran Using Satellite Imagery of 2007 and 2017

Ali Gholami[1,✉]

[1] Ferdowsi University of Mashhad, Iran
✉ aligholami1996@yahoo.com

Keywords: Land cover, Satellite imagery, MODIS, MCD12Q1

1. Introduction

Knowing the different types of land cover and detecting human activities is important basic information for different types of planning. Many investigations have proposed that comprehensive information on land use and land cover is crucial for understanding local and global environmental issues including climate change (Ahmed et al., 2013; Pielke Sr et al., 2002), water pollution (Buck et al., 2004; Zomlot et al., 2017), and air pollution (Superczynski and Christopher, 2011; Afrin et al.,2019).

Maps that represent such activities at different land covers are called land use maps (Dimyati et al., 1996). Many of these maps are created using satellite imagery. Due to increasing land use changes, especially by human activities, monitoring vegetation changes and assessing their trends and their environmental impacts is essential for future planning of measures and resource management. Using remote sensing data, the necessary measurements can be made on the biophysical resources of the Earth at a specific spatial and temporal scale (Ramankutty et al., 2006). The selection of satellite images as well as the choice of methods and algorithms for retrieving and detecting these changes using satellite images has an important impact on the results and their analysis and interpretation (Michener and Houhoulis, 1997).

2. Material and methods

2.1. Study area

Iran, covering an area of 1.65 million km², is the 17th largest country in the world, and located in an arid and semi-arid belt, ranging from 25°03' to 39°47' north latitude and 44°5' to 63°18' east longitude (Fig. 1). Iran has diverse climatic conditions. The average annual precipitation and the average monthly temperature in Iran between 1971 and 2015 were approximately 240 mm and 18 °C, respectively (Khalili and Rahimi, 2018). About 10.9 % of the land area, which is about 180,200 km² of Iran is covered by forests. About 55.5 % of the forested area is covered by oak forests (mostly located in Western Iran), and 19 % are known as the Northern Forests of Iran. Desert forests constitute 3.13 % of this area and mountainous forests and tropical forests 6.6 %, each.

2.2. Methods

In this paper, Moderate Resolution Imaging Spectroradiometer (MODIS) land cover product has been used to identify land covers in the study area (Friedl et al., 2010). MODIS is a sensor onboard on the two Terra and Aqua satellite platforms, which were launched by NASA (Hassan et al., 2018). After field visiting in some parts of the country (East, North and West forests of Iran), the data was identified using the LAADS DAAC website (https://ladsweb.modaps.eosdis.nasa.gov/) and downloaded from the Land Processes Distributed Active Archive Center website (https://lpdaac.usgs.gov/data_access/data_pool). The combined MODIS collections were provided. In the combined MODIS collections the land cover imagery in the MCD12Q1 (MODIS/Terra + Aqua Land Cover) for 2007 and 2017 were downloaded. The spatial and temporal resolutions of the land cover maps are 500 m and yearly, respectively. Furthermore, the MODIS tiles are h21v04, h21v05, h22v04, h22v05, h22v06, h23v05, h23v06. The datasets are in hierarchical data format (hdf) and have to be converted into tiff format and mosaicked to get one image for Iran (Babu, et al. 2019).

In a next step, the images were imported to the ArcMap environment. The different images for each

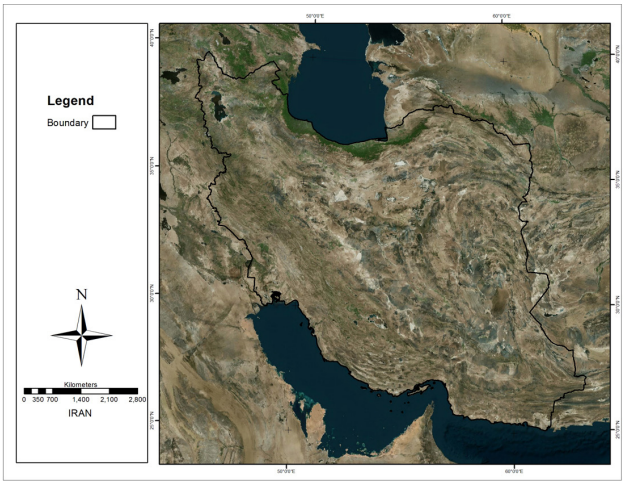

Figure 1: Geographical Map of Iran.

Proceedings of the 5th International YES Congress
DOI: 10.2312/yes19.09

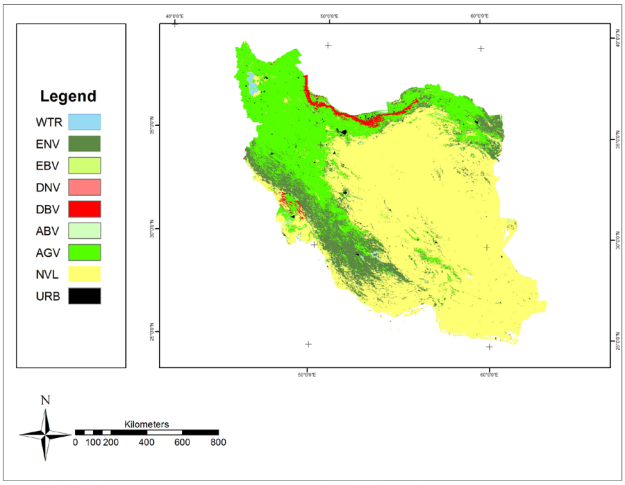

Figure 2: Land Cover Map of Iran in 2007.

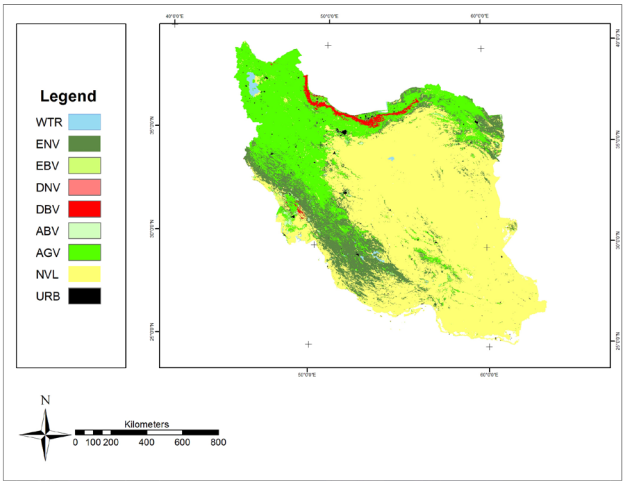

Figure 3: Land Cover Map of Iran in 2017.

date are combined to a single raster file using the mosaic to raster tool. This will enable us to monitor vegetation. After obtaining both the images for 2007 and 2017, using the combine tool, both images were combined to examine the changes that occur over the past 10 years and to obtain the final image.

3. Results

In 2007, non-vegetated lands (NVL) cover an area of 986,080 km² (59.8 % of the total land area of the country) and are therefore the major land cover type of Iran (Fig. 2). After non-vegetated lands, annual grass vegetation (AGV) with the area of 411,032 km² (24.9 %) and evergreen coniferous leaf (ENV) with 204,860 km² (12.5 %) are the next largest groups.

In 2017, the area of non-vegetated lands (NVL) is 993,820 km² (60.3 %) which is an increase of 1 % compared to 2007 (Fig. 3). The annual grass vegetation (AGV) has an area of 426,317 km² and evergreen coniferous vegetation (ENV) land an area 183,383 km². These results indicate an increase in annual grass vegetation and a decrease in evergreen coniferous vegetation.

Fig. 4 maps the changes that occurred over the ten years between 2007 and 2017. The biggest change from one land cover to another is the conversion of evergreen coniferous vegetation to the arid areas with 9,265 km². Following, the conversion of coniferous forests to annual grassland and annual grass vegetation to arid areas are the next biggest conversions.

The deciduous broadleaf vegetation (DBV) of the country has not changed significantly. However, in the southwest of the country, the area of broadleaf species has declined over the past ten years. Finally, the area of Deciduous Coniferous Vegetation (DNV), Evergreen Broadleaf Vegetation (EBV) and Evergreen Coniferous Vegetation (ENV), has remarkably increased over the past 10 years.

4. Discussion

According to the results obtained in the present study, large areas, especially in areas with no cover and pastures with annual plants, remained unchanged from 2007 to 2017. However, a large area of rangelands and arid areas has become coniferous forests, which is still insignificant compared to the arid areas. At the same time, the area of coniferous forests that have become deserts is also considerable.

Due to recent afforestation in the country, the area of coniferous forests in the west and southwest of the country has increased. These measures have been taken to prevent soil erosion and stop deterioration of the quality of land cover. However, most of the land cover that has become arid areas are still coniferous forests, which are estimated to have converted approximately 9,000 km² of these forests into arid areas. Therefore, desertification still overrules afforestation in Iran.

In this research the changes in land cover of 2007 to 2017 has been studied. Sadeghi et al. (2016) concentrated on the importance of considering rainfall partitioning in afforestation initiatives in semiarid climates. Sasanifar et al. (2019) studied on the forest protection policy in Northwest of Iran and there are several other studies on forest degradation and afforestation in some parts of Iran. But since there is no systematic study on vegetation in Iran and also because Iran is a large country it is hard to know what causes may affect forests in this large scale.

5. Conclusions

Given that Iran is in the arid and semi-arid belt, a large area of it is barren. However, due to climatic diversity in Iran, areas in the country have the potential

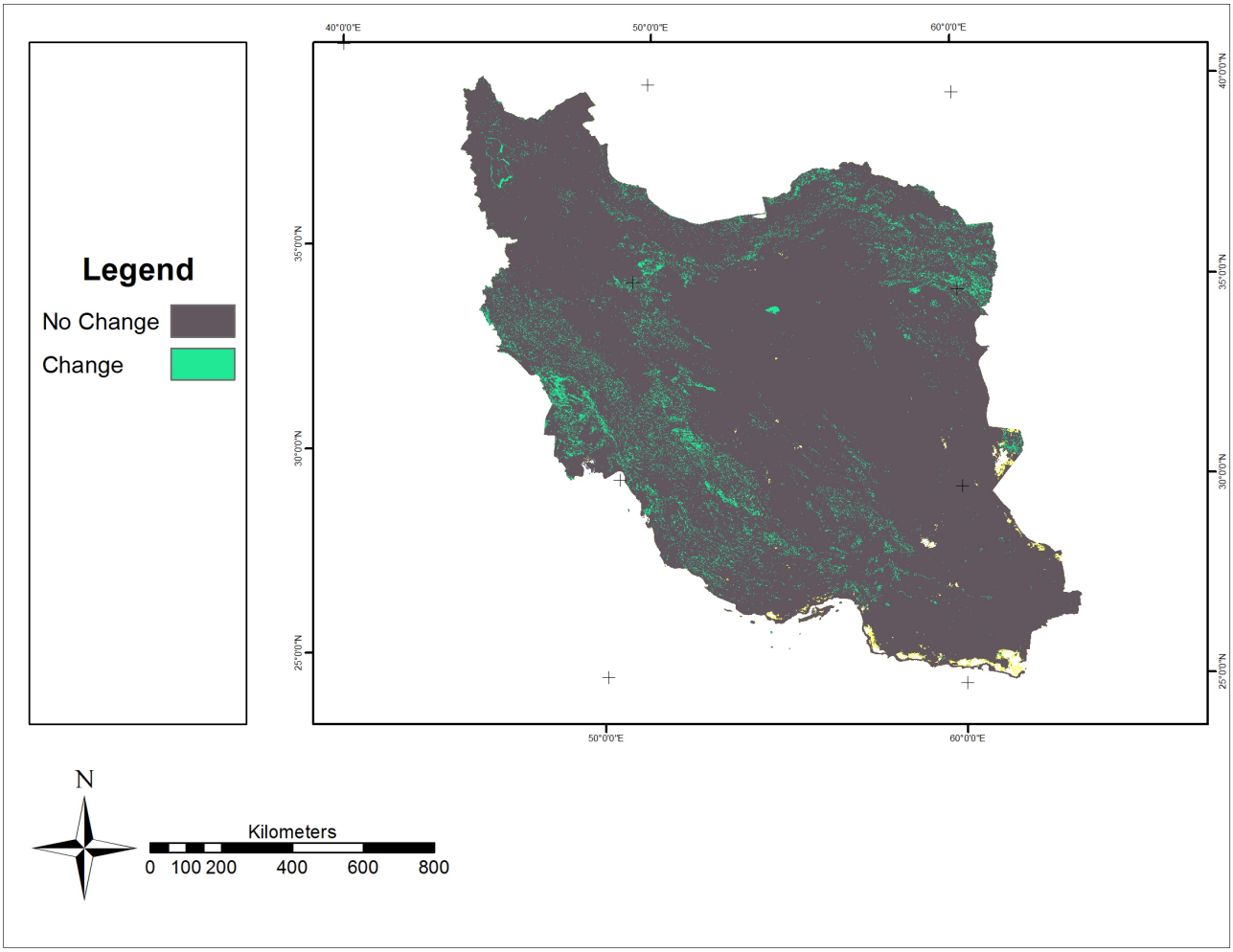

Figure 4: Land Cover Change Map of Iran in 2007 and 2017.

to grow valuable (especially tree) species. At the moment, based on the available results, most of these areas are covered by annual plants. It seems that further studies in areas where the dominant vegetation is one-year vegetation can be used to evaluate the potential of planting higher quality plants to allow for more forestry where possible. On the other hand, due to the severe impacts of land cover and climate change, it is necessary to take the risk of converting vegetated areas into arid areas more seriously and to prevent this happening by clever management, especially by using new techniques like remote sensing for monitoring.

6. References

Afrin, S., Gupta, A., Farjad, B., Ahmed, M.R., Achari, G. and Hassan, Q., 2019. Development of Land-Use/Land-Cover Maps Using Landsat-8 and MODIS Data, and Their Integration for Hydro-Ecological Applications. Sensors 19(22), 4891. https://doi.org/10.3390/s19224891.

Ahmed, B., Kamruzzaman, M., Zhu, X., Rahman, M. and Choi, K., 2013. Simulating land cover changes and their impacts on land surface temperature in Dhaka, Bangladesh. Remote Sensing 5(11), pp. 5969–5998. https://doi.org/10.3390/rs5115969.

Babu, K. V. S., Kabdulova, G., and Kabzhanova, G., 2019. Developing the Forest Fire Danger Index for the Country Kazakhstan by Using Geospatial Techniques. Journal of Environmental Informatics Letters 1(1), pp. 48–59. https://doi.org/10.3808/jeil.201900006.

Buck, O., Niyogi, D.K. and Townsend, C.R., 2004. Scale-dependence of land use effects on water quality of streams in agricultural catchments. Environmental Pollution 130(2), pp. 287–299. https://doi.org/10.1016/j.envpol.2003.10.018.

Dimyati, M., Mizuno, K., Kobayashi, S. and Kitamura, T., 1996. An analysis of land use/cover change in Indonesia. International Journal of Remote Sensing 17(5), pp. 931–944. https://doi.org/10.1080/01431169608949056.

Friedl, M.A.; Sulla-Menashe, D.; Tan, B.; Schneider, A.; Ramankutty, N.; Sibley, A.; Huang, X., 2010. MODIS Collection 5 global land cover: Algorithm refinements and characterization of new datasets. Remote Sensing of Environment 114, pp. 168–182. https://doi.org/10.1016/j.rse.2009.08.016.

Hassan, A., Ismail, S.S., Elmoustafa, A. and Khalaf, S., 2018. Evaluating evaporation rate from High Aswan Dam reservoir using RS and GIS techniques. The Egyptian Journal of Remote Sensing and Space Science 21(3), pp. 285–293. https://doi.org/10.1016/j.ejrs.2017.10.001.

Khalili, A., Rahimi, J., 2018. Climate. In: Roozitalab, M.H., Siadat, H., Farshad, A. (Eds.) The soils of Iran. World Soils Book Series. Springer, Cham, pp. 19–33. https://doi.org/10.1007/978-3-319-69048-3_3.

Michener, W.K. and Houhoulis, P.F., 1997. Detection of vegetation changes associated with extensive flooding in a forested ecosystem. Photogrammetric Engineering and Remote Sensing 63(12), pp. 1363–1374.

Pielke Sr, R.A., Marland, G., Betts, R.A., Chase, T.N., Eastman, J.L., Niles, J.O., Niyogi, D.D.S. and Running, S.W., 2002. The influence of land-use change and landscape dynamics on the climate system: relevance to climate-change policy beyond the radiative effect of greenhouse gases. Philosophical Transactions of the Royal Society of London, Series A: Mathematical, Physical and Engineering Sciences 360(1797), pp. 1705–1719. https://doi.org/10.1098/rsta.2002.1027.

Ramankutty, N., Graumlich, L., Achard, F., Alves, D., Chhabra, A., DeFries, R.S., Foley, J.A., Geist, H., Houghton, R.A., Goldewi-

jk, K.K. and Lambin, E.F., Millington, A., Rasmussen, K., Reid, R.S. and Turner II, B.L., 2006. Global land-cover change: Recent progress, remaining challenges. In: Lambin, E.F., Geist, H. (Eds.) Land-use and land-cover change. Springer, Berlin, Heidelberg, pp. 9–39. https://doi.org/10.1007/3-540-32202-7_2.

Sadeghi, S.M.M., Attarod, P., Van Stan, J.T. and Pypker, T.G., 2016. The importance of considering rainfall partitioning in afforestation initiatives in semiarid climates: A comparison of common planted tree species in Tehran, Iran. Science of the Total Environment 568, pp. 845–855. https://doi.org/10.1016/j.scitotenv.2016.06.048.

Sasanifar, S., Alijanpour, A., Shafiei, A.B., Rad, J.E., Molaei, M. and Azadi, H., 2019. Forest protection policy: Lesson learned from Arasbaran biosphere reserve in Northwest Iran. Land Use Policy 87, 104057. https://doi.org/10.1016/j.landusepol.2019.104057.

Superczynski, S.D. and Christopher, S.A., 2011. Exploring land use and land cover effects on air quality in Central Alabama using GIS and remote sensing. Remote sensing 3(12), pp. 2552–2567. https://doi.org/10.3390/rs3122552.

Zomlot, Z., Verbeiren, B., Huysmans, M. and Batelaan, O., 2017. Trajectory analysis of land use and land cover maps to improve spatial–temporal patterns, and impact assessment on groundwater recharge. Journal of Hydrology 554, pp. 558–569. https://doi.org/10.1016/j.jhydrol.2017.09.032.

Assessment of the Moderate Intensity Tremors of September 6–7th, 2018 in Abuja Nigeria Using Integrated Satellite Thermal Infrared (TIR) and Aeromagnetic Data

Abayomi Osotuyi[1,2,✉], Ayomiposi Falade[1], Abraham Adepelumi[1], Samson Onibiyo[3]

[1] Seismological Research Laboratory, Obafemi Awolowo University, Ile-Ife, Nigeria.
[2] School of Earth and Space Sciences, University of Science and Technology of China Hefei, Anhui 230036, China.
[3] Department of Geosciences, Georgia State University, Atlanta, Georgia, USA.
✉ yomigaius@gmail.com

Keywords: Satellite thermal infrared, anomaly, fault system, mainshock, seismic

1. Introduction

Earthquakes are one of the most significant natural geological hazards. Hence, there is a need for continuous study and research into earthquake prediction and forecasting. From 5th to 7th September 2018, sequences of moderate-intensity earth tremors (IV-V Modified Mercalli Intensity (MMI)) were reported in the capital city of Nigeria and were mainly felt in Mpape and its environment, located in the Northeastern part of the Federal Capital Territory (FCT), Abuja. The IV-V MMI tremor was recorded on 6th September 2018 in an inhabited area located between features such as mountains, hills, and valleys. Although no human casualty was reported, human and economic activities were disrupted. This event has drawn further attention to a series of earthquakes reported on a stable intra-plate region, contrary to previous assumptions that Nigeria is located within an aseismic zone (Adepelumi et al., 2010; Akpan and Yakubu, 2010). Considering past records (Blundell and Banson, 1975; Ajakaye et al., 1987; Amponsah, 2004; Meghraoui et al., 2016), this study is bringing renewed attention to earthquakes as a potential natural hazard in the western African region.

We measured land surface temperature (LST) from thermal infrared (TIR) instruments, which is a key parameter in the physics of land surface processes on both regional and global scales. Also, aeromagnetic investigations known to be versatile in extracting subsurface geologic information were adopted to investigate thermal variations and rock magnetic signatures.

2. Settings, Theories and Methods

2.1. Geology and tectonic settings of the area

The Federal Capital Territory (FCT) is mainly underlain by rocks of the crystalline basement complex within the north-central part of Nigeria, which forms part of the Pan-African mobile belt in the West African Congo cratons (Black, 1980). The rock units are made up of granites, mica schists, hornblende and feldspathic schists, and migmatites. They are highly fractured and jointed, showing essentially three lineament patterns with a NE-SW, N-S, and NW-SE orientation (Fig. 1). Dense fracture networks are present, which may be interconnected and linked to the regional NE-SW trending Ifewara-Zungeru fault line. These networks take the form of cracks and tensional joints resulting from stresses occasioned by alternating heating-up and cooling sequences of rocks. Both horizontal and vertical fractures are very common, with the fracture widths generally decreasing with depth. This may be an indication that the fracture systems are young, still evolving structures (Avci, 1983).

We note the detailed geological report of the study carried out on the Federal Capital Territory by Gauff and Adejumo in 1979, which gives an in-depth and comprehensive background insight into the geologic

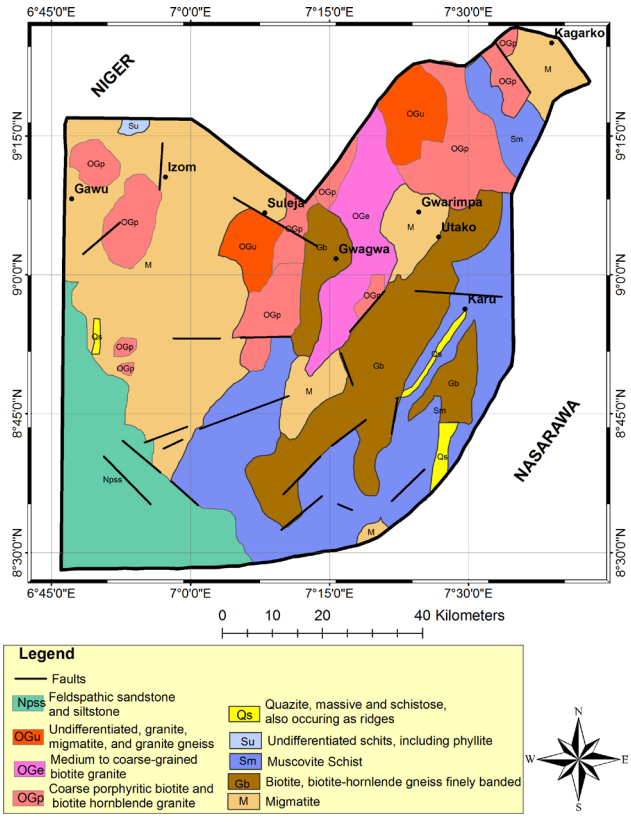

Figure 1: Geological map of the Federal Capital Territory, Abuja (modified after NGSA, 2006).

DOI: 10.2312/yes19.16

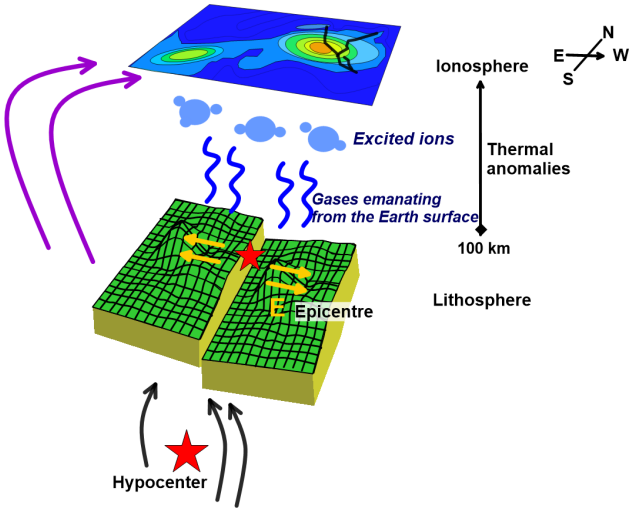

Figure 2: Schematic of the formation of thermal anomalies (modified after Shah et al., 2018).

and tectonic settings of the FCT. The report indicates that the most evident structural features in the basement complex rocks of the FCT are northerly to north-easterly-southwesterly trends of the basement complexes near the eastern and western boundaries, and the easterly trends in the central part. These reflect the presence of a north-trending shear zone along the eastern limb of the FCT. A smaller north-trending shear zone appears just west of Abuja. Many faults and fractures trending NW cut these structures and are therefore of younger origin. They are believed to be the results of at least four major orogenic cycles of deformation, metamorphism and remobilization corresponding to the Liberian (2,700 Ma), the Eburnean (2,000 Ma), the Kibaran (1,100 Ma), and the Pan-African cycles (600 Ma) (Gauff and Adejumo, 1979; Black, 1980). These show that the young tectonic structures may still be developing. The eastern shear zone represents a major regional tectonic feature persisting for many tens of kilometers. Near the northeast corner of the FCT the shear zone is only a few kilometers wide. In the southern part of the eastern shear zone there are, at several places, individual shear zones in schists or granitic gneisses cutting other minor rocks such as amphibolites. Therefore, it is supposed that there have been some tectonic movements causing regional metamorphism which took place in Precambrian times (Gauff and Adejumo, 1979), which could have been reactivated along the faults in the weak/sheared zones. Shear zones are known to be weak zones, which abundantly underlie the FCT (Gauff and Adejumo, 1979). Hence, parts of the FCT may not be immune to tectonic movements and activities that may have caused the reported earth tremor of 6th September 2018.

2.2. Theories of Thermal Infrared Anomalies

Advances in Space technology have led to the measurement of surface geophysical parameters and related quantities associated with ground deformation around tectonic plate boundaries, active faults, and shear zones. Thermal Infrared Anomalies come in along with earthquakes (Huang et al., 2008). Fig. 2 is based on an idea from previous studies of Huang et al., 2008 and Shah et al., 2018, who used to define the earthquake-induced anomalies as “the generation of hole charges on the lithospheric surface and the intensification of the lower atmosphere by the hole charges”. Also, several theories and models have been presented to shed light on thermal anomalies emanating from earth lineaments as a result of stress build-up and subsequent release along these structures due to tectonic activities.

Some attendant signals preceding earthquakes are changes in land and air surface temperature (days or even weeks prior to strong, even moderate earthquakes), gas emissions (including methane, radon, etc.), water level and quality (in wells), and electric and magnetic (electromagnetic) fields of the earth (Freund, 2011; Varotsos et al., 2011). Zoran et al., 2014 stated that earthquake pre-signals for which clear geophysical anomalies are observable can be remotely sensed using different criteria. Also, local and regional airborne measurements, and traditional in-situ and ground based seismological sensor monitoring networks can be complemented with satellite data information from established space observatories. Guangmeng (2008) reported that “Russian scientists discovered short-lived thermal anomalies from satellite image before the earthquake in central Asia”. After that, several researchers have studied and reported this thermal anomaly phenomenon with satellite information for earthquakes in Japan, China, India, Iran and Algeria (Saraf et al., 2004; Pulinets, 2011; Lei et al., 2018). The thermal anomalies are typically short-lived and appear a few days before an earthquake, over an area of several square kilometers, showing a positive rise of 2 to 4 °C or more from the background temperature and disappearing a few days after the event. This method is not without its limitations, as satellite thermal sensors are limited in penetrating thick clouds to acquire land surface temperature data. Hence, we could not obtain continuous temperature data and some components of thermal anomaly would be lost. This forms a major challenge to predicting earthquakes using satellite thermal infrared data (Shah et al., 2018).

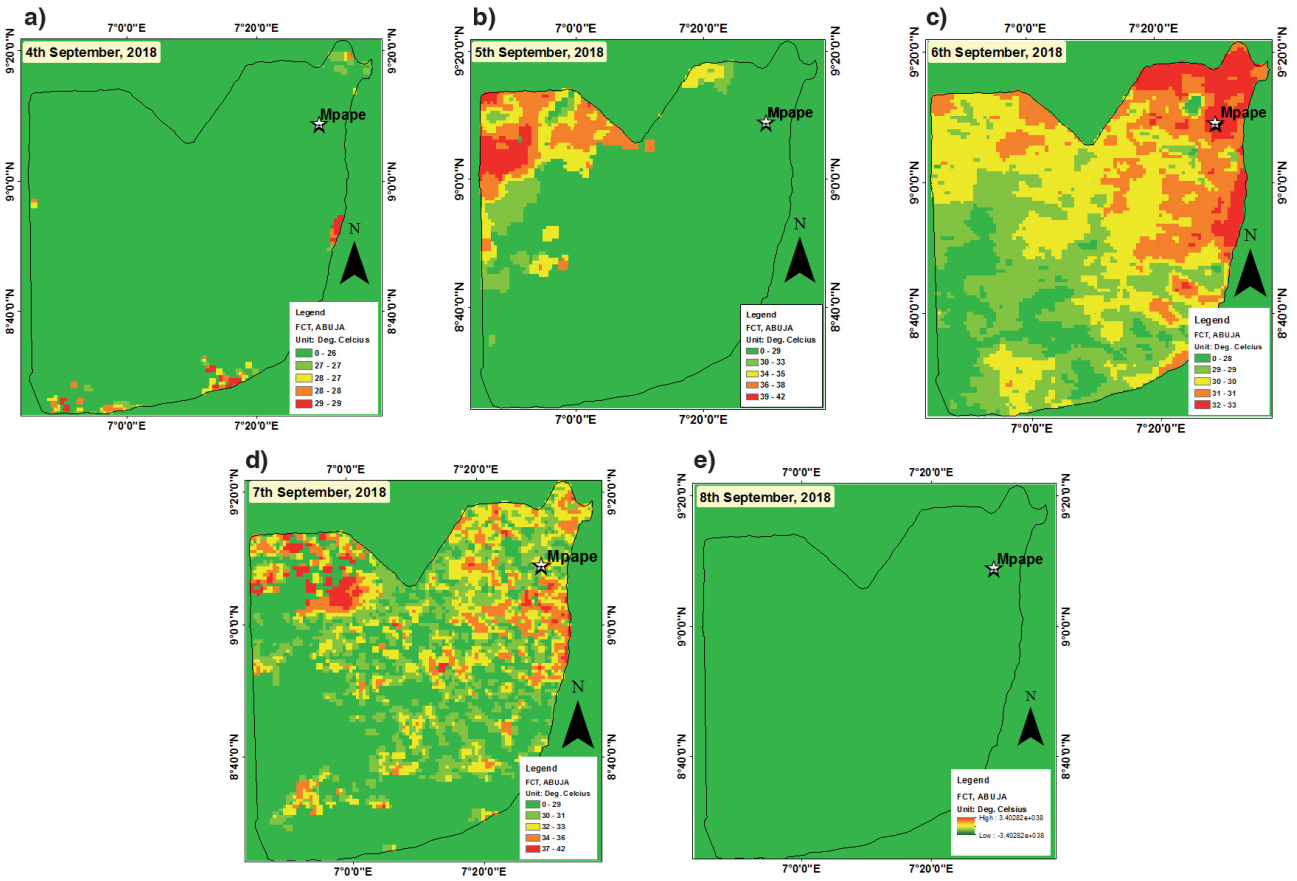

Figure 3: Land Surface Temperature images from (a) 4th to (f) 8th September 2018.

2.3. Research Data and Methodology

MODIS data derived from the NASA official network (NASA's Land Processes Distributed Active Archive Center (DAAC), https://lpdaac.usgs.gov/products/mod11a1v006/) were analyzed for this study. The remote sensing imagery has 1 km spatial resolution. Land Surface Temperature (LST) was extracted from the MODIS data. The Scientific Data sets in the MOD11A1 product include LST 1 km Day/Night, QC Day/Night, View Time Day/Night, View Angle Day/Night, Emissivity Band 31/Band 32, Clear Sky Coverage Day/Night. The daytime data was used. We adjusted preprocessing according to the acquired data. The original data contain Land Surface Temperature (LST) imagery, but the map projection is sinusoidal i.e. LST products are provided in intergerized sinusoidal projection. The MODIS reprojection Tool (MRT) was used in order to reproject and mosaic the tiles of the product. The aeromagnetic data used in this study was acquired by Fugro Airborne Survey on behalf of the Nigerian Geological Survey Agency (NGSA) between the years 2005 and 2007. The aircraft was flown at a mean altitude of 80 m with 500 m line spacing. The total magnetic field intensity was measured using a triaxial magnetic gradiometer that sampled at an interval of 10 Hz (~7.5 m). The TMI anomaly map was reduced to the magnetic equator using magnetic inclination and declination of -6.401 and -2.099 respectively. This transformation was carried out in order to reposition the observed anomalies on their respective causative sources. Anomalies resulting from near-surface features were filtered by upward continuation of the TMI map to a height of 200 m. Thereafter, various edge enhancement techniques, comprising Horizontal Gradient Magnitude (HGM), First Vertical Derivative (FVD), and Euler Deconvolution (ED), were applied on the filtered data. These edge enhancement filters were applied in order to enhance magnetic signatures from subsurface geologic linear structures (such as contact, fractures and faults) and estimate their respective depth of occurrence. The LST and aeromagnetic data were processed using Oasis Montaj and ArcMap (version 10.3) software.

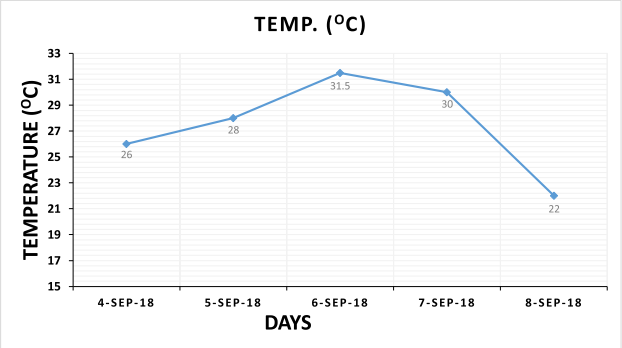

Figure 4: Daily average temperature anomaly from 4th to 8th September 2018.

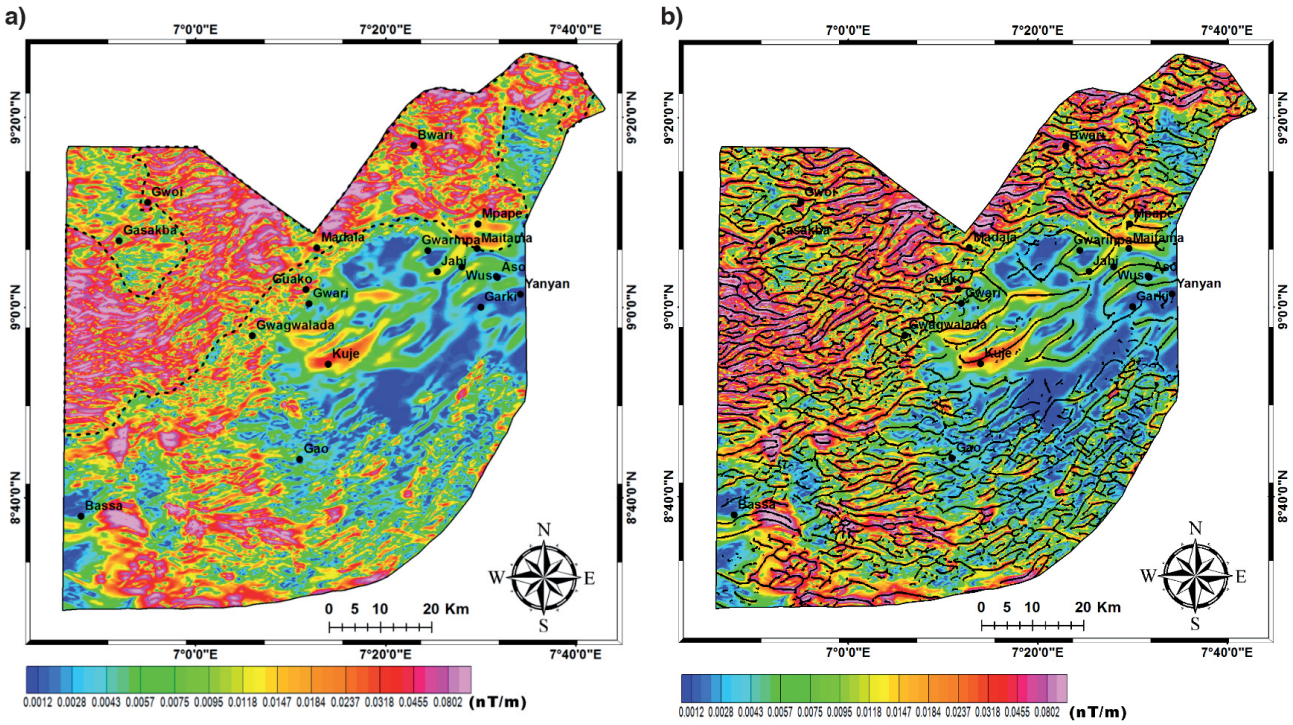

Figure 5: (a) Horizontal Gradient Magnitude (HGM) map; (b) HGM peaks overlain on HGM.

3. Results

The Mpape, FCT tremor was recorded on the 6th of September, 2018 and the data acquired included the 4th to 8th of September, 2018. This is to incorporate the LST for days before, during, and after the events were reported, allowing us to establish spatial thermal infrared variation and the temporal anomaly. Hence, we processed LST data sets for each day and produced the spatial anomaly maps. The LST data are presented as maps (Fig. 3), and averaged temperature values for each day were plotted (Fig. 4) to observe the trend of temperature fluctuations over the days under review. The aeromagnetic structural mapping identified some demarcated region suspected to be sheared zones (Fig. 5), and faults/fractures that could likely trigger the tremor (Fig. 6). These faults/fractures are labeled F1-F7 (Fig. 6). The faults trend in approximately NE-SW and E-W directions. Faults F4, F5, and F6 are deep-seated faults whose depths were estimated at a range > 1000 m, while the depths of F1, F2 and F3 were undetermined. F1 and F2 are regional faults that pass through Abuja and Nasarawa, and possibly extend to Kaduna. F7, which exists between depths of 700 and 1000 m (Fig. 5), had been identified by Eluyemi et al. (2019) as the Romanche Fault/Fracture. The Romanche Fault was found to emanate from the Gulf of Guinea and strikes in the same direction as the Pan African Orogeny.

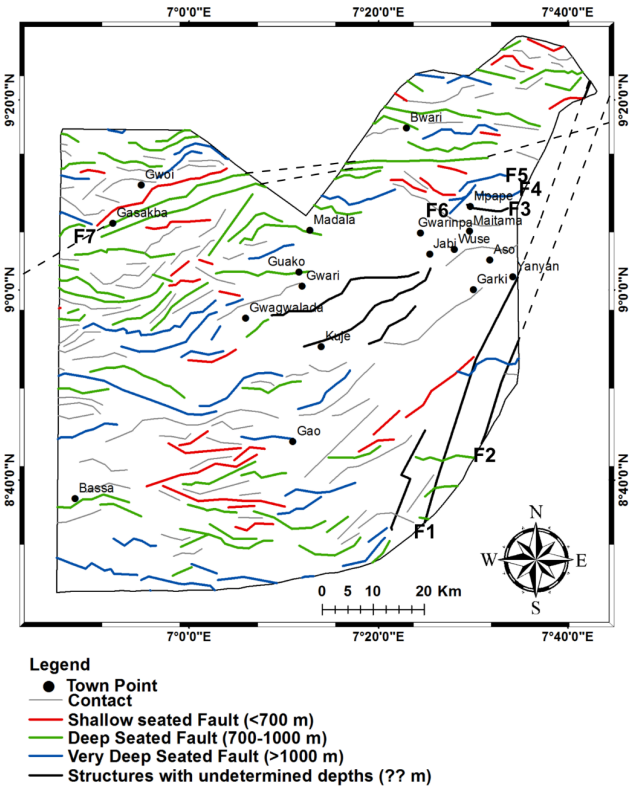

Figure 6: The Inferred Lineament Map of the Study Area.

4. Discussion

The vast area within the FCT was thermally quiet and there was no significant observable thermal energy spread across the area on the 4th of September 2018, except for the southern boundaries that began to pick up some specks of temperature increase relative to the environment (Fig. 3a). On the 5th of September, 2018, a noticeable thermal anomaly began to emerge and build up at the northwestern area of the FCT with respect to the surrounding environment, picking up an increase in temperature (Fig. 3b).

There was a significant energy dissipation across the most northern part of the FCT and more important the entire northeastern and eastern parts where Mpape, is located, which was identified as the epicenter. This trend spread eastward on the 6th of September, 2018 which is just the day before the main shock was reported. There is a rise in the temperature across the northern part on the 6th of September, 2018 with a sharp increase in thermal anomaly in the NE. Hence, it can be deduced that there was a W–E movement of increasing thermal flux from the 5th through to 6th of September, 2018 (Fig. 3b,c). On the 7th of September 2018, there is energy dissipation across the entire FCT relative to the two previous days (Fig. 3d). Energy loss and attenuation are observed across the area when compared to the 6th of September data, though patches of high thermal anomaly were observed on the day the event was recorded. There is complete energy attenuation and there was no observable anomaly on the 8th of September 2018, the day after the tremor was reported. (Fig. 3e). The NE of the FCT, covering about 3,176 km2 across the central areas including Mpape in the northeastern flank of FCT, recorded the highest observable thermal anomaly, with the after-shock of the tremor felt strongest in the Bwari area. Maximum temperatures between 29 °C and 42 °C and were recorded on the 7th of September in the anomalous zone, with a temperature rise between 3 °C and 13 °C across this vast area. After the tremor, the temperature was lower than on other days (Figs. 3 and 4). This suggests that the TIR anomalies existed in association with tectonic activities, plate movement, earth tremor, and/or earthquakes recorded on the 7th of September 2018. From the edge enhancement filters applied to the aeromagnetic data, magnetic signatures from subsurface geologic linear structures (such as contact, fractures and faults) were enhanced and their respective depth of occurrence was estimated (Figs. 5a,b).

5. Conclusions

Earthquakes are natural events that happen all the time. There is no current technology to avert them. Hence, emphasis is placed on monitoring, identifying, and cataloguing their locations as accurately as possible to make improvements on future forecasts in time and space. This study reveals that, since the Gulf of Guinea is seismically active, the tremor observed around Mpape most likely could have been triggered by strain energy released in the Atlantic Ocean. Possibly this tectonic activity propagates through the Romanche Fault/Fracture and is now being felt by the rejuvenation of the weak/sheared zones in the central part of Nigeria where Mpape lies. Also, this study reveals the gradual progressive changes involving the increase and attenuation of the thermal flux across the FCT, Abuja from the NW to NE parts prior to and during the periods of the reported seismic events. Maximum temperatures between 29 °C and 42 °C were recorded on 7th September in the anomalous zone, which coincided with the day the major event was reported. Also, a temperature rise between 3 °C and 13 °C across the vast area was recorded. After the tremor, the temperature was lower than in the other days. TIR should be adopted for continuous monitoring in earthquake-prone areas and regions where such events have been reported in the past.

6. References

Adepelumi, A. A., Onibiyo, O. S., Isogun, M. A. (2010). Short-term probabilistic forecasting of earthquakes occurrence in Southwestern Nigeria. Environtropica, pp. 1–11. https://doi.org/10.1088/1757-899X/413/1/012036.

Ajakaiye, D. E., Daniyan, M. A., Ojo, S. B., Onuoha, K. M. (1987). The July 28, 1984 southwestern Nigeria earthquake and its implications for tectonics and evolution of Nigeria. Journal of Geodynamics 7, 205–214. https://doi.org/10.1016/0264-3707(87)90005-6.

Akpan, O. U., Yakubu, T. A. (2010). A review of earthquake occurrences and observations in Nigeria. Earthquake Science 23, 289−294. https://doi.org 10.1007/s11589-010-0725-7.

Amponsah, P. E. (2004). Seismic activity in Ghana: past, present and future. Annals of Geophysics 47, 539−543. https://doi.org/10.4401/ag-3319.

Avci, M. (1983). Photogeology and Structural interpretation of the Southern section of the New Federal Capital City site, Abuja, Nigeria. Nigeria Journal of Minning and Geology 20(1&2), 51–56.

Black, R. (1980). Precambrian of West Africa. Episodes 4, 3–8.

Blundell, D. J., Banson, J. K. A. (1975). Interpretation of a seismic Reflection survey across the Continental shelf South of Accra and it's bearing on Earthquakes in the Area. Ghana Geological Survey Reports 75/1, 7 p.

Eluyemi, A. A., Sharma, S., Olotu, S. J., Falebita, D. E., Adepelumi, A. A., Tubosun, I. A, Ibitoye, F. I, Baruah, S. A (2019). GIS-Based Site Investigation for Nuclear Power Plants (Npps) In Nigeria. Scientific African 7, e00240. https://doi.org/10.1016/j.sciaf.2019.e00240.

Freund, F. (2008). Seeking out Earth's warning signals. Nature 473(7348), 452. https://doi.org/10.1038/473452d.

Gauff, H. P., Adejumo, O. (1979). Federal Capital Development Authority of the Federal Republic of Nigeria, (1979). Unpublished feasibility study, preliminary engineering and water supply. Conducted by H. P. Gauff GmbH & Co, Adejumo Ogunsola & Partners, and Noyuk Consults, 1–67.

Guangmeng, G. (2008). Studying thermal anomaly before earthquake with NCEP data. The International Archives of the Photogrammetry, Remote Sensing and Spatial Information Sciences XXXVII. Part B8. Beijing 2008, 295-297.

Huang, J., Mao, F., Zhou, W., Zhu, X. (2008). Satellite Thermal IR associated with Wenchuan earthquake in China using Modis Data. The 14th World Conference on Earthquake Engineering, October 12-17, 2008, Beijing, China, 6 p.

Lei, L., Tingjun, Z., Tiejun, W., Xiaoming, Z. (2018). Evaluation of Collection-6 MODIS Land Surface Temperature Product Using Multi-Year Ground Measurements in an Arid Area of Northwest China. Remote Sensing 10(11), 1852. https://doi.org/10.3390/rs10111852.

Meghraoui, M., Amponsah, P., Ayadi, A., Ayele, A., Ateba, B., Bensuleman, A., Delvaux, D., El Gabry, M, Fernandes, R., Midzi, V., Roos., M, Timoulali, Y. (2016). The Seismotectonic Map of Africa. Episodes 39, 9–18. https://doi.org/10.18814/epiiugs/2016/

v39i1/89232.
Nigerian Geological Survey Agency, NGSA, (2006). Geology and Aeromagnetic Maps of Nigeria. Scale 1:80.000. Map sheets 185, 186, 187, 206, 207, 208.
Pulinets, S., Ouzounov, D. (2011). Lithosphere–Atmosphere–Ionosphere Coupling (LAIC) model - An unified concept for earthquake precursors validation, J. Asian Earth Sci. 41, 371–382. https://doi.org/10.1016/j.jseaes.2010.03.005.
Saraf, A. K., Choudhury, S. (2004). Satellite Detects Surface Thermal Anomalies Associated with the Algerian Earthquakes of May, 2003. International Journal of Remote Sensing 26(13), 2705–2713. https://doi.org/10.1080/01431160310001642359.
Shah, M., Khan, M., Ullah, H., Ali, S. (2018). Thermal anomalies prior to the 2015 Gorkha (Nepal) earthquake from MODIS Land Surface Temperature and outgoing Longwave Radiations. Institute of the earth's crust, Siberian branch of Russian Academic of Sciences 9(1), 123–138. https://doi.org/10.5800/GT-2018-9-1-0341.
Varotsos, P. A., Sarlis N. V., Skordas, E. S. (2011). Scale-Specific order parameter fluctuations of seismicity in natural time before main shocks. Europhysics Letters 96, 59002, https://doi.org/10.1209/02955075/96/59002.
Zoran, M. A., Savastru, R. S., Savastru, D. M. (2014). Satellite thermal infrared anomalies associated with strong earthquakes in the Vrancea area of Romania. Open Geoscience 1, 606–617. https://doi.org/10.1515/geo-2015-0046.

Geological and Structural Mapping of the Brunei-Muara District Using Unmanned Aerial Vehicle (UAV)

Dk 'Aaisyah[1], Afroz Ahmad Shah[1,✉], Zulfadzli Zulmajdi[1]

[1] Universiti Brunei Darussalam, Brunei Darussalam
✉ afroz.shah@ubd.edu.bn

Keywords: UAV, Drones, Mapping, Brunei, Borneo

"the best geologists are those who see the most rocks" (Hurst, 2012).

1. INTRODUCTION

Rocks are a primary source material to investigate the historical development of the planetary bodies, and this applies to our home planet as well, where the basic geological knowledge about the lifecycle of the Earth requires interaction with rocks. The various lithological units that have formed over the geological time are often exposed at various crustal levels on the surface, and subsurface ranks for humans to investigate. The interactions with rock outcrops have helped us to unravel, and discover the hidden secrets of our home planet. These discoveries can unfold if such interactions with the planet continue in the future. Therefore, geological field visits are an important learning, and discovery experiences for geoscientists, and particularly for field-oriented courses such as Structural Geology, Geological Mapping, Field Techniques, etc.

Several studies have suggested that field related courses have helped students to improve their understanding of geological concepts and its various processes such as ductile and brittle deformation, sedimentation, volcanism etc, which is usually missing from courses that lack field components (e.g. Elkins, 2007; Dolphin et al., 2019). However, and unfortunately, the geological field exercises have become increasingly difficult to organise because of multiple problems, and as such fieldwork activities have diminished over the years, and even completely stopped at certain places. The problems range from financial constraints, travel restrictions to temporary or permanent loss of outcrops. For example, the processes of weathering, erosion, overburden, landslides, earthquakes, flooding and urbanization can contribute to the loss of geological outcrops. However, these processes can also reveal new outcrops but again it can lead to the same cycle of outcrop exposure, erosion and ultimately the loss of crucial information. Similarly, financial constraints can shrink or altogether stop field components. Furthermore, the complex, tedious, and exhausting field approval procedures can also contribute and exacerbate such problems, and it is mostly observed to impact international field visits where immigration and fieldwork related approvals from the host countries are a winding road to ride! And although geological fieldwork remains an essential component of a typical geological curriculum, the issues raised above could limit or stop such visits, thereby limiting our access to the primary sources of geological curiosities.

Therefore, an alternative has to be explored to preserve geological outcrops, so that such information is archived, and simultaneously used to create a virtual outcrop library that could be used, and made freely available to users. This paper shows such a mission where we are collecting and preserving field data in SE Asia by conducting field visits to record details of exposed geological outcrops. We are using Unmanned Aerial Vehicles (UAV), also known as drones, which are one of the best mapping tools to explore the region, and collect information with more accuracy (see below).

In recent years, the advancements of digital technology has dramatically improved the landscape of the mapping world and this is particularly true for UAVs, which are now easily accessible and are increasingly used for mapping. Geoscientists are also using the UAVs to map the geological outcrops with more precision, and record the entire field work to convert into videos or 3D outcrop models etc. (e.g. Bemis et al., 2014; Jordan, 2015; Rocca, 2017). It is possible that UAVs with digital cameras will become one of the best friends to every field geologist in the future due to their light weight and robust ability to capture and record surface topography, geology, and canopy with accurate details. Compared to satellite images, UAVs can produce high-resolution data up to 4K resolutions and at very low cost (details are below), especially with recent models. This makes UAVs field friendly and therefore an extremely useful tool for mapping purposes (e.g. Piras et al., 2016; Mezghani et al., 2018; King, 2019). One of the best features of such an instrument is its ability to operate in areas that are often inaccessible and/or dangerous (e.g. fear of wild animals, steep slopes, etc.). Below we show our initial work in Brunei Darussalam, which is a small oil-

Proceedings of the 5th International YES Congress
DOI: 10.2312/yes19.02

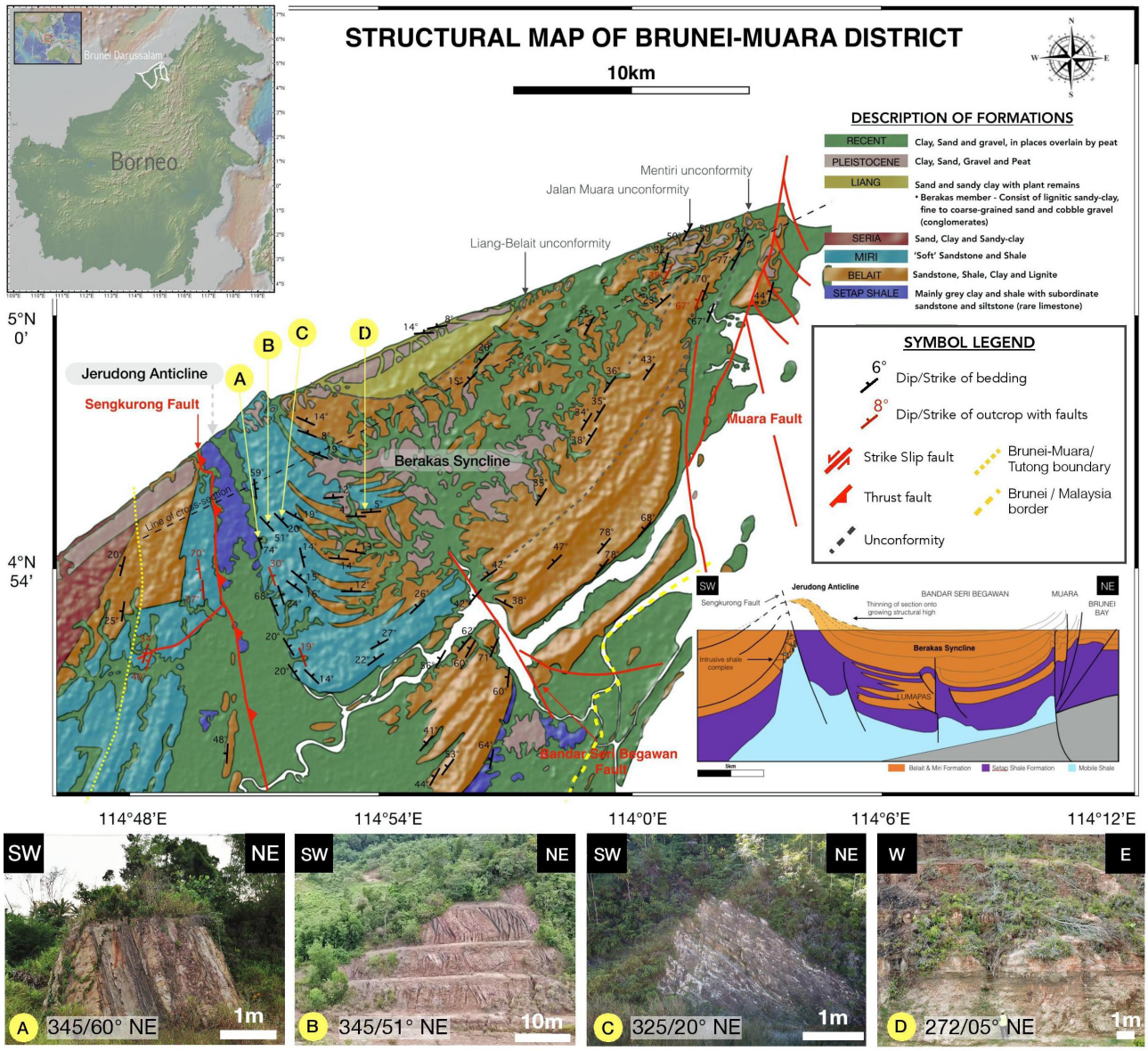

Figure 1: Above: The Geological and structural map of the Brunei-Muara district, which is modified after Wilford (1982), Morley et al. (2003), and Aaisyah et al. (2020). Field evidence of selected outcrops is shown in subsets A to D where the average dip amount of the sedimentary layers varies from steep to gentle angles.

rich country, located within the lush green forests on the north-western part of the Borneo Island (Fig. 1).

The past geological investigations in Brunei are fairly limited with most of the works published with a focus on Petroleum related studies because the country accounts for about 90% of the hydrocarbon exports (Gartrell et al. 2011). The most recent, accessible and significant geological map was compiled by Wilford in 1960 and published by the the Surveyor General Brunei (Wilford, 1982). However, that was about 60 years ago, and much has changed since then. Therefore, there is a strong need to improve the geological and structural maps. Additionally, the outcrop details are largely missing from the previous studies, which is the major challenge that we are solving. More than half of the area of Brunei is still covered with thick foliage therefore aerial photographs are not that useful to uncover the rocks that are hidden under the forests, and the best alternative is to visit the exposed outcrops and film them using UAVs. This is exactly what we have been doing throughout our mission to map the exposed geological outcrops in the region, an exercise that has not been done in any part of the country. Our mission is to create a detailed geological database of the region and convert this data into a 3D model so that classroom field exercises become possible in the near future.

Therefore, the present study explores the possibility to overcome the field-related problems by the use of UAVs carrying a digital camera for an optical survey of exposed geological outcrops with the motivation to map and archive the data in Brunei Darussalam on our university website, which will serve multiple purposes. This data can be used by anyone, particularly students and researchers.

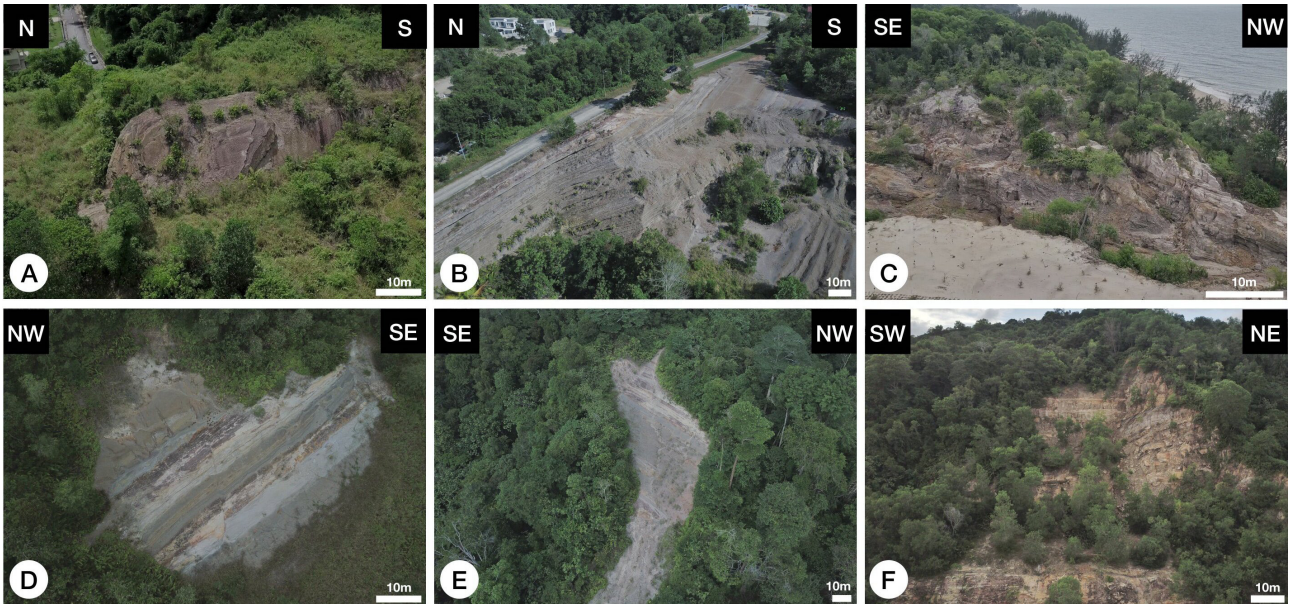

Figure 2: (A-C) Still images of large outcrops captured to show the whole overview of the outcrop that could not be achieved using hand-held cameras. (D-F) Exposed outcrops that were not accessible by foot were surveyed using the UAV by taking still images and videos.

2. REGIONAL SETTING

Brunei Darussalam is part of Borneo Island (Fig. 1), and the present tectonic setting shows that it is enclosed by active plate margins, and it belongs to the Sunda plate. On a regional scale, the Sunda megathrust fault system is the major plate boundary fault system where the Australia plate subducts under the Sunda plate (Shah et al., 2018), and encloses the Island from the south-western side. The eastern portions are marked by a number of basins that are broadly related to the active tectonic developments at the Philippine Sea and the Pacific plates.

The previous geological data of Brunei Darussalam and our field studies suggest that the region is mainly composed of sedimentary beds of alternating sandstone and shale. The bedding data show a folded sequence that is represented by the Berakas syncline in the north and the Belait syncline in the south. Several faults are also mapped in the region (Fig. 1). The geological investigations presented here started in Brunei-Muara district, which is one of the administrative divisions of the country and hosts most of the population. The field area covers the Berakas syncline and the Jerudong anticline which expose rocks of the Setap Shale, Belait, Miri, and Liang Formations, along with the cover sequences of mainly Holocene sediments (Fig. 1). Morley et al. (2003) mapped three major faults in the region, which are named as Muara, Sengkurong, and the Bandar Seri Begawan faults (Fig. 1).

3. MATERIAL AND METHODS

Prior to conducting any field excursion in the region, we created a base map of the study area by updating the latest Brunei-Muara District geological maps (Wilford 1982; Morley et al., 2003). We used QGIS®

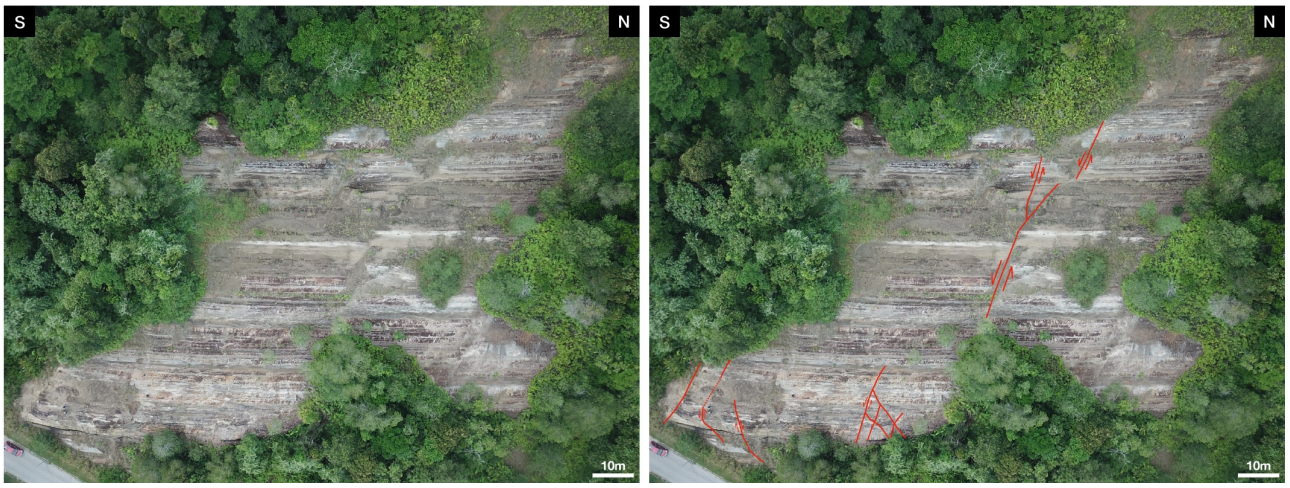

Figure 3: The high-resolution image (4000x3000 pixels) shown on left was captured by the drone, DJI Mavic Pro, and it shows high image quality with clear evidence for faulting (right side) at the “Lion King” outcrop in Jerudong, which is one of the best outcrops to study the faulted sedimentary rocks in Brunei.

Figure 4: Comparison of aerial images of the "Lion King" outcrop in Jerudong (4°53'36.25"N, 114°49'59.01"E): (A) DJI Mavic Pro (resolution: 4000x3000 pixels); (B) Ortho-photo obtained from Survey Department, Ministry of Development, Brunei (resolution: 1085x715 pixels); (C) Satellite image obtained from Google Earth Pro (2019) (resolution: 1175x758 pixels). The images from the DJI Mavic Pro produce much clearer and sharper details.

software to reproduce the map by outlining the Geological formation on a geo-referenced map. These details were then superimposed onto the terrain map of Brunei, which was obtained from GeoMapApp® to show the relief of the research area. The above steps were followed by remote-sensing reconnaissance mapping on the satellite images provided in Google Earth, where we plotted the exposed outcrop sites to be used to conduct the detailed field investigations.We also used scouting survey and from word of mouth to cover the maximum number of exposed outcrops in the region. The fieldwork was conducted from January 2019 until March 2019, and during this time we were able to map the details of a total of 115 outcrops in the Brunei-Muara District. We followed the standard mapping techniques to measure the amount of dip, dip direction, location, and other structural details. Out of the 115 outcrops that we visited, only 65 sites were digitally recorded using the UAV due to time constraints.

The DJI Mavic Pro is one of the best UAVs currently on the market, and we used it for mapping of the exposed geological outcrops. It can capture high-quality images and videos up to 4K resolution at a more affordable cost (€ 700) compared to more sophisticated models such as the Wingtra drone (starting price is € 18,000). The compact size of the UAV makes it easier to carry and the interface is user-friendly. The 12-megapixel camera combined with its 3-axis mechanical gimbal allows the UAV to fly with stability and it can produce detailed data with a < 1.5 % distortion. It is also able to reach remote areas up to 7 km away from the user and this was useful to observe inaccessible outcrops. The images and videos were captured and recorded at various heights: up to the allowed height of 120 m above ground level. The aerial and cross-sectional views of the outcrops (Figs. 2–5) were mapped with ease, and it also includes the focused and detailed views. The collected visual media data was compiled and saved locally on a hard disk drive, along with the necessary geological information of each outcrop.

4. RESULTS AND DISCUSSION

The terrain map provided in Google Earth Pro shows that Brunei Darussalam is part of a folded sequence of rocks that are exposed as plunging folds. The Brunei-Muara region mainly belongs to the ~ N plunging Berakas syncline. The onshore exposed portion of the ~ NE-SW trending right limb of the fold is ~ 29 km long while as the ~ N-S trending left limb is

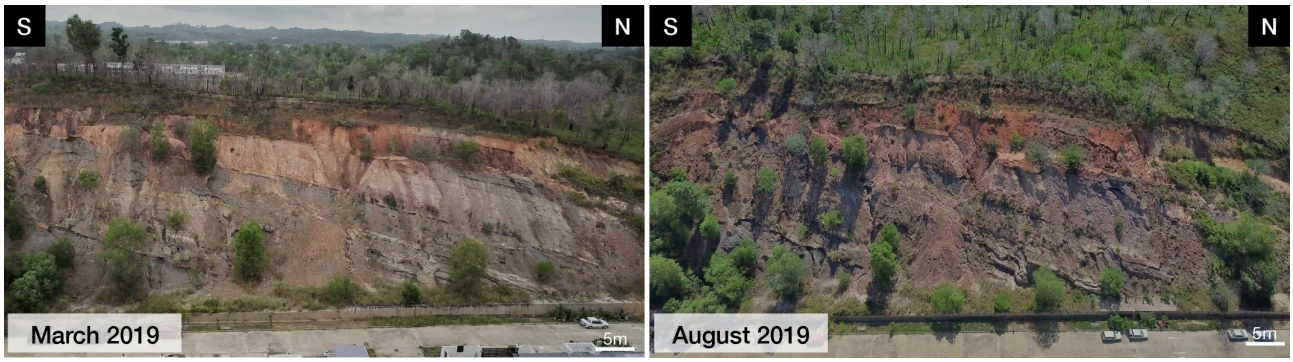

Figure 5: The drone field photograph shows the outcrop coverage at Kg Tungku (4°55'30.2"N, 114°53'51.0"E). The same outcrop was photographed after 5 months (right side). The tropical weather conditions in Brunei facilitate the process of weathering, and erosion, which is usually aided by the frequent rainfall events. This deteriorates the freshness of geological layers and makes observations difficult, which can be captured and preserved via drone footage.

~ 13 km long. We collected data on both the limbs of the Berakas syncline and Jerudong anticline, which are 115 outcrop sites in total. These data were manually plotted on the map (Fig. 1). Most of the outcrops that we visited were composed of alternate layers of sand and shale lithologies with no deformation (Fig. 2). Shallow marine fossils were observed (e.g. bivalve casts, gastrapoda and ophiomorpha) that belong to Miri Formation. The amount of dip of the sedimentary layers varies from 5° to 80° (Fig. 1). Stereonet plots were used to measure the plunging amount and direction of the Berakas syncline that was measured to be 16° towards NNE and for Jerudong anticline it was 9° towards NNW. The different plunging directions of the folds are consistent with the asymmetrical folding geometry of the folded sequence, and this seems to be related to the Sengkurong fault (Fig. 1) that cuts through the fold and runs under the Berakas syncline (Morley et al., 2003).

One of the outcrops with the most prominent exposed structural features is locally known as the “Lion King” outcrop (Aaisyah et al., 2020) and it is located along the Sengkurong fault (Fig. 3). The UAV was used to take the digital details, which was used to map/trace the faults. Due to its large displacement (up to 3 m) that could not be captured using handheld cameras, the drone has proven to be a useful tool at the site. The resolution and details of the images captured using the UAV are better than the data that has been previously published or available as satellite or aerial images of the region, for example the satellite images shown on Google maps and the ortho-photos from the Survey Department of Ministry of Development, Brunei. (Fig. 4). The fault details are easy to map, and quantitative measurements from the digital coverage are possible at ease as the interactive screen provides coverage at various scales, and we can zoom further to capture outcrop details without losing the resolution.

In addition to that, fieldwork exercise shown here has demonstrated that frequent visits to geological sites in tropical rainforests should be preferred. This came to light when we visited one of the outcrops twice over a period of 5 months. Figure 5 shows such an example where photographs taken in March 2019 have recorded a much clearer picture that shows outcrop details that it has lost its sheen in August 2019. This was because of weathering, erosion, and landslides. This also proves the importance of drone mapping and preservation of field evidence in both static and video shots. This is particularly important in regions that experience frequent rains, landslides, or any other activity that erases, and sometimes destroys an outcrop (e.g. urbanization, earthquakes, etc).

5. Conclusions

The work shown above is an on-going project in Southeast Asia where we aim to survey and digitally archive the details of exposed geological outcrops using UAV. We have started this in Brunei, where we have mapped 115 outcrop locations and out of that 65 locations were captured by a drone as still images and videos. Our work has demonstrated the importance of archiving of the geological data where the preservation of outcrop details can be used in the future for education, learning, research, and other uses. It solves problems that are discussed above, and highlights the need to outline a comprehensive framework to improve the mapping courses in sciences and in other disciplines where such exercises are part of the education and learning curriculum. The data produced here provides the first drone coverage of geological outcrops in the region, and will be used to make high-resolution DEM and 3D models using SfM (Structure from motion) photogrammetry, which will further strengthen the geological mapping activities and courses. We strongly believe that recording geological outcrop data is a fundamental step towards improving of the geological maps throughout the world. The COVID-19 world has clearly shown the usability of digital media in education, learning and research. Therefore, such exercises should be done on a priority basis as it solves a number of problems that may hinder or stop geological field activities. The usage of UAVs can greatly aid in the mapping and the preservation of such digital geological data.

6. ACKNOWLEDGEMENT

Funding support was received from the Universiti of Brunei Darussalam under the research grant number: UBD/RSCH/1.4/FICBF(b)/2018/003 for the structural mapping of Brunei. We are also highly thankful to the reviewers for the various comments and suggestions, which have improved the overall quality of the manuscript. The critical comments and valuable suggestions of Dr. Gino De Gelder, Kevin Pedoja and Thomas Rose are highly appreciated. We greatly appreciate the financial support from the Honorable Minister of Development, his Excellency Dato Seri Paduka Awang Haji Suhaimi bin Haji Gafar.

7. REFERENCES

Aaisyah, D, Shah, A.A., Garcia, K., Manan, N., and Anyie, J. 2020. Evidence of Strike-Slip Faulting in Brunei Darussalam, NW Borneo. Conference Proceedings, 82nd EAGE Annual Conference &

Exhibition Workshop Programme, Dec 2020, pp. 1 - 5, https://doi.org/10.3997/2214-4609.202011727.

Bemis, S.P., Micklethwaite, S., Turner, D., James, M.R., Akciz, S. and Thiele, S.T et al., 2017. 'Ground-based and UAV-based photogrammetry: a multi-scale, high-resolution mapping tool for structural geology and paleoseismology', Journal of Structural Geology, vol. 69, pp.163-178, http://dx.doi.org/10.1016/j.jsg.2014.10.007

Dolphin, G., Dutchak, A., Karchewski, B. and Cooper, J., 2019. 'Virtual field experiences in introductory geology: addressing a capacity problem, but finding a pedagogical', Journal of Geoscience Education, vol. 62, no. 2, pp.114-130, http://dx.doi.org/10.1080/10899995.2018.1547034

Elkins, J.T., and Elkins N.M.L., 2007. 'Teaching geology in the field: significant geoscience concept gains in entirely field-based introductory geology courses', Journal of Geoscience Education, vol. 55, no. 2, pp. 126-132, http://dx.doi.org/10.5408/1089-9995-55.2.126

Gartrell, A., Torress, J., and Hoggmascall, N., 2011. 'A regional approach to understanding basin evolution and play systematic in Brunei – unearthing new opportunities in a mature basin', In: International Petroleum Technology Conference, 15-17 November 2011 Bangkok, Thailand. http://dx.doi.org/10.2523/15171-MS

Google Earth Pro 7.3. 2019. Lion King outcrop 4°53'36.25"N, 114°49'59.01"E. Satellite map, viewed 18 August 2020. <https://earth.google.com/web/@4.89346489,114.83302223,225.41282285a,10.00047429d,35y,275.2201h,0t,0r>

Hurst, A., cited in: Friedman, B., 2012. 'Educator seeks to nurture creativity', AAPG Explorer, January 2012, viewed 18 August 2020 <https://explorer.aapg.org/story/articleid/1776/educator-seeks-to-nurture-creativity>

Jordan, B.R., 2015. 'A bird's-eye view of geology: the use of micro drones/UAVs in geologic fieldwork and education', GSA Today, pp 50 – 52, http://dx.doi.org/10.1130/GSATG232GW.1

King, E., 2018. 'Aerial drones in mineral exploration', Geology for Investors, 12 December 2018, viewed 18 August 2020 <https://www.geologyforinvestors.com/aerial-drones-in-mineral-exploration/>

Mezghani, M.M., Mohammed Fallatah and Abdul Jaleel AbuBashait, 2018. 'From drone-based remote sensing to digital outcrop modeling: integrated workflow for quantitative outcrop interpretation', Journal of Remote Sensing & GIS, vol. 7, no. 2, http://dx.doi.org/10.4172/2469-4134.1000237

Morley, C.K., Back, S., Rensbergen, P.V., Crevello, P. and Lambiase, J.J., 2003. 'Characteristics of repeated, detached, Miocene – Pliocene tectonics inversion event, in a large delta province on an active margin, Brunei Darussalam, Borneo', Journal of Structural Geology, vol. 25, no. 7, http://dx.doi.org/10.1016/s0191-8141(02)00130-x

Piras, M., Taddia, G., Forno, M.G., Gattiglio, M., Aicardi, I., Dabove, P., Lo Russo, S. and Lingua, A., 2016. 'Detailed geological mapping in mountain areas using an unmanned aerial vehicle: application to the Rodoretto valley, NW Italian Alps', Geomatics, Natural Hazards and Risk, vol. 8, no. 1, pp. 137-149, http://dx.doi.org/10.1080/19475705.2016.1225228

Rocca, R., 2017. 'Low cost 3d mapping using a commercial drone/UAV: application in structural geology', AAPG International Conference & Exhibition, Barcelona, Spain, 3-6 April, viewed 27 April 2020 <http://www.searchanddiscovery.com/documents/2017/42054rocca/ndx_rocca.pdf>

Shah, A.A., Mohd Zhafri, Jumat, D., and Batmanathan, N.M., 2018. 'Major strike-slip faults identified using satellite data in central Borneo, SE Asia', Geosciences, vol.8, no. 5, p. 156, http://dx.doi.org/10.3390/geosciences8050156

Wilford, G. E., 1982. Geological Map of Brunei and Adjacent Parts of Sarawak, map, scale 1:152000, sheet 2, Surveyor General Brunei, Brunei Darussalam.

Beyond Printing – Communicating Science

What Peer-review Experiences Can Offer to Early Career Scientists and to the Scientific Community

Gwenaëlle Gremion[1,2,✉], Mathieu Casado[3], Kelsey Aho[2,4], Jilda Alicia Caccavo[2,5,6,7], Nicolas Champollion[2,8], Emily Choy[2,9], Sarah L. Connors[10], Rahul Dey[2,11], Alfonso Fernández[2,12], Gerlis Fugmann[2,3], Juan Höfer[2,13], Shridhar Jawak[2,14], Martine Lizotte[2,15], Sarah Maes[2,16], Kyle Mayers[2,17], Katja Mintenbeck[18], Jhon Fredy Mojica[2,19], Prashant Pandit[2,20], Elvira Poloczanska[18], Paul Rosenbaum[2,21], Elisa Seyboth[2,22], Sarah Shakil[2,23], Maud van Soest[2,24]

[1] Institut des Sciences de la Mer, Université du Québec à Rimouski, Rimouski, G5L3A1, Canada;
[2] Association of Polar Early Career Scientists (APECS), D-14473, Germany;
[3] Alfred Wegener Institute, Helmholtz Centre for Polar and Marine Research, Germany;
[4] International Arctic Research Center, University of Alaska Fairbanks, Fairbanks, Alaska 99775-7340, USA;
[5] Alfred Wegener Institute, Bremerhaven, D-27570, Germany;
[6] Berlin Center for Genomics in Biodiversity Research, D-14195, Germany;
[7] Leibniz Institute for Zoo and Wildlife Research, Berlin, D-10315, Germany;
[8] Université Grenoble Alpes, Institut des Géosciences de l'Environnement, Saint-Martin d'Hères 38400, Grenoble, France;
[9] McGill University, 21111 Lakeshore Road, Ste. Anne de Bellevue, Quebec, Canada H9X 3V9;
[10] Université Paris-Saclay, 91190 Saint Aubin, France;
[11] National Centre for Polar and Ocean Research, Goa, India;
[12] Department of Geography, Universidad de Concepción, Chile;
[13] Escuela de Ciencias del Mar, Pontificia Universidad Catolica de Valparaiso, Valparaiso, Chile;
[14] Svalbard Integrated Arctic Earth Observing System (SIOS), Svalbard Forskningspark, P.O. Box 156, N-9171 Longyearbyen, Norway;
[15] Department of Biology, Université Laval, Québec, Québec G1V 0A6;
[16] KU Leuven, 3000 Leuven, Belgium;
[17] NORCE Norwegian Research Centre AS, Nygårdsgaten 112, 5006, Bergen, Norway;
[18] Alfred Wegener Institute Helmholtz Centre for Polar and Marine Research, Am Handelshafen 12, 27570 Bremerhaven, Germany;
[19] Center for global Sea Level Change (CSLC), New York University Abu Dhabi (NYUAD). Abu Dhabi, UAE;
[20] TERI University, New Delhi, India;
[21] Department of Business Studies, Uppsala University, Uppsala, 75120, Sweden;
[22] Centre for Sustainable Oceans, Faculty of Applied Sciences, Cape Peninsula University of Technology, Cape Town 8000, South Africa;
[23] Department of Biological Sciences, University of Alberta, Edmonton, AB, T6G 2E9, Canada;
[24] Geography and Environment, Loughborough University, Loughborough, LE11 3TU, UK
✉ gwenaelle.gremion@gmail.com

Keywords: APECS, Peer-review, Education, IPCC, Early career scientist

In Memoriam:
This work is dedicated to the memory of our friend and colleague Adrian Dahood-Fritz.

1. Motivations

The primary goal of science is the improvement of true and secure knowledge (Bornmann, 2011). Through peer-review, scientific work in many disciplines is assessed through high-quality evaluation ensuring the advancement of scientific knowledge (Bornmann, 2011). The volume of submissions to journals is likely to rise in the years to come due to the phenomenon of "publish or perish" (e.g., Clapham, 2005) and the advent of citation metrics (e.g., Dehon, McCathie and Verardi, 2009; Golden and Schultz, 2012). Therefore, the pressure for peer-reviewing requirements will likely continue to rise. Unfortunately, the availability of qualified referees is often hampered by high workloads of researchers and the necessity for them to produce their own publications, potentially leaving the bulk of reviews to a handful of experts (Rodríguez-Bravo, et al., 2017). In this context, increasing the number of available reviewers would not only be beneficial to the scientific community, but it would also represent an essential step towards the sustainability of the peer-review process (Golden and Schultz, 2012). Early-Career Scientists (ECSs) could take on a greater share of such reviewing processes. Peer-review opportunities can serve as formative experiences for ECSs that could improve their future submissions (Golden and Schultz, 2012), improve their writing skills, and help them build a reputation (Rodríguez-Bravo, et al., 2017).

2. Objectives

The Association of Polar Early Career Scientists (APECS) aimed to demonstrate that the involvement of ECSs in peer-review is not only a crucial catalyst for their careers but also represents a critical contribution to the scientific community in general. APECS, in association with the Intergovernmental Panel on Climate Change (IPCC), used the Second Order Draft (SOD) of the Special Report on the Ocean and Cryosphere (SROCC) as a platform to answer the question: "How motivated and efficient are ECSs in peer-review activities?". We show that, notwithstanding their academic level, ECSs in this study were competent and motivated in their refereeing activities.

DOI: 10.2312/yes19.15

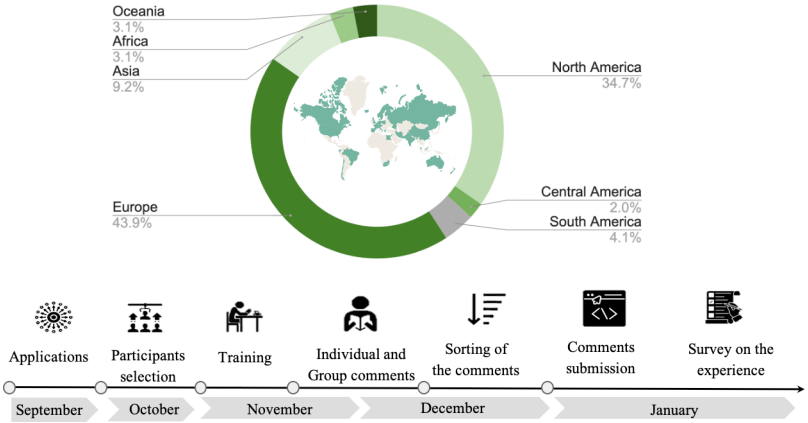

Figure 1: International representation of the selected participants. Countries represented through our participants' institutions appear in green in the World map. A schematic timeline from September to January represents the numerous activities related to the group review.

3. Methods

Based on the previous group review of the First Order Draft (FOD) of the Special Report described in Casado, et al. (2020), a team of 19 council members of APECS chaired the group review of the SOD-SROCC. Chairing activities involved (a) the review of the 201 applications received, (b) the selection of 99 participants, (c) the assignment of chapter sections to the participants, (d) the reviewing and sorting of submitted comments (e.g. finding duplicates and categorizing the comments) and (e) the synthesis of comments into a global review submitted by APECS to the IPCC (Fig. 1). The reviewed comments were sorted into three categories: major, minor, and unfit for submission. 'Major' comments related to scientific content corrections, suggestions for new references, and incoherencies (i.e. substantial). 'Minor' comments encompassed rephrasing and modifications to references. 'Unfit for submission' comments included typos and editorial corrections, duplicates, as well as inappropriate comments defined as unfit for submission; these were not forwarded to the IPCC. Overall, as the evaluation of the comments was conducted by the chairs themselves, and not by an independent panel of experts, we cannot provide an objective evaluation of the quality of comments, and thus limit ourselves to classifying them as the major, minor or unfit. As a result, when we describe the performances in the review process of the participants from different career levels, we only evaluate their efficiency, which we define as the ability to produce a large number of preferentially major comments in a below-average amount of time. Through this opportunity, APECS aimed to offer ECSs the possibility to review chapters and sections of the Special Report that best related to their interests and expertise. ECSs are defined in this project as students (i.e., B.Sc., M.S., or Ph.D.), or early career professionals (ECPs, i.e. Post-Doc researchers, researchers in faculty-level positions for less than 5 years or non-faculty members). The main selection criteria were: motivation, experience, and relevance of the application. A numerus clausus was set up by the chairs based on their availability to efficiently supervise the participants' workload. Then, the final selection was made to allow an equitable distribution of participants by country of residence, and amongst students and ECPs. The selected participants included 36 students and 56 ECPs. The participants were affiliated with non-governmental and governmental organizations from 26 countries (Fig. 1).

A guide explaining the objectives, timeline, and organizational information was created by the project leaders from APECS in association with members of the IPCC Technical Support Unit and representatives from the two Working Groups (WGs) providing scientific leadership to the Special Report (WGI: The Physical Science Basis and WGII: Impacts, Adaptation, and Vulnerability). The guide is included in the supplementary material. In addition, two training webinars were organized to allow discussion between participants and report authors as an introduction to the IPCC goals and mission, the use of the IPCC uncertainty language, as well as an overview of what entailed a constructive review and useful comments. These webinars and the related documentation are included in the supplementary materials as well. Methods for the individual review were, for the most part, similar to those described by Casado, et al. (2020). However, due to prior knowledge of the contents of the Special Report after the FOD, chairs of the SOD were able to allocate specific chapter subsections to participants as a function of their interests and expertise. Moreover, participants were invited, without obligation, to read the entire chapter and provide a synoptic critique. After the submission of the 1083 comments, participants were surveyed on their experience of the review process.

Figure 2: Experience survey from participants indicated a) the personal goals achieved by the selected reviewers among those offered as a choice in our survey, b) the dedicated time they demonstrated for training to proceed to the review by reading the guide and by attending the offered workshops, based on their career level (M.S. grey; Ph.D. blue; Post-Doc. orange; Researcher. yellow), c) the time participants spent doing the review and how much time they would have agreed to provide for the review, based on their career level.

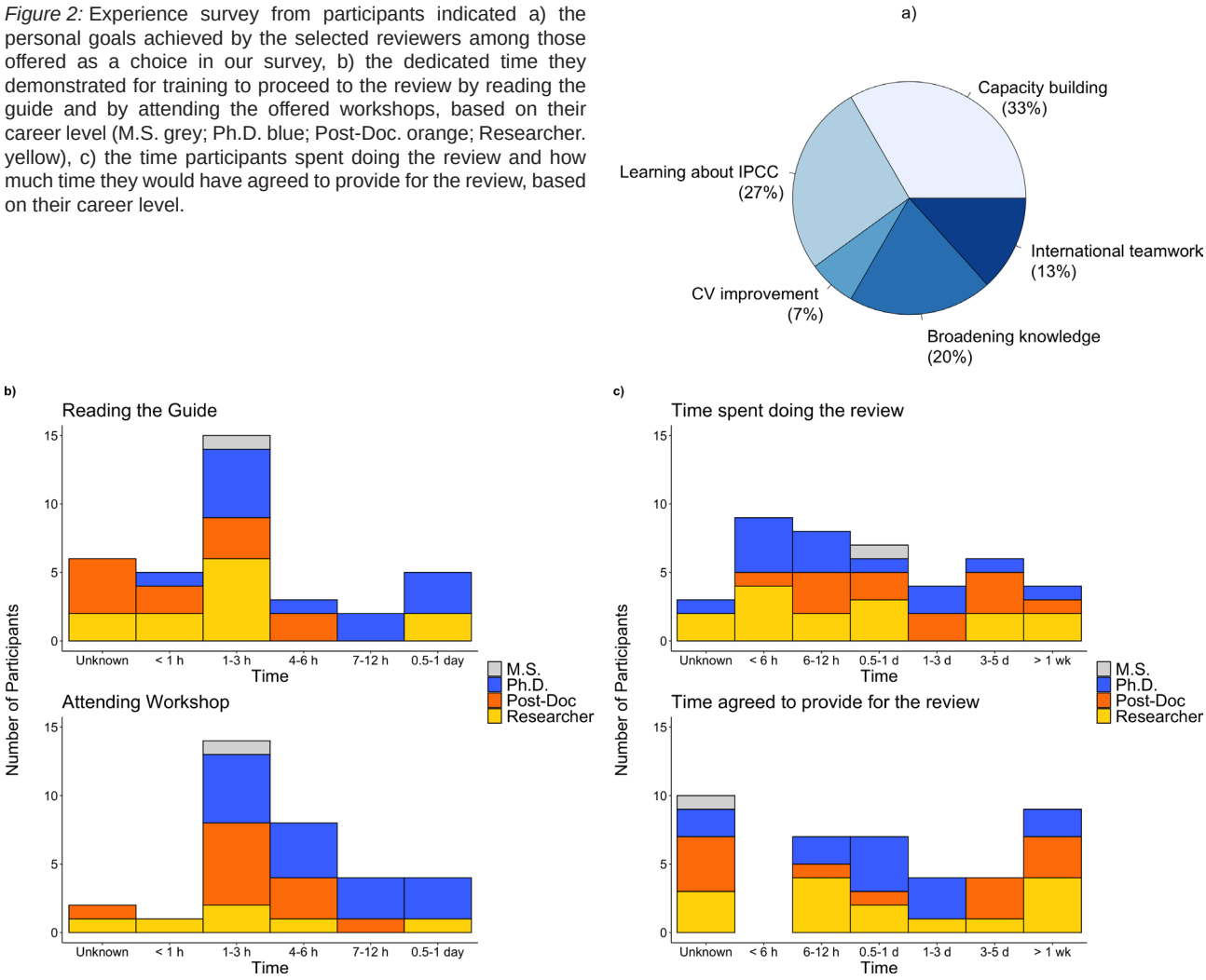

4. Results

Among the 118 reviewers (i.e. participants and chairs), 41 completed the survey representing a 35% rate of participation. The survey demonstrated that the main goals driving the involvement of ECSs in the review were related to capacity building (35 %), the opportunity to expand their literature knowledge (22 %), the opportunity for international collaboration (20 %), and the desire to gain a better understanding of the structure and role of the IPCC (14 %) (Fig. 2a). Distribution charts presented in Figure 2b show that most ECSs dedicated between 1 to 3 h towards preparation on the training guide and webinars before the beginning of the review process. The difference in the amount of time dedicated to preparation by students and early career professionals was not significant neither for the time spent reviewing the guide (chi-squared = 3.101, p-value = 0.3763) nor for the time spent watching the workshops (chi-squared = 6.9272, p-value = 0.07426) (see methods in Casado et al, 2020). ECSs were willing to dedicate more time than they actually needed to proceed with the review (Fig. 2c). Again, no significant difference was found between students and professionals regarding the required time to complete the review (chi-squared = 1.7314, p-value = 0.63). Overall, Ph.D. students provided more comments than their more senior peers (16.4 comments per participant on average for the Ph.D. students, versus 15.6 and 14.0 for Post-Docs and Researchers, respectively), and more minor comments as compared to major ones (218 vs. 187, for the Ph.D. students, which is larger than the Researchers, but smaller than the Post-Docs). Overall, there are no significant differences between the relative number of major comments (chi-squared = 1.3421, p-value = 0.2467), minor comments (chi-squared = 0.7393, p-value = 0.3899) and unfit comments (chi-squared = 1.1427, p-value = 0.2851) between the different career levels (Fig. 3a). Previous review experience of our participants indicates that the majority of individuals in each category had already taken part in review activities prior to this opportunity (Fig. 3b.).

5. Conclusions and perspectives

Following on previous work described by Casado, et al. (2020), results from this study support the idea that ECSs are dedicated and efficient in reviewing activities regardless of their academic level. The

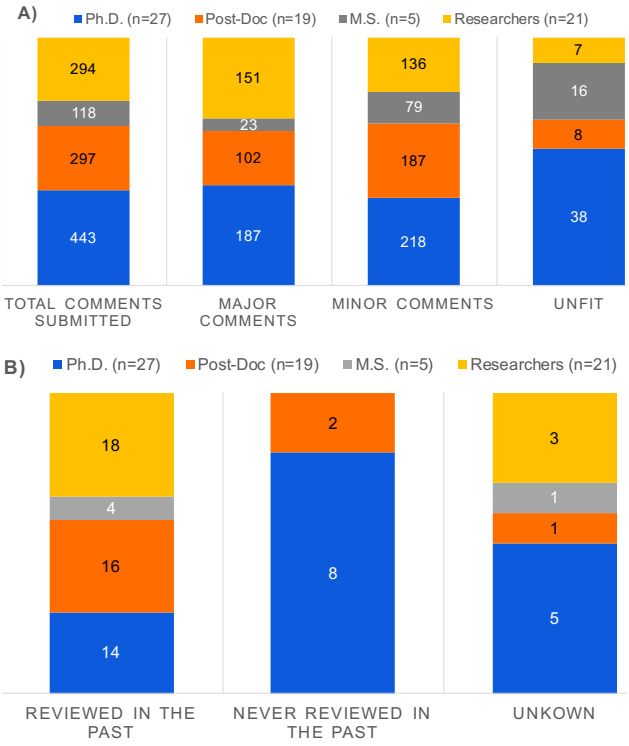

Figure 3: a) Distribution of submitted comments as a function of the participants' position and the quality of submitted comments for each participants' position based on the classification (major comments, minor comments and unfit for submission) of Casado, et al. (2020); b) the review experience of participants depending on their position.

varied review experience of the participants (by career level category), combined with the fact, that the same training was provided to all participants, helps to reduce biases in our results. The quality of comments received from our group was acknowledged by SROCCs authors (Derksen C. and Harper S., Pers. Comm.). As of yet, however, ECS inclusion in the reviewing arena remains marginal and often "ghosted" under the name of their immediate supervisors (MacDowell, 2018). With a mean 2.6 % annual growth in the volume of peer-reviewed articles since 2013 (Publons, 2018), the pressure for scholarly review procedures is intensifying. As it stands, the scientific publishing system and the expansion of a trusted corpus of research literature heavily relies on the scrutiny and critical examination by a limited number of benevolent gatekeepers (Spier, 2002), with 10 % of reviewers being responsible for 50% of all peer-review records (Publons, 2018). There is thus a strategic imperative to transform the peer-review landscape. The shift required to ensure the sustainability of the peer-review process requires the exploration of new approaches and a willingness to tap into a larger and more diversified array of expertise. Findings from the current study advocate for the increased involvement and recognition of ECSs in refereeing activities as submissions and publication outputs continue to rise. Ensuring the quality and integrity of ECS reviews can be explored through a number of ways: (1) participation in group reviews, as is shown in this study and in Casado et al. (2020); (2) exploiting resources such as the Review Quality Instrument that establishes a baseline metric to assess the caliber of a review (van Rooyen, et al., 1999); (3) avoiding ghostwriting practices and instead encouraging senior researchers and editors to recognize co-authored reviews by ECSs (this is the focus of projects such as #ECRPeerReview driven by Future of Research (FoR, Publons, 2018)). The benefits of these approaches are twofold. First and simply put, they alleviate a great deal of the pressure imposed on the global scientific community. Second, these approaches promote capacity-building in ECS by allowing them to keep up-to-date with the latest research trends in their field, to develop their reputation and further their career progression, to improve their own writing skills, and to build relationships with editors and journals. In the current context of rapid climate change and the continued need to develop a meaningful dialogue between knowledge holders, stakeholders, and policymakers (Cortner, 2000), the engagement of well-prepared and proficient ECSs represents an astute investment. The opportunity provided here by the IPCC and APECS is a step forward in the right direction, facilitating the sustainability of the critical reviews of the scientific basis of human-induced climate change risks and the enhancement of sound recommendations for mitigation strategies (Geden, 2015).

6. Supplementary material

Supplementary material to this article can be found online at https://doi.org/10.2312/yes19.15.

7. References

Bornmann, L., 2011. Scientific peer review. Annual Review of Information Science and Technology 45, 197–245. https://doi.org/10.1002/aris.2011.1440450112.

Casado, M., Gremion, G., Rosenbaum, P., Caccavo, J. A., Aho, K., Champollion, N., Connors, S. L., Dahood, A., Fernandez, A., Lizotte, M., Mintenbeck, K., Poloczanska, E., and Fugmann, G., 2020. The benefits to climate science of including early-career scientists as reviewers. Geoscience Communication 3, 89–97. https://doi.org/10.5194/gc-3-89-2020.

Clapham, P., 2005. Publish or perish. BioScience 55, 390–391. https://doi.org/10.1641/0006-3568(2005)055[0390:POP]2.0.CO;2.

Cortner, H. J., 2000. Making science relevant to environmental policy. Environmental Science & Policy 3, 21–30. https://doi.org/10.1016/S1462-9011(99)00042-8.

Dehon, C., McCathie, A., & Verardi, V., 2009. Uncovering excellence in academic rankings: A closer look at the Shanghai ranking. Scientometrics 83, 515–524. https://doi.org/10.1007/s11192-009-0076-0.

Geden, O., 2015. Climate advisers must maintain integrity. Nature 521, 27–28. https://doi.org/ 10.1038/521027a.

Golden, M., & Schultz, D. M., 2012. Quantifying the volunteer effort of scientific peer-reviewing. Bulletin of the American Meteorological Society 93, 337–345.

https://doi.org/10.1175/BAMS-D-11-00129.1.
MacDowell, G., 2018. Recognizing the role of Early Career Researchers in Peer Review. [blog] 13 December 2019. Available at: https://publons.com/blog/recognizing-the-role-of-early-career-researchers-in-peer-review/
Publons, 2018. Global State of Peer Review, Web of Science Group. https://doi.org/10.14322/publons.GSPR2018.
Rodríguez-Bravo, B., Nicholas, D., Herman, E., Boukacem-Zeghmouri, C., Watkinson, A., Xu, J., ... & Świgoń, M., 2017. Peer review: The experience and views of early career researchers. Learned Publishing 30, 269–277. https://doi.org/10.1002/leap.1111.
Spier, R., 2002. The history of the peer-review process. Trends in Biotechnology 20, 357–358. https://doi.org/10.1016/s0167-7799(02)01985-6.
Van Rooyen, S., Black, N., Godlee, F., 1999. Development of the review quality instrument (RQI) for assessing peer reviews of manuscripts. Journal of Clinical Epidemiology 52, 625–629. https://doi.org/10.1016/s0895-4356(99)00047-5.